Shell Evolution in the Region of ^{78}Ni

William Marshall

PhD

University of York

Physics, Engineering and Technology

March 2026

Abstract

The standard nuclear shell model predicts ^{78}Ni to be doubly magic. However, shell evolution may weaken the $Z = 28$ and $N = 50$ closures; whether they persist in this region remains uncertain. The nucleus ^{80}Zn lies on the $N = 50$ shell closure, two protons above ^{78}Ni, probing the shell closure strength. A sensitive probe for nuclear structure is the $R_{BE2} = B(E2, 4_1^+ \rightarrow 2_1^+)/B(E2, 2_1^+ \rightarrow 0_1^+)$. This work presents energy and lifetime measurements of excited states in ^{78,80}Zn from an experiment at the RIBF employing a HPGe tracking array. A $B(E2, 4^+ \rightarrow 2^+)$ value of 153^{+23}_{-16} e^2fm^4 is measured in ^{80}Zn, leading to an R_{BE2} value of $1.05^{+0.20}_{-0.17}$, inconsistent with pure collective expectations. State-of-the-art Discrete Non-Orthogonal Shell Model calculations fail to reproduce these values, predicting a value of 0.616, suggesting additional effects, such as collectivity, may be necessary to describe this nucleus, indicating that the $N = 50$ shell closure may be weaker than previously predicted.

Further experiments are required for a complete understanding, such as the spectroscopy of ^{79}Ni, which will necessitate developments in detector technology. The HYPATIA array is a planned next-generation scintillator array made up of GAGG and $CeBr_3$ scintillators coupled to SiPM detectors. This work develops GAGG SiPM detectors for the array. The best energy resolution of 5.1(2) % FWHM at 662 keV has been achieved. Tests confirmed the detectors' sensitivity to 10 MeV gamma rays and fast neutrons. A sum-amplifier SiPM readout board was developed, achieving a time resolution of 520(20) ps at 1.3 MeV. Improved timing will allow for a reduction in the background and open up the possibility for direct lifetime measurements. Finally, the detectors were clustered into prototype modules that were successfully used in experiments. The HYPATIA array will allow for the spectroscopy of ^{79}Ni, providing a complete understanding of the $N = 50$ shell closure in the region of ^{78}Ni.

Dedication

I would like to dedicate this to Kaori and Hannah.

Acknowledgements

I would like to acknowledge the supervision of Dr Stefanos Paschalis, Dr Pieter Doornebal and Professor Marina Petri. Without their support, this work would not have been possible. I am grateful for the support from the postdocs at the University of York, and the RIKEN Nishina Centre, in particular I would like to thank Dr Ryo Taniuchi, Dr Sidong Chen, Dr Martha Liliana Cortés and Dr Xiaoyu Liu. For their help and expertise in designing, prototyping and manufacturing electronics, I would like to thank: Dr Peter Schury, Dr Hidetada Baba and Timothy Ayers.

I would like to thank the HiCARI and RIBF-181 collaborations for providing me with excellent data and input into the complicated analysis. In particular, I would like to thank Professor Kathrin Wimmer, Dr Serge Franchoo and Professor Daisuke Suzuki. I am grateful to Dr Augusto Macchiavelli for the fruitful discussions on different theoretical models that could be used for interpreting the data. I am thankful for the theoretical calculations from Dr Frédéric Nowacki and Dr Duy-Duc Dao.

I would also like to thank the HYPATIA collaboration for their hard work in preparing and carrying out test experiments for the project. In particular, I would like to thank: Dr Luke Tetley, Dr Gao Ting, Joshua Sharpe, Samuel Guillermo Pozada Barragan and Juan Sebastian Cachaya Munar.

I would like to thank the RIKEN Nishina centre and the BigRIPS group for providing high-quality beams that have allowed for successful experiments. In addition, I would like to thank Dr Tokihiro Ikeda and Asahi Yano for operating the Pelletron tandem accelerator and aiding in the high-energy gamma-ray experiment. Finally, I would like to thank Dr Vi Phong and Dr Shunji Nishimura for their work on the neutron measurements of the GAGG detectors.

Declaration

I declare that this thesis is a presentation of original work and I am the sole author. This work has not previously been presented for an award at this, or any other, University. All sources are acknowledged as References.

Table of contents

Abstract **3**

Dedication **5**

Acknowledgements **7**

Declaration **9**

List of figures **15**

List of tables **31**

1 Introduction **35**

1.1 Atomic Nucleus 35

1.2 ^{78}Ni Shell Closure 36

1.3 Future Gamma-ray Arrays 37

2 Nuclear Structure Theory and The Shell Evolution In the Region of ^{78}Ni **39**

2.1 The Nuclear Shell Model 39

2.2 Deformation and Collectivity 42

2.2.1 Deformation 42

2.2.2 Collectivity 44

2.3 Shell Evolution and Shape Coexistence 45

2.4 DNO-SM - Discrete Non-Orthogonal Shell Model 47

2.5 Gamma-Ray Decay 47

2.6 ^{78}Ni Region 49

2.6.1 ^{78,80}Zn Experimental Measurements 51
2.6.2 ^{78,80}Zn Theoretical Models 55
2.7 Summary 57

3 Gamma-Ray Spectroscopy and Experiments with RI-Beams 59
3.1 Principles of Gamma-ray Detection 59
3.2 Semiconductor Detectors 62
3.2.1 HPGe - High-Purity Germanium 66
3.3 Scintillation Detectors 66
3.3.1 Organic Scintillators 67
3.3.2 Inorganic Scintillators 67
3.3.3 Photo Sensors 69
3.4 Pulse Processing and Data Acquisition 73
3.5 Radioactive Isotope Production and Identification 77
3.6 In-Beam Gamma-ray Spectroscopy 78

4 Fragment Separators, Detectors and Experimental Setup 83
4.1 Isotope Production and Separation 83
4.1.1 Ionisation and Acceleration 83
4.1.2 Fragment Separation and Spectrometry 84
4.1.3 Beam Line Detectors 87
4.2 HiCARI - High-resolution Cluster Array at the RIBF 90
4.2.1 Configuration 93
4.3 DAQ - Data Acquisition System 94

5 Analysis of Neutron Rich Zinc Isotopes 97
5.1 Experimental Details 97
5.2 Simulation 98
5.3 Data Structure and Unpacking 99
5.4 Experimental Doppler Correction 99
5.5 Source Runs and Calibration 100
5.6 Time Alignment and Cuts 102

5.7 Reference Case ^{80}Zn(Be, X)^{80}Zn . . . 104
5.8 Lifetime Analysis . . . 110
5.8.1 ^{81}Ga(Be, X)^{80}Zn . . . 111
5.8.2 ^{78}Zn . . . 111

6 Results and Discussion **115**
6.1 ^{80}Zn - Results . . . 116
6.2 ^{78}Zn - Results . . . 117
6.3 Shell Model Calculations . . . 119
6.4 Zn Systematics . . . 128
6.5 Discussion . . . 129
6.6 Conclusion . . . 132

7 Technical Development for Future Scintillator Arrays **135**
7.1 Scintillator Arrays at the RIBF . . . 135
7.1.1 DALI2+ . . . 135
7.1.2 HYPATIA . . . 136
7.1.3 Expected Efficiency and Resolution . . . 137
7.2 GAGG Characterization . . . 139
7.2.1 Experimental Method . . . 141
7.2.2 Crystal Energy Resolution . . . 142
7.2.3 Time Resolution . . . 148
7.2.4 Crystal Summary and Conclusions . . . 149
7.3 First Generation GAGG Clusters . . . 150
7.3.1 ^{100}Sn Experiment . . . 151
7.3.2 Neutron Discrimination . . . 152
7.3.3 10 MeV Gamma-ray Response . . . 158
7.4 Second Generation GAGG Clusters . . . 166
7.4.1 Board Comparison . . . 170
7.4.2 Time Resolution Measurement . . . 171
7.4.3 Cluster Design and In-Beam Performance . . . 173
7.5 Conclusion . . . 176

8 Conclusion **179**

8.1 Neutron Rich Zn Isotopes 179

8.2 HYPATIA Array 180

8.2.1 Outlook 181

List of figures

2.1 Ordering of proton orbitals calculated using a Woods-Saxon potential [42]. The shell gaps are indicated with the occupancy number. The levels are labelled as nl_j where n is the shell number, l is the orbital angular momentum, and j is the total angular momentum. 40

2.2 Lund convention of quadrupole deformation parameters. The shapes corresponding to the different parameters are shown. Reproduced from [47]. 42

2.3 Energy of orbitals in the N=2 major harmonic oscillator shell varying with deformation parameter δ. The states are labelled according to $\Omega^{\pi}[Nn_3\Lambda]$, where the parameters are explained in the text. Produced using [50], and states are assigned based on [51]. 43

2.4 Diagram showing the effect of shell evolution from the tensor force, where the neutron causes a shift in the proton single particle energies, where $j_{>,<} = l \pm 1/2$. Reproduced from [5]. 45

2.5 Diagram showing the two types of shell evolution. (a) shows the levels before the evolution. (b) and (c) show type I shell evolution. (b) shows the shift due to two neutrons in the $j'_>$ shell and (c) shows the shift due to four neutrons in the $j'_>$ shell. (d) and (e) show type II shell evolution. Where (d) shows the shift due to $2p-2h$ excitations and (e) shows the shift due to $4p-4h$ excitations. Reproduced from [8]. . 46

2.6 Theoretically predicted occupation numbers for 0^+ states in ^{68}Ni. (a) shows the proton occupation numbers, and (b) shows the neutron occupation numbers. Reproduced from [8]. 46

2.7 Evolution of excited states approaching ^{78}Ni, indicating the shifting of single particle energies. (a) shows the low-lying excited states in the $N = 51$ isotones. Data are taken from [60]. The grey area shows missing data. The lowering of the $9/2^+$ state suggests a weakening of the $N = 50$ shell closure. (b) shows the evolution of excited states in Cu ($Z = 29$) isotopes. Data are taken from [60, 61]. The crossing of the $\pi 1p_{3/2}$ and $\pi 0f_{5/2}$ states is observed at ^{75}Cu. The arrows show the trend of the evolution and the levels that are the origin of the states. The insets show the expected configuration of the ground states. The lines are only for indicating the shell effects and are not trend lines. 49

2.8 Experimentally determined excited states in ^{78}Ni. Two bands are observed, which are explained theoretically as a spherical band and a deformed band. The predicted shapes of the excited states are indicated. Data reproduced from [9]. 50

2.9 Literature level schemes of ^{78}Zn (a) and ^{80}Zn (b) compiled from literature [60, 17, 18, 19, 20]. 54

2.10 (a) shows excitation energy systematics for the first 2_1^+ and 4_1^+ states in the Zn isotopes values from literature. Literature values are taken from [60, 64, 20, 17, 18]. The lower plot shows the $R_{42} = E(4_1^+)/E(2_1^+)$ systematics. (b) shows the $B(E2)$ systematics for the Zn isotopes. The literature values are from [65, 17, 18, 20, 19]. The bottom plots shows the $R_{BE2} = B(E2, 4_1^+ \rightarrow 2_1^+)/B(E2, 2_1^+ \rightarrow 0_1^+)$ systematics. 54

2.11 VS-DMRG calculations of $N = 50$ nuclei. The top plot shows the ratio of the 4_1^+ to 2_1^+ energies compared with previous calculations [66]. The middle plot shows the structure of the 2_1^+ and 4_1^+ states and the $B(E2)$ values for transitions between the states in units of $e^2\text{fm}^4$. The bottom plot shows the contribution to the ground state wave function of the 0p-0h configuration in the orange fraction. Reproduced from [67]. 55

2.12 Calculated potential energy surfaces from DNO-SM [21] for ^{79}Zn and ^{80}Zn where β and γ are defined previously. The basis states' deformation parameters are indicated by the red circles, and the size indicates the magnitude of their contribution to the wave function. In ^{79}Zn, the non-deformed $9/2^+$ ground state is shown in the top left plot, the $1/2^+$ deformed isomer observed in [10, 22] is shown in the top middle plot, and a $5/2^+$ deformed state is shown in the top right plot. In ^{80}Zn, a spherical 0^+_1 ground state is predicted, shown in the bottom left plot, whilst a deformed 0^+_2 is predicted at 2.16 MeV, shown in the bottom right plot. Reproduced from [22]. 56

2.13 Potential energy surfaces for the 0^+_1 and 0^+_2 states in $N = 50$ isotones predicted by MCSM [68]. Q_0 shows the a_{20} deformation and Q_2 shows the a_{22} deformation. The basis states, and the circles show their contribution to the wave function. Reproduced from [69]. 57

3.1 Schematic diagram of photoelectric absorption. An electron gains energy by the absorption of a photon, leading to the electron being liberated from the bound state [44]. E_γ is the gamma ray energy and E_0 is the ionisation energy of the electron . . . 60

3.2 Schematic diagram of Compton scattering [70]. γ is the incoming photon, γ' is the scattered photon, and e^- is the scattered electron. θ and ϕ are the photon and electron scattering angles, respectively. 60

3.3 Attenuation coefficient of GAGG [72] and the contributions of the different interactions. Data is from the NIST photon cross-sections database [73]. The attenuation coefficient, μ, gives the probability of interaction, dp, in a short length of material, dx, by the equation $dp = \mu\rho dx$, where ρ is the density of the material. 61

3.4 Monte-Carlo simulations [74] of a NaI(Tl) detector for different energy gamma rays. (a) shows the response for a 662 keV gamma ray. The Compton edge is seen at ≈500 keV, whilst the full-energy peak is seen at 662 keV. The backscatter peak is observed at 184 keV. (b) shows the response for a 10.8 MeV gamma ray. The full-energy peak is seen at 10.8 MeV whilst the single and double escape peaks are seen at 10.2 MeV and 9.7 MeV, respectively. A 511 keV peak is observed from pair production in the surrounding material. Energy deposited shows the energy deposited in the detector, and the measured energy shows the energy smeared by the detector energy resolution. The energy resolution was taken from [75]. 62

3.5 Diagram of the electronic structure of a pn-junction under different conditions. The area under the bottom line shows the valence band, the region between the lines shows the forbidden region, and the area above the top line shows the conduction band. $E_{F\mathrm{p}}$ and $E_{F\mathrm{n}}$ show the Fermi energy for the p and n regions, respectively. V_{bi} is the voltage generated across the pn-junction. Reproduced from [76]. 63

3.6 Simulation of a 2D Si pixel detector. (a) shows the electric potential for a 2D Si detector with one n-type contact at 100 V and three p-type pixels at 0 V. The green lines show the electrode locations. The calculated trajectories of eh-pairs generated at different points marked by crosses are shown. The trajectories of holes are shown in red and electrons in blue. The inset shows the geometry of the detector; the p-type pixels are labelled 1-3. (b) shows the weighting potential for pixel 1 for the same geometry as in (a). (c) shows the induced charges on the pixels calculated using the Shockley-Ramo theory [70, 76]. It is assumed that 1×10^6 *eh*-pairs were generated from a single interaction at the crosses shown in (a); the line colours correspond to the cross colours. As can be seen, the shape of the induced charge on the collecting electrode and nearby electrodes is dependent on the position of origin of the charge. . 65

3.7 Diagram showing the typical configuration of a scintillator detector. The scintillating material is shown in yellow, the photo sensor is shown in black, and the reflector is shown in white. Incoming radiation is depicted using a green arrow, and the resulting scintillation light is shown in red. 66

3.8 Monte Carlo simulation [74] of a $2.5\times2.5\times7.5$ cm^3 BC-400 [82] scintillator detector for a 662 keV gamma ray. Energy deposited shows the energy deposited by the gamma ray in the detector, whilst the measured energy shows the deposited energy smeared by the detector response [83]. 67

3.9 Schematic diagram of the scintillation mechanism in an inorganic scintillator. Electron-hole pairs are produced by the ionised electron, the electron deexcites via a luminescence centre producing a photon, and goes on to recombine with the hole. Quenching shows non-radiative decays, which reduce the scintillation efficiency. Traps show low-lying electron traps, which also reduce the scintillation efficiency. Reproduced from [80]. 68

3.10 Quantum efficiency (QE) of different Hamamatsu PMTs varying with photon wavelength. Data are taken from [93]. 70
3.11 Left shows a schematic diagram of an SiPM. The right shows the electric field varying with position across the SiPM. A depletion region is formed between the p^+ and n^+ layers, causing any electron that enters the region to cause an avalanche breakdown, creating a large gain. Reproduced from [94]. 71
3.12 Quantum efficiency of Hamamatsu SiPMs varying with photon wavelength, two SiPMs are shown corresponding to the S13 and S14 generation SiPMs. Data are from [96, 92]. 72
3.13 SiPM response to different gamma ray energies for different considerations using a HR-GAGG detector [86], and the S13361-6050AE04 SiPM [97]. Ideal shows the case where every photon produced leads to a pixel firing, PDE only shows the case where only the quantum efficiency is considered, and PDE and Non-Linearity shows the case when the quantum efficiency and the limited number of pixels are considered. Using $N_{\text{pixel}} = 229376$, $Q = 0.35$ [97], and $N_{\text{ph}} = 54$ keV^{-1} [86]. The dashed lines show the energy resolution for the different cases, only considering counting statistics and a 5 % energy resolution at 662 keV for the PDE and non-linearity case. 72
3.14 Flow diagram showing the typical layout of an analogue electronics DAQ system. The detector is biased using a voltage supply. The signal from the detector may be passed to a preamplifier if necessary, after which the signal is split. The first stage is for measuring the energy, where the signal is sent to a shaping amplifier followed by an ADC. The second stage is for measuring the time of the event using a discriminator, followed by a TDC. The data from the TDC and ADC are then passed to a computer (event builder) to correlate and save the recorded events. 73
3.15 Circuit diagram of an Ortec 142 type preamplifier [102]. The bias voltage is connected to the bias. The detector is connected to an input where the bias is supplied, and the charge is collected from. Test is an input for a test pulse. E shows the output for energy measurements, and T is the output for timing. Reproduced from [102]. 74

3.16 Diagram showing the process of a CFD. The top left plot shows the incoming wave. The top right plot shows the delayed wave. The bottom left plot shows the inverted and scaled wave (25 %). The bottom right plot shows the sum of the bottom left plot and the top right plot, and the subsequent zero crossing point is indicated with the dashed line. 75

3.17 Diagram of a digital QDC algorithm [104]. A digital CFD is used for triggering and determining the time of the event; a dashed line indicates the zero crossing point. The green gate shows an integration gate used for determining the energy of the event. The red gate shows a shorter gate that can be used for pulse shape analysis. 76

3.18 Diagram of the trapezoidal filter. A sample waveform is shown in orange, the trapezoidal filter output is shown in blue, and the peaking time is shown in black. The peaking time is the sample of the trapezoid that is used to calculate the energy. 76

3.19 Diagram of a typical in-beam gamma-ray spectroscopy experiment in inverse kinematics. An incoming heavy ion interacts with the target, producing a beam-like product in an excited state. The beam-like product decays via the emission of a gamma-ray that is measured in a detector. β is the velocity of the ion at the time of gamma-ray decay, and θ is the angle of emission relative to the motion of the beam-like product. 79

3.20 Energy resolution after Doppler correction varying with emission angle θ in the lab-frame [30] for $E_{\gamma 0} = 1.0$ MeV, $E_{res}(662\text{ keV}) = 5$ %, $\sigma_\beta = 0.01$, and $\sigma_\theta = 0.025$ rad. The individual contributions to the resolution are included in the plot. 80

3.21 Diagram showing the lifetime effect in in-beam gamma-ray spectroscopy. The left shows the origin of the effect, an ion decaying at the target centre is shown in red, and an ion decaying later is shown in blue. Θ is assumed in the Doppler correction, whilst Θ' is the correct value; this leads to the asymmetric peak shape shown in the right plot. Reproduced from [112]. 80

4.1 Schematic diagram of ionisation and acceleration path for a ^{238}U primary beam at the RIBF. Reproduced from [115]. 83

4.2 Layout of the BigRIPS Zerodegree beam line at the RIBF. The final two acceleration stages are shown along with the fragment separators. The focal planes of the separators are shown using F*i*. The HiCARI label shows the position at which in-beam gamma-ray spectroscopy is performed. Diagram is adapted from [122, 9]. 84

4.3 Schematic diagram of the plastic scintillator detector used in the beam line. There is a plastic scintillator in the centre with two PMTs attached, labelled PMT-L and PMT-R. 87
4.4 Diagram of a PPAC detector. Reproduced from [127]. 88
4.5 Diagram of a MUSIC detector, the black shows the cathodes, and the red shows the anodes. Reproduced from [126]. 90
4.6 Picture of the HiCARI array, detectors are marked with their type: MB, Miniball; SC, Superclovers; and GR, GRETINA. 91
4.7 Diagram of crystal structure for a Miniball detector and electronics, and picture of a complete Miniball triplet. Reproduced from [23]. 91
4.8 Left shows a cross-section of one Superclover cluster, the hollow centre shows the central contact of the detector. Centre shows the geometry of the detector and cryostat. Right shows the segmentation of crystals. Adapted from [132]. 92
4.9 Geometry of GRETINA Quad detectors. (a) shows the internal geometry of a quad GRETINA detector (a.a), and the crystal segmentation (a.b). (b) shows the external geometry with the outside shell, electronics and liquid nitrogen dewar. Reproduced from [29]. 92
4.10 Angular distribution of events relative to the HiCARI array centre, where θ is the angle between the beam direction, and ϕ is the azimuthal angle, with the x direction being defined parallel to the ground. 93
4.11 Simplified block diagram of the DAQ system for the experiment. 94

5.1 Residual energy calibration fits to ^{152}Eu calibration runs. The calibrated spectra were fitted to obtain the calibrated peak positions. The obtained energies were plotted against the true energy and fitted with a first-order polynomial. Summary shows an arbitrary crystal ID. (a) shows the residual calibration parameters from after the experiment, and (b) shows the residual calibration parameters from before the experiment. 101
5.2 Calibrated sum spectrum of Miniball and Superclovers for run 244 with ^{152}Eu source. 102

5.3 Time analysis of the HiCARI detectors. (a) shows the time difference between the F8 plastic signal and the HiCARI events separated by crystal after time alignment. (b) shows the time difference between the F8 plastic time and the HiCARI event time with the Doppler-corrected gamma-ray energy after time alignment, and separated into non-tracking and tracking detectors. Gates have been applied to remove non-coincident background, which is shown by the black lines. 103

5.4 PID and velocities for ^{80}Zn inelastic scattering. (a) shows PID plots for BigRIPS (left) and ZeroDegree (right). The ZeroDegree PID is after gating on ^{80}Zn in BigRIPS. The gates applied for ^{80}Zn inelastic scattering are shown by the black lines. (b) shows the determined velocities for BigRIPS (F5-F7) and Zerodegree (F9-F11) alongside the interpolated mid-target velocity. 104

5.5 Doppler corrected spectra for ^{80}Zn inelastic scattering separated into the different detector groups, and the sum of the histograms. The $2_1^+ \rightarrow 0_1^+$ transition is located at $\approx$ 1.5 MeV. 105

5.6 χ^2 graphs for the target position variation from different methods. HiCARI is from fitting the sum histogram of all detectors, and Global is from fitting the independent detector groups and summing the χ^2 values. The minima were determined to be 12.46(21) mm and 12.70(22) mm from quadratic fits. 106

5.7 Determining GRETINA crystal position resolutions from the 2^+ transition in ^{80}Zn(Be,X)^{80}Zn. (a) shows the χ^2 graph for Quad 0 fitting the $2_1^+ \rightarrow 0_1^+$ transition in $^{80}\mathrm{Zn(Be,X)}^{80}$Zn for different position resolutions. The fitted polynomial function is shown in red. (b) shows the determined position resolution for different crystals of GRETINA detectors. 106

5.8 Neutron background determination in $^{80}\mathrm{Zn(Be,X)}^{80}$Zn. (a) shows the non-Doppler corrected sum-spectrum for all HiCARI detectors, with the simulated background gamma-rays shown in red. (b) summarises the background lines observed in the non-Doppler corrected spectrum of $^{80}\mathrm{Zn(Be,X)}^{80}$Zn with the background source listed. Energies and sources are taken from [144, 145]. 107

5.9 χ^2 surfaces for the different detector groups varying the energy and half-life of the 2_1^+ state in ^{80}Zn. The minimum simulated χ^2 is shown with the x, and the +2.3 contour is shown in black. 109

5.10 Systematic uncertainty calculation for ^{80}Zn(Be,X)^{80}Zn, the central values and uncertainties are determined by polynomial fittings to the χ^2 surfaces. Best fit refers to using the minimised values, whilst $\pm 1\sigma$ shows the χ^2 surfaces corresponding to shifting the values by the stated systematic uncertainties. (a) shows the target position variation to determine the energy systematic uncertainty, and (b) shows the position resolution determination to determine the half-life systematic uncertainty. 110

5.11 ^{81}Ga(Be,X)^{80}Zn spectrum separated by detector type. Five clear peaks are observed, consistent with previous measurements [19]. 111

5.12 ^{78}Zn spectra from three different reaction channels: (a) ^{78}Zn(Be,X)^{78}Zn, (b) ^{79}Zn(Be,X)^{78}Zn, and (c) ^{80}Ga(Be,X)^{78}Zn. In all three channels, structures are observed around the 576, 730, and 908/890 keV gamma-ray transitions. In addition, in inelastic scattering, a peak around 1230 keV is observed. For n knockout: a doublet of 1230 and 1270 keV peaks, a peak at 1450 keV, and 1800 keV are observed. In pn knockout, the doublet at 1250 keV, and the peak at 1450 keV are observed. 112

6.1 Best fits for the ^{80}Zn channels. (a) shows the spectra and fits for ^{80}Zn(Be,X)^{80}Zn, and (b) shows the spectra and fits for ^{81}Ga(Be,X)^{80}Zn. The minima determined using the GR P3 and GR Quad analysis were used, but the other detectors are included for reference. 116

6.2 Levels schemes for ^{80}Zn from literature [17, 18, 19] (a), and determined from the experimental channels: ^{80}Zn(Be,X)^{80}Zn (b), and ^{81}Ga(Be,X)^{80}Zn (c). As can be seen, the results are in good agreement with the literature. The black lines indicate the excited states, and the red lines indicate the gamma-ray transitions that have been observed. 117

6.3 Best fits for the ^{78}Zn channels are shown in: (a) for ^{78}Zn(Be,X)^{78}Zn, (b) for ^{80}Ga(Be,X)^{78}Zn, and (c) for ^{79}Zn(Be,X)^{78}Zn. The minima determined using the GR P3 and GR Quad analysis were used, but the other detectors are included for reference. 118

6.4 Levels schemes for ^{78}Zn determined from literature [60] (a), and the experimental channels: ^{78}Zn(Be,X)^{78}Zn (b), ^{80}Ga(Be,X)^{78}Zn (c), and ^{79}Zn(Be,X)^{78}Zn (d). The higher energy transitions have been tentatively assigned as decays directly to the ground state. 120

6.5 Level schemes from the two different theoretical models, (a) for the SDI and (c) for the SDI+QQ, after the minimisation. (b) shows the experimental level scheme for comparison. 124

6.6 Level scheme of ^{80}Zn from DNO-SM (b) [21, 22] calculations compared to the experimental level scheme from ^{81}Ga(Be,X)^{80}Zn (a). The 0_2^+ and 2_2^+ have been plotted independently of the main band as they have a different shape to the main band states. The states in the experimental level scheme have been assigned based on the DNO-SM predictions and the literature values. 126

6.7 Comparison between experimental results and theoretical predictions for ^{80}Zn. (a) shows the excitation energies of the 2_1^+ and 4_1^+ states and their ratio for ^{80}Zn predicted by different models compared with the experimental results. (b) shows the reduced transition probabilities and the R_{BE2} from the experiment compared with the theoretical predictions of different models. 127

6.8 Comparison between experimental results and theoretical predictions for ^{78}Zn. (a) shows the excitation energies of the 2_1^+ and 4_1^+ states of ^{78}Zn predicted by different models compared with the experimental results. (b) shows the reduced transition probabilities from the experiment compared with the theoretical predictions of different models. 128

6.9 (a) shows excitation energy systematics for the first 2^+, and 4^+ states in the Zn isotopes values from literature, and the experiment. Literature values are taken from [60, 64, 20, 17, 18]. The lower plot shows the $R_{42} = E(4_1^+)/E(2_1^+)$ systematics. (b) shows the $B(E2)$ systematics for the Zn isotopes. The literature values are from [65, 17, 18, 20, 19]. The bottom plots shows the $R_{BE2} = B(E2, 4_1^+ \rightarrow 2_1^+)/B(E2, 2_1^+ \rightarrow 0_1^+)$ systematics. 129

6.10 Calculations of excited states in ^{18}Ne compared to the experimental results. The left level scheme shows the calculation with an SDI in the basis $0d_{5/2}$, and $1s_{1/2}$, the middle level scheme shows the same in the basis $0d_{5/2}$, $0d_{7/2}$, and $1s_{1/2}$, and the right shows the experimental values. In both calculations, the separation between the 2_1^+ and 4_1^+ states is not replicated. Reproduced from [2]. 130

7.1 Rendering of a cross-section of the DALI2+ array. The NaI(Tl) is encased in an Al housing with a PMT attached. Reproduced from [84]. 136

7.2 HYPATIA array simulation geometry for Geant4 [74]. There are two parts of the array, a GAGG forward wall and a barrel made up of $CeBr_3$ modules, each containing 2×2 crystals. The beam direction is shown in red. 137
7.3 Simulated performance of the HYPATIA and DALI2+ arrays for in-flight decays at a beam energy of 200 $MeVu^{-1}$. (a) the simulated efficiency of the arrays, and (b) the simulated energy resolution of the arrays. Only points that could be well described by the fit function are included. 139
7.4 Simulated spectra of ^{79}Ni for HYPATIA and DALI2+. (a) shows the simulation for unrealistic statistics. The level scheme is inset; the branching ratios are based on the Weisskopf estimates [43]. The level scheme was adapted from [159]. As can be seen, HYPATIA resolved the doublet whilst DALI2+ fails to do so. (b) shows the case for semi-realistic statistics. The expected counts were calculated using a 2000 pnA ^{238}U beam [154] in LISE++ [125], a 40 mb cross-section on a 150 mm LH target with position reconstruction for a 14 day experiment. In the case of realistic statistics, the peaks are still resolved, whilst in the DALI case, only a single peak is observed. . . . 140
7.5 Circuit diagram for the readout board for the SiPM. P_i refers to the individual pixels of the SiPM. 142
7.6 Definitions of different configurations used for testing the energy resolutions of the crystals. (a) shows the definition of different sides 1 and 2 for a detector. The choice of the labelling is arbitrary. (b) shows the definition of top and side illumination. The red dot shows the source location. 143
7.7 Energy histogram from Epic 1 measurement with top illumination for the 1836 keV ^{88}Y peak. The different fits used in determining the energy resolution and estimating the systematic uncertainty are shown. Original shows the fit used for obtaining the resolution, Narrow Range shows just fitting the region around the peak, Wide Range shows the effect of fitting too large a region, and Pol2 Bkg shows the fit using a quadratic function as the background, as opposed to the linear background used in the remaining cases. 144

7.8 Determined energy resolutions FWHM for different configurations. The top graph shows the energy resolutions for all the tested gamma rays, whilst the lower graph isolates only the resolutions at 662 keV. The labels S-i-S/T refer to Side-i-Side/Top, where side i is the side to which the SiPM is attached and Side/Top refers to whether the illumination is from the side or the top. 144
7.9 Spectra from CETC 2 obtained with ^{137}Cs, ^{60}Co, ^{88}Y sources, with sources placed at the length of the crystal and at the top of the crystal. The spectra were normalised based on the counts at 662 keV. 146
7.10 Setup for collimator scan of the crystals. Left shows a picture of the setup, and right shows a schematic of the setup from the side and from the top. The green line shows the cascade gamma rays being measured in coincidence. 146
7.11 Plots obtained from the collimator scans. 0.0 cm is the top of the crystal, and 7.5 cm is the side with the SiPM. (a) shows the spectra obtained at different collimator positions. Each spectrum has been fitted with a double Gaussian plus a quadratic background. (b) shows the determined peak positions of the ^{60}Co peaks varying with the collimator position. (c) shows the resolution FWHM of the ^{60}Co peaks varying with the collimator position. 147
7.12 Diagram of time resolution measurement, and example time difference spectrum obtained from the measurement. (a) shows a schematic diagram of the setup used for measuring the time resolution of the GAGG detectors. (b) is the time difference between IBS 3 and the $LaBr_3$ reference detector. Ungated is for all events, and gated shows the histogram after the energy gates are applied. 148
7.13 GAGG encapsulated in the plastic housing with the feed-through PCB shown. 150
7.14 Energy resolution of GAGG crystals mounted in the DALI2 frame using the DALI2 DAQ with calibration sources. 151

7.15 Setup for neutron measurement experiment. One cluster from the in-beam experiment makes up the 2×2 cluster, and a single C&A [33] sample was tested. A EJ-200 [81] scintillator was used as the start time. Right shows the schematic with the detector location and the digitiser channel of the detector; the distances are not to scale. S2 refers to sample 2, SE*i* refers to sample Epic *i*, and SK*i* refers to sample Kinheng *i*. Left shows a picture of the setup. Sample 2 is located in its own housing, whilst the remaining GAGGs are in the 3D printed cluster. 152

7.16 Time difference between Sample 2 and the EJ-200 [81] start detector with the energy deposited in Sample 2. Two bands can be seen corresponding to the fast gamma rays and the slow neutrons. The gates used for gating on gamma-ray and neutron events are shown. 153

7.17 Plots showing the waveform analysis for Sample 2 for neutron and gamma ray gates. (a) shows a histogram of normalised waveforms for sample 2 after gating on neutron events from the TOF. The histogram is filled with each sample from each waveform after normalisation and time alignment. (b) shows a graph of the average of the normalised waveforms gated on the TOF. The inset shows a zoomed-in view showing the point of difference in the two curves. (c) shows the normalised histograms of the 10 % to 90 % rise time for the neutron and gamma TOF gates. 154

7.18 Schematic diagram showing the PSD gates used for discriminating gamma rays and neutrons. g_1 integrates the start of the signal, g_2 integrates the tail of the signal, and g_3 integrates the full signal. 155

7.19 PSD discrimination plots and the corresponding FOM values. (a) shows the PSD peaks for neutron and gamma events for different short gate end points. Using PSD $= g_1/g_3$. The fits used to obtain the FOM values are also shown. (b) shows the FOM values obtained for the PSD $= g_1/g_3$ for different gate lengths. (c) shows the FOM values obtained for the PSD $= g_2/g_3$ for different gate lengths. 157

7.20 (a) shows the level scheme for the 0.6, and 1.7 MeV resonances in the $^{12}\mathrm{C}(\mathrm{p},\gamma)^{13}\mathrm{N}$ reaction. Data taken from [60]. (b) shows the level scheme for the 0.992 MeV resonance in the $^{27}\mathrm{Al}(\mathrm{p},\gamma)^{28}\mathrm{Si}$ reaction. The level scheme has been simplified to only show the decay paths relevant to this analysis. The energies are shown in units of keV. Data taken from [178]. 158

7.21 Schematic diagram of the RIKEN Pelletron accelerator facility. The H^- ions are produced in the SNICS (Source of Negative Ions by Caesium Sputtering) [180] ion-source, which are then accelerated by the tandem accelerator, leaving the ions as H^+, which are then directed to the desired beam line using the switching magnet. Reproduced from [181]. 159

7.22 Setup for the experiment. (a) shows a picture of the detectors surrounding the beam pipe. Beam direction is left to right. (b) shows the setup diagram. The grey detectors are the DALI2 detectors, and the GAGG detectors are shown in yellow. Left and right are defined with respect to the beam direction. 160

7.23 Varying the time window to find the optimal gate length. Al spectrum for Epic 1, varying the event building time window, with Compton suppression. The 10.8 MeV peak and its two escape peaks are visible. 162

7.24 Calibration of Al target runs using ^{88}Y, ^{137}Cs, ^{60}Co, and ^{28}Si lines. Including single and double escape peaks for the 10.8 MeV gamma ray. 163

7.25 Plots showing the calibration of DALI detectors. (a) shows the carbon calibration for Ch23, a NaI detector, using the calibration sources and in-beam data. (b) shows the calibrated spectrum from Ch23, a DALI2 detector, for the carbon runs. Can see a 511 keV from pair production, and the 2.4, and 3.5 MeV gamma rays from ^{13}N [60]. In addition, two unknown gamma rays are seen at 437 keV and 1629 keV. 164

7.26 Determined energy resolutions for the different samples using the bias voltage V_2. With the data from the Aluminium target runs and calibration runs after the beam time. The trends are fitted with the $p_0 + p_1 E^{p_2}$ function. 164

7.27 Saturation energy of the quadratic calibration varying with overvoltage from the carbon target data. CETC 1 and 2 are not included due to poor performance. The samples are labelled with the type of SiPM used 4×4 indicates the S13361-6050AE-04 [97], and 8×8 indicates the S13361-3050AE-08 [96]. A dashed line indicates the +3 V recommended by Hamamatsu [96, 97]. 166

7.28 Comparison of S133161-6050, and S144161-6050 SiPM quantum efficiencies data taken from [97, 92]. The GAGG emission spectrum, taken from [38], is overlaid on top. As can be seen, a small improvement in quantum efficiency is observed. 167

7.29 S14161-6050HS-04 SiPM PCB. (a) shows a rendering of the SiPM PCB for S14161-6050HS-04 with labels of the elements of the PCB. (b) shows the SiPM soldered on the board alongside the other components. 167
7.30 Circuit diagram of simple readout board alongside pictures of the assembled PCB for the circuit shown in Figure 7.5. 167
7.31 Circuit diagrams used to test different possible circuit diagrams, looking to reduce the effect of the larger capacitance of the S14 SiPMs. (a) shows the circuit with the capacitively coupled fast output, and (b) shows the sum-amplifier circuit. 168
7.32 Simulated response of the different readout circuits. Single pixel shows the response of a single pixel passed through an inverting operational amplifier. Fast output 4×4 shows the response of the circuit shown in Figure 7.31a. Inverting amplifier shows the response of 16 pixels connected in parallel with an inverting operational amplifier. Sum amplifier 4×4 shows the response of the circuit shown in Figure 7.31b. The responses have been baseline corrected and normalised to make the comparison easier. 169
7.33 Constructed readout board PCB with the sum-amplifier configuration. (a) shows the bottom of the PCB, and (b) shows the top of the PCB. (c) shows the oscilloscope output of the initial values, showing the oscillations. 170
7.34 CETC 1 for top illumination energy resolution for different photosensor readouts. The S13 data is repeated from Section 7.2, in comparison to the S14 with simple readout and sum-amplifier readout. The errors are determined using the method from Section 7.2. 171
7.35 Schematic diagram for the time resolution measurement. The left shows the $LaBr_3$ detector, and the right shows the GAGG detector. The source is shown in red, two sources were used: ^{60}Co and ^{22}Na. 171
7.36 CTR optimisation with a ^{22}Na source for CETC 1. (a) shows the optimisation of the CFD delay with a bias voltage of 41 V. It appears that the CTR decreases with decreasing CFD delay, but going below 16 ns caused issues with the trigger. A delay of 16 ns was used. (b) shows the optimisation of the bias voltage for CETC 1; it was decided that a bias of 43.5 V was used. 172

7.37 (a) shows the CTR values obtained for the different samples varying with the gamma ray energy deposited in the GAGG detector. There is a large variation in the performance. (b) shows the average waveforms for 662 keV gamma rays obtained using the same process used in the neutron analysis. 172
7.38 Time resolution after subtraction for the GAGG samples. Due to the fast reference detector, the difference between the CTR and individual resolutions is small. 173
7.39 The left graph shows the calibration of Kinheng 1 for the in-beam gamma-ray experiment. Whilst the right graph shows the determined energy resolution after calibration for Kinheng 1. 174
7.40 Doppler corrected spectra for events gated on the ^{51}Ca(C, X)^{50}Ca reaction channels for HYPATIA and DALI2+ detectors. The $2_1^+ \rightarrow 0_1^+$ transition is fitted using a Gaussian plus a linear background. 176

List of tables

1.1 Table comparing the properties of different scintillator materials, showing the energy resolutions, densities, whether the material is hygroscopic and if the material has internal activity and the source of the radiation. Energy resolution is FWHM at an energy of 662 keV. Data taken from [32, 33, 34, 35]. 37

2.1 Energies (keV) of gamma-rays from ^{78}Zn excited states from literature. I indicates isomer decay, CX indicates Coulomb excitation, K indicates knockout, and ENSDF stands for the Evaluated Nuclear Structure Data File [60]. Uncertainties are omitted if they are not present in the corresponding publication. J_i^π and J_f^π indicate the initial and final state angular momentum and parity. In cases where the transition is not present in the data set, the space is left with a hyphen. 52

2.2 Energies (keV) of gamma-rays from ^{80}Zn excited states from literature. CX indicates Coulomb excitation, and K indicates knockout. J_i^π and J_f^π indicate the initial and final state angular momentum and parity, respectively. X is used in cases where the J^π is unreported, and the space is left empty when the initial and final states are unknown. In cases where the transition is not present in the data set, the space is left with a hyphen. 52

2.3 $B(E2\downarrow)$ and $t_{1/2}$ values for ^{78,80}Zn from literature. A hyphen indicates the values are not present in the corresponding publications. 53

4.1 Detectors and other material in the beam-line for BigRIPS (F0-F7). The devices are listed in order of their position in the beam line from the most upstream to the most downstream [124]. Mix refers to detectors made up of multiple materials. β_{after} is the beam velocity after the element for ^{80}Zn ions calculated using LISE++ [125]. 85

4.2 Detectors and other material in the beam-line for ZeroDegree (F8-F11). The devices are listed in order of their position in the beam line from the most upstream to the most downstream. Mix refers to detectors made up of multiple materials. β_{after} is the beam velocity after the element for ^{80}Zn ions calculated using LISE++ [125]. 87

5.1 Summary of experimental runs. HiCARI run no. refers to the tun number of the HiCARI DAQ, and BigRIPS run no. refers to the run number of the beam-line DAQ. 97

5.2 Initial half-lives and statistical uncertainties for the 2_1^+ state in ^{80}Zn for different detector groups. - indicates that no minimum was found in the simulated range. . . . 109

6.1 χ^2_{red} values for the best fits for the ^{80}Zn channels. For both channels the χ^2_{red} values are close to 1. 115

6.2 Determined energies and half-lives of excited states in ^{80}Zn. The first columns show the literature values, the middle columns show the results from $^{80}\text{Zn}(\text{Be},\text{X})^{80}\text{Zn}$, and the final columns show the results from $^{81}\text{Ga}(\text{Be},\text{X})^{80}\text{Zn}$. The first uncertainty shows the statistical uncertainty, and the second shows the systematic uncertainty. Cases where the measurement is not available are indicated with a hyphen. 116

6.3 Reduced χ^2 values for the best fits for the three reaction ^{78}Zn channels. GR P3 and GR Quad both achieve a χ^2_{red} of ≤ 2.2. 118

6.4 Determined energies and half-lives of excited states in ^{78}Zn. The first column shows the literature values, and the other columns show the results measured in this experiment. The first uncertainty shows the statistical uncertainty, and the second shows the systematic uncertainty. Cases where the measurement is not available are indicated with a hyphen. 119

6.5 Best fit parameters determined by the χ^2 minimisation. SDI is the model with only the SDI, and SDI+QQ is the model with the QQ interaction added. The C_0 and κ values are of the expected order, whilst e_{eff} is large. 123

6.6 The weights of the components of the wave functions of the calculated excited states for the interactions: SDI and SDI+QQ. 124

6.7 Selected experimental observables compared with the values predicted from the theoretical models. The values were taken from the ^{81}Ga(Be,X)^{80}Zn channel results, except for the $B(E2,2_1^+ \rightarrow 0_1^+)$ which was taken from [20]. Both models underpredict the $B(E2,4_1^+ \rightarrow 2_1^+)$ relative to $B(E2,2_1^+ \rightarrow 0_1^+)$, and the ratio of the 4_1^+ to 2_1^+ energies. 125

6.8 Comparison between the jun45 and jj44pna calculations of ^{78,80}Zn and the experimental measurements. The $E(4_1^+)$ for ^{78}Zn is taken from [64], and the $B(E2,2_1^+ \rightarrow 0_1^+)$ for ^{80}Zn is from [20]. 125

6.9 $B(E2)$ values from the DNO-SM calculations for ^{80}Zn. 126

6.10 Occupation numbers of states in ^{80}Zn from DNO-SM. n_ν^*, and n_π^* show the number of neutrons and protons above the $Z = 28$ and $N = 50$ shell closures, respectively. The $0_{1,2}^+$ occupation numbers are also reported in [22]. 127

7.1 GAGG samples tested for the HYPATIA array alongside their dimensions and manufacturer. 140

7.2 Coincidence time resolution (FWHM) of different samples measured in coincidence with a large volume $LaBr_3$ detector. 149

7.3 Different bias voltages used to power the SiPMs for the different GAGG samples. V_i are the labels for the different voltage conditions used in the experiment. 161

7.4 List of experimental runs and a description of the conditions used. V shows the voltage of the tandem terminal, E_p shows the estimated proton energy, and T shows the target used. See Table 7.3 for the bias voltage information. 161

7.5 Energy resolution of the 10.8 MeV full-energy peak for the Al runs. Only detectors that resolved the 10.8 MeV peak are included. 165

7.6 Coincidence time resolutions for CETC 1 taken with ^{60}Co source in coincidence with a large volume $LaBr_3$. 171

7.7 GAGG prototype clusters used for the experiment. Feed-through refers to the connectors used to pass the HV and signal in and out of the housing. 174

Chapter 1

Introduction

1.1 Atomic Nucleus

The atomic nucleus is made up of protons and neutrons and presents a unique many-body quantum system, where simplified models are required to describe nuclear properties. A common simplification is seen in the nuclear shell model [1], where a central plus spin-orbit potential is used to calculate the energy of nucleon orbitals with residual interactions between the nucleons [2].

In addition, the atomic nucleus presents novel phenomena not observed in other systems. A naive approach would predict the nucleus to be spherical; however, elements of the nuclear interaction can induce deformation and non-spherical shapes [3]. In particular nuclei, it is possible to observe two states at similar energies that have very different shapes; this is known as shape coexistence [4].

The nuclear shell model predicts the shell closures at proton and neutron numbers: 2, 8, 20, 28, 50, 82 [1]. However, interactions between the nucleons cause the evolution of the shells depending on the occupancy of the other shells [5]. This effect causes traditional shell gaps to weaken and new ones to emerge, such as has been observed in the $N = 20$ island of inversion [6, 7]. Shell evolution is suggested as the cause of shape coexistence [8]. Additional information is necessary to explain the forces involved in shell evolution.

This work explores two pathways for expanding the knowledge of nuclear structure. The first looks at the analysis of excited states in ^{78,80}Zn. The second explores the development of a novel scintillator array that will allow for the exploration of previously unaccessible regions of the nuclear chart. Both projects will provide for a better understanding of the atomic nucleus and the forces involved.

1.2 ^{78}Ni Shell Closure

The nucleus ^{78}Ni lies on the standard shell model closures $Z = 28$ and $N = 50$. It is naively expected that the closures are preserved in this region. $E(2_1^+)$ systematics would suggest the shell closure is maintained; however, evidence for shape coexistence is presented [9]. Zn lies at $Z = 30$, two protons more than Ni, meaning it can be used as a probe of the shell model closure. Shape coexistence has been directly observed in ^{79}Zn and has been suggested to be due to intruder states across the $N = 50$ shell closure, as a result of shell evolution [10]. This work looks at ^{78,80}Zn to draw conclusions about the persistence of the $N = 50$ shell closure and look for evidence of shape coexistence. Of particular interest is ^{80}Zn due to its lying on the $N = 50$ neutron shell closure. It is key to understand this region because it will provide a better understanding of the forces involved in shell evolution.

The nuclei ^{78,80}Zn excited state energies and half-lives have been explored with the use of the High-resolution Cluster Array at the RIBF (HiCARI), a high-purity germanium (HPGe) array at the Radioactive Isotope Beam Factory (RIBF) [11]. These results will then be compared to theoretical calculations to extract information about nuclear structure in this region.

Excited states in ^{78}Zn have been measured to a high precision via decay spectroscopy [12, 13, 14, 15, 16]. The $B(E2, 2_1^+ \rightarrow 0_1^+)$ has been evaluated by low-energy Coulomb excitation [17, 18], but has not been determined by other methods. In addition, other transitions have been observed from knockout reactions [19]. This work calculates the $B(E2, 2_1^+ \rightarrow 0_1^+)$ via lifetime measurements and has measured several higher energy transitions that are as yet unreported.

The energy and $B(E2)$ of the 2_1^+ state in ^{80}Zn have been measured by low and high energy Coulomb excitation [17, 18, 20]. Higher-lying states have been observed by knockout reactions, where the $B(E2, 4_1^+ \rightarrow 2_1^+)$ was assessed by lifetime measurements with a significant uncertainty [19]. This work reports the $B(E2, 4_1^+ \rightarrow 2_1^+)$, to improve on the uncertainty of the previous values. This allows for conclusions about the nuclear structure of ^{80}Zn to be drawn. In addition, the lifetimes of other states will be determined to look for evidence of shape coexistence.

These results are then compared to several theoretical models, including state-of-the-art calculations from the Discrete Non-Orthogonal Shell Model (DNO-SM) [21, 22]. From these measurements, conclusions about the persistence of the $N = 50$ shell closure in the region are drawn. In addition, evidence of shape coexistence in ^{80}Zn will be presented, which is interpreted as intruder configurations

	HR-GAGG(Ce)	$CeBr_3$	$LaBr_3$(Ce)	NaI(Tl)
Energy resolution/%	5	4	3	6
Decay time/ns	90-170	17	35	230
Density/gcm^{-3}	6.3	5.2	5.08	3.67
Hygroscopic	×	✓	✓	✓
Internal activity	×	×	^{138}La	×

Table 1.1 Table comparing the properties of different scintillator materials, showing the energy resolutions, densities, whether the material is hygroscopic and if the material has internal activity and the source of the radiation. Energy resolution is FWHM at an energy of 662 keV. Data taken from [32, 33, 34, 35].

across the $N = 50$ shell gap [22]. These results will be important for understanding the forces involved in shell evolution and will have impacts across the nuclear chart.

1.3 Future Gamma-ray Arrays

Currently, two main types of gamma-ray detection arrays exist: segmented HPGe detectors such as Miniball [23] and scintillator arrays such as the Detector Array for Low Intensity Radiation 2 (DALI2) [24]. These technologies have been used successfully for studying nuclear structure, such as Miniball observing evidence of octupole deformation [25], or DALI2 observing new shell closures in ^{54}Ca [26].

Pulse shape position reconstruction has been used to develop HPGe detectors with sub-segment position resolution in the Advanced Gamma Tracking Array (AGATA) [27] and the Gamma-Ray Energy Tracking In-beam Nuclear Array (GRETINA) [28, 29] projects. These developments have allowed for improvements in the Doppler-corrected energy resolutions for high-velocity experiments [30]. This technology was implemented in the HiCARI [11] array, which was used in the Zn experiment. However, the low efficiency [31] of HPGe detectors limits the applications.

In recent decades, the development of scintillator materials has progressed rapidly to produce high-density, high-luminosity and fast inorganic scintillators [35]. These materials can be used in scintillator arrays to provide arrays with a high efficiency and excellent energy resolution, with the improved timing performance allowing for the reduction of background and for high-beam rate experiments, a lower probability of pileup. Table 1.1 shows a comparison of several different scintillators. NaI(Tl) is an older material that has been used in many arrays, such as DALI2 [24]. It can be produced in large volumes but suffers from a poor energy resolution, low density and being hygroscopic. The

current leader of scintillator detectors is $LaBr_3$ and is used in arrays such as the International Detector Assembly for Fast-Timing Measurements of Exotic Nuclei (IDATEN) array [36]. It has a high density, fast decay time and an exceptional energy resolution for a scintillator detector, but is hygroscopic and has significant internal activity [34], making it unsuitable for low count rate experiments. $CeBr_3$ [37] presents a competitive choice for low count rate experiments thanks to it having similar properties to $LaBr_3$ without the internal activity. HR-GAGG [38] has a worse energy resolution than $CeBr_3$, but has the advantage of a higher density and being non-hygroscopic, allowing for higher efficiencies.

For the reasons stated above, a planned new array known as the Hybrid Photon Detection Array to Investigate Atomic Nuclei (HYPATIA) will use HR-GAGG and $CeBr_3$ scintillators in a hybrid configuration [39, 40]. HR-GAGG will be placed at forward angles, where, thanks to its high density and being non-hygroscopic, they can be packed tightly into a high-efficiency forward wall. The $CeBr_3$ will be arranged into a barrel configuration at higher angles to exploit the excellent energy and time resolution of $CeBr_3$.

This work will focus on the testing and development of HR-GAGG detectors, looking at the energy and timing performance of samples from different manufacturers. In addition, novel electronics systems have been designed and characterised, and the results will be presented here. From this development, the ideal manufacturers will be inferred. The HYPATIA array will allow for the first spectroscopy of ^{79}Ni, providing crucial information on the $N = 50$ shell closure.

Chapter 2

Nuclear Structure Theory and The Shell Evolution In the Region of ^{78}Ni

The atomic nucleus is a many-body bound quantum system made up of protons and neutrons. For ^{2}H, the system can be solved analytically with the one-pion exchange potential (OPEP) [41]; however, as more nucleons are added, simplifications are needed.

2.1 The Nuclear Shell Model

Nuclei containing magic numbers (2, 8, 20, 28, 50, ...) of protons and/or neutrons exhibit specific properties not observed in other nuclei [1]. To interpret this, the nuclear shell model [1, 43] is employed. The Hamiltonian, H, for the nuclear system considering two-body interactions is written as

$$H = \sum_{i=1}^{A} \frac{p_i^2}{2m_i} + \sum_{\substack{i,j=1 \\ j>i}}^{A} V(\vec{r}_i, \vec{r}_j) \tag{2.1}$$

where p_i is the momentum operator, m_i is the mass of the nucleon, A is the number of nucleons and $V(\vec{r}_i, \vec{r}_j)$ is the potential generated between two nucleons. In the shell model approach, the

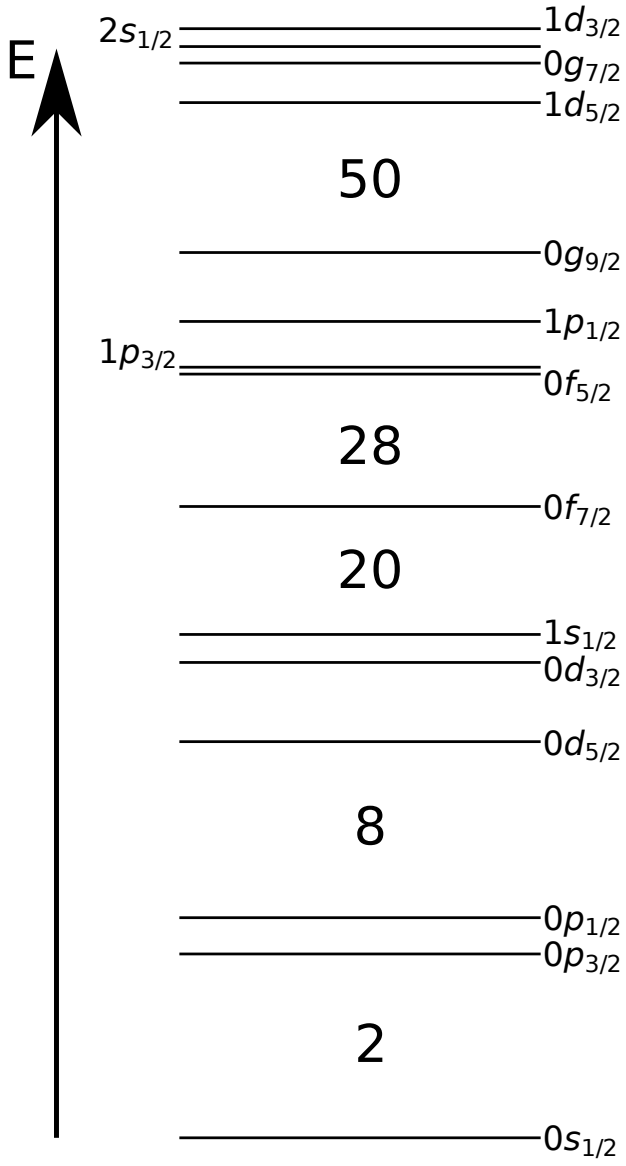

Fig. 2.1 Ordering of proton orbitals calculated using a Woods-Saxon potential [42]. The shell gaps are indicated with the occupancy number. The levels are labelled as nl_j where n is the shell number, l is the orbital angular momentum, and j is the total angular momentum.

nucleon-nucleon interaction is reduced to a mean-field and residual term by

$$H = \left(\sum_{i=1}^{A} \frac{p_i^2}{2m_i} + \sum_{i=1}^{A} V(\vec{r}_i) \right) + \left(\sum_{\substack{i,j=1 \\ j>i}}^{A} V(\vec{r}_i, \vec{r}_j) - \sum_{i=1}^{A} V(\vec{r}_i) \right) \tag{2.2}$$

$$H = H_{MF} + H_{RES} \tag{2.3}$$

$$H_{MF} = \sum_{i=1}^{A} \frac{p_i^2}{2m_i} + \sum_{i=1}^{A} V(\vec{r}_i) \tag{2.4}$$

$$H_{RES} = \sum_{\substack{i,j=1 \\ j>i}}^{A} V(\vec{r}_i, \vec{r}_j) - \sum_{i=1}^{A} V(\vec{r}_i) \tag{2.5}$$

where $V(\vec{r}_i)$ is the mean-field potential, H_{MF} is the mean-field Hamiltonian and H_{RES} is the residual Hamiltonian [2]. Typically, the mean-field potential is modelled by a central potential, for example, a harmonic oscillator potential or a Woods-Saxon potential and a spin-orbit term of the form

$$V_{ls} = -\frac{2}{\hbar^2} \alpha(\vec{r}) \vec{l} \cdot \vec{s} \tag{2.6}$$

where $\alpha(\vec{r})$ is the potential strength, $\vec{l}$ is the orbital angular momentum operator and $\vec{s}$ is the spin operator. In the mean-field limit ($H_{RES} \approx 0$), the model predicts a shell structure with shell gaps corresponding to the magic numbers [1]. The single particle orbitals of a Woods-Saxon potential plus a strong spin-orbit interaction, calculated using Nucracker [42], are shown in Figure 2.1; as can be seen, the magic numbers are recreated.

The independent particle model assumes that only the non-interacting valence nucleons contribute to the nuclear structure, with the remaining nucleons forming an inert core [44]. In cases with one valence nucleon outside a strong closed core, this can describe nuclear properties well. However, with many valence nucleons, it is necessary to include interactions between the nucleons [43]. These interactions can be included by using a two-body interaction. This can be approximated using a surface delta interaction [45] or effective interactions such as jun45 [46].

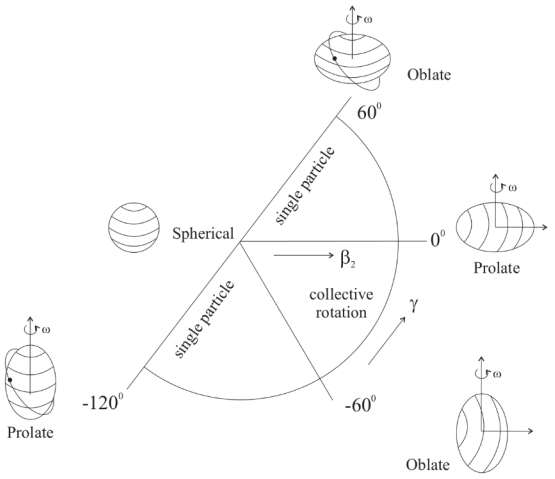

Fig. 2.2 Lund convention of quadrupole deformation parameters. The shapes corresponding to the different parameters are shown. Reproduced from [47].

2.2 Deformation and Collectivity

Doubly magic nuclei contain both magic numbers of protons and neutrons, such as ^{40}Ca. The spherical shell model can describe nuclei in the region of doubly magic nuclei well, but others require more complicated considerations, such as deformation and collectivity.

2.2.1 Deformation

Many nuclei exhibit evidence of being nonspherical [48]. The shape of nuclei can be described by a multipole expansion

$$R(\theta,\phi) = R_0\left(1+\sum_{\mu,\lambda} a_{\mu\lambda}Y_{\mu\lambda}(\theta,\phi)\right) \tag{2.7}$$

where $R(\theta,\phi)$ is the nuclear radius, R_0 and $a_{\mu\lambda}$ are constants and $Y_{\mu\lambda}$ are spherical harmonics [49]. The most important component of deformation is the $\mu = 2$ component corresponding to quadrupole deformation. The constants can be converted to deformation parameters β and γ

$$a_{20} = \beta\cos\gamma \tag{2.8}$$

$$a_{22} = \frac{1}{\sqrt{2}}\beta\sin\gamma \tag{2.9}$$

where β describes the magnitude of the deformation and γ the type of deformation [49]. This can be seen in Figure 2.2.

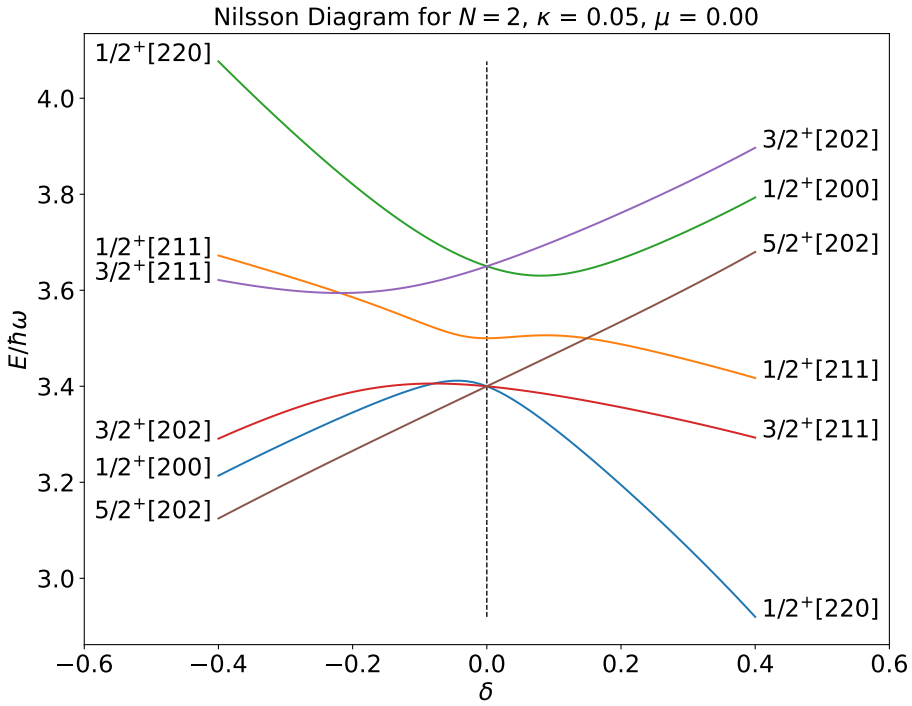

Fig. 2.3 Energy of orbitals in the N=2 major harmonic oscillator shell varying with deformation parameter δ. The states are labelled according to $\Omega^{\pi}[Nn_3\Lambda]$, where the parameters are explained in the text. Produced using [50], and states are assigned based on [51].

This deformation emerges away from closed shells due to it being energetically favourable. This can be explored in single particle terms using the Nilsson model with the Hamiltonian, H,

$$H = \frac{p^2}{2M} + \frac{1}{2}M(\omega_1^2 x_1^2 + \omega_2^2 x_2^2 + \omega_3^2 x_3^2) - 2\hbar\omega_0\kappa\vec{l}.\vec{s} - \hbar\omega_0\kappa\mu\vec{l}^2 \tag{2.10}$$

$$\omega_1 = \omega_2 = \omega_0^2\left(1 + \frac{2}{3}\delta\right) \tag{2.11}$$

$$\omega_3 = \omega_0^2\left(1 - \frac{4}{3}\delta\right) \tag{2.12}$$

$$\omega_0(\delta) = \omega_0(0)\left(1 - \frac{4}{3}\delta^2 - \frac{16}{27}\delta^3\right)^{-1/6} \tag{2.13}$$

where ω_i are the potential constants along the different axes, ω_0 is the energy value, M is the nucleons mass, κ is a constant and δ is a deformation parameter where $\delta \approx 0.95\beta$ [43, 3].

This deformation parameter leads to a reordering of single-particle orbitals. This reordering can be seen in Figure 2.3 for the $N = 2$ major oscillator shell. Due to the non-spherical potential, orbital angular momentum is no longer a good quantum number and states are labelled according to

$\Omega^{\pi}[Nn_3\Lambda]$, where Ω is the projection of the total angular momentum along the deformation axis, π is the parity, N is the oscillator shell, n_3 is the oscillator level along the deformation axis and Λ is the projection of the orbital angular momentum along the deformation axis [3, 48].

2.2.2 Collectivity

So far, only single-particle states have been considered. However, nuclei can also exhibit collective behaviour. There are two key types of collective behaviour: vibration and rotation. For a rotor with no intrinsic angular momentum, it has an energy of

$$E_{\text{rot}} = \frac{\hbar^2}{2\mathscr{J}} I(I+1) \tag{2.14}$$

where $\mathscr{J}$ is the moment of inertia and I is the angular momentum [43]. This leads to a noticeable signature for a rigid rotor of

$$\frac{E(4_1^+)}{E(2_1^+)} = 3.33 \tag{2.15}$$

allowing for the determination of collective rotational bands.

The second collective motion is vibrations, where the nuclear surface can be described by

$$R(t) = R_{av} + \sum_{\lambda \geq 1} \sum_{\mu=-\lambda}^{\lambda} \alpha_{\lambda\mu}(t) Y_{\lambda\mu}(\theta, \phi) \tag{2.16}$$

where R_{av} is the average radius and $a_{\lambda\mu}(t)$ are the vibration amplitudes [44]. The energy, $E_{vib}(n)$, of the systems are given by

$$E_{\text{vib}}(n) = (n + 1/2)\hbar\omega \tag{2.17}$$

where n is the number of phonons and ω is the oscillation frequency. This model leads to a distinct signature in the excitation energies of

$$\frac{E(4_1^+)}{E(2_1^+)} = 2 \tag{2.18}$$

from which nuclear vibrations can be identified [44].

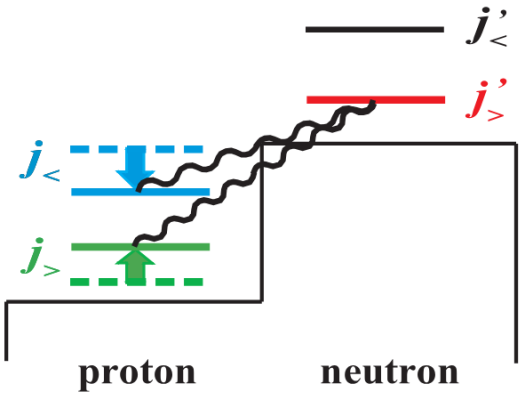

Fig. 2.4 Diagram showing the effect of shell evolution from the tensor force, where the neutron causes a shift in the proton single particle energies, where $j_{>,<} = l \pm 1/2$. Reproduced from [5].

2.3 Shell Evolution and Shape Coexistence

It is naively expected that the magic numbers are fixed across the nuclear chart. However, it has been observed in several regions that the conventional shell closures can weaken, and new ones may emerge [26, 6]. A well-known example is the $N = 20$ island of inversion around ^{32}Mg, in which the weakening of the $N = 20$ shell gap is observed [7]. Shell evolution is suggested to be driven by residual interactions, and shape coexistence occurs due to the weakening of the shell gap, which allows for intruder deformed configurations [8, 52].

This shell evolution can be explained by the tensor term in the OPEP [5, 53]. A schematic of the effect of the tensor interaction on shell ordering is shown in Figure 2.4, where $j_{>,<} = l \pm 1/2$. Neutrons in the $j'_>$ orbit attract the $j_<$ proton orbit, leading to its lowering in energy, whilst they repel the $j_>$ orbit, leading to its raising in energy [5].

Two distinct types of shell evolution are noted, type I being the shell evolution across various isotopes and type II being the evolution of shell ordering due to the different occupation numbers of excited states [8]. A diagram of these effects can be seen in Figure 2.5.

Shell evolution weakening shell closures and allowing intruder configurations across shell gaps has been suggested as the cause of shape coexistence [52]. This can be seen in ^{68}Ni with a spherical 0^+_1 state, a mildly oblate-deformed 0^+_2 state and a strongly prolate-deformed 0^+_3 state [8]. Figure 2.6 shows the occupation numbers for the different excited states in ^{68}Ni. The increase in occupation of the $\nu 0g_{9/2}$ in the 0^+_2 and 0^+_3 states leads to the energy of the $\pi 0f_{7/2}$ increasing and the $\pi 0f_{5/2}$ decreasing, allowing for intruder configurations across the $Z = 28$ shell gap inducing the deformation

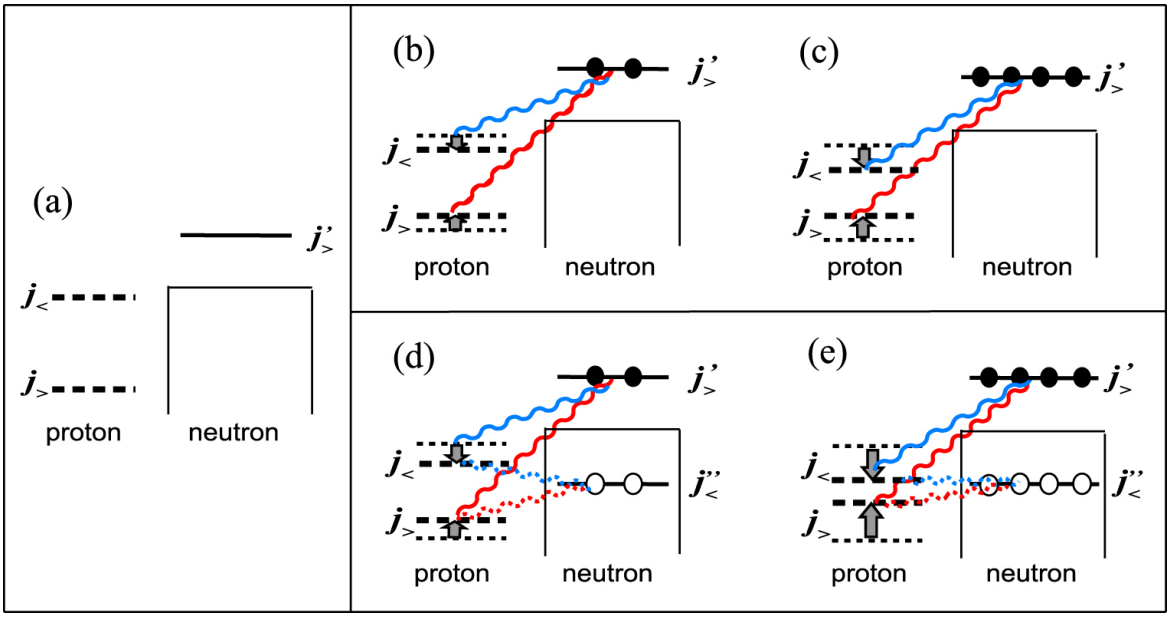

Fig. 2.5 Diagram showing the two types of shell evolution. (a) shows the levels before the evolution. (b) and (c) show type I shell evolution. (b) shows the shift due to two neutrons in the $j'_>$ shell and (c) shows the shift due to four neutrons in the $j'_>$ shell. (d) and (e) show type II shell evolution. Where (d) shows the shift due to $2p-2h$ excitations and (e) shows the shift due to $4p-4h$ excitations. Reproduced from [8].

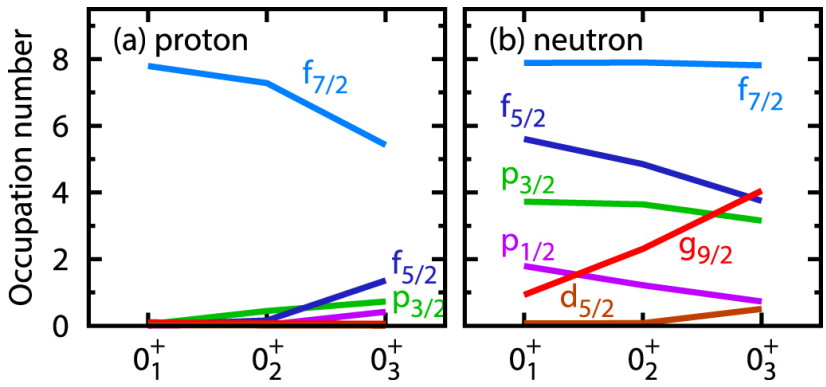

Fig. 2.6 Theoretically predicted occupation numbers for 0^+ states in ^{68}Ni. (a) shows the proton occupation numbers, and (b) shows the neutron occupation numbers. Reproduced from [8].

of these excited states [8]. This is an example of type II shell evolution producing shape coexistence. Type I shell evolution is also proposed as a mechanism for shape coexistence in some nuclei, for example, deformed states in ^{32}Mg are interpreted as neutron $p-h$ excitations across the $N=20$ shell gap [54].

2.4 DNO-SM - Discrete Non-Orthogonal Shell Model

The standard shell model uses spherical basis states, whilst the Nilsson model requires a fixed deformation. In order to include states of different deformation, more complex theoretical models are necessary. One such method is DNO-SM [21]. The method uses a set of basis states with different deformation parameters [21]; therefore, this model is capable of predicting deformed configurations. The minimisation method allows for a dramatic reduction in the number of basis states. For instance, in a model of ^{24}Mg in the *sd* shell, the exact shell-model approach predicts a binding energy of -87.10445 MeV with 28503 basis states, whilst the DNO-SM approach predicts -87.10405 MeV with only 16 basis states [55], allowing this model to make accurate predictions in heavy nuclei. In ^{84}Mo the model predicts a $B(E2,2_1^+ \rightarrow 0_1^+)$ of 1512 e^2fm^4 in agreement with the experimental value of 1740^{+580}_{-430} e^2fm^4 [55]. The method has been shown to be capable of predicting shape coexistence, as is the case in ^{62}Cr [56].

2.5 Gamma-Ray Decay

Excited states in nuclei primarily decay to the ground state via a series of gamma-ray decays. For instance, this is observed in the β decay of ^{137}Cs, which primarily decays to an excited state in ^{137}Ba, which decays to its ground state by the emission of a 662 keV gamma ray [57].

The transition probability between the initial state i and the final state f is given by

$$T_{fi}^{(\sigma\lambda\mu)} = \frac{2}{\varepsilon_0\hbar}\frac{\lambda+1}{\lambda[(2\lambda+1)!!]^2}\left(\frac{E_\gamma}{\hbar c}\right)^{2\lambda+1}\left|\left\langle \xi_f J_f m_f|\mathscr{M}_{\sigma\mu\lambda}|\xi_i J_i m_i\right\rangle\right|^2 \tag{2.19}$$

$$T_{fi}^{(\sigma\lambda)} = \frac{1}{2J_i+1}\sum_{m_i\mu m_f} T_{fi}^{(\sigma\lambda\mu)} \tag{2.20}$$

where $\lambda\mu$ is the multipolarity of the transition, σ is the type of transition, E_γ is the energy of the gamma ray, $\mathscr{M}_{\sigma\mu\lambda}$ is the operator associated with the radiation and J_k, m_k and ξ_k are the total

angular momentum, the axis projection of the angular momentum and an arbitrary quantum number, respectively for state k. $T_{fi}^{(\sigma\lambda\mu)}$ is the partial transition rate and $T_{fi}^{(\sigma\lambda)}$ is the summed transition rate [2]. The reduced transition probabilities are calculated using

$$\begin{aligned} B(\sigma\lambda, J_i \to J_f) &= \frac{1}{2J_i+1} \sum_{m_i \mu m_f} \left| \left\langle \xi_f J_f m_f | \mathscr{M}_{\sigma\mu\lambda} | \xi_i J_i m_i \right\rangle \right|^2 \\ &= \frac{1}{2J_i+1} \left| \left\langle J_f || \mathscr{M}_{\sigma\lambda} || J_i \right\rangle \right|^2 \end{aligned} \tag{2.21}$$

where B is the reduced transition probability and $\left\langle J_f || \mathscr{M}_{\sigma\lambda} || J_i \right\rangle$ is the reduced matrix element [2, 43]. There are two types of transitions, either electric or magnetic, denoted E or M, respectively, with angular momentum L, with L having integer values greater than or equal to 1. The change in parity, $\Delta\pi$, is given by

$$\Delta\pi = \begin{cases} (-1)^L & EL \\ (-1)^{L+1} & ML \end{cases} \tag{2.22}$$

. Gamma-ray decay obeys both parity and angular momentum conservation, limiting the possible decays [44].

The $B(E2)$ values provide an observable of the overlap of two states without being influenced by the energy contribution to the transition rate. One method for this is by measuring the half-life of states, which can be converted to $B(E2)$ values using the equations

$$t_{1/2} = \frac{\ln(2)}{T_{fi}^{(E2)}} \tag{2.23}$$

$$B(E2, J_i \to J_f) = 75 \varepsilon_0 \hbar \left(\frac{\hbar c}{E_\gamma} \right)^5 \frac{\ln(2)}{t_{1/2}} \tag{2.24}$$

where $t_{1/2}$ is the half-life of the state, assuming that the $E2$ decay is dominant [2]. The ratio of the $B(E2, 4_1^+ \to 2_1^+)$ and the $B(E2, 2_1^+ \to 0_1^+)$ can be used to determine the nuclear structure. For the harmonic oscillator, an $R_{BE2} = 2$ is expected, for a rotor, a value of 1.43 is expected, whilst single particle transitions typically lead to values ≤ 1 [58, 59]. Weisskopf estimates of reduced transition

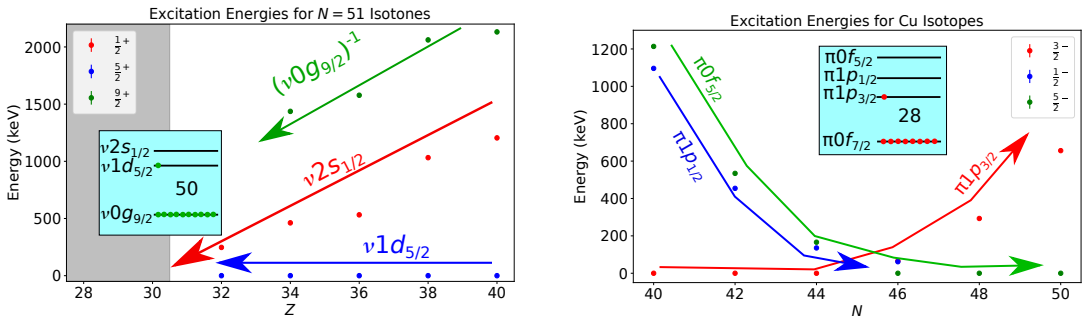

(a) (b)

Fig. 2.7 Evolution of excited states approaching ^{78}Ni, indicating the shifting of single particle energies. (a) shows the low-lying excited states in the $N = 51$ isotones. Data are taken from [60]. The grey area shows missing data. The lowering of the $9/2^+$ state suggests a weakening of the $N = 50$ shell closure. (b) shows the evolution of excited states in Cu ($Z = 29$) isotopes. Data are taken from [60, 61]. The crossing of the $\pi 1p_{3/2}$ and $\pi 0f_{5/2}$ states is observed at ^{75}Cu. The arrows show the trend of the evolution and the levels that are the origin of the states. The insets show the expected configuration of the ground states. The lines are only for indicating the shell effects and are not trend lines.

probabilities are given as

$$B(EL) = \frac{(1.2)^{2L}}{4\pi}\left(\frac{3}{L+3}\right)^2 A^{\frac{2L}{3}} e^2 fm^{2L} \tag{2.25}$$

$$B(ML) = \frac{10}{\pi}(1.2)^{2L-2}\left(\frac{3}{L+3}\right)^2 A^{\frac{2L-2}{3}}\left(\frac{e\hbar}{2Mc}\right)^2 (fm)^{2L-2} \tag{2.26}$$

where M is the mass of the proton [43].

2.6 ^{78}Ni Region

^{78}Ni lies on the conventional shell closures $N = 50$ and $Z = 28$. ^{78}Ni lies 14 neutrons from the nearest stable isotope, ^{64}Ni, making it difficult to access experimentally. It is still under investigation whether the standard shell model closures are maintained in this region. Figure 2.7a shows the evolution of the $9/2^+$, $1/2^+$ and $5/2^+$ states in even-odd $N = 51$ isotones. As can be seen, the lowering of the $1/2^+$ and $9/2^+$ states as the number of protons decreases indicates the weakening of the $N = 50$ shell closure approaching ^{78}Ni.

Shell evolution is also observed in the proton orbitals. This is seen in Figure 2.7b. The lowering of the $\pi 0f_{5/2}$ relative to the $\pi 1p_{3/2}$ state is observed, and the levels cross at ^{75}Cu. This is predicted

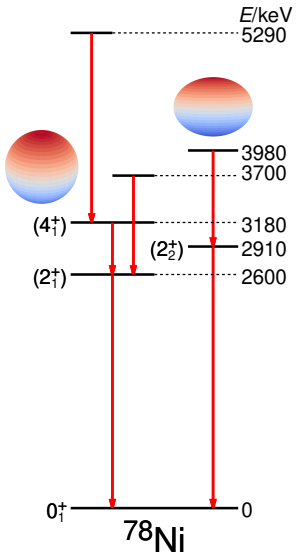

Fig. 2.8 Experimentally determined excited states in ^{78}Ni. Two bands are observed, which are explained theoretically as a spherical band and a deformed band. The predicted shapes of the excited states are indicated. Data reproduced from [9].

theoretically, driven by the tensor force, but the lowering of the $\pi 1p_{1/2}$ is not reproduced [5]. In addition, the weakening of the $Z = 28$ shell gap is also predicted [5].

The first measurement of spectroscopic information on ^{78}Ni was from the RIBF [9]. The experiment used DALI2 [24] array alongside the MINOS (quasi acronym: nuclear MagIc Numbers Off Stability) [62] hydrogen target to perform in-beam gamma-ray spectroscopy of ^{78}Ni from $(\mathrm{p}, 2\mathrm{p})$ and $(\mathrm{p}, 3\mathrm{p})$ reactions [9]. The level scheme obtained from the experiment is shown in Figure 2.8. The energy of the 2^+_1 state suggests the persistence of the $Z = 28$ and $N = 50$ shell closures. However, two sets of states are observed, which are theoretically explained using shell model calculations as a set of spherical states and a secondary set of prolate-deformed states [9]. This shape coexistence is interpreted as intruder configurations across the $N = 50$ shell closure, suggesting competition between spherical shell stability and deformation correlations [52, 9, 22]. Shape coexistence has been suggested in a $1/2^+$ isomer state of ^{79}Zn using laser spectroscopy [10, 22]. The shape coexistence is interpreted as intruder configurations across the $N = 50$ shell gap, indicating the weakness of the $N = 50$ shell gap in this region.

It still is not clear if the $N = 50$ shell closure is maintained in this region, and additional measurements are necessary. Positioned two protons beyond the Ni isotopic chain, Zn presents an interesting opportunity to explore the $Z = 28$ and $N = 50$ shell closures. This work will focus on the isotopes

^{78,80}Zn. ^{80}Zn is particularly interesting as it lies directly on the $N = 50$ shell closure, allowing for conclusions to be drawn about the shell closure's persistence.

2.6.1 ^{78,80}Zn Experimental Measurements

The first spectroscopic information for ^{78}Zn was obtained at the Grand Accélérateur National d'Ions Lourds (GANIL) facility using isomer spectroscopy with HPGe detectors [12]. The decay chain allowed for the measurement of the energies of the 2_1^+, 4_1^+, 6_1^+ and 8_1^+ candidate states to a high precision. A similar measurement was performed at RIBF using the BigRIPS and ZeroDegree spectrometer to look at the isomer in ^{78}Zn. The same transitions were observed at the RIBF measurement as in the GANIL measurement [14].

The nucleus ^{78}Zn has also been measured using β and βn decay at the Isotope Separator On-Line Device (ISOLDE) facility, the Holifield Radioactive Ion Beam Facility (HRIBF) and the RIBF [16, 15, 13]. The ISOLDE measurement implanted ^{78}Cu into the setup and used HPGe to measure the gamma rays after β decay. Transitions corresponding to the 2_1^+ and (4_1^+) states were observed [16]. For the HRIBF experiment, Cu isotopes were implanted onto a moving tape, and the decaying gamma rays were measured with HPGe detectors. The 2_1^+ and 4_1^+ levels were measured alongside the 2529 keV level and a new state at 3105 keV [15]. Finally, the RIBF experiment used BigRIPS and ZeroDegree [63] to identify and transport the isotopes to a silicon array, where the gamma rays emitted after the decay were measured with HPGe detectors. The same transitions that were seen at HRIBF were observed [13].

The first spectroscopic information on ^{80}Zn was measured at ISOLDE [17, 18] performing low energy Coulomb excitation of even-even ^{74,76,78,80}Zn isotopes. The cross section for the excitation to the 2_1^+ states was measured using the Miniball array [23]. The experiment successfully measured the 2_1^+ excitation energies and the $B(E2, 2_1^+ \rightarrow 0_1^+)$ values of ^{78,80}Zn. Inelastic scattering of ^{80}Zn has also been performed at the RIBF with the MINOS hydrogen target and the DALI2 array [24], extracting the $B(E2, 0_1^+ \rightarrow 2_1^+)$ via cross-section measurements [20].

Further spectroscopic information on ^{80}Zn has been obtained at the RIBF using knockout reactions on a Be target using the DALI2 array [19]. The channels ^{81}Ga(Be, X)^{80}Zn and ^{80}Zn(Be, X)^{80}Zn were analysed, observing for the first time four new states including the 4_1^+ state. In addition, the lifetime of the 4_1^+ state was measured using peak-shape analysis [19]. In the same experiment, a new transition

at $\approx$ 1.3 MeV was reported in ^{78}Zn following its production through the ^{80}Ga(Be, X)^{78}Zn reaction channel [19].

	ENSDF	GANIL	HRIBF	ISOLDE		RIBF		
		I	β/βn	β	CX	K	β	I
J_i^π, J_f^π	[64]	[12, 60]	[15]	[16]	[17, 18]	[19]	[13]	[14]
$2_1^+, 0_1^+$	730.2(4)	729.6(5)	730.2	730.4(3)	730	740(11)	730	730.0
$(4_1^+), 2_1^+$	890.5(4)	889.9(5)	890.5	890.7(3)	891	902(14)	890	890.5
$(6_1^+), (4_1^+)$	908.3(6)	908.3(5)	908.3	-	-	-	909	909.1
$(8_1^+), (6_1^+)$	144.7(10)	144.7(5)	-	-	-	-	-	145.7
$(4_2^+, 8_1^+), (6_1^+)$	576(1)	-	576	-	-	580(9)	576	-
-	-	-	-	-	-	1271(19)	-	-

Table 2.1 Energies (keV) of gamma-rays from ^{78}Zn excited states from literature. I indicates isomer decay, CX indicates Coulomb excitation, K indicates knockout, and ENSDF stands for the Evaluated Nuclear Structure Data File [60]. Uncertainties are omitted if they are not present in the corresponding publication. J_i^π and J_f^π indicate the initial and final state angular momentum and parity. In cases where the transition is not present in the data set, the space is left with a hyphen.

Table 2.1 shows the reported energies from the literature and from an evaluation of the literature. The energies of the transitions are measured with high precision, with good agreement between the experiments. The 1271(19) keV transition has only been observed once and has yet to be placed in the level scheme [19].

	ENSDF	ISOLDE	RIBF	
J_i^π, J_f^π	[60]	CX [17, 18]	CX [20]	K [19]
$2_1^+, 0_1^+$	1492(1)	1492(1)	1487(8)	1497(22)
$4_1^+, 2_1^+$	-	-	487(3)	482(7)
$X, 4_1^+$	-	-	-	841(13)
$X', 4_1^+$	-	-	-	1195(18)
$X'', 0_1^+$	-	-	-	2627(39)
-	-	-	3280(20)	-
-	-	-	3690(30)	-

Table 2.2 Energies (keV) of gamma-rays from ^{80}Zn excited states from literature. CX indicates Coulomb excitation, and K indicates knockout. J_i^π and J_f^π indicate the initial and final state angular momentum and parity, respectively. X is used in cases where the J^π is unreported, and the space is left empty when the initial and final states are unknown. In cases where the transition is not present in the data set, the space is left with a hyphen.

Table 2.2 shows the literature values for gamma rays emitted by ^{80}Zn. The $2_1^+ \rightarrow 0_1^+$ transition energy is determined with high precision from low-energy Coulomb excitation at ISOLDE [17, 18]. The $4_1^+ \rightarrow 2_1^+$ transition has been observed twice at the RIBF with energies of 482(7) [19] and

	^{78}Zn		^{80}Zn			
	2_1^+		2_1^+		4_1^+	
	$B(E2\downarrow)/e^2\text{fm}^4$	$t_{1/2}$/ps	$B(E2\downarrow)/e^2\text{fm}^4$	$t_{1/2}$/ps	$B(E2\downarrow)/e^2\text{fm}^4$	$t_{1/2}$/ps
[17, 18]	154(38)	18(4)	144(29)	0.53(11)	-	-
[20]	-	-	146(18)	-	-	-
[19]	-	-	-	-	160^{+156}_{-65}	136^{+92}_{-67}

Table 2.3 $B(E2\downarrow)$ and $t_{1/2}$ values for ^{78,80}Zn from literature. A hyphen indicates the values are not present in the corresponding publications.

487(3) keV [20], both in agreement within 1σ. The 841(13), 1195(18) and 2627(39) keV transitions have only been observed at the RIBF using knockout reactions, where the precision was limited by Doppler broadening and the limited energy resolution of the detector array [19, 30]. Inelastic scattering measurements at the RIBF also observed transitions of 3280(20) and 3690(30) keV that have not been reported elsewhere and are not yet placed in the level scheme [20].

Table 2.3 shows the literature $B(E2)$ and $t_{1/2}$ values. In ^{78}Zn, only the $B(E2, 2_1^+ \rightarrow 0_1^+)$ value has been reported; measuring the $B(E2, 4_1^+ \rightarrow 2_1^+)$ is difficult due to the $4_1^+ \rightarrow 2_1^+$ gamma-ray lying close in energy to the $6_1^+ \rightarrow 4_1^+$ energy [64]. In ^{80}Zn the $B(E2, 2_1^+ \rightarrow 0_1^+)$ has been extracted using low and intermediate energy Coulomb excitation [17, 18, 20]. The $B(E2, 4_1^+ \rightarrow 2_1^+)$ has been measured with a large uncertainty through lifetime measurements [19].

Figure 2.9 shows the level schemes for ^{78,80}Zn. Figure 2.9a was compiled from the ENSDF evaluation [60]. Figure 2.9b was compiled using the 2_1^+ from low-energy Coulomb excitation [17, 18], the 4_1^+ from inelastic scattering at the RIBF [20], and the remaining levels are constructed using the data from knockout experiments at the RIBF [19].

Figure 2.10a shows the excitation energies of the first 2_1^+ and 4_1^+ states in the Zn isotopes in the region of ^{78}Ni. There is a dramatic rise in the 2_1^+ energy at $N = 50$, which can be explained as a result of the shell closure. The energies of excited states in Zn isotopes are well determined using high-resolution HPGe detectors up until the 4_1^+ in ^{80}Zn. The lower plot in Figure 2.10a shows the ratio of the 4_1^+ to 2_1^+ excitation energies. Other than at $N = 50$ shell closure, all the isotopes have a ratio close to the value expected for harmonic oscillators. Whilst for ^{80}Zn the value falls below the harmonic oscillator value, suggesting that the low-lying states are due to single-particle excitations.

Figure 2.10b shows the $B(E2)$ values for the Zn isotopes. The $B(E2, 4_1^+ \rightarrow 2_1^+)$ value for ^{78}Zn is not yet measured. In addition, the $B(E2, 4_1^+ \rightarrow 2_1^+)$ for the ^{80}Zn is measured with a significant uncertainty [19], limiting the conclusions that can be drawn from the measurements. The lower plot

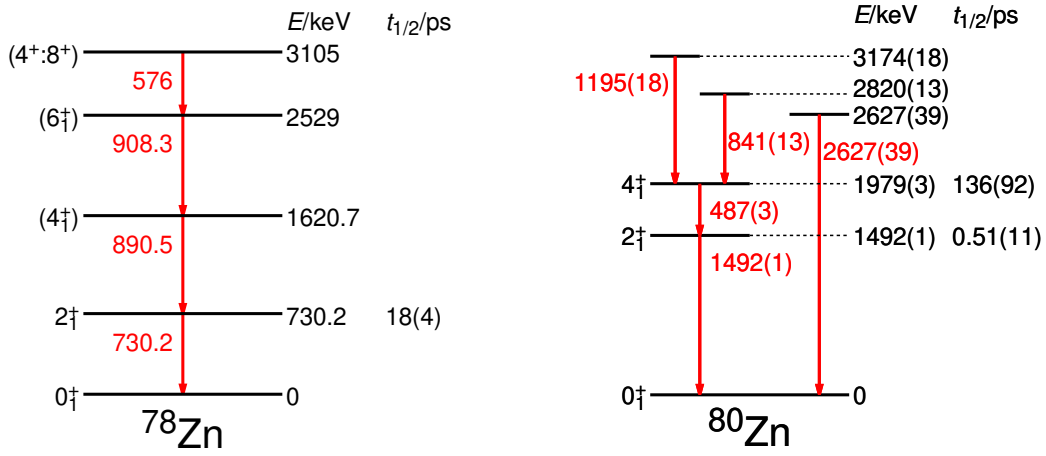

(a) (b)

Fig. 2.9 Literature level schemes of ^{78}Zn (a) and ^{80}Zn (b) compiled from literature [60, 17, 18, 19, 20].

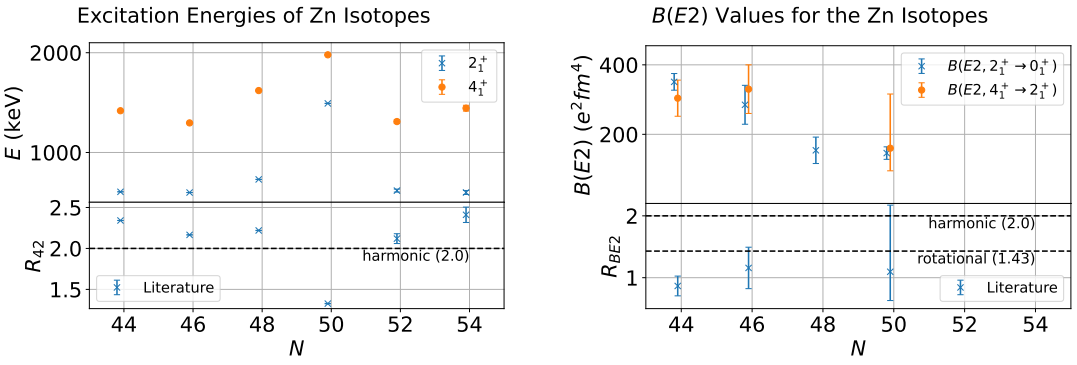

(a) (b)

Fig. 2.10 (a) shows excitation energy systematics for the first 2_1^+ and 4_1^+ states in the Zn isotopes values from literature. Literature values are taken from [60, 64, 20, 17, 18]. The lower plot shows the $R_{42} = E(4_1^+)/E(2_1^+)$ systematics. (b) shows the $B(E2)$ systematics for the Zn isotopes. The literature values are from [65, 17, 18, 20, 19]. The bottom plots shows the $R_{BE2} = B(E2, 4_1^+ \rightarrow 2_1^+)/B(E2, 2_1^+ \rightarrow 0_1^+)$ systematics.

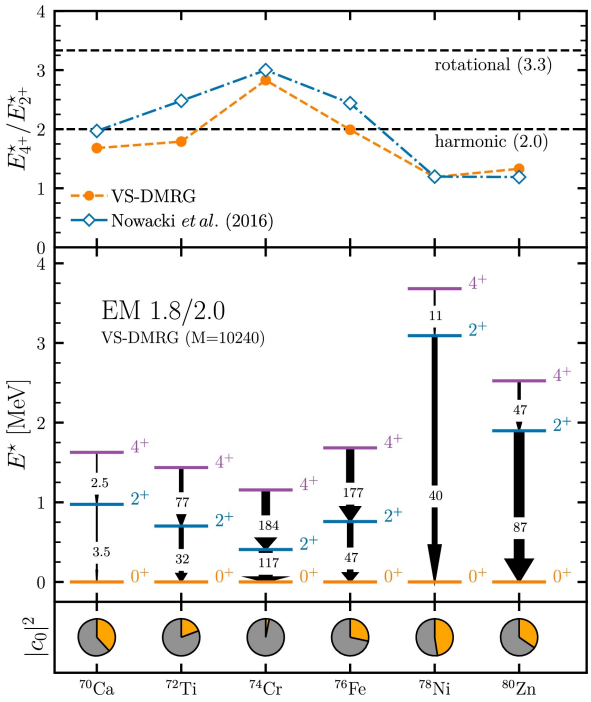

Fig. 2.11 VS-DMRG calculations of $N = 50$ nuclei. The top plot shows the ratio of the 4_1^+ to 2_1^+ energies compared with previous calculations [66]. The middle plot shows the structure of the 2_1^+ and 4_1^+ states and the $B(E2)$ values for transitions between the states in units of $e^2\text{fm}^4$. The bottom plot shows the contribution to the ground state wave function of the 0p-0h configuration in the orange fraction. Reproduced from [67].

in Figure 2.10b shows the ratio of the $R_{BE2} = B(E2, 4_1^+ \to 2_1^+)/B(E2, 2_1^+ \to 0_1^+)$ for the Zn isotopes. From the value for ^{80}Zn, it is clear that no clear conclusion from this number can be drawn due to the large uncertainty of the $B(E2, 4_1^+ \to 2_1^+)$ value, indicating the necessity for a new measurement with improved precision, which has been the objective of the current work. An improved precision in the R_{BE2} would allow for a conclusion to be drawn about the origin of low-lying states in ^{80}Zn, providing evidence for the persistence of the $N = 50$ shell closure in this region.

2.6.2 ^{78,80}Zn Theoretical Models

Several theoretical calculations have been carried out in this region. One such method using spherical basis states with the Valence-Space Density Matrix Renormalisation Group (VS-DMRG) method calculated the low-lying structure of $N = 50$ nuclei [67]. The predictions of this model can be seen in Figure 2.11. The model overpredicts the 2_1^+ and 4_1^+ energy and underpredicts the $B(E2, 2_1^+ \to 0_1^+)$ and $B(E2, 4_1^+ \to 2_1^+)$ values, suggesting additional effects are necessary to describe ^{80}Zn.

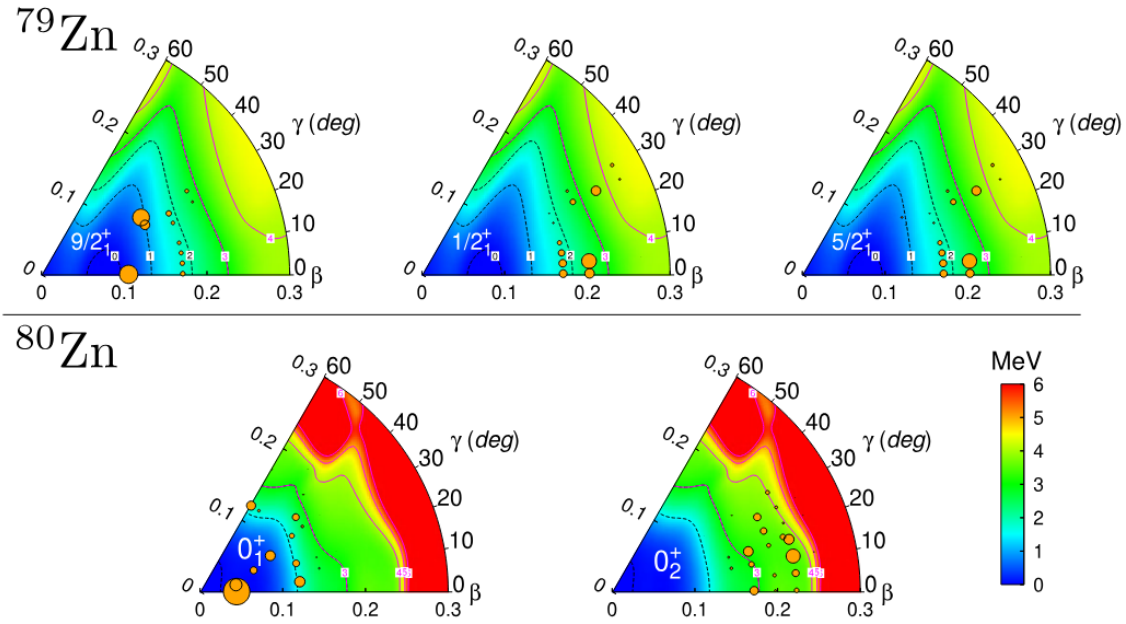

Fig. 2.12 Calculated potential energy surfaces from DNO-SM [21] for ^{79}Zn and ^{80}Zn where β and γ are defined previously. The basis states' deformation parameters are indicated by the red circles, and the size indicates the magnitude of their contribution to the wave function. In ^{79}Zn, the non-deformed $9/2^+$ ground state is shown in the top left plot, the $1/2^+$ deformed isomer observed in [10, 22] is shown in the top middle plot, and a $5/2^+$ deformed state is shown in the top right plot. In ^{80}Zn, a spherical 0^+_1 ground state is predicted, shown in the bottom left plot, whilst a deformed 0^+_2 is predicted at 2.16 MeV, shown in the bottom right plot. Reproduced from [22].

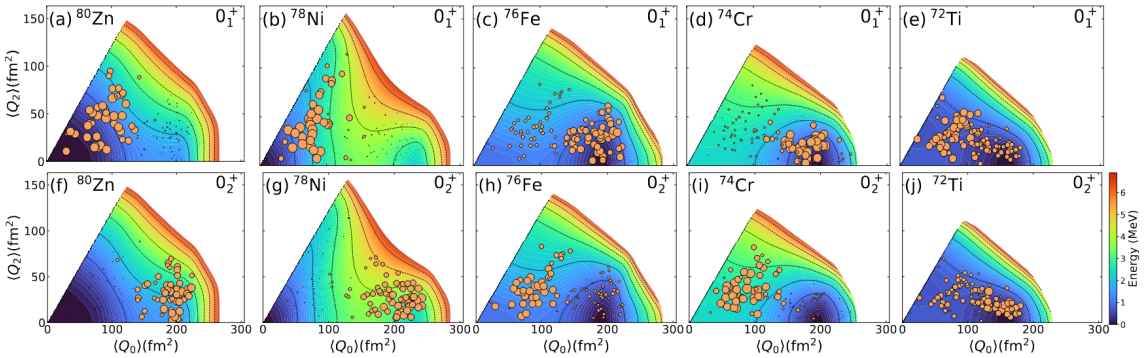

Fig. 2.13 Potential energy surfaces for the 0_1^+ and 0_2^+ states in $N = 50$ isotones predicted by MCSM [68]. Q_0 shows the a_{20} deformation and Q_2 shows the a_{22} deformation. The basis states, and the circles show their contribution to the wave function. Reproduced from [69].

A method that could properly describe ^{80}Zn is DNO-SM [21]. Calculations of ^{79,80}Zn have been performed in [22]. The potential energy surfaces are shown in Figure 2.12. The model predicts the observed deformed $1/2^+$ isomer at 830 keV [10, 22], in reasonable agreement with the experimental value of 943(3) keV [22]. The calculation for ^{80}Zn predicted a spherical ground state and a deformed 0_2^+ state at 2.16 MeV [22]. The state at 2.6 MeV observed in [19] may be a candidate 2_2^+ state in a deformed band, associated with this deformed 0_2^+ and state decaying predominantly to the ground state driven by the energy term in the transition rate, in line with what is predicted in ^{78}Ni [9].

Another suitable method is the Monte-Carlo shell model (MCSM) [68]. This has been performed in the $N = 50$ isotones around ^{78}Ni. The model predicts a deformed 0_2^+ state in ^{80}Zn at 2.59 MeV [69]. The shapes of $N = 50$ isotones in the region of ^{78}Ni predicted by MCSM can be seen in Figure 2.13. MCSM and DNO-SM predict a similar deformation for the 0_2^+ state in ^{80}Zn.

2.7 Summary

Nuclear structure has been studied extensively for over a century. However, questions of nuclear structure remain, particularly near the nuclear drip lines. Of particular interest is the region around ^{78}Ni, where observations of shape coexistence and shell evolution suggest weakening of the $N = 50$ shell closure. Further information is necessary to understand this region. For this work, the Zn isotopes ^{78,80}Zn will be examined, looking to measure $B(E2)$ values and extract information on the persistence of the $N = 50$ and $Z = 28$ shell gaps in this region. These results will provide information on the forces involved in shell evolution and will have implications across the nuclear chart.

Chapter 3

Gamma-Ray Spectroscopy and Experiments with RI-Beams

The energy of gamma rays emitted during the decay of nuclear excited states provides a direct window into nuclear structure. To precisely measure these energies, specialised detector materials are required to measure radiation interactions, paired with sophisticated electronics for signal processing. This chapter examines the mechanisms of energy deposition within detector media, the conversion of that energy into measurable electrical signals, and the subsequent processing techniques used to extract timing and energy information. Finally, the production of radioactive isotopes (RI) and the experimental methodologies that emerge from the integration of RI beams with gamma-ray spectroscopy will be discussed.

3.1 Principles of Gamma-ray Detection

Energy deposition of gamma rays in materials is dominated by three interactions: photoelectric absorption, Compton scattering, and pair production [44]. Photoelectric absorption is the full absorption of a photon, ionising a bound electron. A schematic of this process can be seen in Figure 3.1. The probability of the process can be approximated as

$$\tau \propto \frac{Z^n}{E_\gamma^{3.5}} \tag{3.1}$$

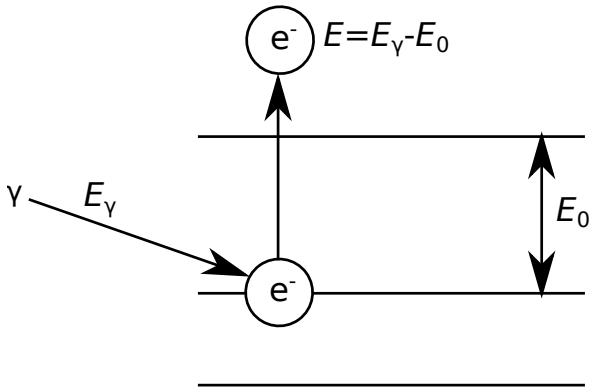

Fig. 3.1 Schematic diagram of photoelectric absorption. An electron gains energy by the absorption of a photon, leading to the electron being liberated from the bound state [44]. E_γ is the gamma ray energy and E_0 is the ionisation energy of the electron

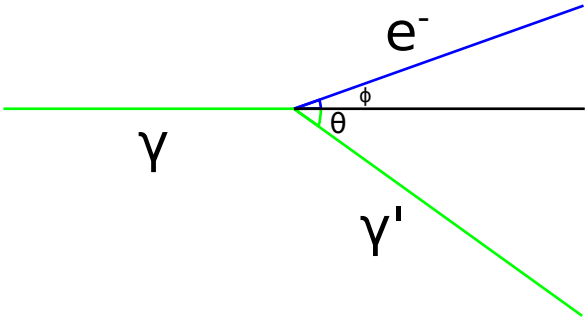

Fig. 3.2 Schematic diagram of Compton scattering [70]. γ is the incoming photon, γ' is the scattered photon, and e^- is the scattered electron. θ and ϕ are the photon and electron scattering angles, respectively.

where τ is the probability of absorption per atom, Z is the atomic number of the atom, E_γ is the energy of the gamma ray, and n is an empirical value typically around 4-5 [70]. From this, it is clear that to have a high efficiency for photoabsorption, a high density and a high-Z material is favoured. In addition, photoelectric absorption dominates at lower energies. The shell structure of the atomic electrons causes sharp jumps in the probability of photoelectric absorption once the threshold for exciting electrons from a more bound shell is met [70].

The second process is Compton scattering. Compton scattering is the scattering of a photon off an electron, in which a partial exchange of the photon's energy occurs. The energy of the scattered photon can be described by the equation

$$E'_\gamma = \frac{E_\gamma}{1 + \frac{E_\gamma}{m_e c^2}(1 - \cos\theta)} \tag{3.2}$$

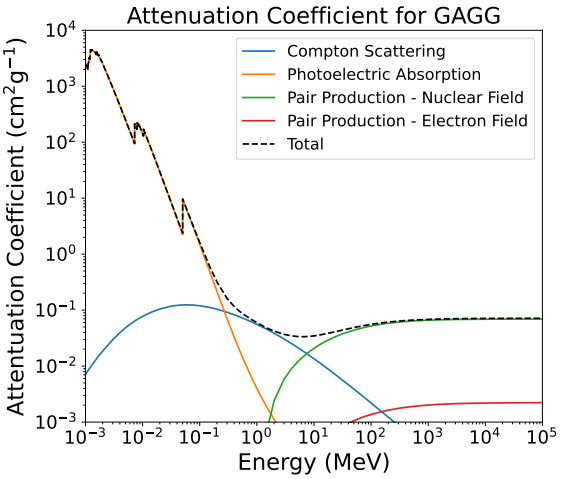

Fig. 3.3 Attenuation coefficient of GAGG [72] and the contributions of the different interactions. Data is from the NIST photon cross-sections database [73]. The attenuation coefficient, μ, gives the probability of interaction, dp, in a short length of material, dx, by the equation $dp = \mu\rho dx$, where ρ is the density of the material.

where E'_γ is the scattered photon energy, E_γ is the initial energy, m_e is the electron mass, c is the speed of light, and θ is the angle of scattering [70]. This process is shown in Figure 3.2. The probability for the angular scattering is dictated by the Klein-Nishina formula [71].

The final process is pair production, where a gamma ray with energy ≥ 1.022 MeV, produces an electron-positron pair in the electric field of a nucleus [70]. The electron deposits energy via interactions with the electrons in the material, whilst the positron loses energy and finally annihilates to produce two 511 keV photons.

Figure 3.3 shows the attenuation coefficient for GAGG [72], illustrating both the total attenuation coefficient and the individual contributions from the different interactions. From this, it is clear that photoelectric absorption dominates at low energies, Compton scattering takes over in the mid-energy region, ≈ 1 MeV, and pair production governs at higher energies $\gtrsim 10$ MeV.

The discussed effects allow for the production of gamma-ray spectra. Figure 3.4 shows representative gamma ray spectra for different gamma-ray energies simulated using the Geant4 toolkit [74] for a $2.5\times2.5\times7.5$ cm^3 NaI(Tl) detector [75]. Figure 3.4a shows the simulated response for a 662 keV gamma ray. The Compton edge is seen at 478 keV, corresponding to the maximum energy that can be deposited by a single Compton scattering interaction, which will occur at a scattering angle of $\theta = 180°$. The full-energy peak is located at 662 keV and corresponds to the full absorption of the gamma ray. A gamma ray that Compton scatters in the surrounding material at 180° leads to

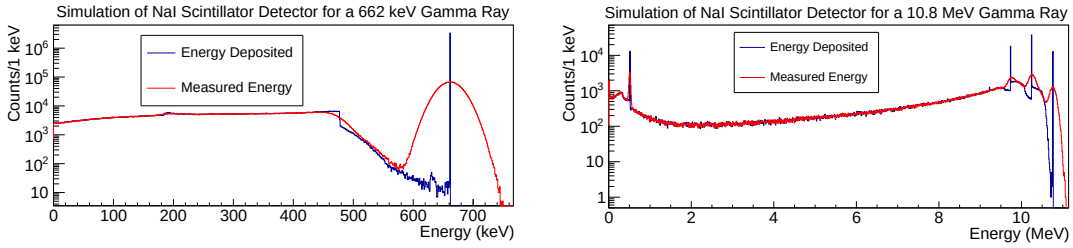

(a) (b)

Fig. 3.4 Monte-Carlo simulations [74] of a NaI(Tl) detector for different energy gamma rays. (a) shows the response for a 662 keV gamma ray. The Compton edge is seen at ≈500 keV, whilst the full-energy peak is seen at 662 keV. The backscatter peak is observed at 184 keV. (b) shows the response for a 10.8 MeV gamma ray. The full-energy peak is seen at 10.8 MeV whilst the single and double escape peaks are seen at 10.2 MeV and 9.7 MeV, respectively. A 511 keV peak is observed from pair production in the surrounding material. Energy deposited shows the energy deposited in the detector, and the measured energy shows the energy smeared by the detector energy resolution. The energy resolution was taken from [75].

a backscatter peak. For the 662 keV gamma ray, this is located at 184 keV. Figure 3.4b shows the response of a NaI(Tl) detector to a 10.8 MeV gamma ray. The full-energy peak is located at 10.8 MeV. The single escape peak corresponds to when a gamma ray undergoes pair production, and the positron annihilates, and one of the 511 keV gamma rays escapes the detector, and is located at 10.2 MeV. The double escape peak is the same as the first escape peak except that both 511 keV gamma rays escape the detector, and is located at 9.7 MeV. Pair production in the surrounding material produces 511 keV gamma-rays, which can interact with the detector to produce a peak at 511 keV.

3.2 Semiconductor Detectors

Semiconductors are materials where the gap between the valence and conduction bands is ≈ 1 eV [76]. By doping the material, the densities of electrons or holes can be manipulated. n-type semiconductors are doped with electron donors, leading to an excess of electrons, while p-type semiconductors are doped with electron acceptors, leading to an excess of holes [76].

When a p-type and an n-type semiconductor are attached, they form a pn-junction, which is the basis of semiconductor radiation detectors. Figure 3.5 shows a pn-junction under different conditions. Under thermal equilibrium, diffusion of electrons and holes leads to a depletion region between the pn-junction devoid of mobile charge carriers. This produces a potential gradient between the p and n layers. Under a forward bias, this potential is reduced, and current can flow. If a reverse bias is

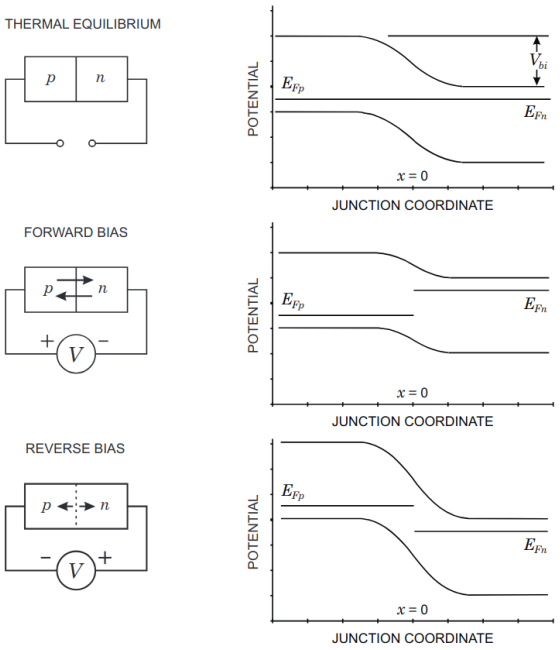

Fig. 3.5 Diagram of the electronic structure of a pn-junction under different conditions. The area under the bottom line shows the valence band, the region between the lines shows the forbidden region, and the area above the top line shows the conduction band. $E_{F\mathrm{p}}$ and $E_{F\mathrm{n}}$ show the Fermi energy for the p and n regions, respectively. V_{bi} is the voltage generated across the pn-junction. Reproduced from [76].

applied, the potential barrier increases, and the depletion region expands. The width of the depletion region is described by

$$w = \sqrt{\frac{2\varepsilon V_b}{e}\frac{N_a + N_d}{N_a N_d}} \tag{3.3}$$

where V_b is the reverse-bias voltage, w is the width of the depletion region, ε is the dielectric constant of the material, e is the electron charge, and N_a and N_d are the densities of the acceptor and donor ions, respectively [76]. Utilising a reverse-biased pn-junction is the basis for radiation detection with semiconductors.

Ionising radiation interacting in the depletion region will produce electron-hole pairs, allowing for the detection of radiation with semiconductors. The number of *eh*-pairs will be proportional to the energy deposited in the detector. The electrons drift to the n electrode and the holes to the p electrode. The motion of the electrons and holes induces a charge on the electrodes, leading to charge accumulation occurring before the charge carriers reach the electrodes. This can be described by the

Shockley-Ramo theory, where the charge induced on an electrode is described by

$$\Delta Q_k = q(\phi_k(2) - \phi_k(1)) \tag{3.4}$$

where ΔQ_k is the charge induced on electrode k due to a charge carrier of charge q moving from point 1 to point 2 with $\phi_k(j)$ being the weighting potential of electrode k at position j [76, 70]. The weighting potential is calculated by setting the potential on electrode k to 1 V and setting all other electrodes to 0 V and solving the Poisson equation, $\nabla^2\phi_k = 0$, for the given boundary conditions [76, 70].

This effect causes a charge to begin accumulating on the electrodes before the charge carriers arrive at the electrode. The total collected charge will be proportional to the energy deposited in the detector. In detectors with multiple electrodes, this causes charge to accumulate on nearby electrodes that do not collect the produced charge. Figure 3.6a shows the potential generated for a 0.30×0.19 mm^2 Si detector with one long n-type electrode at the top of the detector at 100 V and three equally spaced 0.05 mm p-type electrodes at 0 V at the bottom. The potential was calculated by solving $\nabla^2\phi = 0$ for the given boundary conditions. Using this, the trajectories of electrons and holes were calculated according to the drift velocity

$$\vec{v}_d = \mu\vec{E} \tag{3.5}$$

where $\vec{v}_d$ is the drift velocity of the charge carrier, $\vec{E}$ is the electric field calculated using the potential, and μ is a constant which is 0.145, and 0.045 m^{2}V^{-1}s^{-1} for electrons and holes, respectively [77]. The resultant trajectories for events involving a single point of *eh*-pair generation are overlaid on Figure 3.6a. The weighting potential for pixel 1 is shown in Figure 3.6b. Using the weighting potentials and the Shockley-Ramo theory, the induced charges for the trajectories shown in Figure 3.6a were calculated. The induced charges for each pixel varying with time from the generation of the eh-pairs are shown in Figure 3.6c. As can be seen, the pulse shape in the collecting electrode and the neighbouring electrodes are strongly dependent on the position of interaction. This can be exploited for the reconstruction of the position of interaction [78]. The charges induced on the electrodes are processed using a charge-sensitive preamplifier to produce a measurable voltage signal [79].

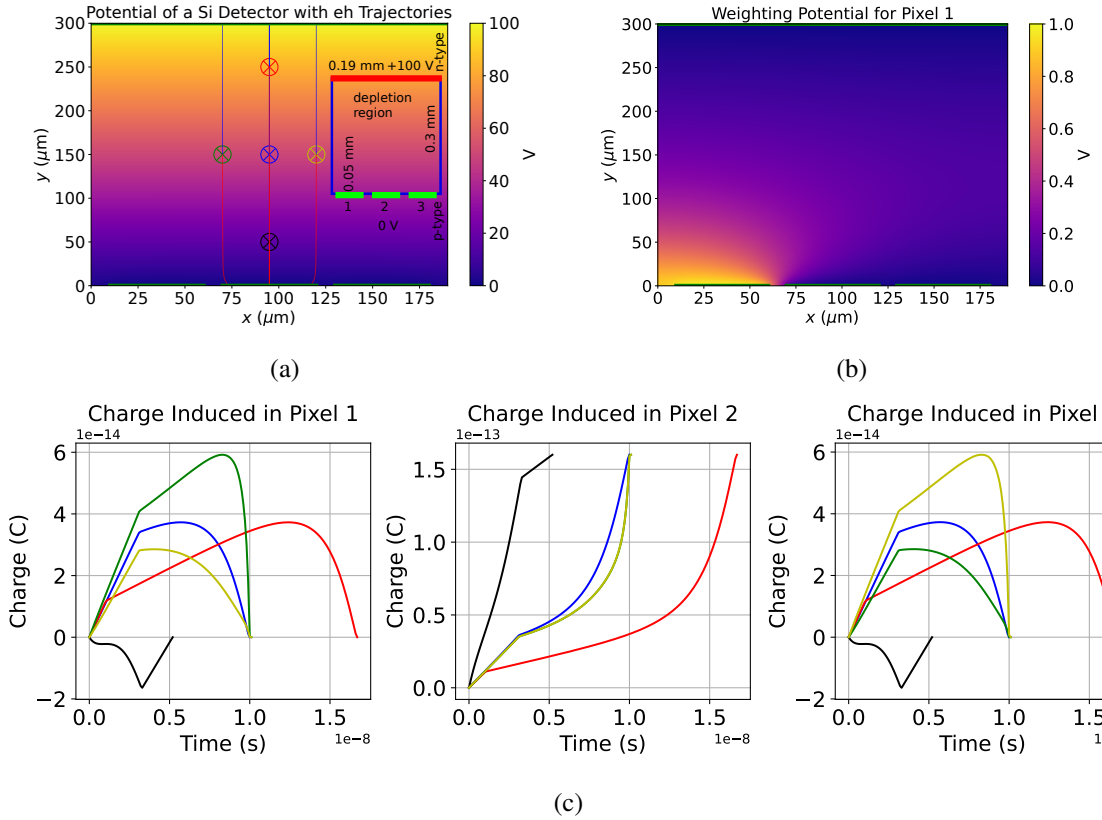

Fig. 3.6 Simulation of a 2D Si pixel detector. (a) shows the electric potential for a 2D Si detector with one n-type contact at 100 V and three p-type pixels at 0 V. The green lines show the electrode locations. The calculated trajectories of eh-pairs generated at different points marked by crosses are shown. The trajectories of holes are shown in red and electrons in blue. The inset shows the geometry of the detector; the p-type pixels are labelled 1-3. (b) shows the weighting potential for pixel 1 for the same geometry as in (a). (c) shows the induced charges on the pixels calculated using the Shockley-Ramo theory [70, 76]. It is assumed that 1×10^6 *eh*-pairs were generated from a single interaction at the crosses shown in (a); the line colours correspond to the cross colours. As can be seen, the shape of the induced charge on the collecting electrode and nearby electrodes is dependent on the position of origin of the charge.

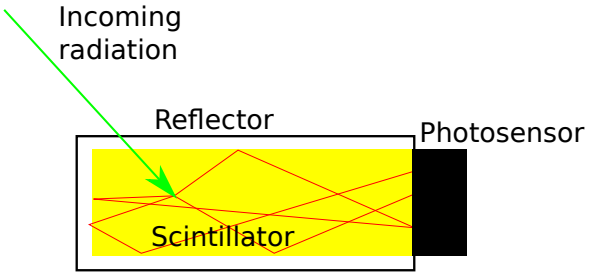

Fig. 3.7 Diagram showing the typical configuration of a scintillator detector. The scintillating material is shown in yellow, the photo sensor is shown in black, and the reflector is shown in white. Incoming radiation is depicted using a green arrow, and the resulting scintillation light is shown in red.

3.2.1 HPGe - High-Purity Germanium

For gamma ray detection with excellent energy resolution and a large sensitive volume, HPGe semiconductor detectors are used [70]. HPGe detectors are made up of an n-layer and a p-layer with a p/n region in the centre. The low density of impurities allows for the formation of a large depletion region [70]. When a gamma ray interacts in the active region, the ionised electron will go on to produce a number of eh-pairs. The electrons travel to the n-type contact and the holes to the p-type contact [70]. The signals need to be passed through a charge-sensitive preamplifier in order to convert the charge produced in the detector to a measurable voltage [79].

Simple HPGe detectors use two contacts, typically a central core to read out the signal from the detector, and an external electrode. In order to achieve better position resolution of the gamma-ray interaction position, segmented HPGe detectors were developed; these were used in the Miniball array [23]. More recently, pulse shape position reconstruction has been used to obtain sub-segment position resolution, such as in the AGATA [27] and GRETINA [29] projects.

3.3 Scintillation Detectors

Scintillators present a competitive alternative to gamma ray spectroscopy with HPGe. Scintillators produce photons in response to the energy deposited by interacting radiation, which can then be converted into an electrical signal using a photosensor [70]. The number of scintillation photons produced is proportional to the energy deposited in the detector. A typical scintillator detector is shown using Figure 3.7. The diagram includes a scintillator wrapped in a reflective material with a photosensor attached.

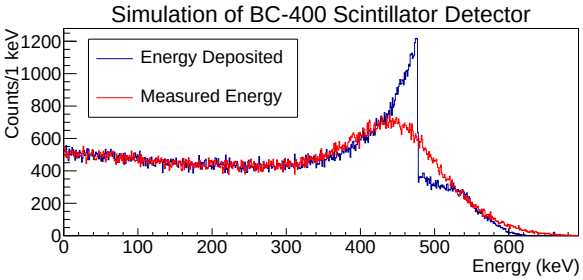

Fig. 3.8 Monte Carlo simulation [74] of a 2.5×2.5×7.5 cm^3 BC-400 [82] scintillator detector for a 662 keV gamma ray. Energy deposited shows the energy deposited by the gamma ray in the detector, whilst the measured energy shows the deposited energy smeared by the detector response [83].

3.3.1 Organic Scintillators

Organic scintillators are made out of hydrocarbons, and the luminescence emerges from the molecular structure [80]. They typically achieve fast decay times of around 2-30 ns [80]. Organic scintillators are typically used in cases where a very good time resolution is required, such as time-of-flight (TOF) detectors for magnetic spectrometers [63]. In plastic form, organic scintillators typically have densities around 1 gcm^{-3} [81].

Due to the low Z of organic scintillators, they have a low efficiency for photoelectric absorption [70]. Figure 3.8 shows the simulated response of a BC-400 [82] organic scintillator, the blue histogram shows the energy deposited in the scintillator, and the red histogram shows the energy deposited smeared by the detector resolution [83]. As can be seen, very few gamma rays are fully absorbed in the detector due to the low probability for photoelectric absorption. The spectrum is dominated by Compton scattering. This means plastic scintillators are a poor choice for gamma-ray spectroscopy. Nuclear physics experiments tend to choose inorganic scintillators for gamma-ray spectroscopy [24, 36].

3.3.2 Inorganic Scintillators

Thanks to their high-density and Z, inorganic scintillators present a high-efficiency alternative to HPGe detectors [84, 31]. Inorganic scintillators are crystalline scintillators where the scintillation emerges from the band structure of the crystal. Figure 3.9 shows the scintillation mechanism for an inorganic material. Impurities are added to create luminescence centres. Gamma-ray interactions in the crystal ionise electrons, which will lose energy generating eh-pairs in the scintillator. The eh-pairs then recombine through a luminescence centre via the emission of a scintillation photon [80]. By

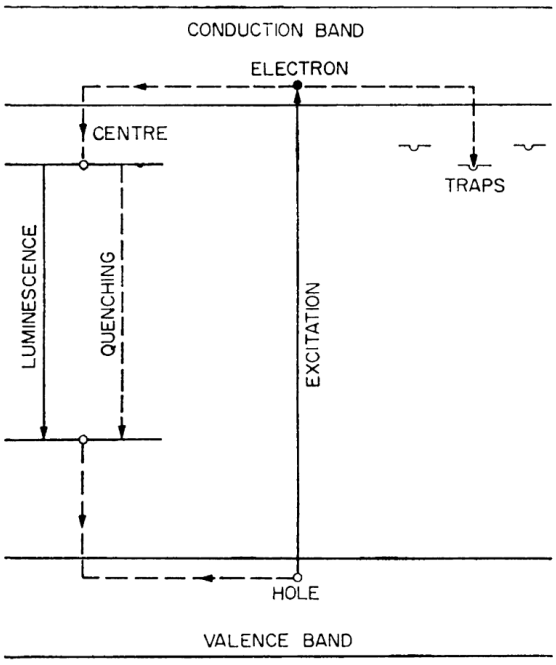

Fig. 3.9 Schematic diagram of the scintillation mechanism in an inorganic scintillator. Electron-hole pairs are produced by the ionised electron, the electron deexcites via a luminescence centre producing a photon, and goes on to recombine with the hole. Quenching shows non-radiative decays, which reduce the scintillation efficiency. Traps show low-lying electron traps, which also reduce the scintillation efficiency. Reproduced from [80].

measuring the number of photons produced, the energy deposited in the material can be determined. Quenching is the recombination via non-radiative decays, leading to a reduced scintillation efficiency. Metastable states called traps can prevent recombination and lead to a loss of scintillation efficiency [80]. Inorganic scintillators are typically slower than organic scintillators with decay times around 50-500 ns [70]. However, they are generally made out of higher Z elements, increasing the probability of photoelectric absorption and typically have densities of >3 gcm^{-3} [80].

Figure 3.4a shows the response of NaI(Tl), an inorganic scintillator, to a 662 keV gamma ray. As can be seen, in comparison to Figure 3.8, the full energy peak is much more prominent due to the higher Z and the higher density. This makes inorganic scintillators more suitable for gamma-ray spectroscopy than organic scintillators.

GAGG

GAGG(Ce) is an inorganic scintillator made up of $Gd_3Ga_xAl_yO_{12}$ where $x+y=5$ and is doped with Ce with the scintillation light emerging from the $5d\ 4f$ transition in Ce [72]. Standard GAGG uses $y=3$, and $x=2$, but it has been shown that the Ga:Al ratio has a significant effect on the properties of the scintillator [72, 38, 85].

It has been observed that a $5\times5\times5$ mm^3 crystal with $y=3$, $x=2$, and an energy resolution of 5.1(2) % at 662 keV, whilst a crystal of the same size with $x=2.4$, $y=2.6$ produces an energy resolution of $3.7(2)$ % at 662 keV, both were measured using an avalanche photodiode [38]. Due to the improved resolution $x=2.4$, $y=2.6$ GAGG is referred to as an HR-GAGG, High-Resolution GAGG by C&A [33]. However, it has been observed that HR-GAGG has longer decay times [38], and more afterglow [85] than typical GAGG. It is also possible to produce HR-GAGG or HL-GAGG, High-Luminosity GAGG, by other methods this is done by companies such as EPIC crystals, but how this is achieved is not public information [86].

HR-GAGG is grown using the Czochralski method [38, 87]. Several manufacturers are capable of manufacturing HR-GAGG [33, 88, 89, 86], but the energy and time resolution of the different crystals is yet to be determined.

3.3.3 Photo Sensors

To convert the scintillation light into a measurable signal, a photo sensor is necessary. An ideal photo-sensor provides a sufficient gain of the signal whilst maintaining a linear response in a wide dynamic

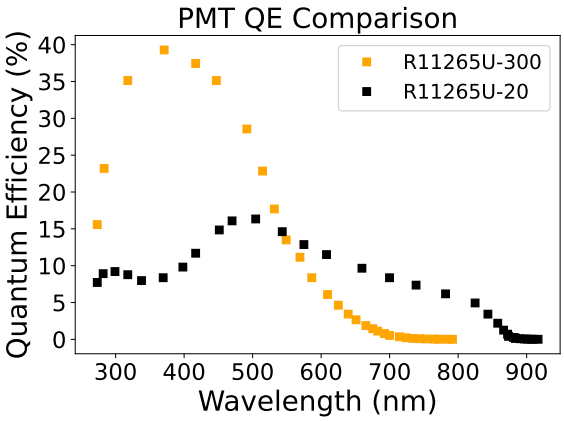

Fig. 3.10 Quantum efficiency (QE) of different Hamamatsu PMTs varying with photon wavelength. Data are taken from [93].

range. Traditionally, photo-multiplier tubes have been used [70], but more recently, semiconductor photosensors such as silicon photo-multipliers [90] have emerged as competitors, due to their compact size, insensitivity to magnetic fields [91], and high quantum efficiency [92].

PMT - Photo-Multiplier Tube

PMTs start with a photocathode, on which an incident photon can undergo photoelectric absorption to produce an electron [70]. The probability for an incident photon to undergo photoelectric absorption and produce a photoelectron is known as the quantum efficiency. Figure 3.10 shows the quantum efficiencies of different photocathodes; as can be seen, the choice of photocathode has a large impact on the quantum efficiency. The choice of photocathode needs to be made to match the emission wavelength of the scintillation light.

The photoelectron produced from the photocathode is then accelerated using electric fields towards a dynode, where the incoming initial electron causes the emission of around 4-6 electrons [70]. This is repeated a number of times in the tube until the total number of electrons is collected at the anode, producing a measurable signal. This process leads to a gain of around 10^6 [93].

SiPM - Silicon Photo-Multiplier

An SiPM is a semiconductor photosensor made up of numerous avalanche photodiodes operated in Geiger mode. The structure and electric field inside an SiPM are shown in Figure 3.11. Photons interact inside the silicon, producing an electron-hole pair. The electron will drift to the high-field

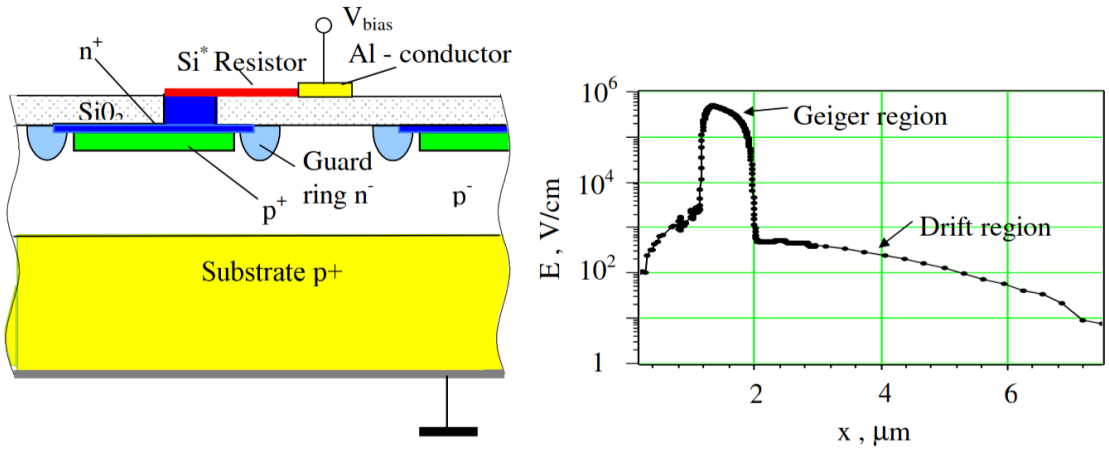

Fig. 3.11 Left shows a schematic diagram of an SiPM. The right shows the electric field varying with position across the SiPM. A depletion region is formed between the p^+ and n^+ layers, causing any electron that enters the region to cause an avalanche breakdown, creating a large gain. Reproduced from [94].

depletion region between the n^+ and p^+ layers, which will cause an avalanche producing a gain of around 10^6 [94]. The voltage at which the SiPM is capable of producing a Geiger avalanche is known as the breakdown voltage [95], and the voltage over breakdown has a large influence on the response of the SiPM [92].

Figure 3.12 shows the quantum efficiency of two different SiPMs. The SiPMs have much broader quantum efficiency curves than the PMTs in Figure 3.10. This allows for SiPMs to be applied to more detector types. In addition, the peak quantum efficiency of SiPMs is comparable to or higher than that of the PMTs.

Once a pixel fires a second photon, an incident photon on the same pixel is unable to produce a second avalanche event. The recovery time is the time for the pixel to be capable of producing an avalanche event, and is typically ≈10 ns [98]. Due to this and the finite number of pixels, SiPMs exhibit non-linearity as the number of photons approaches the number of pixels. This can be described by

$$N_{\text{fired}} = N_{\text{total}} \left(1 - e^{-\frac{N_{\text{ph}} Q}{N_{\text{total}}}} \right) \tag{3.6}$$

N_{fired} is the number of pixels fired, N_{total} is the total number of pixels, N_{ph} is the number of photons, and Q is the photon detection efficiency (PDE) and is equivalent to the quantum efficiency [98]. Figure 3.13 shows the effect of the non-linearity. This effect causes the number of photons contributing to the

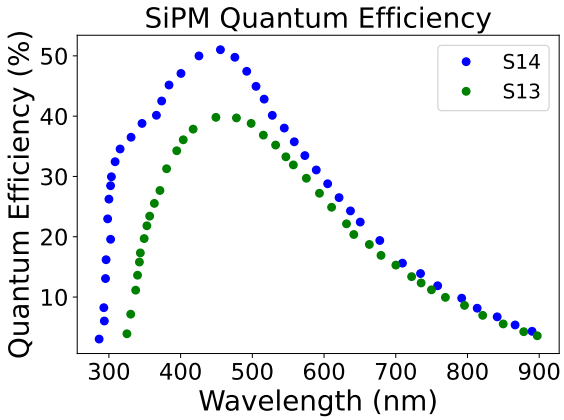

Fig. 3.12 Quantum efficiency of Hamamatsu SiPMs varying with photon wavelength, two SiPMs are shown corresponding to the S13 and S14 generation SiPMs. Data are from [96, 92].

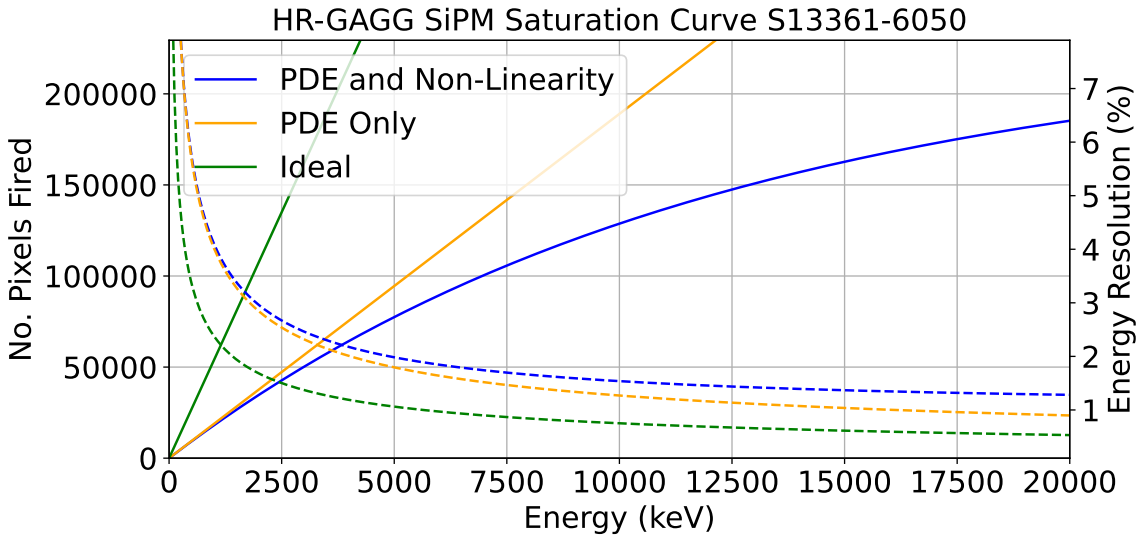

Fig. 3.13 SiPM response to different gamma ray energies for different considerations using a HR-GAGG detector [86], and the S13361-6050AE04 SiPM [97]. Ideal shows the case where every photon produced leads to a pixel firing, PDE only shows the case where only the quantum efficiency is considered, and PDE and Non-Linearity shows the case when the quantum efficiency and the limited number of pixels are considered. Using $N_{\text{pixel}} = 229376$, $Q = 0.35$ [97], and $N_{\text{ph}} = 54\ \text{keV}^{-1}$ [86]. The dashed lines show the energy resolution for the different cases, only considering counting statistics and a 5 % energy resolution at 662 keV for the PDE and non-linearity case.

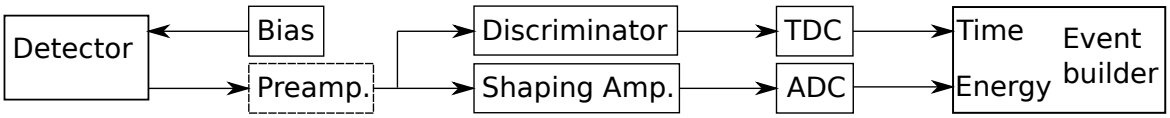

Fig. 3.14 Flow diagram showing the typical layout of an analogue electronics DAQ system. The detector is biased using a voltage supply. The signal from the detector may be passed to a preamplifier if necessary, after which the signal is split. The first stage is for measuring the energy, where the signal is sent to a shaping amplifier followed by an ADC. The second stage is for measuring the time of the event using a discriminator, followed by a TDC. The data from the TDC and ADC are then passed to a computer (event builder) to correlate and save the recorded events.

signal to be smaller, which leads to a worse energy resolution at higher energies than expected from a model only including the quantum efficiency.

In order to cover large areas, smaller SiPM arrays are connected to form larger arrays [96, 97, 92]. For instance, the S14160-6050HS is a 6×6 mm^2 array of 14331 pixels, and 16 of these arrays are then combined into a 4×4 grid to produce the S14161-6050HS-04 array covering an area of 25×25 mm^2 [92]. For such a device, how the individual arrays are connected together needs to be considered carefully, as when connected in parallel, the capacitances add, leading to long signals and poor time resolutions. One method for fast timing with SiPM has been achieved using capacitively coupled fast outputs [99, 100]. However, this method requires two signals per detector, increasing the number of DAQ channels and introducing additional complexity. Other methods have been performed using multiple op-amps for summing the pixels [101], which produces a single fast signal. Yet, this method requires large PCBs, requiring additional space between the detectors in an array, reducing the detection efficiency, and the op-amps produce heat, which may be an issue for large detector arrays.

3.4 Pulse Processing and Data Acquisition

In order to produce spectra and extract physical results from the electrical signals produced by the detector, a DAQ is needed to process the signals and save the results. Currently, two distinct DAQ systems exist, one based on analogue signal processing, and the second based on digital signal processing [70].

Figure 3.14 shows a flow diagram of a typical DAQ utilising analogue electronics. The detector is biased using a voltage supply. The signal may be passed through a pre-amplifier. The signal is then split into two paths, one for determining the energy and one for determining the signal timing. The energy path first uses a shaping amplifier [70] to shape the input into a Gaussian-like signal that is

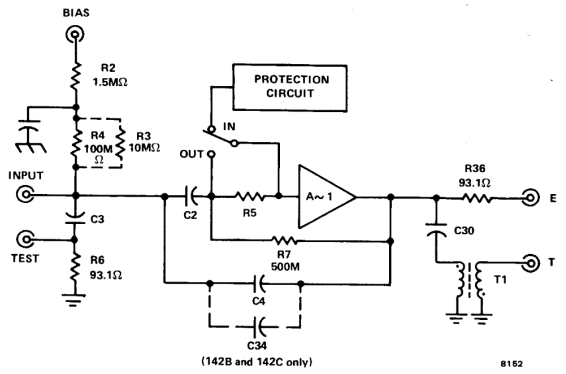

Fig. 3.15 Circuit diagram of an Ortec 142 type preamplifier [102]. The bias voltage is connected to the bias. The detector is connected to an input where the bias is supplied, and the charge is collected from. Test is an input for a test pulse. E shows the output for energy measurements, and T is the output for timing. Reproduced from [102].

then passed to an analogue-to-digital converter (ADC) [70] to convert the peak height to digital. The time path requires a discriminator to trigger on the signal [70]. If the discriminator triggers, a logic signal will then be produced and sent to a time-to-digital converter (TDC), where the time will be converted to a digital value and saved. The information from the ADC and TDC is sent to an event builder, where the two pieces of information are correlated, and events are built and saved.

Certain detectors, such as HPGe, require charge-sensitive preamplifiers to produce a measurable signal [79]. A circuit diagram of a typical charge-sensitive preamplifier is shown in Figure 3.15. The circuit acts to integrate and amplify the charge produced in the detector. Typical pre-amplifier signals have a decay time of $O(100\ \mu\text{s})$ [102].

Shaping amplifiers are used to create a signal where the peak height correlates to the energy deposited in the detector. Shaping amplifiers use RC integration and differentiation to shape the signal into a near-Gaussian signal [103]. Several factors need to be optimised for the specific detector, in particular, the integration time (RC) and the amplifier gain. Due to the input signal decay time, if only an RC integration circuit is used, there will be an undershoot on the far end of the signal. In order to fix this, pole-zero correction is implemented [103]. The processed signal from the shaping amplifier is then sent to an ADC to determine the peak height of the signal.

Two main types of discriminators exist: leading edge discriminator (LED) and constant fraction discriminator (CFD) [70]. LEDs use a voltage reference. Once the signal goes beyond the reference voltage, a trigger signal is generated. Due to the fixed voltage reference, smaller signals will trigger

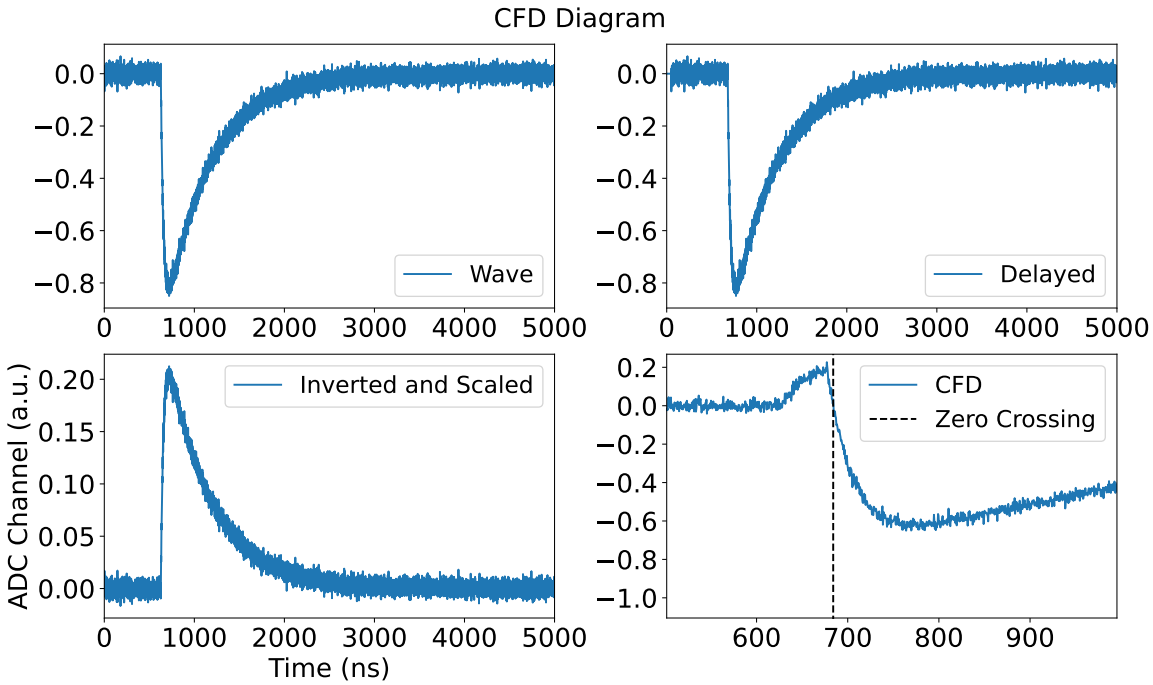

Fig. 3.16 Diagram showing the process of a CFD. The top left plot shows the incoming wave. The top right plot shows the delayed wave. The bottom left plot shows the inverted and scaled wave (25 %). The bottom right plot shows the sum of the bottom left plot and the top right plot, and the subsequent zero crossing point is indicated with the dashed line.

later than a larger signal with the same rise time; this is referred to as time walk [70]. This effect degrades the time resolution when an LED is used.

CFDs are used to eliminate the effect of time walk from LEDs. A CFD creates two copies of the same wave, one inverted and scaled, and the second is delayed. By summing the two waves, a zero crossing point is produced, and this point is used as the time reference for generating the trigger signal [70]. This process is shown in Figure 3.16.

The second type of DAQ is a digitiser DAQ. Digitisers are based on ADCs, creating a digital waveform [70] that can then be processed with different algorithms to determine the time and energy of the signal. Digitisers typically use a digital algorithm of an LED or CFD to trigger the event and determine the time of the event [104].

Figure 3.17 shows an example of a charge-to-digital converter (QDC) algorithm. In the algorithm, a gate is defined that sums the points inside the gate. A long gate is used for determining the energy of the signal, whilst several smaller gates can be used for pulse shape analysis [105].

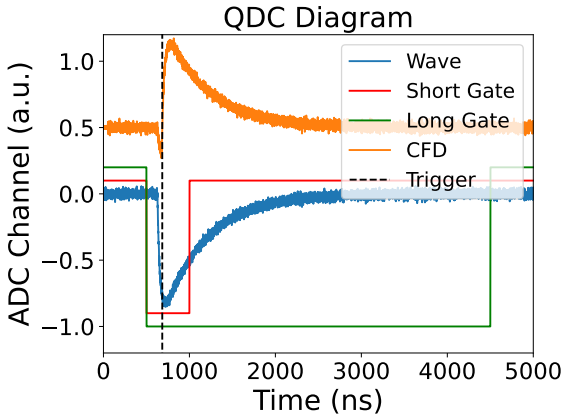

Fig. 3.17 Diagram of a digital QDC algorithm [104]. A digital CFD is used for triggering and determining the time of the event; a dashed line indicates the zero crossing point. The green gate shows an integration gate used for determining the energy of the event. The red gate shows a shorter gate that can be used for pulse shape analysis.

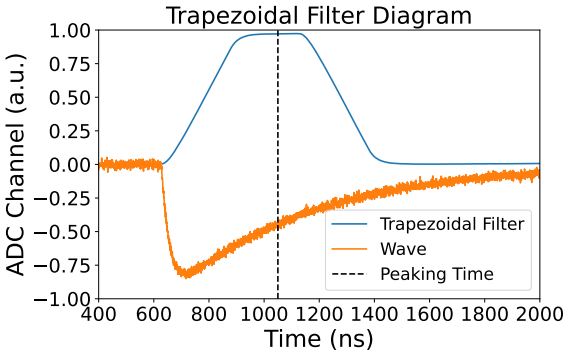

Fig. 3.18 Diagram of the trapezoidal filter. A sample waveform is shown in orange, the trapezoidal filter output is shown in blue, and the peaking time is shown in black. The peaking time is the sample of the trapezoid that is used to calculate the energy.

Trapezoidal shaping is also a common algorithm used for digital pulse shape processing [104, 106]. The algorithm can be written as

$$d^{k,l}(j) = v(j) - v(j-k) - v(j-l) + v(j-k-l) \tag{3.7}$$

$$p(n) = p(n-1) + d^{k,l}(n) \tag{3.8}$$

$$s(n) = s(n-1) + p(n) + d^{k,j}(n)M \tag{3.9}$$

where $v(j)$ is the input sample j, $d^{k,l}(j)$ and $p(n)$ is a parameter of the algorithm, and $s(n)$ is the output trapezoidal signal at point n. l and k are the shaping parameters of the trapezoid, where the flat top time is given as $l-k$, and the rise time of the trapezoid is k. M is the pole-zero adjustment to account for the decay of the signal [106]. Figure 3.18 shows an example of this algorithm. The energy is determined by taking a sample at the top of the signal. A single sample can be taken, or several samples can be taken, and an average of the samples can be used [104]. This method is optimal for slow signals, such as those produced by pre-amplifiers.

3.5 Radioactive Isotope Production and Identification

In order to increase the understanding of the nuclear chart, it is crucial to study exotic nuclei. The two main methods that are used for producing exotic nuclei are isotope separation on-line (ISOL) [107], and in-flight separation [108]. ISOL typically involves impinging a proton beam on a heavy target, producing radioactive isotopes inside the target. The target is heated to cause the produced isotopes to diffuse out of the target. Due to this, the nuclei that can be produced are limited to isotopes with a half-life longer than the diffusion time [109] and with a boiling point lower than the melting point of the target [107].

In-flight production involves accelerating a heavy ion beam and impinging the beam on a target, and producing exotic nuclei by fission or fragmentation reactions. This has the benefit of being able to produce isotopes with shorter half-lives and not being limited by the boiling point of the isotope. However, drawbacks of this method are: the beam purity is worse than ISOL, and it requires intermediate to high energies, which causes issues with Doppler shifts [108, 30]. This work will focus on isotope production using in-flight methods.

An ion travelling through a dipole magnet will bend according to the equation

$$\frac{A}{Q} = \frac{B\rho}{\beta c \gamma m_u} \tag{3.10}$$

where A is the mass of the nucleus in atomic mass units, m_u, Q is the charge of the ion, B is the magnetic field strength of the dipole, β is the velocity of the ion in units of c, $\gamma = \frac{1}{\sqrt{1-\gamma^2}}$, and ρ is the radius of curvature [110]. Dipole separators allow for a separation based on the A/Q, but are limited and cannot distinguish two different nuclei with the same A/Q, but different Q values. In addition, if there is an energy spread among ions of the same isotope, the A/Q separation will be poor. A degrader can be used to separate out different nuclei with the same A/Q, but a different Z, due to the energy loss being $\propto Z^2$. By using a wedge-shaped degrader, the separation can be done achromatically [111].

Other techniques for isotope identification use TOF to measure the velocity of the ion by

$$\text{TOF} = \frac{L}{\beta c} \tag{3.11}$$

where TOF is the time of flight, and L is the flight path length [110]. This allows for a measurement of the particle's velocity. In addition, the energy loss in a material is given as

$$\Delta E \propto \frac{Z^2}{\beta^2} \tag{3.12}$$

allowing for a measurement of the ion charge when combined with a TOF measurement [110].

3.6 In-Beam Gamma-ray Spectroscopy

Traditional gamma-ray spectroscopy favours using a light-stable beam impinging on a heavy target to produce target-like nuclei in an excited state. This method is limited by the nuclei that can be made into targets. Utilising in-flight production and magnetic spectrometers, reactions can be performed in inverse kinematics with a heavy-ion beam and a light target. Inverse kinematics with the use of unstable beams allows for the investigation of more exotic nuclei [111]. In addition, inverse kinematics allows for the use of magnetic spectrometers before and after the target, allowing for gating on specific reactions [111].

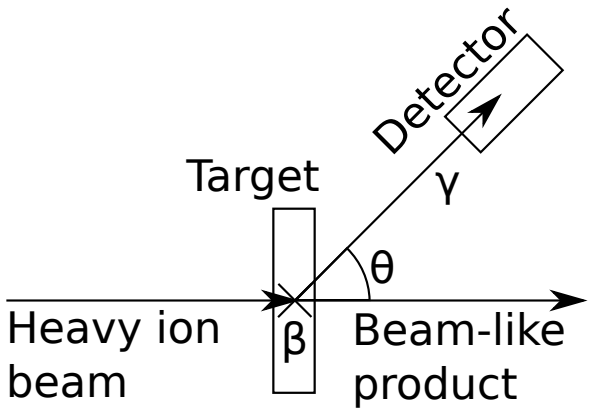

Fig. 3.19 Diagram of a typical in-beam gamma-ray spectroscopy experiment in inverse kinematics. An incoming heavy ion interacts with the target, producing a beam-like product in an excited state. The beam-like product decays via the emission of a gamma-ray that is measured in a detector. β is the velocity of the ion at the time of gamma-ray decay, and θ is the angle of emission relative to the motion of the beam-like product.

One type of experiment that can be performed in inverse kinematics is in-beam gamma-ray spectroscopy [30]. Figure 3.19 shows a diagram of in-beam gamma-ray spectroscopy in inverse kinematics. A heavy ion incident on a target reacts, producing a beam-like product in an excited state, which decays via gamma-ray emission. As the nucleus decays in flight, the energy of the gamma ray is Doppler shifted according to

$$E_\gamma = \frac{\sqrt{1-\beta^2}}{1-\beta\cos\theta} E_{\gamma 0} \tag{3.13}$$

where E_γ is the lab-frame energy, $E_{\gamma 0}$ is the rest frame energy, and θ and β are defined in Figure 3.19 [30]. This will need to be corrected to determine the rest-frame energy of the gamma ray to extract information about the nucleus's excited states.

Several factors affect the energy resolution after Doppler correction: the angular uncertainty $\sigma\theta$, the velocity uncertainty $\sigma\beta$, and the intrinsic energy resolution [30]. This effect can be seen in Figure 3.20. The intrinsic resolution is determined by the detector material. The angular uncertainty is determined by the size and position of the detector and may be reduced by position sensitivity [28]. The uncertainty in β primarily emerges from the finite thickness of the target. Energy loss in the target reduces the velocity across the target, and depending on the point in the target where the reaction happens, the β value will be different. This can be reduced by using a thin target, but this would reduce the luminosity; therefore, a balance needs to be achieved between the two.

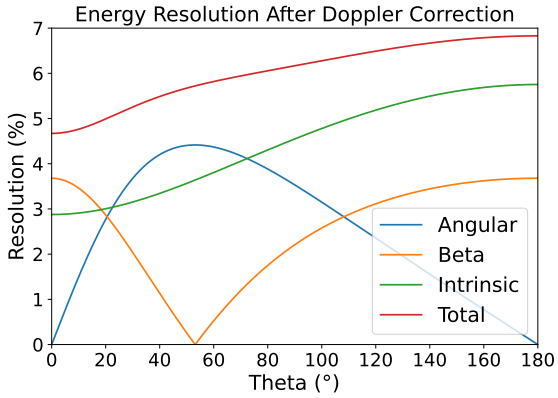

Fig. 3.20 Energy resolution after Doppler correction varying with emission angle θ in the lab-frame [30] for $E_{\gamma 0} = 1.0$ MeV, $E_{res}(662\text{ keV}) = 5$ %, $\sigma_\beta = 0.01$, and $\sigma_\theta = 0.025$ rad. The individual contributions to the resolution are included in the plot.

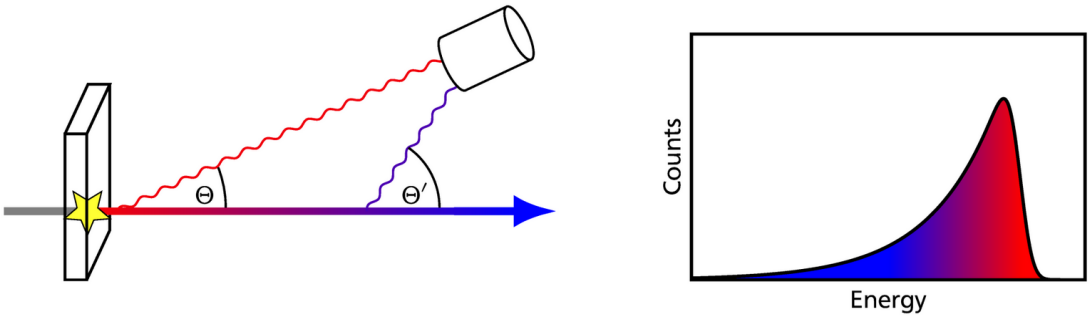

Fig. 3.21 Diagram showing the lifetime effect in in-beam gamma-ray spectroscopy. The left shows the origin of the effect, an ion decaying at the target centre is shown in red, and an ion decaying later is shown in blue. Θ is assumed in the Doppler correction, whilst Θ' is the correct value; this leads to the asymmetric peak shape shown in the right plot. Reproduced from [112].

In the Doppler correction, it is typically assumed that the decay occurs at the target centre. However, if the state has a significant lifetime, the ion will move some distance before decaying. This causes the assumed velocity and θ to be different from the true value, which leads to an asymmetric peak shape. This effect can be seen in Figure 3.21. This effect can be used to perform lifetime measurements, typically by comparing the experimental data to simulated response functions of different lifetimes and energies [113, 114].

Chapter 4

Fragment Separators, Detectors and Experimental Setup

An experiment was carried out at the RIBF to examine neutron-rich Zn isotopes, with the purpose of measuring the lifetimes and energies of excited states in this region via in-beam gamma-ray spectroscopy. This chapter will present the accelerator, separator and the spectrometer used to produce and identify RI beams, and finally, the gamma-ray detection system will be discussed.

4.1 Isotope Production and Separation

4.1.1 Ionisation and Acceleration

A ^{238}U primary beam was used for the experiment. The path of acceleration for ^{238}U can be seen in Figure 4.1. The Uranium is ionised using a 28 GHz Superconducting Electron Cyclotron Resonance

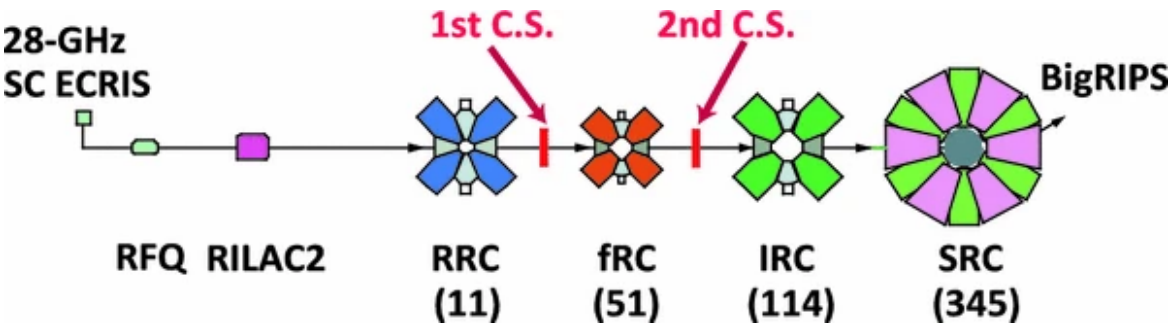

Fig. 4.1 Schematic diagram of ionisation and acceleration path for a ^{238}U primary beam at the RIBF. Reproduced from [115].

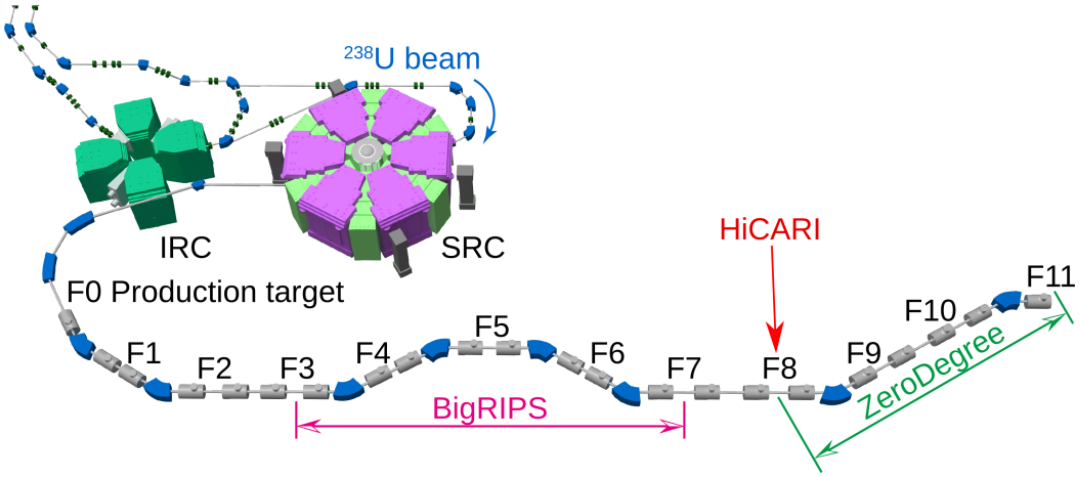

Fig. 4.2 Layout of the BigRIPS Zerodegree beam line at the RIBF. The final two acceleration stages are shown along with the fragment separators. The focal planes of the separators are shown using F*i*. The HiCARI label shows the position at which in-beam gamma-ray spectroscopy is performed. Diagram is adapted from [122, 9].

Ion-Source (SC ECRIS), producing the U^{35+} charge state [116, 117, 118]. These ions are accelerated using RIKEN Linear Accelerator 2 (RILAC2) up to 670 keVu^{-1} [119]. The accelerated ions are accelerated further to 11 MeVu^{-1} by the RIKEN Ring Cyclotron (RRC). The first charge stripper is designed to convert U^{35+} to U^{71+}. The ions are then inputted into the fixed-frequency Ring Cyclotron (fRC), where they are accelerated to 51 MeVu^{-1}. Then the second charge stripper ring removes further electrons, aiming to leave the ions in the U^{86+} charge state. The ions are then passed to the Intermediate-stage Ring Cyclotron (IRC), and the ions leave the IRC with $E = 114$ MeVu^{-1}. Finally, the ions are accelerated to 345 MeVu^{-1} using the Superconducting Ring Cyclotron (SRC) [120]. After the SRC, the ions are directed to a 4 mm Be production target located at F0, where the ions undergo fission, producing exotic nuclei [121].

4.1.2 Fragment Separation and Spectrometry

To identify and separate nuclei, magnetic spectrometers were used. For this experiment, the Big RIKEN Projectile-fragment Separator (BigRIPS) and the ZeroDegree spectrometer [63] were utilised. Figure 4.2 shows the layout of the RIBF in this configuration. For the experiment, a 6.8 mm-thick Be secondary target was placed at F8. BigRIPS was used to separate and identify the nuclei before the

Device	Material	Thickness/mm	β_{after}
Primary Target	Be	4	0.6525
F1 degrader	Al	8	0.6390
F3 plastic scintillator	plastic	0.2	0.6390
F3 double PPAC 1	mix		0.6388
F3 double PPAC 2	mix		0.6386
F5 double PPAC 1	mix		0.6384
F5 wedge degrader	Al	2	0.6240
F5 double PPAC 2	mix		0.6238
F7 double PPAC 1	mix		0.6236
F7 MUSIC	mix		0.6199
F7 double PPAC 2	mix		0.6196
F7 plastic scintillator	plastic	0.2	0.6189

Table 4.1 Detectors and other material in the beam-line for BigRIPS (F0-F7). The devices are listed in order of their position in the beam line from the most upstream to the most downstream [124]. Mix refers to detectors made up of multiple materials. β_{after} is the beam velocity after the element for ^{80}Zn ions calculated using LISE++ [125].

secondary target, whilst ZeroDegree was used for identifying the outgoing nuclei after the secondary target, for the purpose of gating on specific reactions.

BigRIPS

BigRIPS extends from F0 to F7 [111]. It is used to separate and identify the nuclei produced from the primary target. The first stage from F0-F2 is used to separate the nuclei, and the second stage from F3-F7 is used for identifying the nuclei [123].

The device consists of 14 superconducting triplet quadrupoles (STQ) [123], and six dipoles [111]. A list of beam line detectors and devices can be seen in Table 4.1. The STQs are used to focus the beam, whereas the dipoles are used to bend the beam. The degrader located at F1 and the dipole between F1 and F2 are used for the separation of the nuclei at F2; an additional degrader is located at F5 to further separate the nuclei [111].

To identify nuclei, the TOF-$B\rho$-ΔE method is used [110]. The plastic scintillators are used as time references to measure the TOF according to

$$\text{TOF} = t_{F7} - t_{F3} \tag{4.1}$$

where t_{Fi} is the time measured using the scintillators at the respective focal points. The energy loss is measured in the MUSIC detector at F7. Finally, the $B\rho$ values before and after the F5 degrader are determined using the position measurements from the PPACs located at F3, F5, and F7 using the ion-optical matrix. Two $B\rho$ values are calculated: $B\rho_{35}$, and $B\rho_{57}$ corresponding to the $B\rho$ of F3-F5, and F5-F7, respectively.

The largest energy losses in BigRIPS occurred in the F1 degrader, the F5 degrader, and the F7 MUSIC. Due to the energy loss in the F5 degrader for the TOF measurement, two velocities need to be considered, β_{35} and β_{57}. Where the TOF is given as

$$\mathrm{TOF} = \frac{L_{35}}{\beta_{35}c} + \frac{L_{57}}{\beta_{57}c} \tag{4.2}$$

where L_{ij} is the flight length between focal planes i and j. The A/Q values are given as

$$\left(\frac{A}{Q}\right)_{35} = \frac{B\rho_{35}}{\beta_{35}\gamma_{35}}\frac{c}{m_u} \tag{4.3}$$

$$\left(\frac{A}{Q}\right)_{57} = \frac{B\rho_{57}}{\beta_{57}\gamma_{57}}\frac{c}{m_u} \tag{4.4}$$

by combining these measurements, the A/Q is determined, assuming no change in A/Q occurs in the degrader. Whereas the MUSIC [126] detectors measure the energy loss of the particle, ΔE, which is then used to determine the charge using the relation

$$\Delta E \propto \frac{Z^2}{\beta^2} \tag{4.5}$$

where β is the determined β_{57}. Using the Z, and A/Q values, nuclei are identified [110].

ZeroDegree

ZeroDegree is located from F8 to F11. A list of materials in the beam line can be seen in Table 4.2. For this experiment, ZeroDegree was used to identify the reaction products from the secondary target and the outgoing momenta.

For particle identification, the TOF is measured using the plastic scintillators at F8 and F11. The $B\rho$ between F9 and F11 is used and combined with the TOF to measure the A/Q. Finally, the MUSIC at F11 is used for measuring the charge of the ion. This allows for the identification of the final

Device	Material	Thickness/mm	β_{after}
F8 PPAC 1	mix		0.6187
F8 plastic scintillator	plastic	0.2	0.6179
F8 PPAC 2	mix		0.6177
Secondary target	Be	6.8	0.5728
F8 PPAC 3	mix		0.5725
F9 PPAC 1	mix		0.5727
F9 PPAC 2	mix		0.5724
F11 PPAC 1	mix		0.5723
F11 plastic scintillator	plastic	0.2	0.5713
F11 PPAC 2	mix		0.5709
F11 MUSIC	mix		0.5645

Table 4.2 Detectors and other material in the beam-line for ZeroDegree (F8-F11). The devices are listed in order of their position in the beam line from the most upstream to the most downstream. Mix refers to detectors made up of multiple materials. β_{after} is the beam velocity after the element for ^{80}Zn ions calculated using LISE++ [125].

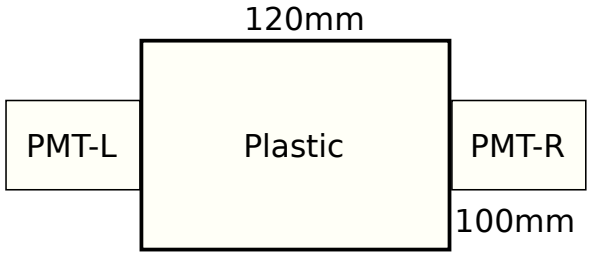

Fig. 4.3 Schematic diagram of the plastic scintillator detector used in the beam line. There is a plastic scintillator in the centre with two PMTs attached, labelled PMT-L and PMT-R.

reaction product. The PPACs located at F8 are also used for tracking the scattering angle of the nucleus after the reaction in the secondary target.

4.1.3 Beam Line Detectors

To identify the exotic nuclei, various detectors were used. Properties such as position, charge, and velocity were measured. The detectors used for these measurements will be discussed in this section.

Plastic Scintillators

Due to the fast timing properties of plastic scintillators, they are used as time references for the particles at different points in the separator. 0.2 mm-thick EJ-212 and EJ-230 scintillators are used [124, 81] of dimensions 120x100 mm^2. Each scintillator has two H1949-50 PMTs [124], one located

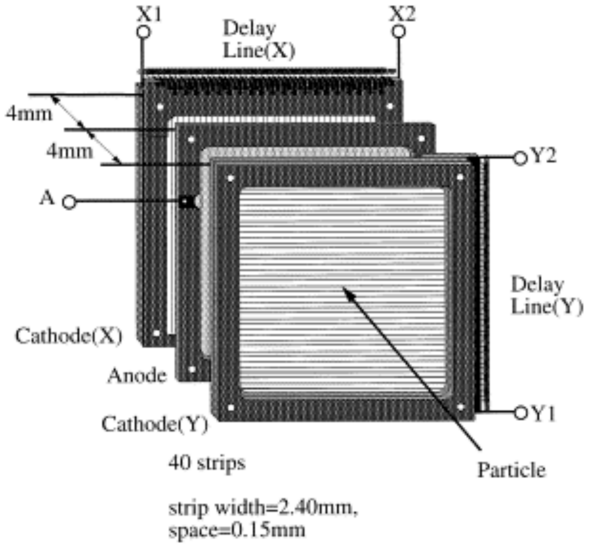

Fig. 4.4 Diagram of a PPAC detector. Reproduced from [127].

on each of the thin sides of the scintillator. A schematic diagram of this can be seen in Figure 4.3. The PMT electrical signals are split into two signals, one going to a QDC to measure the energy deposition, and the second to an LED to pick up the time of the interaction, which is recorded using a TDC. Each of the PMTs provides a time reference $T_{R,L}$ for the right and left PMT, respectively. The two-time references are used to determine the particle impingement time, T, as

$$T = \frac{T_L + T_R}{2} \tag{4.6}$$

where the left-right coincidence is used to reduce the background and reduce the effect from the position of interaction.

PPAC - Parallel Plate Avalanche Counter

To track the position of the particles, PPACs are used [127, 128]. The PPACs have two sets of parallel strips, one in the x direction and one in the y direction, with the xy plane perpendicular to the beam, which act as the cathodes with a film in the centre acting as the anode, this is shown in Figure 4.4. The anode is biased to $\approx$800 V. The PPAC chamber is filled with isobutene. When the ions pass through the PPAC, they cause avalanches in which the electrons travel towards the cathode wire closest to the path of the ion. This produces a pulse on said wire, knowing the wire that fired would give one

dimension of the ion's position. By having two sets of perpendicular cathode wires, the position of the ion in 2D space can be determined.

Rather than reading each wire individually, the wires are multiplexed using a delay line system, allowing the signals from one cathode plane to be reduced down to two signals for each cathode plane [127]. The signals are passed through a preamplifier and then to a fast-timing amplifier, and finally, the signal time is determined with a CFD. Where the position of the particle is determined using the time difference between the two signals of the x and y planes, according to

$$x = k_x \frac{T_{x1} - T_{x2}}{2} + x_{\text{off}} \tag{4.7}$$

$$y = k_y \frac{T_{y1} - T_{y2}}{2} + y_{\text{off}} \tag{4.8}$$

$$\tag{4.9}$$

where x, and y are the determined positions of the particles, T_{x1}, and T_{x2} are the times from the two sides of the delay line for the x plane and the same for T_{y1}, and T_{y2} for the y plane. $k_{x,y}$ are constants to determine the positions, and x, y_{off} are the offsets [127].

The PPACs are combined into double PPACs with 2 sets of x and y wires. This is done to increase the efficiency of the PPACs. If both PPACs triggered, then the average of the two coordinates is taken as the position; if only one fired, then these coordinates are taken; and if no PPAC fired, then no coordinate is available, and the event is discarded.

MUSIC - MUlti Sampling Ionisation Chamber

To determine the charge of a particle, the energy loss in a material is measured. According to the Bethe-Bloch formula [70], assuming the velocity change is small relative to the velocity itself, the mean energy loss is given as

$$\Delta E \propto \left(\frac{Z}{\beta}\right)^2 \tag{4.10}$$

where ΔE is the energy loss, Z is the charge of the particle, and β is the velocity [129]. To measure the energy loss, MUSIC detectors are used [126]. MUSIC detectors are constructed of 24 4 μm parallel plates used as alternating cathodes and anodes inside a case filled with a counter gas, as shown in Figure 4.5. The anode signals are used to determine the energy deposited in the detector [126]. Two neighbouring anode plates are summed together before a preamplifier, after which the pre-amplifier

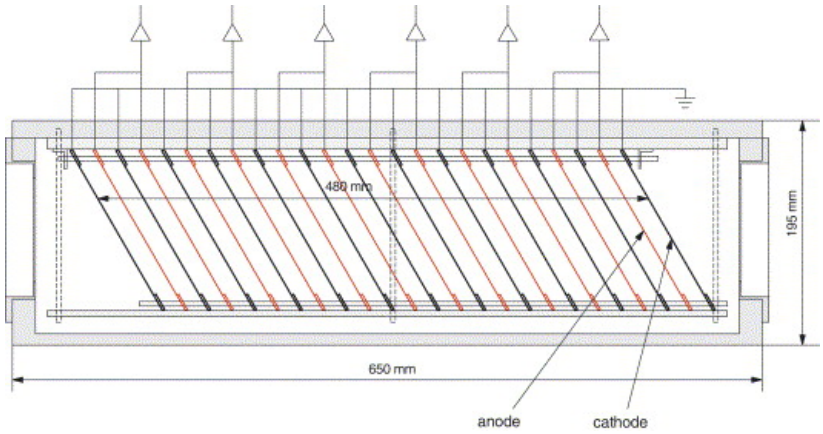

Fig. 4.5 Diagram of a MUSIC detector, the black shows the cathodes, and the red shows the anodes. Reproduced from [126].

signals are sent to a shaping amplifier, followed by an ADC module. Where the energy loss, ΔE is calculated according to

$$\Delta E = \alpha \left(\prod_{i=1}^{N} (\mathrm{ADC}_i - c_i) \right)^{1/N} \tag{4.11}$$

where α is a calibration coefficient, ADC_i is the measured ADC channel, N is the number of triggered channels, and c_i are offset corrections for each channel [129].

4.2 HiCARI - High-resolution Cluster Array at the RIBF

The aim of this experiment is to measure the lifetime and energy of excited states in neutron-rich Zn isotopes in the range $^{78-81}$Zn. To do this, excited states of neutron-rich Zn isotopes were populated by knockout reactions and inelastic scattering on a 6.8 mm thick Be target located at F8. The prompt gamma rays were then measured using the HiCARI array. A 0.5 mm thick lead shield was placed around the beam pipe at F8 to reduce the low-energy background [30].

HiCARI was an array of HPGe detectors [11]. A picture of the array can be seen in Figure 4.6. The array was made of three different types of HPGe detectors: Miniball (MB) [130], Superclovers (SC) [131], and GRETINA-type tracking detectors (GR) [29, 28]. Five Miniball triplets, four Superclover quadruplets, and two GRETINA clusters were used for the experiment [11].

The structure of the Miniball detectors can be seen in Figure 4.7. Miniball clusters are made up of three crystals, which are each electronically segmented into six segments, giving greater granularity to the position of interaction [23, 130]. The core electrodes were used for energy measurements, and the

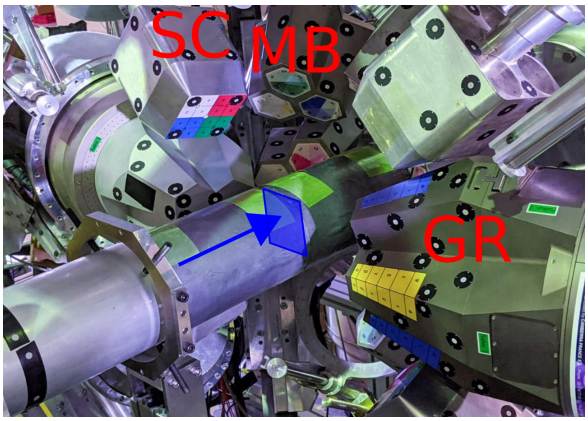

Fig. 4.6 Picture of the HiCARI array, detectors are marked with their type: MB, Miniball; SC, Superclovers; and GR, GRETINA.

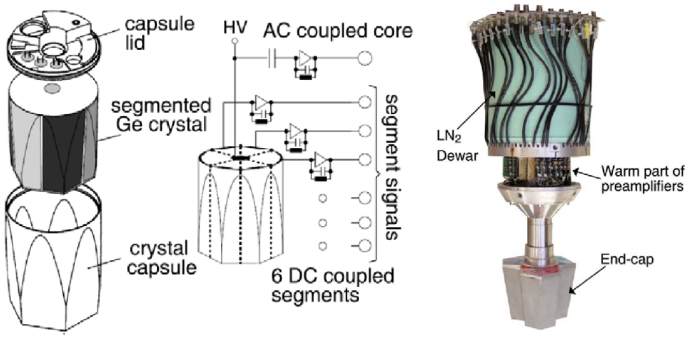

Fig. 4.7 Diagram of crystal structure for a Miniball detector and electronics, and picture of a complete Miniball triplet. Reproduced from [23].

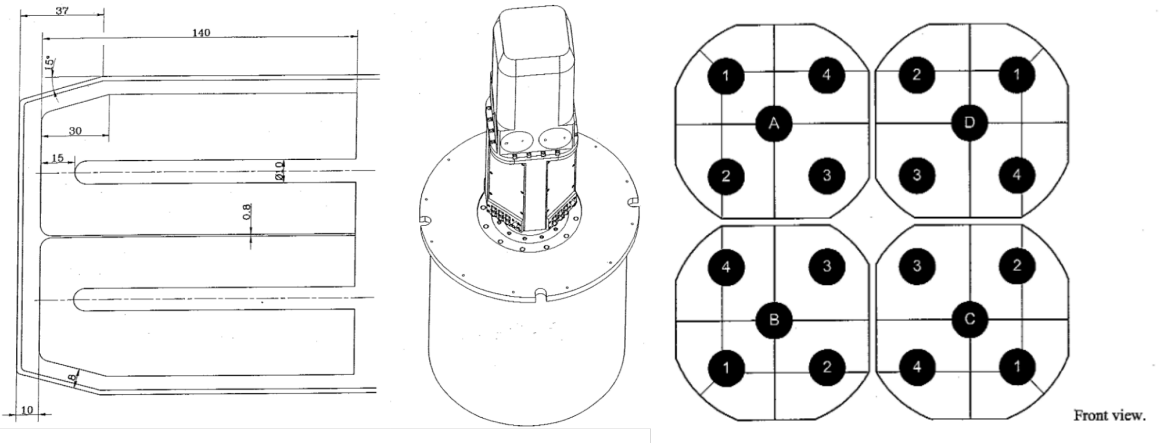

Fig. 4.8 Left shows a cross-section of one Superclover cluster, the hollow centre shows the central contact of the detector. Centre shows the geometry of the detector and cryostat. Right shows the segmentation of crystals. Adapted from [132].

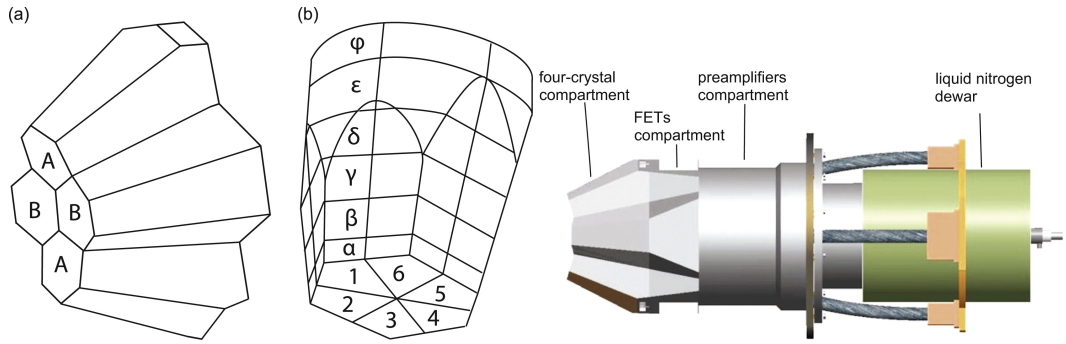

Fig. 4.9 Geometry of GRETINA Quad detectors. (a) shows the internal geometry of a quad GRETINA detector (a.a), and the crystal segmentation (a.b). (b) shows the external geometry with the outside shell, electronics and liquid nitrogen dewar. Reproduced from [29].

segment electrodes were used for position determination. One of the Miniball clusters was removed from the analysis due to the poor Doppler-corrected performance.

Superclovers are clusters made of four crystals in a 2×2 configuration. The geometry of Superclover detectors is shown in Figure 4.8. Each crystal has four segments, which are used for gamma-ray position determination and a core used for energy and timing [132, 133].

GRETINA crystals are HPGe crystals that are segmented into 36 segments, as shown in Figure 4.9. GRETINA has position reconstruction capabilities allowing for sub-segment position resolutions [29]. This position reconstruction is achieved via waveform analysis based on the Shockley-Ramo theorem [76, 134]. Two clusters were used for the experiment: one quad (two working crystals) from the

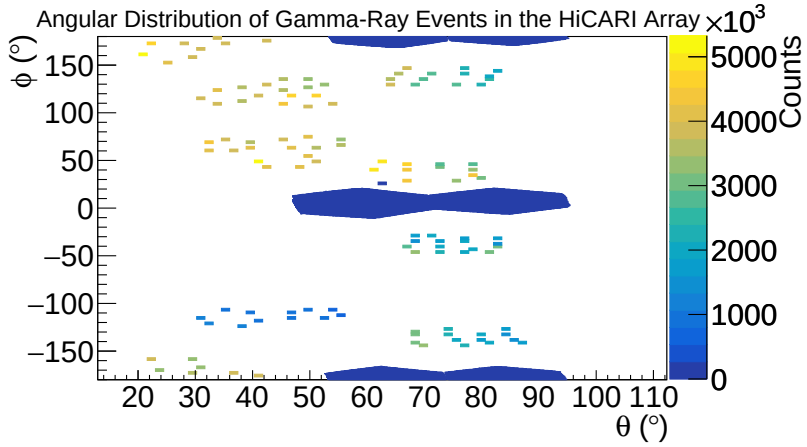

Fig. 4.10 Angular distribution of events relative to the HiCARI array centre, where θ is the angle between the beam direction, and ϕ is the azimuthal angle, with the x direction being defined parallel to the ground.

Research Center for Nuclear Physics, Osaka University, Japan and a prototype triplet (two working crystals) from the Lawrence Berkeley National Laboratory, USA, which will be referred to as the quad and P3, respectively [135].

4.2.1 Configuration

The detectors were mounted in a custom detector frame and cooled with liquid nitrogen, which was refilled every eight hours. The detectors were biased to 3-5 kV using a Caen SY4527 power supply [136]. The signals from the preamplifiers of the detectors were sent to GRETINA digitisers [137] using a trapezoid filter to determine the energy. The central contacts of the crystal were used for timing and energy, whereas the segment contacts were used for the position of the gamma-ray interaction. Cluster add back was used to recover the full energy peak from multi-segment or multi-crystal hits within a cluster.

To determine the detector positions in the lab, photogrammetry was used alongside the engineering drawings to determine the segment centres, which are used for the position of interaction in the lab frame. The reconstructed positions of the detectors can be seen in Figure 4.10. The single points are the Miniball and Superclovers, whereas the detectors with distributions of events are the GRETINA detectors. The Miniball detectors were placed at the forward angles, whereas the Superclover and GRETINA detectors were placed closer to 90° in the centre-of-mass frame. This was because, at small angles, the resolution is dominated by σ_β, whereas at 90° in the centre-of-mass frame, the

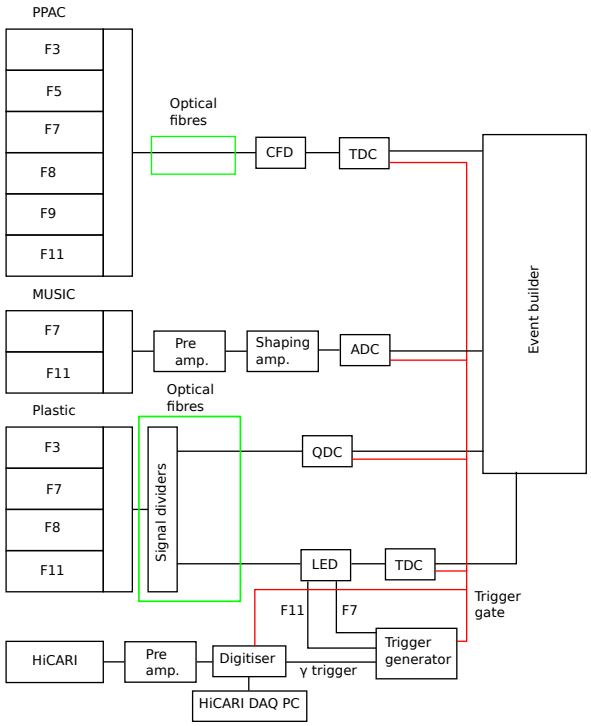

Fig. 4.11 Simplified block diagram of the DAQ system for the experiment.

resolution is dominated by σ_θ. Therefore, by locating the GR detectors at 90° in the centre-of-mass frame, $\approx 60°$ in the lab frame, the improved energy resolution from the position reconstruction could be exploited.

4.3 DAQ - Data Acquisition System

A schematic diagram of the DAQ system can be seen in Figure 4.11. The PPAC signals were first converted into optical signals, which were then sent to the DAQ unit. The optical signals were then converted back to electrical signals, where they were processed with an analogue CFD, and the timing information was then recorded using a multi-hit TDC. The MUSIC signals were first amplified using pre-amplifiers, then the signals were processed with a shaping amplifier, and the energy loss was recorded using an ADC. The PMT signals of the plastic scintillators were first sent using optical fibres, where the optical signal was divided and sent to the DAQ unit. One of the split signals was sent to an LED module, followed by a TDC to record the time of the plastic event, and the second was sent to a QDC to record the energy deposited in the plastic.

The pre-amplifier signals from the HiCARI detectors were sent to digitiser modules, the same used for GRETINA [137]. The energy of the gamma rays was recorded using a trapezoidal filter and the timing from a digital LED. For the two tracking clusters, the positions were determined using the GRETINA algorithm [29]. When the digitisers triggered, a logic signal was generated by the digitisers.

Coincidence triggers for the plastic scintillators were generated using the LED triggers for the left and right PMT signals. The coincidence triggers of the F7 and F11 plastics were sent to a logic circuit alongside the trigger signal from the HiCARI digitiser. Gate and delay generators were used to align the trigger gates of these detectors. If all three of the trigger signals were received, the trigger generator output an accepted trigger signal. This was sent to the DAQ modules, allowing for data to be recorded. In addition to this, downscale modules were used to record 1/7 of F7$\times$F11 events and 1/100 of F7 only events [138]. The data for the beam-line detectors was sent to the RIBF DAQ, where the PID information was reconstructed. The HiCARI data was saved into the HiCARI DAQ PC and saved separately. A timestamp module was used to share the timestamp of the event from the HiCARI DAQ with the beam line DAQ. Using the shared timestamp, the gamma-ray data were then correlated and merged with the beam line data offline. In addition, the F8 plastic signals were divided and passed to the HiCARI DAQ to serve as a time reference.

Chapter 5

Analysis of Neutron Rich Zinc Isotopes

The details of the experimental analysis will be discussed here. The first step in the data analysis was the correlation of beamline data and gamma-ray data. Then the data was reaction gated, and Doppler corrected to obtain the spectra. χ^2 minimisation was then used to determine the energy and lifetime, by fitting the simulated response function to the experimental data.

5.1 Experimental Details

The experiment ran from the 9th to the 16th of April 2021. For the experiment, BigRIPS was centred on ^{80}Zn, and ZeroDegree was centred on ^{79}Cu. A 6.8 mm Be target was placed at the centre of the HiCARI array located at F8. On the 12th of April 2021, the PPACs were exchanged at F3 and F7 as the PPACs were drawing too much current. This requires that the PID has two different analysis matrices for the period before the 12th of April 2021, 14:59 and after. A summary of the experiment can be seen in Table 5.1.

Date	Time	HiCARI run no.	BigRIPS run no.	Details
09/04/21	18:19-00:26	3-7	20-42	Empty target
10/04/21	00:26	8	47	First physics run 6.8 mm Be
12/04/21	14:59	117	155	Exchanged PPACs at F3 and F7
16/04/21	5:38	235	269	Last physics run
16/04/21	6:31	238-241	271-283	Empty target
16/04/21	10:01:41	244	-	^{152}Eu calibration

Table 5.1 Summary of experimental runs. HiCARI run no. refers to the tun number of the HiCARI DAQ, and BigRIPS run no. refers to the run number of the beam-line DAQ.

5.2 Simulation

The array was simulated with the Geant4 framework [74], using a specialist code developed by the HiCARI collaboration [139]. The code is arranged into three components. The first part was used to simulate an incoming nucleus, ${}^{A}_{Z}\mathrm{X}$ with kinetic energy E per nucleon. The energy loss and reaction in the target were emulated, producing a new nucleus ${}^{A'}_{Z'}\mathrm{X}'$ in an excited state. The nucleus then emitted gamma rays according to a user-provided level scheme. Outside the beam pipe, a 0.5 mm thick Pb shield was simulated. The detector and housings were simulated according to the geometry from the photogrammetry measurements. The energy deposited in each detector region was recorded alongside the beam velocity after the target. The data was saved in a binary file. The simulation also output the average first interaction position, which was used for the Doppler correction of the simulated and experimental data.

The second part of the simulation was used to produce a ROOT [140] file, which contained the response of the detectors. The energy deposited in the detectors was converted to the response of the detectors by using user input files, which contained the thresholds and resolutions of each detector. The resolution parameter randomly shifted the energy deposited in the detector according to a Gaussian function of width given in the input file. The threshold parameters gave a threshold probability function which randomly removed or allowed events according to said distribution. Additionally, for the GRETINA detectors, a position resolution parameter was input for each crystal, which took the position of interaction and shifted the x, y, and z values randomly according to a Gaussian distribution. The program also performed cluster-based add-back.

The final section was used to perform the Doppler correction and create the histograms of the gamma-ray energies. The emission angle was determined from the target position and the average first interaction positions, or the position of interaction for GRETINA. The velocity β, was determined according to,

$$\beta = \langle\beta\rangle \left(1 + \frac{\beta_{TA} - \langle\beta_{TA}\rangle}{\langle\beta_{TA}\rangle}\right) \tag{5.1}$$

where β_{TA} is the after-target velocity, $\langle\beta\rangle$, and $\langle\beta_{TA}\rangle$ are the average mid-target velocity and the average after-target velocities, both are user-inputted values. It then output the results into histograms for the individual detector groups.

5.3 Data Structure and Unpacking

From the experiment, three different binary files were filled. One corresponding to the PID, one for the non-tracking HiCARI detectors and one for the tracking HiCARI detectors. The first step in the analysis was to unpack the binary files and convert them into ROOT [140] files. Then the ROOT files were merged into a single ROOT file containing the correlated gamma ray and beam data. Finally, the data were Doppler corrected and gated on reaction channels by applying visual cuts to the BigRIPS and ZeroDegree PID plots, producing histograms of the gamma-ray energy.

5.4 Experimental Doppler Correction

The gamma rays were Doppler shifted according to the equation

$$E_\gamma = \frac{\sqrt{1-\beta^2}}{1-\beta\cos\theta} E_{\gamma 0} \tag{5.2}$$

where E_γ is the lab frame gamma-ray energy, $E_{\gamma 0}$ is the gamma-ray energy in the centre-of-mass frame, β is the velocity at the time of emission, and θ is the angle of emission of the gamma ray [30]. In order to Doppler correct the gamma-ray energy, the θ and β needed to be determined.

To obtain the β values, the $B\rho$ measurements were used, according to

$$\beta = \frac{1}{\sqrt{1+\left(\frac{mc^2}{ZB\rho c}\right)^2}} \tag{5.3}$$

where m is the nuclear mass, Z is the nuclear charge, and c is the speed of light. From the spectrometers, four different $B\rho$ values could be used: F3-5, F5-7, F8-9, and F9-11. F9-11 was chosen as it has the smallest amount of energy loss between the target position, except for F8-9, which includes contributions from before and after the target position. From the F9-11 β, the β before and at the centre of the target was calculated using the same relation as the simulation. The LISE++ [125] kinematic calculator was used to calculate the average mid-target and before-target β and energies, using the average F9-11 β as a starting point.

To determine the θ value, three values needed to be determined: the scattering angle of the nucleus, the nucleus's position at the target, and the gamma-ray interaction position. The nucleus was tracked using the three PPACs at F8. The three PPACs give three different positions, which are denoted as

(x_i, y_i, z_i). Using the positions from the first two PPACs, the nucleus's path was extrapolated to the target position using

$$x_{\text{targ}} = \frac{x_1 - x_0}{z_1 - z_0} z_{\text{targ}} + \frac{x_0 z_1 - x_1 z_0}{z_1 - z_0} \tag{5.4}$$

$$y_{\text{targ}} = \frac{y_1 - y_0}{z_1 - z_0} z_{\text{targ}} + \frac{y_0 z_1 - y_1 z_0}{z_1 - z_0} \tag{5.5}$$

where z_{targ} is the centre of the target, and $(x_{\text{targ}}, y_{\text{targ}})$ is the extrapolated target position. Using the extrapolated target position and the final PPAC-determined position, the scattering vector of the nucleus was determined according to

$$a = \frac{x_2 - x_{\text{targ}}}{z_2 - z_{\text{targ}}} \tag{5.6}$$

$$b = \frac{y_2 - y_{\text{targ}}}{z_2 - z_{\text{targ}}} \tag{5.7}$$

where a, b are the x, and y scattering vectors, respectively. The scattering vector is defined as $\vec{a} = (a, b, 1)$.

The detector positions were determined using photogrammetry [141]. The positions for GR detectors were used for translating the determined interaction position from the crystal frame to the lab frame. For MB and SC, the photogrammetry positions were used to build the simulation geometries, and the first interaction positions from the simulation were used for the Doppler correction in both the simulation and the data analysis.

From all this information and the lab-frame energy measured by the detectors, the Doppler-corrected energy can be determined according to

$$E_{\gamma 0} = E_\gamma \frac{1}{\sqrt{1-\beta^2}} \left(1 - \beta \frac{\vec{a} \cdot (\vec{x} - \vec{x}_{\text{targ}})}{|\vec{a}||(\vec{x} - \vec{x}_{\text{targ}})|} \right) \tag{5.8}$$

where $\vec{x}$ is the gamma-ray interaction position, $\vec{x}_{\text{targ}}$ is the extrapolated target position, $\vec{a}$ is the scattering vector, E_γ is the measured energy in the lab frame, and $E_{\gamma 0}$ is the Doppler corrected energy.

5.5 Source Runs and Calibration

To determine the lab-frame energies, the detectors needed to be calibrated. This was done by applying linear calibration functions to the ADC values. For the GRETINA detectors, the online calibration

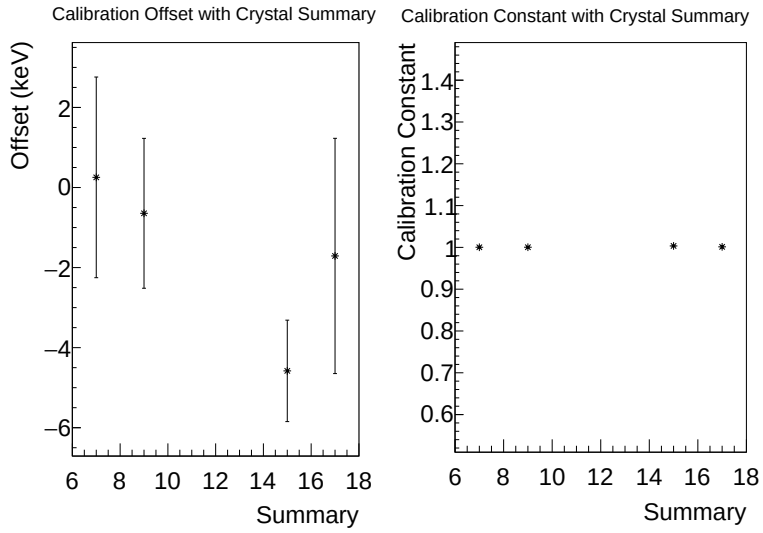

(a)

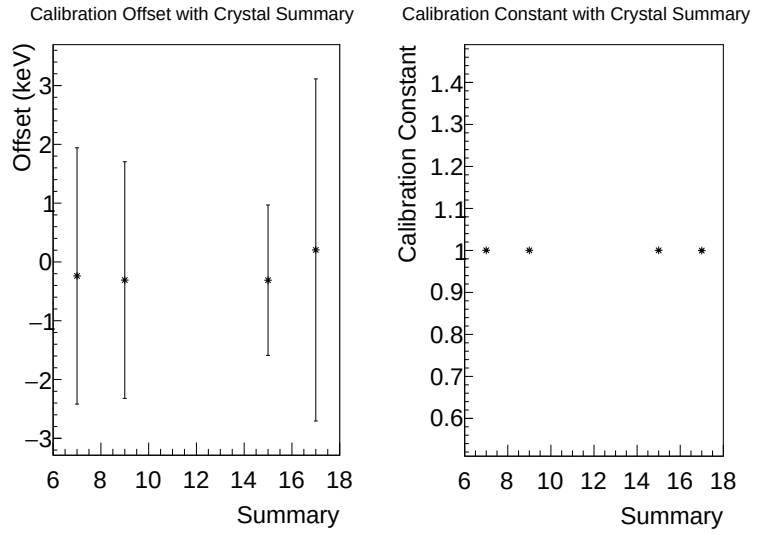

(b)

Fig. 5.1 Residual energy calibration fits to ^{152}Eu calibration runs. The calibrated spectra were fitted to obtain the calibrated peak positions. The obtained energies were plotted against the true energy and fitted with a first-order polynomial. Summary shows an arbitrary crystal ID. (a) shows the residual calibration parameters from after the experiment, and (b) shows the residual calibration parameters from before the experiment.

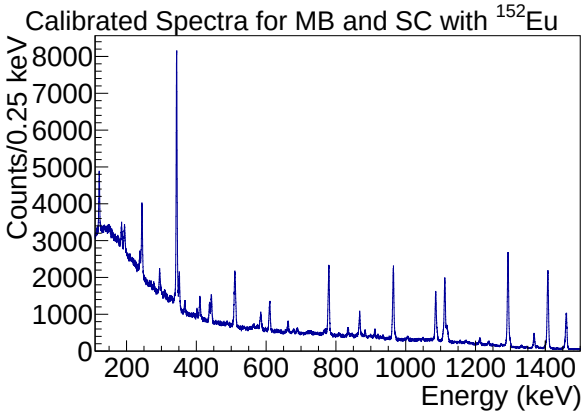

Fig. 5.2 Calibrated sum spectrum of Miniball and Superclovers for run 244 with ^{152}Eu source.

was used. The residual calibration was calculated for calibration runs before and after the experiment. The results for this can be seen in Figure 5.1. All the detectors have a good calibration for the start of the beam time. Most of the detectors performed well after the beam time, except for detector ID 15 corresponding to P3 crystal 0. However, the difference is small, and the calibration is reasonable.

For Miniball and Superclovers, the calibration was done offline. Run 244 was used; the run was a ^{152}Eu run after the experiment. The peaks in the Eu spectra were fitted crystal by crystal using a Gaussian signal plus a linear background. The energy to ADC graph was then fitted with a linear fit to obtain the calibration parameters. The resulting calibrated spectrum is shown in Figure 5.2.

5.6 Time Alignment and Cuts

To gate on prompt gamma rays, the HiCARI detectors had to be time-aligned, and a time gate needed to be applied. This was done for Miniball and Superclovers, and GRETINA separately. First, histograms containing the time difference between the F8 plastic time from the HiCARI DAQ and the gamma-ray time were filled for each crystal of HiCARI. Then, the peaks corresponding to the prompt gamma rays were fitted with a Gaussian to find the time offset of each crystal, and then the time offsets were subtracted in the analysis to align the prompt gamma-ray peaks of the crystals. The result of this analysis can be seen in Figure 5.3a.

Following this, the time gates could be applied. It was decided that time and energy gates would be applied to account for any time walk at lower gamma-ray energies. First, 2D histograms for MB, SC and GR were filled for the time difference between the F8 plastic and the lab-frame energy of

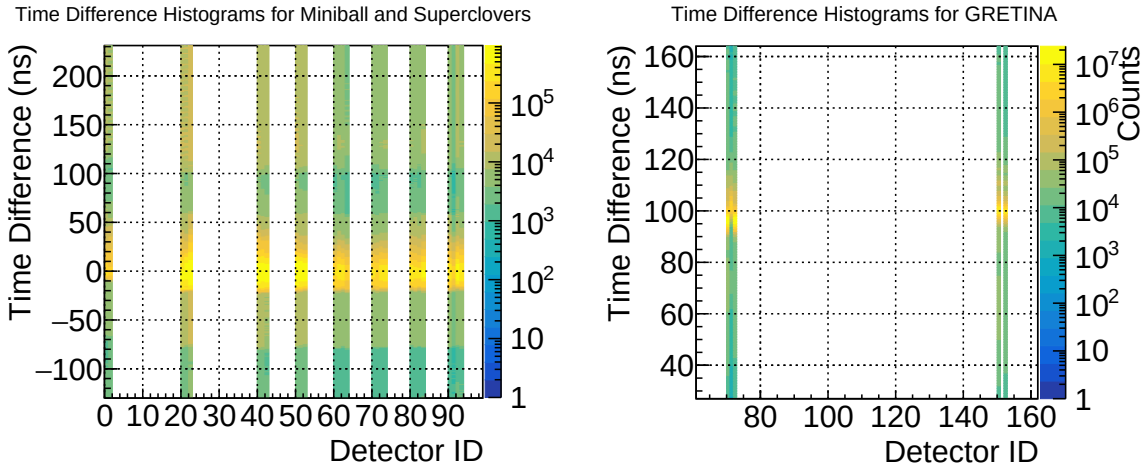

(a)

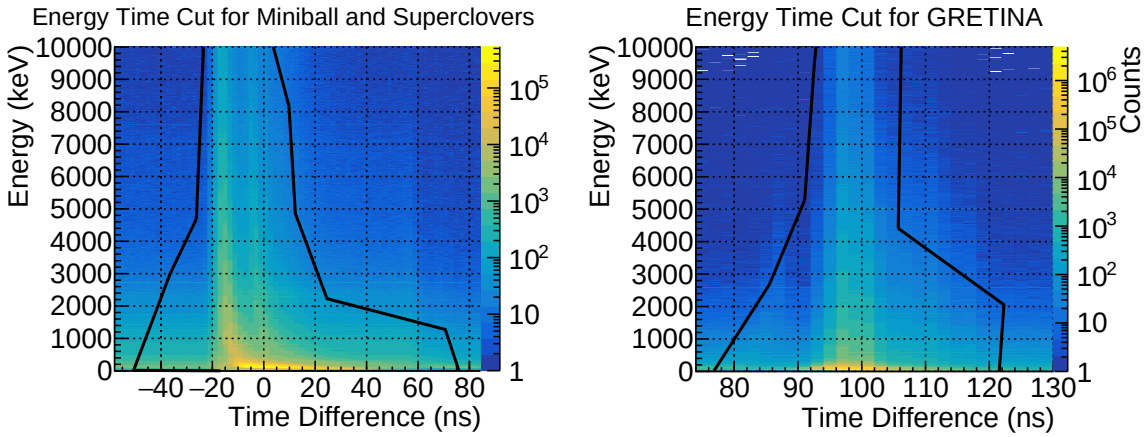

(b)

Fig. 5.3 Time analysis of the HiCARI detectors. (a) shows the time difference between the F8 plastic signal and the HiCARI events separated by crystal after time alignment. (b) shows the time difference between the F8 plastic time and the HiCARI event time with the Doppler-corrected gamma-ray energy after time alignment, and separated into non-tracking and tracking detectors. Gates have been applied to remove non-coincident background, which is shown by the black lines.

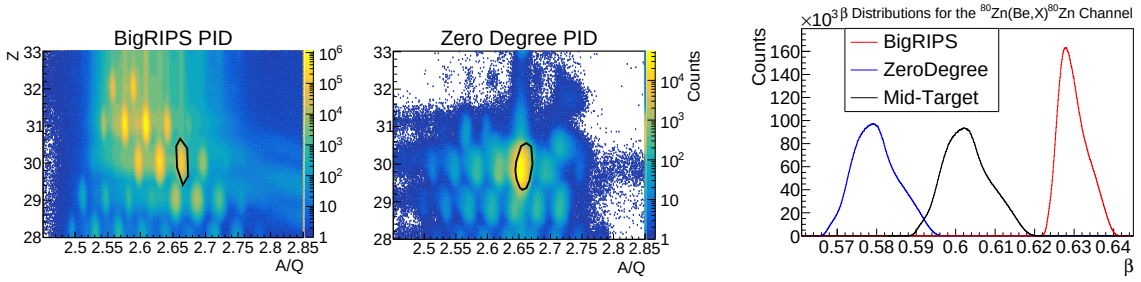

(a) (b)

Fig. 5.4 PID and velocities for ^{80}Zn inelastic scattering. (a) shows PID plots for BigRIPS (left) and ZeroDegree (right). The ZeroDegree PID is after gating on ^{80}Zn in BigRIPS. The gates applied for ^{80}Zn inelastic scattering are shown by the black lines. (b) shows the determined velocities for BigRIPS (F5-F7) and Zerodegree (F9-F11) alongside the interpolated mid-target velocity.

the gamma ray. Then a visual cut was drawn onto the prompt peak, allowing for a reduction in the background. The histograms and cuts are shown in Figure 5.3b.

5.7 Reference Case ^{80}Zn(Be, X)^{80}Zn

Inelastic scattering of ^{80}Zn was used as a reference case for fixing some of the analysis parameters. This was due to the short-lived 2_1^+ state, which was determined to have a lifetime of $\tau = 0.74(16)$ ps from cross-section measurements at ISOLDE [142]. This is a good reference case as it is a simple spectrum with one gamma ray, which is fast enough to have minimal lifetime effects.

The data is gated on ^{80}Zn in BigRIPs, and ^{80}Zn in ZeroDegree. The PID and gates used are shown in Figure 5.4a. The velocities determined at different points in the spectrometer are shown in Figure 5.4b. The average after target β was 0.580(6), corresponding to an average mid-target velocity of 0.603. These values were used in the Doppler correction. The incoming energy was set to 259.2 MeVu^{-1} in the simulation, which was extrapolated from the ZeroDegree velocity.

Figure 5.5 shows the Doppler corrected spectra for the ^{80}Zn(Be, X)^{80}Zn channel separated by detector group. Only one peak is observed, the 1492 keV gamma ray corresponding to the transition from the 2_1^+ to the ground state [142]. One concern is the long-lived 4_1^+ state that decays via a 482 keV gamma ray to the first 2_1^+ state [19]. The $4_1^+ \rightarrow 2_1^+$ transition is not observed, allowing this channel to be used as a test case to fix the Doppler correction parameters. From Figure 5.5, it can be seen that the peak consistently falls below the expected energy value regardless of detector group.

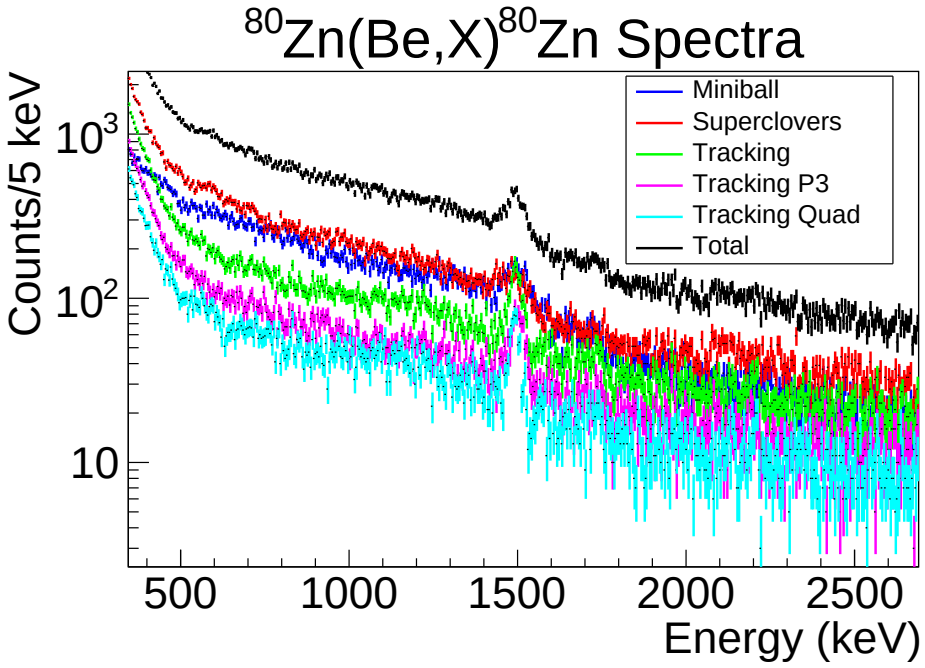

Fig. 5.5 Doppler corrected spectra for ^{80}Zn inelastic scattering separated into the different detector groups, and the sum of the histograms. The $2_1^+ \rightarrow 0_1^+$ transition is located at $\approx$ 1.5 MeV.

Target Position Determination

To determine the true target position, the target position value used in the data Doppler correction was varied. The gamma ray was simulated using Geant4 with the energy and lifetime fixed to the literature values: 1492 keV and 0.74 ps [142]. The Doppler-corrected data histograms were fitted using the simulated histogram plus an exponential background. The χ^2 value from the fit was used to determine the true target position. Two methods were used: one fitting each detector group (MB, SC, GR) separately and summing the individual χ^2 values [143] referred to as Global, and one fitting the summed histogram of all the detectors and getting a single χ^2 referred to as HiCARI. The χ^2 distributions were fitted with quadratic functions to find the target position corresponding to the minimum χ^2 value. The statistical uncertainty was obtained by finding the values corresponding to the minimum χ^2 +1.

The results of the target position analysis can be seen in Figure 5.6. Both methods yielded an offset of approximately 2 mm. The minimum determined from the Global method was used, 12.46(21) mm. From this, a systematic uncertainty in the target position of 0.3 mm was assumed.

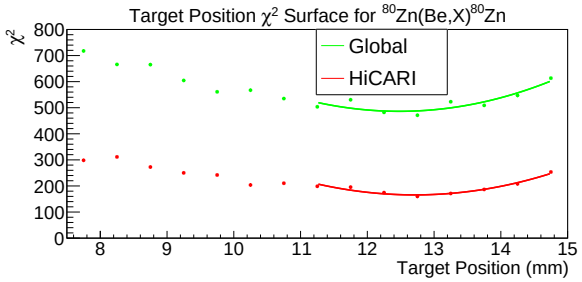

Fig. 5.6 χ^2 graphs for the target position variation from different methods. HiCARI is from fitting the sum histogram of all detectors, and Global is from fitting the independent detector groups and summing the χ^2 values. The minima were determined to be 12.46(21) mm and 12.70(22) mm from quadratic fits.

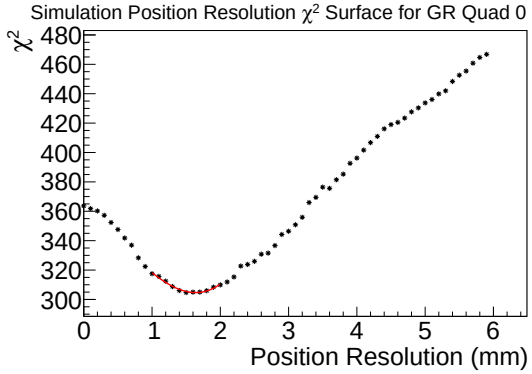

(a)

Cluster	Crystal	Position Resolution/mm
Quad	0	1.6(2)
	2	1.7(3)
P3	0	2.6(2)
	2	3.2(2)

(b)

Fig. 5.7 Determining GRETINA crystal position resolutions from the 2^+ transition in ^{80}Zn(Be,X)^{80}Zn. (a) shows the χ^2 graph for Quad 0 fitting the $2_1^+ \rightarrow 0_1^+$ transition in $^{80}\mathrm{Zn(Be,X)}^{80}$Zn for different position resolutions. The fitted polynomial function is shown in red. (b) shows the determined position resolution for different crystals of GRETINA detectors.

Position Resolution Determination

Due to the short lifetime of the first 2^+, its decay gamma ray was used to determine the position resolution of the crystals. To do this, the position resolution parameter in the simulation was varied. The $^{80}\mathrm{Zn(Be,X)}^{80}$Zn channel was simulated, varying the position resolutions only including the $2_1^+ \rightarrow 0_1^+$ transition with the literature values for the energy and lifetime [142]. For each crystal in the GRETINA detectors, the spectra were fitted with their corresponding simulated spectrum plus an exponential background. The χ^2 values were fitted with polynomial functions to obtain the minimum and statistical uncertainty. These values were implemented in the simulations.

The χ^2 values for Quad 0 can be seen in Figure 5.7a, using the fit, the minimum is determined. The results of this analysis for each GRETINA crystal can be seen in Table 5.7b. The average value for

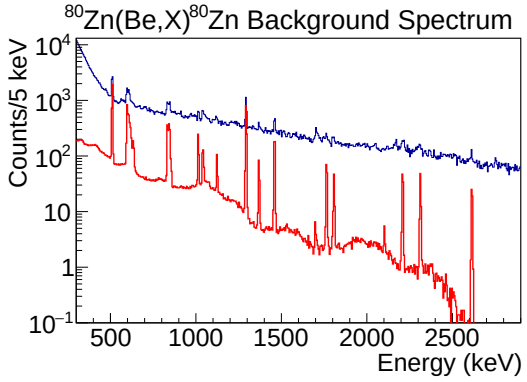

(a)

Energy/keV	Origin
511	e^+e^-
595.84	^{74}Ge(n,γn′)^{74}Ge*
846.76	^{56}Fe(n,γn′)^{56}Fe*
1014	^{27}Al(n,γn′)^{27}Al*
1039.51	^{70}Ge(n,γn′)^{70}Ge*
1129.90	^{54}Fe(n,γn′)^{54}Fe*
1303.40	^{56}Fe(n,γn′)^{56}Fe*
1368.63	^{24}Na(β)^{24}Mg*
1460.80	^{40}K(β)^{40}Ar*
1764.49	^{214}Bi(β)^{214}Po*
1810	^{56}Fe(n,γn′)^{56}Fe*
2212.01	^{27}Al(n,γn′)^{27}Al*
2213	^{14}N(n,γn′)^{14}N*
2614.51	^{208}Pb(n,γn′)^{208}Pb*

(b)

Fig. 5.8 Neutron background determination in ^{80}Zn(Be,X)^{80}Zn. (a) shows the non-Doppler corrected sum-spectrum for all HiCARI detectors, with the simulated background gamma-rays shown in red. (b) summarises the background lines observed in the non-Doppler corrected spectrum of ^{80}Zn(Be,X)^{80}Zn with the background source listed. Energies and sources are taken from [144, 145].

GRETINA detectors of 1.9(9) mm [29]. The values obtained here are either in agreement or slightly worse. The worse-performing detectors likely have a poor signal basis for position reconstruction. For the systematic uncertainty estimation, it is assumed that the Quad can take position resolution values between 1.4 and 2.0 mm, while P3 can take values between 2.4 and 3.4 mm. For the determination of central values, the minimised values are used.

Background Gamma Rays and Neutrons

Background gamma ray and neutron interactions with the HPGe detectors produce background lines, as shown in Figure 5.8a. In order to properly fit the spectrum, this background needs to be included in the fit of the spectra. For this, only background lines observed in the non-Doppler corrected sum spectrum were used; the full list used is in Table 5.8b. A single simulation was run to simulate all the background gamma rays, with each gamma ray given individual weights. The weights of the lines were determined by fitting the individual peaks with a scaled simulated peak plus an exponential background. The simulation weights of the peaks were varied iteratively until all the peak scaling factors were in agreement to within 1σ. The weighted mean of all scaling factors was used to

determine the optimal scaling factor, which was set as a fixed parameter in the lifetime and energy determinations. This process was repeated for all analysis channels independently.

Energy and Lifetime Determination

To determine the energy and lifetime, the energy and half-life in the simulation were varied. The region from 700 to 1900 keV was fitted with the simulated histogram plus a double exponential histogram and the determined background gamma-ray lines with a fixed weighting factor. 5 keV binning of the simulated and data histograms was used. The fit function, $f(E)$, is given as

$$f(E) = A_1 \exp(-A_2 E) + A_3 \exp(-A_4 E) + A_5 h^{sim}_{2^+,E',t'_{1/2}}(E) + A_6 h^{sim}_{bkg}(E) \tag{5.9}$$

where A_i are the fit parameters, E is the energy of the histogram bin, $h^{sim}_{2^+,E',t'_{1/2}}$ is the simulated histogram simulating a state at energy E', with half-life $t'_{1/2}$, and h^{sim}_{bkg} is the Doppler corrected simulated background histogram. Parameter A_6 was fixed according to the value obtained from the previous analysis. Whilst the remaining parameters were allowed to vary freely.

Incoming ^{80}Zn was simulated interacting with the target and being excited to the first 2^+_1 state. A 2D variation of the energy and lifetime was done. The energy was varied between 1482 and 1512 keV in steps of 1 keV, and the half-life was varied between 0 and 10 ps in steps of 0.5 ps. Each simulation simulated 5×10^6 events. For each of the cases, the simulated histograms were fitted to the data histograms separated by detector group. The groups were MB, containing the Miniball events; SC, containing the Superclover events; GR, containing the GRETINA events; GR Quad, containing events from the GRETINA Quad; and GR P3, containing the GRETINA P3 events. The χ^2 values from the fits were filled into a TGraph2D [140] with the energy on the x-axis and half-life on the y-axis. In addition, a sixth graph was filled, containing the sum χ^2 of the two GRETINA clusters. For each χ^2 plot, the minimum value and the corresponding E, and $t_{1/2}$ were found alongside the contour of $\chi^2_{\text{min}} + 2.3$ corresponding to the 1σ region.

Figure 5.9 shows the χ^2 surfaces for the different detector groups. As can be seen, no clear minimum is found for MB and SC in the simulated region. Additionally, it appears the minima will occur at opposite ends of the simulated range, indicating some issues with the MB and SC analysis. This is consistent with observations from other experiments with the HiCARI array. This is likely due to incorrect internal geometries being used to generate the crystal centres, causing systematic shifts in

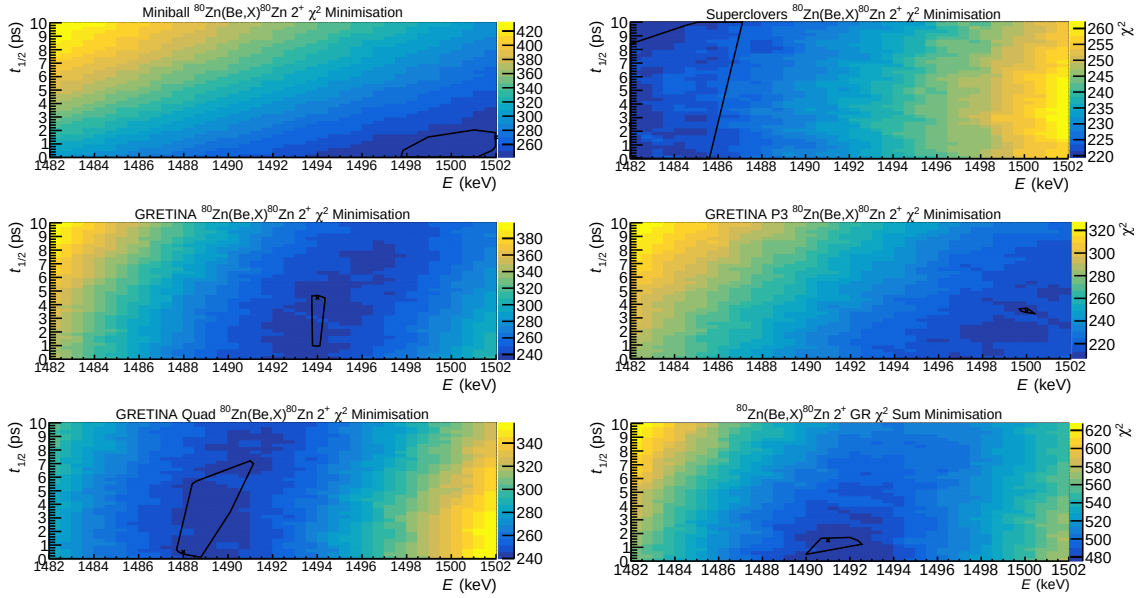

Fig. 5.9 χ^2 surfaces for the different detector groups varying the energy and half-life of the 2_1^+ state in ^{80}Zn. The minimum simulated χ^2 is shown with the x, and the +2.3 contour is shown in black.

Detector Group	Energy/keV	$t_{1/2}$/ps
GR χ^2 Sum	1491(2)	<2
MB	-	-
SC	-	-
GR	1494(1)	$4.5^{+1.0}_{-4.0}$
GR P3	1500(1)	3.5(5)
GR Quad	1488^{+4}_{-1}	<7.5

Table 5.2 Initial half-lives and statistical uncertainties for the 2_1^+ state in ^{80}Zn for different detector groups. - indicates that no minimum was found in the simulated range.

the Doppler corrected energies of the two detector groups. However, it is clear that the GRETINA sum χ^2 forms a well-defined minimum. It was decided that only the GRETINA sum χ^2 would be used for energy and half-life determination. The half-lives and energies determined from the minimum fitted χ^2 are shown in Table 5.2. As can be seen, the value determined from the GR χ^2 sum is consistent with the previously measured values of 1492 keV, and 0.51(11) ps [142]. Additionally, it can be seen that there is an offset between the GR P3 and Quad results.

Due to fluctuations in the χ^2 larger than the uncertainty range of 2.3, simply using the fitted χ^2 values fails to properly capture the minimum value and uncertainty. To do this, the 2D histogram was projected around the minimum to obtain the 1D χ^2 surface, which was fitted with polynomials. In addition, 1D χ^2 surfaces were used for determining the systematic uncertainties. For the energy

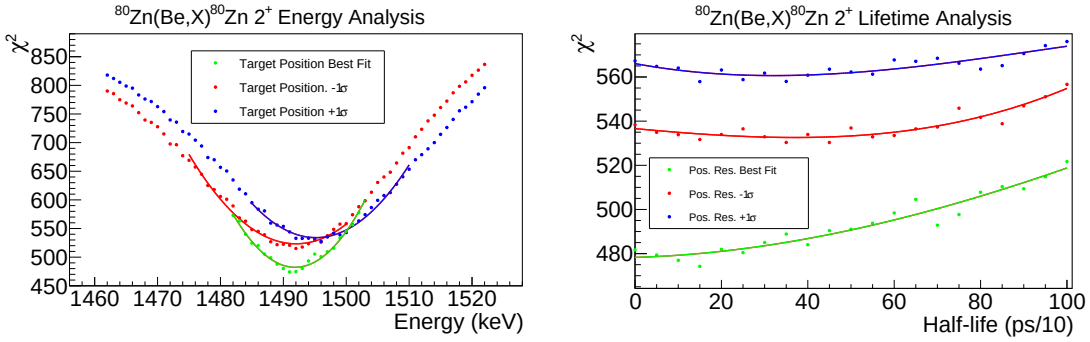

(a) (b)

Fig. 5.10 Systematic uncertainty calculation for ^{80}Zn(Be, X)^{80}Zn, the central values and uncertainties are determined by polynomial fittings to the χ^2 surfaces. Best fit refers to using the minimised values, whilst $\pm 1\sigma$ shows the χ^2 surfaces corresponding to shifting the values by the stated systematic uncertainties. (a) shows the target position variation to determine the energy systematic uncertainty, and (b) shows the position resolution determination to determine the half-life systematic uncertainty.

systematic uncertainty, the target position was varied by ± 0.3 mm about the 12.46 mm determined target position. For the half-life systematic, the position resolution was varied between the minimum and maximum values, treating P3 and Quad as separate ranges, being 2.4-3.4 mm and 1.4-2.0 mm, respectively.

Figure 5.10 shows the energy and half-life determination alongside the systematic uncertainty variations. For the energy, a value of $1492(2)^{+5}_{-2}$ keV consistent with previously measured values [142]. The half-life measurement is consistent with 0 ps, so only an upper limit can be determined. The upper limit is determined as $<$6 ps, also consistent with the value determined by Coulomb excitation measurements [142]. This indicates that the method is appropriate and can be applied to other channels.

5.8 Lifetime Analysis

It was decided that ^{78,80}Zn would be analysed. In particular, ^{81}Ga(Be, X)^{80}Zn, ^{78}Zn(Be, X)^{78}Zn and ^{79}Zn(Be, X)^{78}Zn channels were analysed. ^{79}Ga(Be, X)^{78}Zn could not be measured in this setting, therefore ^{80}Ga(Be, X)^{78}Zn was analysed instead.

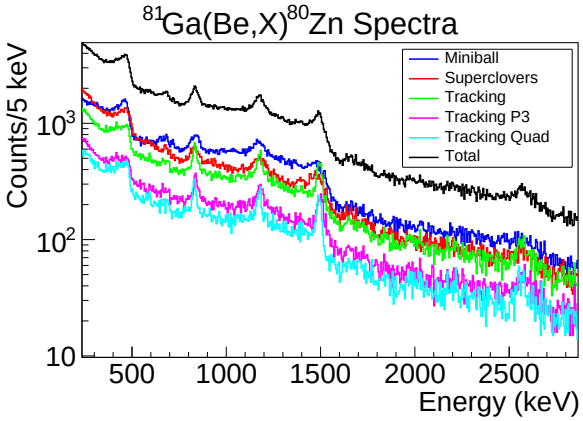

Fig. 5.11 ^{81}Ga(Be,X)^{80}Zn spectrum separated by detector type. Five clear peaks are observed, consistent with previous measurements [19].

5.8.1 ^{81}Ga(Be,X)^{80}Zn

Due to HiCARI's low efficiency, no $\gamma-\gamma$ coincidences are visible in the ^{81}Ga(Be,X)^{80}Zn; therefore, the analysis was based on a literature level scheme. Figure 2.9b shows the literature level scheme used as a basis for the analysis. Figure 5.11 shows the spectrum obtained from the ^{81}Ga(Be,X)^{80}Zn channel. Five peaks are observed, consistent with the level scheme. The peak at 487 keV exhibits a clear asymmetry, indicating a transition from a long-lived state with a $t_{1/2} \approx$100 ps, which also explains the stepped structure of the 1492 keV peak.

To minimise all energies and half-lives simultaneously would require a 10-D phase space. Performing such a minimisation reliably is currently unrealistic. It was therefore decided that states would be minimised one at a time, reducing the minimisation to five 2-D minimisations. The minimisation was started using the highest-lying levels, specifically the 3174, 2820, and 2627 keV levels. For the initial minimisation of the 3174 and 2820 keV levels, the lifetimes and energies of the other peaks were fixed to their literature values. Due to the lower statistics of the 2627 keV peak, it was fitted separately for the minimisation using 20 keV bins as opposed to 5 keV bins for the remaining peaks. Secondly, the minimisation of the 4_1^+ state was completed, including the feeding from the higher lying states. Finally, the 2_1^+ state was minimised, including the feeding from higher lying states.

5.8.2 ^{78}Zn

Figure 5.12 shows the channels leading to ^{78}Zn that were analysed. In all channels, peaks corresponding to the transitions shown in Figure 2.9a, a structure at 576 keV, a well-defined peak at

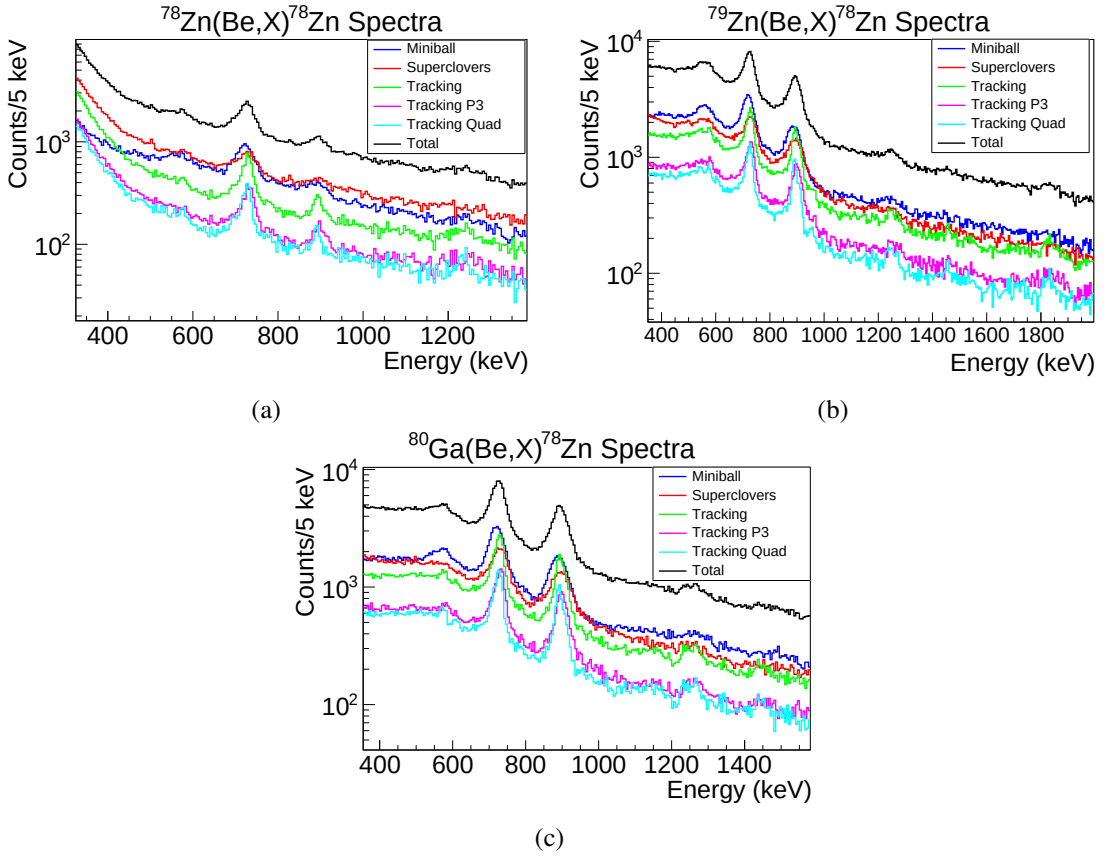

Fig. 5.12 ^{78}Zn spectra from three different reaction channels: (a) $^{78}\mathrm{Zn}(\mathrm{Be},\mathrm{X})^{78}\mathrm{Zn}$, (b) $^{79}\mathrm{Zn}(\mathrm{Be},\mathrm{X})^{78}\mathrm{Zn}$, and (c) $^{80}\mathrm{Ga}(\mathrm{Be},\mathrm{X})^{78}\mathrm{Zn}$. In all three channels, structures are observed around the 576, 730, and 908/890 keV gamma-ray transitions. In addition, in inelastic scattering, a peak around 1230 keV is observed. For n knockout: a doublet of 1230 and 1270 keV peaks, a peak at 1450 keV, and 1800 keV are observed. In pn knockout, the doublet at 1250 keV, and the peak at 1450 keV are observed.

730.2 keV, and a doublet corresponding to the 890 and 908 keV transitions. A transition at 1271 keV has previously been reported from a DALI2 experiment [19]. However, it appears this is a doublet of 1230 and 1270 keV transitions observed in both n and pn knockout, but in inelastic scattering, only the 1230 keV peak is observed. In pn, n knockout, a peak is observed around 1450 keV. Finally, a peak at 1830 keV is observed in the n knockout channel only.

For minimising the high-energy peaks, the fit range was from 1000 keV to 2100 keV with a 10 keV binning. Due to the low gamma-gamma coincidence efficiency, the high-energy peaks could not be placed in the spectrum. It was assumed that the gamma rays decayed directly to the ground state, and no feeding was considered. For inelastic scattering, the 1230 keV peak was minimised for lifetime and energy. For n knockout, the doublet was minimised only for energy, whilst the 1450 and 1800 keV peaks were minimised for energy and half-life. For pn knockout, the doublet at 1200 keV was minimised for energy only, whilst the 1450 peak was minimised for lifetime and energy.

For the peaks below 1 MeV, a fitting range of 300-2100 keV was used with a 5 keV binning, including the higher energy gamma rays, in order to properly replicate the Compton scattering background. Several attempts were made to fit the 576 keV peak; however, no consistent value could be determined. This is ascribed to the complexity of the 576 keV structure, likely a combination of the Compton scattering from the 908, 890 and 730 keV gamma rays and additional unresolved transitions. Therefore, only the $2_1^+ \rightarrow 0_1^+$ transition was minimised for half-life and energy, and the 890, 908 and 576 keV transitions were fixed to their literature values. A 30 ps half-life for the 576 keV level was assumed to account for its asymmetric peak shape.

Chapter 6

Results and Discussion

The results obtained from the previous chapter will be presented here. Where possible, reduced transition probabilities have been extracted. Several shell-model calculations were performed for ^{78,80}Zn. Two calculations were performed assuming a ^{78}Ni core with valence protons restricted to the $1p_{3/2}$ and $0f_{5/2}$ orbitals; one utilized a potential based on the surface delta interaction (SDI) [45], while the other incorporated the SDI plus a quadrupole-quadrupole (QQ) interaction [146]. In addition, calculations using the jun45 [46], and jj44pna [147] effective interactions have been performed using KSHELL [148]. Finally, results from a cutting-edge DNO-SM calculation [21] were examined for comparison. The calculated excitation energies and reduced transition probabilities have been compared to the experimental values, and the implications for nuclear structure in this region have been explored.

	^{80}Zn(Be, X)^{80}Zn	^{81}Ga(Be, X)^{80}Zn
Detector	χ^2_{red}	χ^2_{red}
MB	1.3	1.8
SC	1.2	1.4
GR	1.2	1.5
GR P3	1.2	1.5
GR Quad	1.3	1.4

Table 6.1 χ^2_{red} values for the best fits for the ^{80}Zn channels. For both channels the χ^2_{red} values are close to 1.

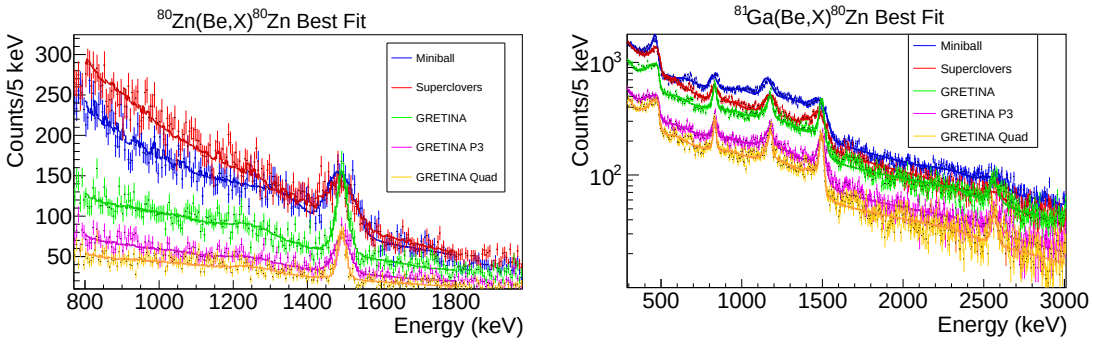

(a) (b)

Fig. 6.1 Best fits for the ^{80}Zn channels. (a) shows the spectra and fits for ^{80}Zn(Be,X)^{80}Zn, and (b) shows the spectra and fits for ^{81}Ga(Be,X)^{80}Zn. The minima determined using the GR P3 and GR Quad analysis were used, but the other detectors are included for reference.

Literature [17, 18, 19, 20]			^{80}Zn(Be,X)^{80}Zn		^{81}Ga(Be,X)^{80}Zn	
J^π	E/keV	$t_{1/2}$/ps	E/keV	$t_{1/2}$/ps	E/keV	$t_{1/2}$/ps
2_1^+	1492(1)	0.51(11)	$1492(2)^{+5}_{-2}$	< 6	1495(1){2}	< 3
4_1^+	1979(3)	136^{+92}_{-67}	-	-	1980(2){3}	$138(13)^{+10}_{-16}$
-	2820(13)	-	-	-	2814(2){4}	$9(3)^{+3}_{-5}$
-	3174(18)	-	-	-	3161(3){5}	22(4){4}
-	2627(39)	-	-	-	2562(5){9}	< 2

Table 6.2 Determined energies and half-lives of excited states in ^{80}Zn. The first columns show the literature values, the middle columns show the results from ^{80}Zn(Be,X)^{80}Zn, and the final columns show the results from ^{81}Ga(Be,X)^{80}Zn. The first uncertainty shows the statistical uncertainty, and the second shows the systematic uncertainty. Cases where the measurement is not available are indicated with a hyphen.

6.1 ^{80}Zn - Results

Figure 6.1 shows the best-fit results for the ^{80}Zn(Be,X)^{80}Zn, and ^{81}Ga(Be,X)^{80}Zn spectra. The transition energies and half-lives were determined using GR-P3 and GR-Quad spectra. The χ^2_{red} values for the best-fits are summarised in Table 6.1; all values are close to 1, indicating the fits provide proper descriptions of the experimental data.

Table 6.2 shows the measured energies and half-lives of excited states in ^{80}Zn alongside the literature values from [17, 18, 19, 20]. As can be seen, the measured energy of the 2_1^+ state is in good agreement with the literature values; however, only an upper limit could be determined for the half-life due to the setup's insensitivity to short half-lives. For the 4_1^+ state, the energy and half-life are in good agreement with the literature values. The half-life has a smaller uncertainty than

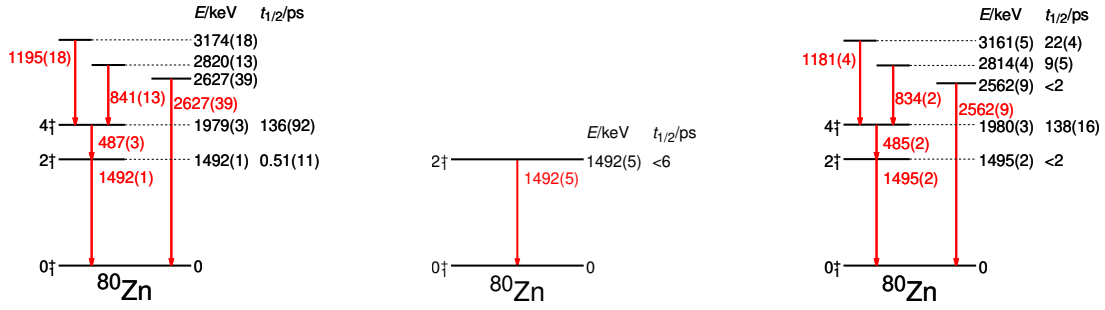

(a) (b) (c)

Fig. 6.2 Levels schemes for ^{80}Zn from literature [17, 18, 19] (a), and determined from the experimental channels: ^{80}Zn(Be,X)^{80}Zn (b), and ^{81}Ga(Be,X)^{80}Zn (c). As can be seen, the results are in good agreement with the literature. The black lines indicate the excited states, and the red lines indicate the gamma-ray transitions that have been observed.

the previous measurement. For the 2814 and 3161 keV states, the measured energies are in good agreement with the literature values, and with smaller uncertainties. In addition, the half-lives of the 2814 and 3161 keV states are measured for the first time. The energy of the 2562 keV state is within 2σ of the previously measured value of 2627(39) keV, and an upper limit for the half-life is measured for the first time. The corresponding transition strengths are $B(E2, 2_1^+ \rightarrow 0_1^+) > 25\ e^2\text{fm}^4$, and $B(E2, 4_1^+ \rightarrow 2_1^+) = 153^{+23}_{-16}\ e^2\text{fm}^4$, calculated using the values from the ^{81}Ga(Be,X)^{80}Zn channel.

Figure 6.2 shows the level scheme from the literature compared to the results from this analysis. The uncertainties were symmetrised for visual simplicity. No new levels are observed. Two new half-lives and one new upper limit are measured. In addition, the uncertainty on the 4_1^+ half-life has been significantly reduced.

6.2 ^{78}Zn - Results

Figure 6.3 shows the best fits for the ^{78}Zn channels. The χ^2_{red} for the ^{78}Zn channels are summarised in Table 6.3. The fits for ^{78}Zn(Be,X)^{78}Zn channel are all reasonable with χ^2_{red} close to 1. Whilst for ^{79}Zn(Be,X)^{78}Zn, and ^{80}Ga(Be,X)^{78}Zn, the χ^2_{red} values are closer to 2, the fits are still reasonable.

Table 6.4 shows the results measured in the ^{78}Zn channels. The measured energy of the 2_1^+ is consistent with the literature values. Whilst the half-life is consistently $\approx 1\sigma$ below the literature

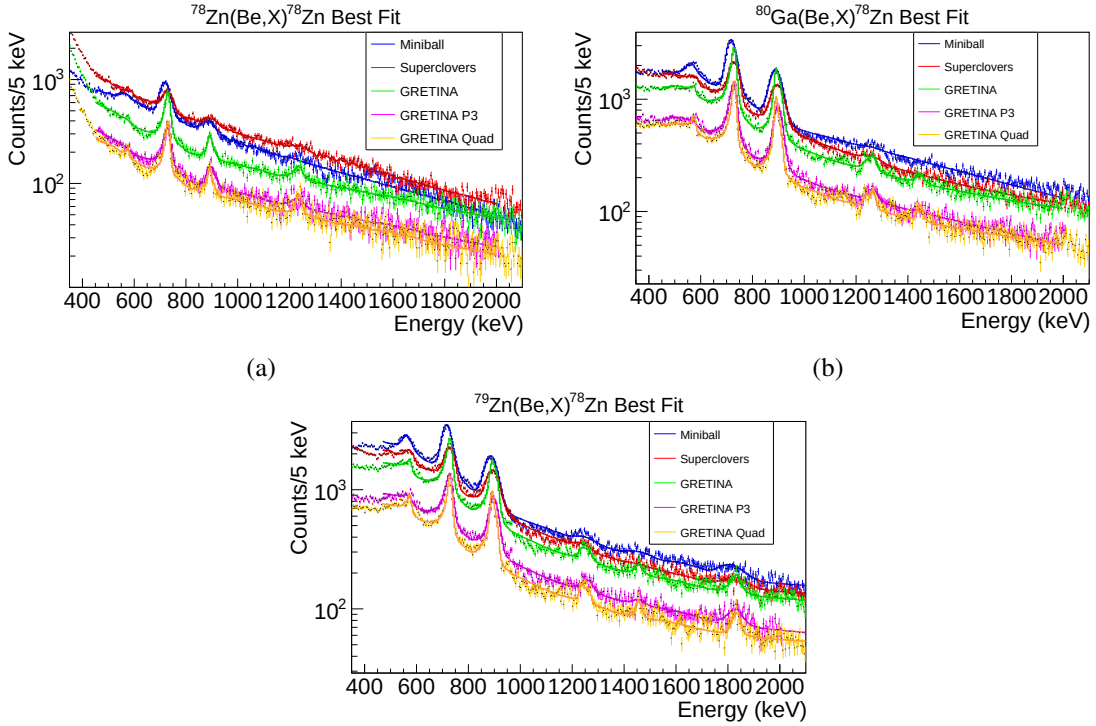

Fig. 6.3 Best fits for the ^{78}Zn channels are shown in: (a) for ^{78}Zn(Be,X)^{78}Zn, (b) for ^{80}Ga(Be,X)^{78}Zn, and (c) for ^{79}Zn(Be,X)^{78}Zn. The minima determined using the GR P3 and GR Quad analysis were used, but the other detectors are included for reference.

Detector	^{78}Zn(Be,X)^{78}Zn χ^2_{red}	^{80}Ga(Be,X)^{78}Zn χ^2_{red}	^{79}Zn(Be,X)^{78}Zn χ^2_{red}
MB	1.6	2.7	3.3
SC	1.3	1.9	2.3
GR	1.1	1.8	2.2
GR P3	1.0	2.2	2.1
GR Quad	1.3	2.0	1.9

Table 6.3 Reduced χ^2 values for the best fits for the three reaction ^{78}Zn channels. GR P3 and GR Quad both achieve a χ^2_{red} of ≤ 2.2.

Literature [64, 19]			^{78}Zn(Be,X)^{78}Zn		^{80}Ga(Be,X)^{78}Zn		^{79}Zn(Be,X)^{78}Zn	
J^π	E/keV	$t_{1/2}$/ps	E/keV	$t_{1/2}$/ps	E/keV	$t_{1/2}$/ps	E/keV	$t_{1/2}$/ps
2_1^+	730.2(4)	18(4)	732(1){2}	14(2){2}	731(1){1}	$13(1)^{+2}_{-1}$	731(1){1}	$13(1)^{+2}_{-1}$
-	-	-	1237(4){5}	< 18	$1238(5)^{+4}_{-7}$	-	1237(3){2}	-
-	1271(19)	-	-	-	1264^{+4+5}_{-1-3}	-	1261^{+8}_{-3}{4}	-
-	-	-	-	-	1446(5){7}	< 6	1455(4){5}	< 6
-	-	-	-	-	-	-	1832(6){7}	< 14

Table 6.4 Determined energies and half-lives of excited states in ^{78}Zn. The first column shows the literature values, and the other columns show the results measured in this experiment. The first uncertainty shows the statistical uncertainty, and the second shows the systematic uncertainty. Cases where the measurement is not available are indicated with a hyphen.

value. However, the results are consistent with preliminary values from a new ISOLDE measurement reported in [149]. A new transition at 1237 keV is observed, and an upper limit for the state's half-life is determined. The energy of the 1271 keV transition has been measured to a higher precision, but no half-life information was obtained. A new transition at $\approx$ 1450 keV has been measured for the first time, and a half-life upper limit is measured. Finally, a new transition at 1832 keV has been measured alongside an upper limit for the half-life. The $B(E2, 2_1^+ \rightarrow 0_1^+) = 206^{+18}_{-29} e^2\text{fm}^4$ was calculated using the energy and half-life values of 731(1) keV and 13^{+2}_{-1} ps.

Figure 6.4 shows the level schemes obtained from the experiment compared to the literature level scheme. Due to the low efficiency, no $\gamma - \gamma$ information could be extracted; therefore, the new higher energy transitions have been placed as tentative transitions to the ground state.

6.3 Shell Model Calculations

^{80}Zn provides an excellent testing ground for evaluating a simple model using a ^{78}Ni core with two protons in a $0f_{5/2}$ and $1p_{3/2}$ model space. The first model was constructed using an SDI pairing interaction [45], and the second model was constructed using the SDI plus a QQ interaction [146]. The interactions were optimised using χ^2 minimisations to reproduce the excitation energies and $B(E2)$ values in ^{80}Zn.

The first step was to determine the energies of the $0f_{5/2}$ and $1p_{3/2}$ orbitals. This was done using Nucracker [42]. The Woods-Saxon parameters were tuned to reproduce the $S_p = 16.53$ MeV [60], and a $\sqrt{< r^2 >} \approx 4$ fm [10]. The single-particle energies were determined to be -16.5287 MeV and -16.0215 MeV for the $0f_{5/2}$ and $1p_{3/2}$ orbitals, respectively. From this, a base Hamiltonian, H_0, was

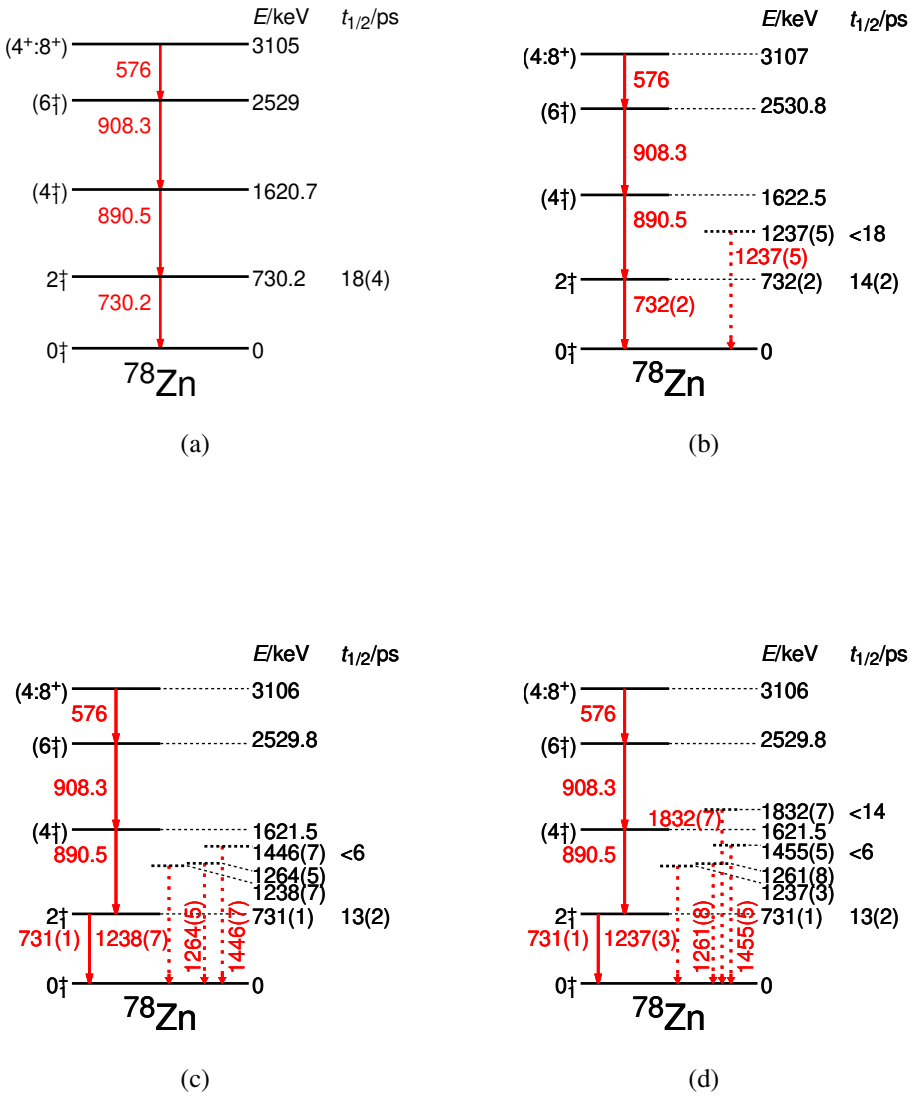

Fig. 6.4 Levels schemes for ^{78}Zn determined from literature [60] (a), and the experimental channels: ^{78}Zn(Be,X)^{78}Zn (b), ^{80}Ga(Be,X)^{78}Zn (c), and ^{79}Zn(Be,X)^{78}Zn (d). The higher energy transitions have been tentatively assigned as decays directly to the ground state.

constructed as

$$H_0 = \begin{pmatrix} 2\varepsilon_{0f_{5/2}} & 0 & 0 \\ 0 & \varepsilon_{0f_{5/2}} + \varepsilon_{1p_{3/2}} & 0 \\ 0 & 0 & 2\varepsilon_{1p_{3/2}} \end{pmatrix} \tag{6.1}$$

where ε_i is the single-particle energy of state i. The basis states correspond to

$$\begin{pmatrix} |(0f_{5/2})^2, J^\pi\rangle \\ |0f_{5/2}1p_{3/2}, J^\pi\rangle \\ |(1p_{3/2})^2, J^\pi\rangle \end{pmatrix} \tag{6.2}$$

where J^π is the state to which the two particles are coupled.

The second step was to add the SDI. This was done using the equation

$$\langle j_1 j_2, J^\pi | V_{\text{SDI}} | j_3 j_4, J^\pi \rangle = C_0 f(j_1, j_2, J) f(j_3, j_4, J) \tag{6.3}$$

$$f(j_1, j_2, J) = (-1)^{j_2+1/2} \sqrt{\frac{2(2j_1+2)(2j_2+1)}{(2J+1)(1+\delta_{j_1,j_2})}} \langle j_1, m_1 = 1/2, j_2, m_2 = -1/2 | J0 \rangle \tag{6.4}$$

where C_0 is a constant, and $\langle j_1, m_1 = 1/2, j_2, m_2 = -1/2 | J0 \rangle$ is the Clebsch-Gordan coefficient [45]. Using this, an SDI Hamiltonian was constructed $H_{\text{SDI}}(J^\pi)$. This was performed for 0^+, 2^+, and 4^+ couplings. By combining the two Hamiltonians, a full Hamiltonian can be constructed as

$$H(J^\pi) = H_0 + H_{\text{SDI}}(J^\pi) \tag{6.5}$$

where H is the total Hamiltonian for two states coupled to J^π. By solving the eigenvalue problem

$$H |J^\pi\rangle = E_{J^\pi} |J^\pi\rangle \tag{6.6}$$

the eigenvalues, E_{J^π}, and eigenvectors, $|J^\pi\rangle$ were found. This was done for 0^+, 2^+, and 4^+ states. The C_0 value is expected to fall around -0.2 MeV [150].

Following the SDI-only interaction attempt, a quadrupole-quadrupole interaction was also built upon the potential

$$V_{QQ} = \kappa Q_2 \cdot Q_2 \tag{6.7}$$

where V_{QQ} is the potential, κ is the strength of the potential, Q is the quadrupole operator [146]. The matrix elements of the interaction were calculated as

$$\langle j_1 j_2, J^\pi | V_{QQ} | j_3 j_4, J^\pi \rangle = \kappa (-1)^{j_3+j_2+J} \sqrt{2J+1} \begin{Bmatrix} j_1 & j_2 & J \\ j_4 & j_3 & 2 \end{Bmatrix} \langle j_1 | Q_2 | j_3 \rangle \langle j_2 | Q_2 | j_4 \rangle \tag{6.8}$$

where the curly brackets indicate the Wigner 6j symbol [2], and $\langle j_1 | Q_2 | j_3 \rangle$ are the single-particle matrix elements of the quadrupole interaction [2, 146]. From this, a Hamiltonian was constructed as

$$H(J^\pi) = H_0 + H_{\mathrm{SDI}}(J^\pi) + H_{QQ}(J^\pi) \tag{6.9}$$

where $H_{\mathrm{QQ}}(J^\pi)$ is the matrix for the QQ interaction for states coupling to J^π. The eigenvalue problem was then solved in the same manner as the SDI-only case.

Once the wave functions had been determined, the $B(E2)$ values were calculated. The single-particle $E2$ matrix elements, $\langle a | |Q_2| | b \rangle$, where Q_2 is the electric quadrupole operator, were taken from [2]. The single-particle matrix elements are given in units of eb^2, where e is the electron charge, and b is calculated using

$$b = 1.005 A^{1/6} \text{ fm} \tag{6.10}$$

where $A = 80$ for this case [2]. From this, the two-particle matrix elements were calculated using

$$\begin{aligned} \langle a_f b_f, J_f | |Q_2| | a_i b_i, J_i \rangle = \hat{J}_i \hat{J}_f \mathcal{N}_{a_i b_i}(J_i) \mathcal{N}_{a_f b_f}(J_f) \\ \Bigg[\delta_{b_i b_f} (-1)^{j_{a_f}+j_{b_f}+J_i} \begin{Bmatrix} J_f & J_i & 2 \\ j_{a_i} & j_{a_f} & j_{b_f} \end{Bmatrix} \langle a_f | |Q_2| | a_i \rangle \\ + \delta_{a_i b_f} (-1)^{j_{a_f}+j_{b_i}} \begin{Bmatrix} J_f & J_i & 2 \\ j_{b_i} & j_{a_f} & j_{b_f} \end{Bmatrix} \langle a_f | |Q_2| | b_i \rangle \\ + \delta_{a_i a_f} (-1)^{j_{a_i}+j_{b_i}+J_f} \begin{Bmatrix} J_f & J_i & 2 \\ j_{b_i} & j_{b_f} & j_{a_f} \end{Bmatrix} \langle b_f | |Q_2| | b_i \rangle \\ + \delta_{b_i a_f} (-1)^{J_i+J_f+1} \begin{Bmatrix} J_f & J_i & 2 \\ j_{a_i} & j_{b_f} & j_{a_f} \end{Bmatrix} \langle b_f | |Q_2| | a_i \rangle \Bigg] \end{aligned} \tag{6.11}$$

	SDI	SDI+QQ
C_0/MeV	-0.239	-0.262
κ/MeVfm$^{-4}e^{-2}$	0	0.00328
e_{eff}	2.85	2.82

Table 6.5 Best fit parameters determined by the χ^2 minimisation. SDI is the model with only the SDI, and SDI+QQ is the model with the QQ interaction added. The C_0 and κ values are of the expected order, whilst e_{eff} is large.

where $|a_i b_i, J_i\rangle$ is the two-particle state coupled to J_i, the curly brackets indicate Wigner 6j symbols [2]. The normalisation coefficients are given as

$$\mathcal{N}_{ab}(J) = \frac{\sqrt{1-\delta_{ab}(-1)^{J+T}}}{1+\delta_{ab}} \tag{6.12}$$

$$\hat{J} = \sqrt{2J+1} \tag{6.13}$$

where T is the isospin, which for this case is $T = 1$ [2]. Then, using the two-particle matrix elements, the $B(E2)$ values were calculated using

$$B(E2, J_i \to J_f) = \frac{1}{2J_i+1} |\langle J_f || Q_2 || J_i \rangle|^2 \tag{6.14}$$

where $|J_i\rangle$ are the eigenvectors calculated previously.

The $B(E2)$ values were scaled by a factor e_{eff}^2, e_{eff} was left as a free parameter for the minimisation. The effective charge, e_{eff}, is used to take into account additional effects not included in the model, such as core particle-hole excitations [2].

A χ^2 minimisation was performed to determine the optimal values for the free parameters C_0, κ, and e_{eff} with the single-particle energies fixed to the calculated Woods-Saxon energies. This was done by comparing the calculated values to the experimentally determined values of: $E(2_1^+) = 1495(2)$ keV, $E(4_1^+) = 1980(3)$ keV, $B(E2, 2_1^+ \to 0_1^+) = 144(29)$ e^2fm^4 [17, 18], and $B(E2, 4_1^+ \to 2_1^+) = 153(18)$ e^2fm^4. For the minimisation, the uncertainties were made symmetric to simplify the analysis. Table 6.5 shows the determined optimal parameters. The C_0 and κ values are of the expected orders. In both cases $e_{\text{eff}} \approx 3$, suggesting that this model space is too small to describe ^{80}Zn.

Using the determined optimal values, all eigenvectors in these models were calculated, and a level scheme was constructed. Figure 6.5 shows the calculated level schemes for the two different models. Figure 6.5a shows the calculated level scheme for ^{80}Zn with the SDI interaction. As can

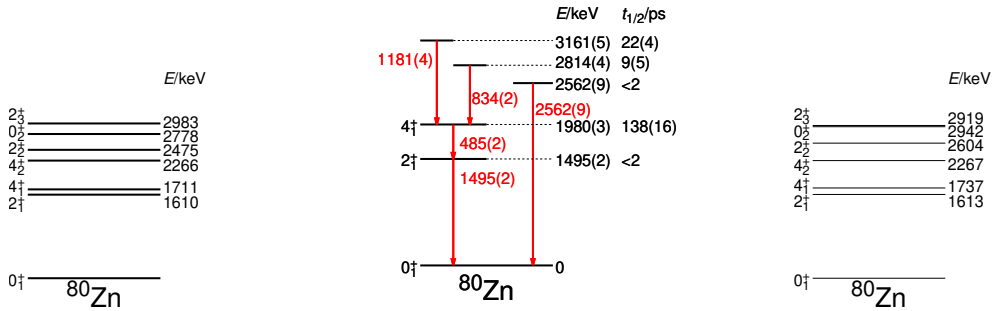

(a) (b) (c)

Fig. 6.5 Level schemes from the two different theoretical models, (a) for the SDI and (c) for the SDI+QQ, after the minimisation. (b) shows the experimental level scheme for comparison.

	SDI			SDI+QQ		
J^π	$\|(0f_{5/2})^2\rangle$	$\|0f_{5/2}1p_{3/2}\rangle$	$\|(1p_{3/2})^2\rangle$	$\|(0f_{5/2})^2\rangle$	$\|0f_{5/2}1p_{3/2}\rangle$	$\|(1p_{3/2})^2\rangle$
0_1^+	-0.87	-	-0.49	-0.87	-	-0.49
0_2^+	0.49	-	-0.87	0.49	-	-0.87
2_1^+	-0.92	0.31	-0.22	-0.89	0.38	-0.25
2_2^+	0.35	0.92	-0.17	0.41	0.91	-0.072
2_3^+	-0.15	0.24	0.96	-0.20	0.17	0.97
4_1^+	-0.77	0.64	-	-0.89	0.45	-
4_2^+	-0.64	-0.77	-	-0.45	0.89	-

Table 6.6 The weights of the components of the wave functions of the calculated excited states for the interactions: SDI and SDI+QQ.

Observable	Experiment	SDI	SDI+QQ
$E(2_1^+)$/keV	1495(2)	1610	1613
$E(4_1^+)$/keV	1980(3)	1711	1737
$B(E2,2_1^+ \to 0_1^+)/e^2\text{fm}^4$	146(18)	211	204
$B(E2,4_1^+ \to 2_1^+)/e^2\text{fm}^4$	153^{+16}_{-23}	98	111

Table 6.7 Selected experimental observables compared with the values predicted from the theoretical models. The values were taken from the ^{81}Ga(Be,X)^{80}Zn channel results, except for the $B(E2,2_1^+ \to 0_1^+)$ which was taken from [20]. Both models underpredict the $B(E2,4_1^+ \to 2_1^+)$ relative to $B(E2,2_1^+ \to 0_1^+)$, and the ratio of the 4_1^+ to 2_1^+ energies.

	^{78}Zn			^{80}Zn		
Observable	Experiment	jun45	jj44pna	Experiment	jun45	jj44pna
$E(2_1^+)$/keV	731(1)	1045	1104	1495(2)	1172	1709
$E(4_1^+)$/keV	1620.7(6)	1784	1931	1980(3)	1767	2708
$B(E2,2_1^+ \to 0_1^+)/e^2\text{fm}^4$	206^{+18}_{-29}	196.7	10.7	146(18)	89.1	86.7
$B(E2,4_1^+ \to 2_1^+)/e^2\text{fm}^4$	-	142.1	12.4	153^{+16}_{-23}	55.1	70.8

Table 6.8 Comparison between the jun45 and jj44pna calculations of ^{78,80}Zn and the experimental measurements. The $E(4_1^+)$ for ^{78}Zn is taken from [64], and the $B(E2,2_1^+ \to 0_1^+)$ for ^{80}Zn is from [20].

be seen, the separation of 4_1^+ and 2_1^+ states is not reproduced. Figure 6.5c shows the case for the SDI+QQ interaction. The separation between the 4_1^+ and 2_1^+ energies is slightly improved, but it still underestimates the observed separation. The wave functions of the excited states in the two models are shown in Table 6.6.

Table 6.7 shows the comparison of the calculated excitation energies and $B(E2)$ values for the 2_1^+ and 4_1^+ states to the experimentally determined values. As previously mentioned, the SDI+QQ marginally improved the separation of the 4_1^+ and 2_1^+ energies. However, both cases underpredict the R_{BE2} value.

KSHELL [148] was used to calculate the excited state energies and $B(E2)$ values of ^{78,80}Zn. Two interactions were used, namely jun45 [46], and jj44pna [147], both in the $1p_{3/2}$, $0f_{5/2}$, $1p_{1/2}$, and $0g_{9/2}$ model space for both protons and neutrons with a fixed ^{56}Ni core. Table 6.8 summarises the results of these calculations. As can be seen, these models capture the energy gap between the 2_1^+ and 4_1^+ states. For ^{78}Zn, the $B(E2,2_1^+ \to 0_1^+)$ predicted by jun45 is in good agreement with the experimental value; the jj44pna value is significantly lower than the experimental value. For ^{80}Zn the $B(E2,2_1^+ \to 0_1^+)$ and $B(E2,4_1^+ \to 2_1^+)$ are underpredicted by jun45 and jj44pna, and both predict the $B(E2,4_1^+ \to 2_1^+)$ to be smaller than the $B(E2,2_1^+ \to 0_1^+)$ value. Both models use a limited proton

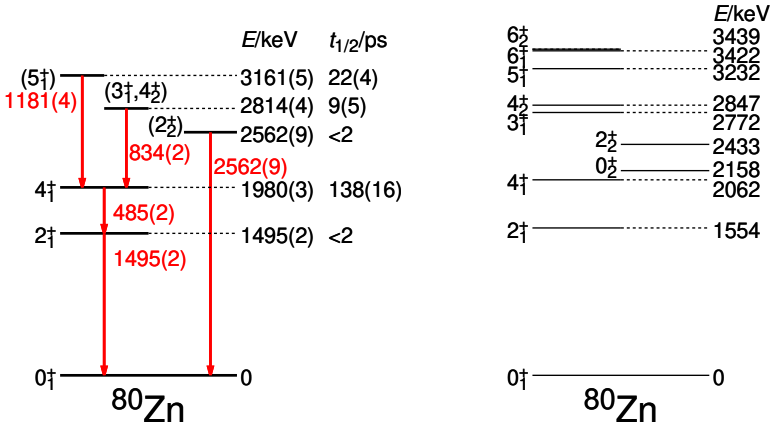

Fig. 6.6 Level scheme of ^{80}Zn from DNO-SM (b) [21, 22] calculations compared to the experimental level scheme from ^{81}Ga(Be,X)^{80}Zn (a). The 0_2^+ and 2_2^+ have been plotted independently of the main band as they have a different shape to the main band states. The states in the experimental level scheme have been assigned based on the DNO-SM predictions and the literature values.

		$B(E2, J_i^\pi \rightarrow J_f^\pi)/e^2\text{fm}^4$					
J_i^π	$t_{1/2}$/ps	J_f^π		J_f^π		J_f^π	
2_1^+	0.5	0_1^+	199	-	-	-	-
4_1^+	135	2_1^+	123	-	-	-	-
2_2^+	0.5	0_1^+	13	2_1^+	50	0_2^+	355
4_2^+	73	2_1^+	0.1	4_1^+	21	2_2^+	79

Table 6.9 $B(E2)$ values from the DNO-SM calculations for ^{80}Zn.

space with only two protons outside the core, possibly explaining why the models do not reproduce the observations.

Finally, DNO-SM [21] calculations of ^{80}Zn have been performed by F. Nowacki and D. Dao. The calculations used the PSFDG-U interaction using a ^{60}Ca core in the model space of: $1p_{1/2}$, $1p_{3/2}$, $0f_{5/2}$, and $0f_{7/2}$ for protons, and $0g_{7/2}$, $0g_{9/2}$, $1d_{5/2}$, $1d_{3/2}$, and $2s_{1/2}$ for neutrons [66]. The calculations are the same as in [22], but higher J states have been calculated, and $B(E2)$ values have been extracted.

Figure 6.6 shows the levels from DNO-SM [21] calculations of ^{80}Zn, compared with the experimental findings. The $B(E2)$ values are shown in Table 6.9. The 0_2^+ state is the same shape coexisting

J^π	n^*_ν	$\nu 0g_{9/2}$	$\nu 1d_{5/2}$	$\nu 2s_{1/2}$	$\nu 0g_{7/2}$	$\nu 1d_{3/2}$	n^*_π	$\pi 0f_{7/2}$	$\pi 0f_{5/2}$	$\pi 1p_{3/2}$	$\pi 1p_{1/2}$
0^+_1	0.50	9.50	0.23	0.03	0.19	0.04	2.48	7.52	1.90	0.44	0.14
2^+_1	0.58	9.42	0.30	0.04	0.20	0.04	2.40	7.60	1.90	0.35	0.15
4^+_1	0.50	9.50	0.24	0.04	0.19	0.04	2.31	7.69	1.76	0.48	0.07
0^+_2	2.74	7.26	1.20	0.71	0.52	0.31	3.08	6.92	1.33	1.28	0.47
2^+_2	2.11	7.89	0.95	0.48	0.44	0.24	2.85	7.15	1.33	1.11	0.41

Table 6.10 Occupation numbers of states in ^{80}Zn from DNO-SM. n^*_ν, and n^*_π show the number of neutrons and protons above the $Z = 28$ and $N = 50$ shell closures, respectively. The $0^+_{1,2}$ occupation numbers are also reported in [22].

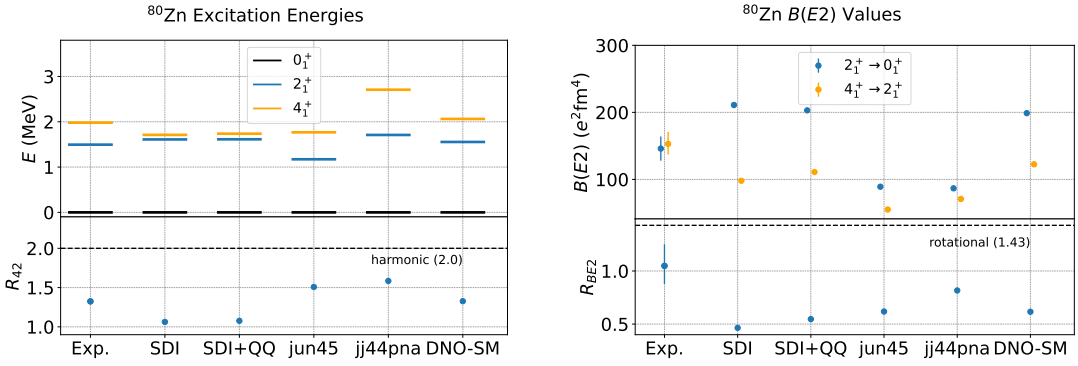

(a) (b)

Fig. 6.7 Comparison between experimental results and theoretical predictions for ^{80}Zn. (a) shows the excitation energies of the 2^+_1 and 4^+_1 states and their ratio for ^{80}Zn predicted by different models compared with the experimental results. (b) shows the reduced transition probabilities and the R_{BE2} from the experiment compared with the theoretical predictions of different models.

state shown in Figure 2.12, and the 2^+_2 is a deformed state associated with the 0^+_2. Based on the $E2$ transition rates, the branching ratios for the 2^+_2 state were calculated as 97.57 % to 0^+_1, 2.38 % to 2^+_1, and 0.05 % to 0^+_2, which is in agreement with the observations of the 2562 keV state. The states have been assigned in Figure 6.6a based on literature and the DNO-SM predictions.

Table 6.10 summarises the occupation numbers [2] of the states in ^{80}Zn from the DNO-SM calculations. The spherical 0^+_1, 2^+_1, and 4^+_1 states all have similar occupation numbers with ≈ 2.4 protons above the $Z = 28$ shell gap, and ≈ 0.5 neutrons above the $N = 50$ shell gap. Whilst the deformed states, 0^+_2 and 2^+_2, have a very different configuration with > 2 neutrons above the $N = 50$ shell gap, and ≈ 3 protons above the $Z = 28$ shell gap.

Figure 6.7 shows a comparison between the experimental results and the different theoretical predictions for ^{80}Zn. Figure 6.7a shows the excitation energies of the 2^+_1 and 4^+_1 states and the ratio of the energies. The SDI and SDI+QQ models do not replicate the energy gap between the 2^+_1 and 4^+_1

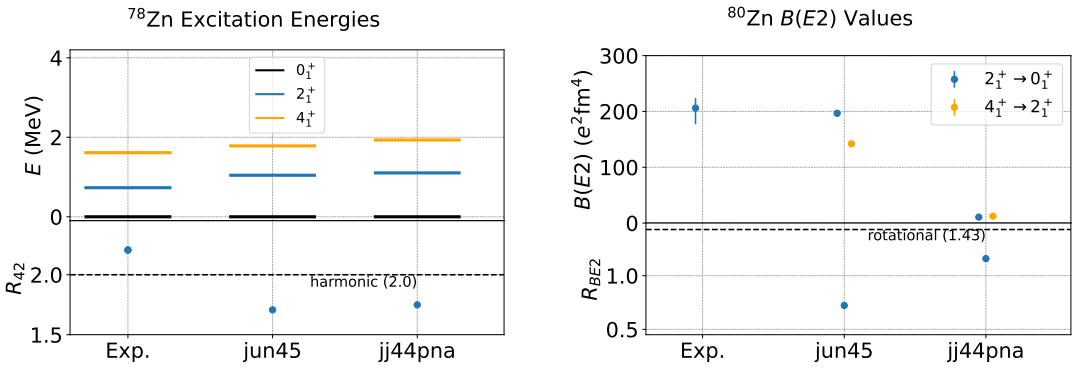

(a) (b)

Fig. 6.8 Comparison between experimental results and theoretical predictions for ^{78}Zn. (a) shows the excitation energies of the 2_1^+ and 4_1^+ states of ^{78}Zn predicted by different models compared with the experimental results. (b) shows the reduced transition probabilities from the experiment compared with the theoretical predictions of different models.

levels. jun45 and jj44pna predict an energy gap between the 2_1^+ and 4_1^+ levels, but fail to replicate the energies and overpredict the R_{42} value. Whilst DNO-SM replicates the observed energy well. Figure 6.7b shows the $B(E2)$ values for ^{80}Zn. All the theoretical models underpredict the R_{BE2} value.

Figure 6.8 shows the same comparison for ^{78}Zn. Figure 6.8a shows the comparison of the experimental excitation energies with the theoretical predictions. The jun45 and jj44pna interactions both underpredict the R_{42} values. Figure 6.8b shows the $B(E2)$ values for ^{78}Zn. The jun45 interaction properly replicates the $B(E2, 2_1^+ \rightarrow 0_1^+)$ values, whilst jj44pna greatly underpredicts the value. The $B(E2, 4_1^+ \rightarrow 2_1^+)$ is currently unmeasured.

6.4 Zn Systematics

Figure 6.9a shows the excitation energy systematics for the Zn isotopes. The measured energies are in good agreement with the literature values. The R_{42} values would suggest that the low-lying states in ^{80}Zn are single-particle excitations, indicating that the $N = 50$ neutron shell closure holds. Figure 6.9b shows the $B(E2)$ values for the Zn isotopes near ^{78}Ni. The new measurement of the $B(E2, 2_1^+ \rightarrow 0_1^+)$ in ^{78}Zn is within 2σ of the previous measurement. The $B(E2, 4_1^+ \rightarrow 2_1^+)$ in ^{80}Zn has been remeasured and is in agreement with the previous value with a smaller uncertainty. The $B(E2, 2_1^+ \rightarrow 0_1^+)$ in ^{80}Zn could only be measured as a lower limit. The R_{BE2} uncertainty has been improved compared to the previous measurement [19] and is no longer consistent with the collective model expectations.

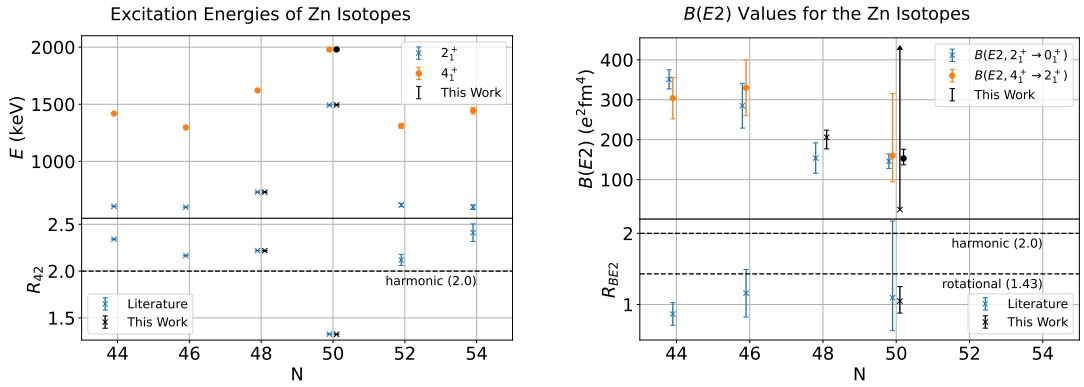

(a) (b)

Fig. 6.9 (a) shows excitation energy systematics for the first 2^+, and 4^+ states in the Zn isotopes values from literature, and the experiment. Literature values are taken from [60, 64, 20, 17, 18]. The lower plot shows the $R_{42} = E(4_1^+)/E(2_1^+)$ systematics. (b) shows the $B(E2)$ systematics for the Zn isotopes. The literature values are from [65, 17, 18, 20, 19]. The bottom plots shows the $R_{BE2} = B(E2,4_1^+ \rightarrow 2_1^+)/B(E2,2_1^+ \rightarrow 0_1^+)$ systematics.

6.5 Discussion

For ^{78}Zn only a $B(E2)$ for the $2_1^+ \rightarrow 0_1^+$ transition could be determined. A greater precision could be achieved from this measurement than the value from [17, 18] and the values are in agreement within 2σ. However, no measurement of the $B(E2,4_1^+ \rightarrow 2_1^+)$ could be done, due to the overlap with the 908.3 keV transition [64]. To measure this $B(E2,4_1^+ \rightarrow 2_1^+)$ value, a low-energy Coulomb excitation experiment could be performed similar to [65].

The excitation energy of the 2_1^+ state in ^{78}Zn has been measured and is consistent with previous high-precision measurements [12, 13, 14, 15, 16]. The ratio of the 4_1^+ and 2_1^+ energies would suggest that collective effects are significant in this nucleus.

The $B(E2,4_1^+ \rightarrow 2_1^+)$ value of ^{80}Zn has been remeasured to a much higher precision than the previous measurement [19]. This allowed for a significant improvement in the R_{BE2} value. A further improvement in the $B(E2,4_1^+ \rightarrow 2_1^+)$ uncertainty may be possible by using fast timing measurements to measure the lifetime [151].

For ^{80}Zn, the R_{42} would suggest that ^{80}Zn is dominated by single-particle structure. However, the R_{BE2} values lie near the rotor value, suggesting the possibility of collectivity. In addition, the SDI and SDI+QQ models using a ^{78}Ni core not agreeing with the observations would suggest that a larger

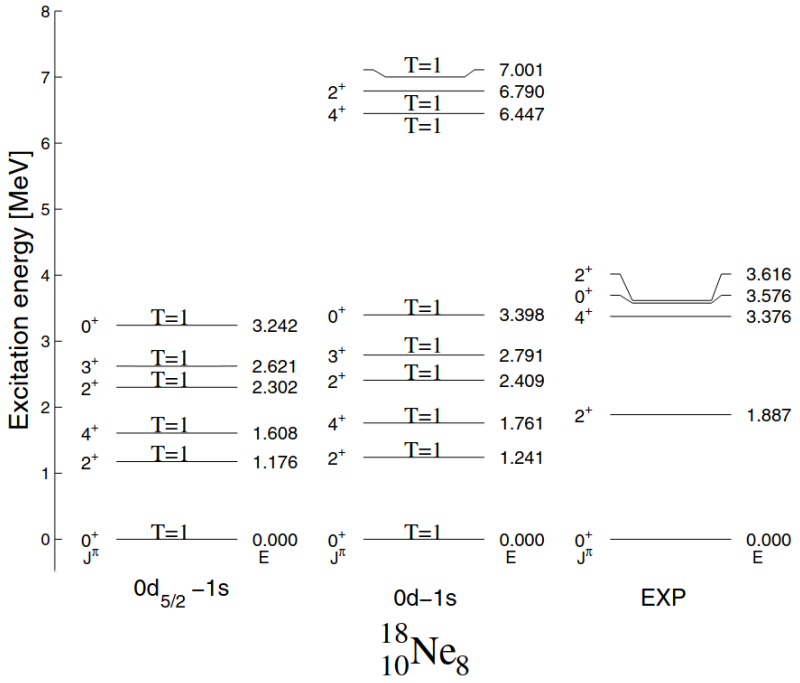

Fig. 6.10 Calculations of excited states in ^{18}Ne compared to the experimental results. The left level scheme shows the calculation with an SDI in the basis $0d_{5/2}$, and $1s_{1/2}$, the middle level scheme shows the same in the basis $0d_{5/2}$, $0d_{7/2}$, and $1s_{1/2}$, and the right shows the experimental values. In both calculations, the separation between the 2_1^+ and 4_1^+ states is not replicated. Reproduced from [2].

model space or collective effects are necessary to describe ^{80}Zn properly. This is further supported by the large effective charges required to optimally reproduce the $B(E2)$ values.

The SDI and SDI+QQ model calculations are quite limited; a similar calculation on ^{18}Ne, two protons above the $Z = 8$, and $N = 8$ shell closures was performed in [2]. Figure 6.10 shows the results of calculations of ^{18}Ne compared to the experimental data. As can be seen, the experimental separation between the 2_1^+ and 4_1^+ is not replicated, as is also seen in the calculation of ^{80}Zn. Even in the strong shell closure at ^{16}O, cross-shell excitations are necessary to properly describe the excited states, explaining why these models fail to describe the observations. However, the calculation of ^{18}Ne only requires an $e_{\text{eff}} = 1.9$ to replicate the experimental $B(E2, 2_1^+ \rightarrow 0_1^+)$ value [2], in comparison to the value used for ^{80}Zn, $e_{\text{eff}} = 2.85$. The large effective charge suggests that collective effects are more important in ^{80}Zn, indicating that the $Z = 28$ and $N = 50$ shell closures are weaker than the $Z = 8$ and $N = 8$ shell closures.

The Jun45 and jj44pna interactions both overpredict the excitation energies of the 2_1^+, and 4_1^+ states alongside the R_{42} value in ^{78}Zn. The jj44pna interaction greatly underpredicts the $B(E2)$ values

for ^{78}Zn. The jun45 interaction reproduces the $B(E2, 2_1^+ \rightarrow 0_1^+)$ correctly. The jun45 interaction is capable of extracting some of the properties of ^{78}Zn, but with incorrect excitation energies. In ^{80}Zn, jj44pna and jun45 fail to reproduce the excitation energies of the 2_1^+ and 4_1^+ states. In addition, the $B(E2)$ values are underpredicted compared to the experimental values, suggesting the need for higher effective charges. jun45 underpredicts the ratio of the $B(E2)$ values, whilst jj44pna falls within 2σ of the experimental value. Some properties of ^{80}Zn can be extracted from these models, but not others.

DNO-SM calculations properly predict the excitation energies of the 2_1^+ and 4_1^+ states in ^{80}Zn. However, the $B(E2, 2_1^+ \rightarrow 0_1^+)$ is overpredicted, and the $B(E2, 4_1^+ \rightarrow 2_1^+)$ value is underpredicted relative to the experimental values. As such, the ratio of the $B(E2)$ values is underpredicted. The correct extraction of the excitation energies and the poor replication of the $B(E2)$ values suggest the necessity for collective effects to properly describe this nucleus. Indicating that the $N = 50$ shell closure is weak in this region.

To identify the newly observed states in ^{80}Zn, the experimental results were compared to the DNO-SM calculations. The identification of the 2_1^+ and 4_1^+ states is based on previous experimental measurements [18, 17, 19, 20], and the energy and half-life of the excited states from DNO-SM. The state at $3161(5)$ keV is closest in energy to the 5_1^+ state from the DNO-SM calculations, therefore it is assigned as a tentative (5_1^+) state. The state at $2814(4)$ keV is close in energy to the 3_1^+, and 4_2^+ states; therefore, it is ascribed as a $(3_1^+, 4_2^+)$ state. More theoretical information on the expected half-life of the 3_1^+ would be necessary to properly identify the state.

Finally, the $2562(9)$ keV state is ascribed as the (2_2^+) state as the predicted energy is close in energy, the measured half-life limit is consistent with the predicted values, and the predicted branching ratios of the 2_2^+ state explain why the $2_2^+ \rightarrow 0_2^+$ and $2_2^+ \rightarrow 4_1^+$ transitions are not observed experimentally. The observation of the (2_2^+) state suggests the presence of shape coexistence in this nucleus. MCSM [68] calculations also predicted a deformed 0_2^+ state at 2.59 MeV, further supporting that the (2_2^+) is a deformed state associated with the deformed 0_2^+ state. DNO-SM predicts the 2_2^+ to have 2.11 neutrons above the $N = 50$ shell gap; the indication of shape coexistence further supports the weakening of the $N = 50$ shell closure.

The ratio of the 4_1^+ to the 2_1^+ energy in ^{80}Zn would suggest that the $N = 50$ shell closure is maintained, and single-particle excitations dominate the low-lying states in ^{80}Zn. However, the failure of the shell model calculations to recreate the ratio of the $B(E2)$ values would suggest additional effects are necessary to describe this nucleus, indicating the weakness of the shell closure. This

suggests the forces involved in the shell evolution may not be fully understood, and more information in the region of ^{78}Ni is necessary for a proper explanation.

6.6 Conclusion

The energy and half-life of the 2_1^+ state in ^{78}Zn have been measured from three separate channels, and all values are within 2σ of the literature value [17, 18]. In addition, the energies of several tentative states have been measured, and upper limits for the half-life have been established where possible. Further measurements will be required to understand their position in the level scheme. The $B(E2, 4_1^+ \rightarrow 2_1^+)$ value is still not measured.

For ^{80}Zn, the energy has been measured and agrees to within 2σ of the literature value, and an upper-limit for the half-life has been measured and is in agreement with the previous measurement [17, 18]. The 4_1^+ excitation energy was remeasured as $1980(2)\{3\}$ keV with a half-life of $138(13)^{+10}_{-16}$ ps, both in agreement with the previously measured values [19, 20]. In addition, the energies of two states feeding the 4_1^+ are measured to be $2814(2)\{4\}$ keV, and $3161(3)\{5\}$ keV, both within 1σ of the previous measurement [19]. The half-lives of these states have been measured for the first time to be $9(3)^{+3}_{-5}$ ps, and $22(4)\{4\}$ ps, respectively. Finally, a state decaying to the ground state has been measured to be $2562(5)\{9\}$ keV, significantly lower than the previous measurement of 2627(39) keV [19], but still within 2σ. An upper limit for the half-life of this state was measured as < 2 ps for the first time.

Calculations of ^{80}Zn were performed with a ^{78}Ni core and two protons in the $0f_{5/2}$, and $1p_{3/2}$ model space with an SDI and SDI+QQ interactions [2, 45, 146]. The models do not replicate the separation between the 2_1^+ and 4_1^+ states due to the limited model space. The determined e_{eff} values of ≈ 3 are much larger than the expectation, indicating the necessity for a larger model space. In addition, the models underestimate the ratio of the $B(E2)$ values, suggesting that additional effects are necessary to explain this nucleus. Shell model calculations [148] were also done using jun45 [46], and jj44pna [147] effective interactions, some features of ^{80}Zn are replicated, but others are not. The lack of agreement would indicate the weakness of the $N = 50$ shell closure, and calculations that can include effects of deformation are necessary to describe this nucleus.

DNO-SM [21] calculations of ^{80}Zn were compared to the experimental results; the excitation energies of the 2_1^+ and 4_1^+ states agree well with the experimental values. However, the predicted

$B(E2)$ values and the R_{BE2} value do not agree with the experimental results, suggesting the existence of collective effects in ^{80}Zn and indicating that the $N = 50$ shell closures is weak in this region. In addition, a state at $2562(5)\{9\}$ keV was observed that was consistent with the expectations of the deformed 2_2^+ state predicted by the DNO-SM calculations, suggesting the presence of shape coexistence. The predicted occupation numbers show significant excitations across the $N = 50$ shell gap. The presence of shape coexistence suggests that the $N = 50$ shell closure is weak for ^{80}Zn.

The results indicate the $N = 50$ shell closure is weak in this region. Further information will be necessary to understand this region, such as examining single-particle structure in ^{81}Zn or $1p-2h$ states in ^{77}Ni, which would be attainable with current technology and accelerators. However, for a complete understanding of this region, structure information on ^{79}Ni is necessary, which will require developments in both accelerator and detector technology. In the next chapter, the development of new detector technologies that will allow for the further investigation of this region will be presented.

Chapter 7

Technical Development for Future Scintillator Arrays

7.1 Scintillator Arrays at the RIBF

The first in-beam gamma-ray spectroscopy experiment with scintillators at the RIBF was carried out in 1995 at the RIKEN Projectile-fragment Separator (RIPS) facility [152] with the Detector Array for Low Intensity Radiation (DALI), array looking at ^{32}Mg [153]. This array was advanced into DALI2 [24], performing many successful and groundbreaking experiments [9, 26]. A planned upgrade of the RIBF accelerators [154] will require improved detector systems in order to capitalise on the new areas of exploration. This is being pursued via the Hybrid Photon Detection Array to Investigate Atomic Nuclei (HYPATIA) project [40, 39].

7.1.1 DALI2+

The DALI2 array was constructed of 186 NaI(Tl) detectors with PMTs [24]. It was later expanded to DALI2+ with 226 NaI(Tl) detectors [84]. A rendering of a cross-section of the array can be seen in Figure 7.1. DALI2+ has been used successfully in many experiments, such as performing the first spectroscopy of ^{100}Sn [155].

DALI2+ uses an analogue DAQ where the PMT signals are first sent to a shaping amplifier, which has a shaped output and a fast output. The fast output is sent to a CFD module, followed by a multi-hit TDC to record the time of the signal. The shaped output is sent straight to a peak sensing

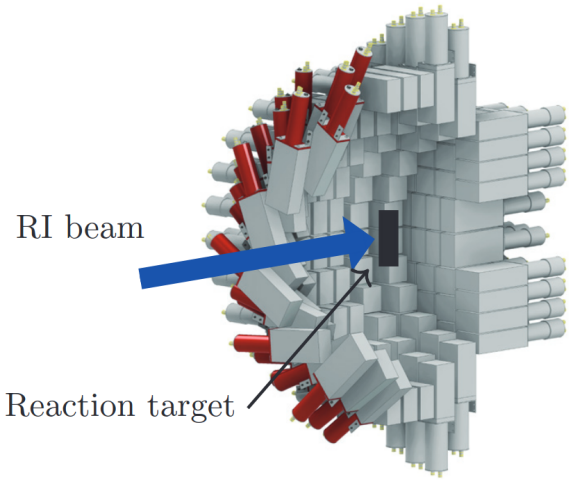

Fig. 7.1 Rendering of a cross-section of the DALI2+ array. The NaI(Tl) is encased in an Al housing with a PMT attached. Reproduced from [84].

ADC to record the signal amplitude. The trigger for the DAQ is made using the OR output from the CFD modules being passed through a logic circuit; the trigger is then made in coincidence with the beam-line trigger to gate on physics events. The DALI2+ data is recorded in a slave DAQ before being sent to the global event builder to be merged with the data from the beam-line DAQ.

7.1.2 HYPATIA

HYPATIA is a next-generation scintillator array under construction for use at the RIBF. The HYPATIA geometry is shown in Figure 7.2. HYPATIA is made up of a forward wall of HR-GAGG [38], and a barrel made of 2×2 $CeBr_3$ [37] quads. Both are novel scintillators with properties improved from the traditional NaI(Tl) [35]. GAGG is chosen for its significant stopping power [35] and is placed at forward angles to increase the detection efficiency for the Lorentz boosted gamma rays [30]. In addition, GAGG being non-hygroscopic [33] allows for the crystals to be packed tightly together with limited encapsulation, enabling the formation of high-efficiency configurations. GAGG also provides an improved energy resolution compared to NaI(Tl) and has a fast decay time of 90-170 ns, faster than NaI(Tl) with a decay time of 230 ns [35]. $CeBr_3$ provides excellent energy resolution and decay time (17 ns), but is hygroscopic and has a smaller stopping power than GAGG [35]. The $CeBr_3$ detectors are located at larger angles to exploit the improvements whilst mitigating the losses in detection efficiency due to the encapsulation and lower density. The array will use SiPM photosensors [156] to read out the signals and digitisers for data acquisition [157]. SiPMs were chosen over PMTs

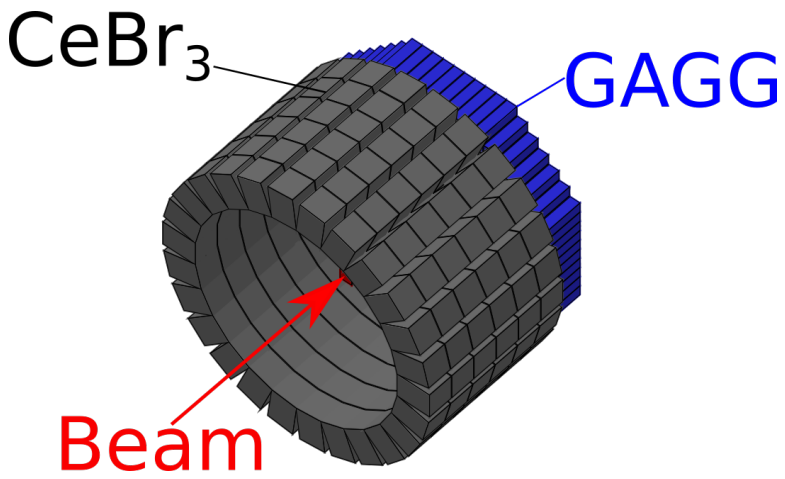

Fig. 7.2 HYPATIA array simulation geometry for Geant4 [74]. There are two parts of the array, a GAGG forward wall and a barrel made up of $CeBr_3$ modules, each containing 2×2 crystals. The beam direction is shown in red.

due to the quantum efficiency response being a better match for the photon wavelengths emitted by GAGG [97, 92, 38], the more compact form factor, and their insensitivity to magnetic fields [91]. HYPATIA aims to achieve a significantly improved energy resolution and full-energy peak efficiency compared to DALI2+.

7.1.3 Expected Efficiency and Resolution

To estimate the expected performance of the array, a simulation package based on the Geant4 framework [74, 158] was used. The simulation is performed in three steps. The first step simulates the incoming nucleus reacting with the target and emitting gamma rays, which are Doppler boosted in the lab frame according to the nucleus's velocity at the time of gamma emission. The information about the gamma ray and the nucleus is saved in a ROOT file [140]. The second step simulates the gamma rays generated in the first step interacting with the detector array. The energy deposited in each detector is recorded and smeared by a Gaussian distribution according to the expected detector energy resolution. The FWHM energy resolution, ΔE, is estimated using the function

$$\Delta E = aE_\gamma^b \tag{7.1}$$

where E_γ is the energy deposited in the detector, and a and b are parameters determined from the resolution curve of each type of detector. The data from this step is then saved into a new ROOT file.

The final step analyses the data from the simulation. The Doppler correction is performed according to the calculated average interaction position, the beam velocity at the target centre, and the smeared energy deposited in the detector. Add back analysis is performed by summing the energies of the detectors within a radius of 15 cm to achieve a better full-energy peak efficiency. For the add back analysis, the position of the detector with the highest energy deposition is used for calculating the angle of gamma-ray emission for the Doppler correction. Finally, the array is also treated as a single unit where all the energies in all the crystals are summed together. This is referred to as calorimeter mode.

To demonstrate the expected improvements of the HYPATIA array over its predecessor, simulations were performed using a ^{49}Ca beam with an energy of 200 MeVu^{-1} impinging on a 1 mgcm^{-2} thick Be target. The use of a thin target avoids the Doppler broadening effect from the β uncertainty, providing a benchmark for the array's performance. Simulations were performed for gamma ray emissions from 500 to 6000 keV in steps of 500 keV. One million events were simulated for each gamma-ray energy.

The HYPATIA configuration used in the simulations contains 384 25×25×100 mm^3 GAGG detectors and 624 30×30×80 mm^3 $CeBr_3$ detectors. A reflector of 0.065 mm was simulated surrounding each crystal. In addition, a detector housing of 1 mm Al was included for the $CeBr_3$ detectors. The parameters for the detector energy resolution were set to $a = 1.45$ and $b = 0.5$ for GAGG, corresponding to 5.6 % (FWHM) at 662 keV, and for $CeBr_3$ were $a = 0.95$ and $b = 0.5$, corresponding to 3.7 % (FWHM) at 662 keV. The average first interaction points used in the Doppler correction were generated using the data from the 1 MeV energy gamma-ray simulation and used for all the cases.

The spectra for single, add back, and calorimeter modes were fitted using a Gaussian peak on top of a quadratic background. The energy resolution and efficiency were calculated using the fitted Gaussian parameters. For the single mode, spectra up to 3 MeV gamma ray simulations could be fitted properly. Above this energy, the overlap between the Compton edge and the full-energy peak prevents a reasonable description using this fitting function.

The results can be seen in Figure 7.3. DALI2+ simulations are included for comparison. As can be seen, HYPATIA provides an improvement in both energy resolution and efficiency, allowing for the extension of analysis to more exotic nuclei.

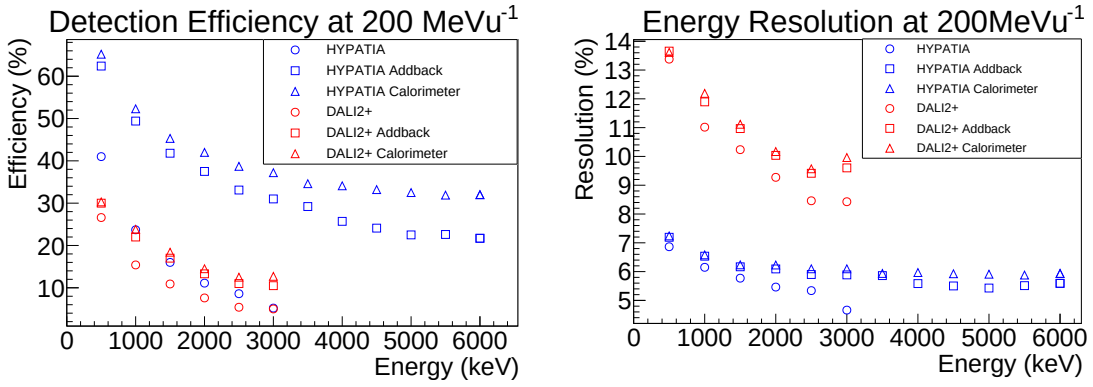

(a) (b)

Fig. 7.3 Simulated performance of the HYPATIA and DALI2+ arrays for in-flight decays at a beam energy of 200 MeVu^{-1}. (a) the simulated efficiency of the arrays, and (b) the simulated energy resolution of the arrays. Only points that could be well described by the fit function are included.

Illustrative Experiment: The First Spectroscopy of ^{79}Ni

As discussed previously, the missing pieces in the systematics of shell evolution in the $N = 51$ isotones are ^{81}Zn and ^{79}Ni. HYPATIA will allow for the first spectroscopy of ^{79}Ni. Figure 7.4 shows the expected response of HYPATIA compared with DALI2+. Due to the small energy difference between the $5/2^+$ and $1/2^+$ states, the $5/2^+$ state is expected to have a lifetime of the order of 1 μs based on the Weisskopf estimates; therefore, the decay is unobservable by in-beam gamma-ray spectroscopy. However, the $3/2^+$ state can decay to both the $1/2^+$ and $5/2^+$ states via $M1$ transitions. By measuring the energy difference between the two gamma-rays, the energy of the $5/2^+$ state could be determined. With the improved energy resolution of HYPATIA, a separation between the peaks can be achieved, which would allow for an accurate measurement of the $5/2^+$ state, determining the crossing point of the $\nu 2s_{1/2}$, and $\nu 1d_{5/2}$ orbitals and illuminating the tensor interaction in atomic nuclei.

7.2 GAGG Characterization

In order to confirm that the array's expected performance can be achieved, the crystal performance needs to be tested. In this section, GAGG samples' performance is evaluated and compared to the required benchmarks for the array.

HR-GAGG can be produced by several manufacturers. Crystals from four different manufacturers were tested: C&A [33], Epic crystals [86], Kinheng [88], and CETC [89]. 13 GAGG samples were

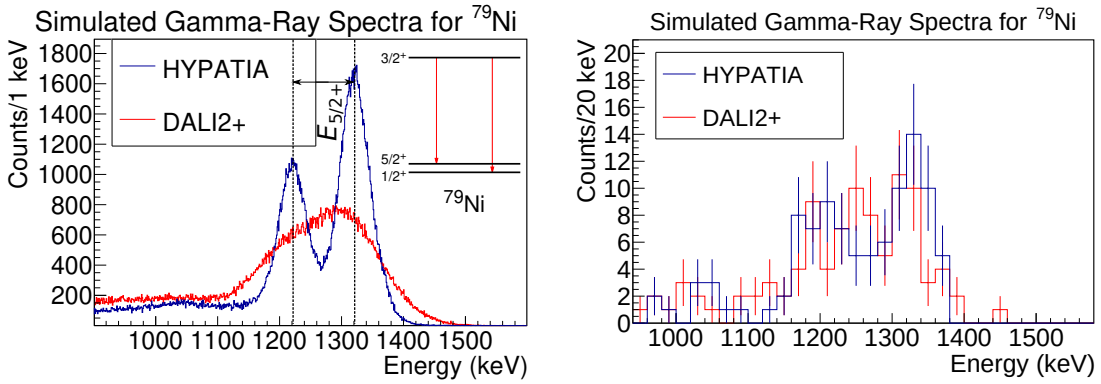

(a) (b)

Fig. 7.4 Simulated spectra of ^{79}Ni for HYPATIA and DALI2+. (a) shows the simulation for unrealistic statistics. The level scheme is inset; the branching ratios are based on the Weisskopf estimates [43]. The level scheme was adapted from [159]. As can be seen, HYPATIA resolved the doublet whilst DALI2+ fails to do so. (b) shows the case for semi-realistic statistics. The expected counts were calculated using a 2000 pnA ^{238}U beam [154] in LISE++ [125], a 40 mb cross-section on a 150 mm LH target with position reconstruction for a 14 day experiment. In the case of realistic statistics, the peaks are still resolved, whilst in the DALI case, only a single peak is observed.

Sample Name	Manufacturer	Dimensions/mm^3
1	C&A[33]	25×25×75
2	C&A	25×25×75
Epic 1	Epic[86]	25×25×75
Epic 2	Epic	25×25×75
Kinheng 1	Kinheng[88]	25×25×75
Kinheng 2	Kinheng	25×25×75
CETC 1	CETC[89]	25×25×75
CETC 2	CETC	25×25×75
IBS 1	EPIC	25×25×100
IBS 2	EPIC	25×25×100
IBS 3	EPIC	25×25×100
IBS 4	EPIC	25×25×100
IBS 5	EPIC	25×25×100

Table 7.1 GAGG samples tested for the HYPATIA array alongside their dimensions and manufacturer.

obtained and tested to evaluate their suitability for the HYPATIA array. Table 7.1 shows a list of the samples. All samples were produced using the Czochralski method [160].

The aim of this work was to characterise the crystals and find the best supplier for the array. For this, three performance criteria are required: good energy resolution (<6 % FWHM at 662 keV), good time resolution (<1 ns FWHM at ∼1 MeV), and high uniformity throughout the crystal volume. To

evaluate this, the energy resolution measurements, time resolution measurements, and crystal scans have been performed.

7.2.1 Experimental Method

To read out the crystals, firstly, a photosensor was mounted to one of the smaller sides of the crystal using EJ-550 optical grease [161]. The grease was spread liberally, and the photosensor was pressed to remove any air bubbles that could reduce the transmission efficiency of photons to the photosensor. Secondly, the crystal was wrapped in 4 layers of 0.1 mm-thick PTFE tape. The high reflectivity [162] reduces the photon loss due to transmission out of the crystal. Finally, the crystal was mounted in a dark box to prevent ambient light from reaching the photosensor.

It was found that the GAGG crystals exhibited strong afterglow (phosphorescence) following exposure to ambient light. This led to a drift in the ADC channel of the full-energy peak with time, likely due to the increased baseline current in the photosensor output. To mitigate this effect, the crystals were kept in the dark until their peak positions had stabilised, before taking measurements.

Three photosensors were used, two SiPMs S13361-6050AE-04 [97] and S13361-3050AE-08 [97], and one PMT R11265U-20 [93]. As the PMT quantum efficiency response is a poor match for the photon emission wavelength distribution of GAGG, it was only used for time resolution measurements [163]. The PMT was powered using an NHQ 204M power supply [164].

The SiPM breakdown voltage varies as a function of temperature; for the S13 series, this is 54 mVK^{-1} [97]. To deal with this, a special readout board, utilising an LM94021 temperature sensor [165] to measure the temperature, was used. A power supply designed by H. Baba [166] was used to read the temperature sensor and supply a temperature-corrected bias voltage. For these tests, the bias voltage was set to 57 V. This power supply will be referred to as Baba-san's power supply. The schematic for the biasing and readout can be seen in Figure 7.5. The bias voltage is passed through an RC filter to suppress high-frequency noise before applying the voltage to the cathode of the SiPM. The anodes of the SiPM are connected together and then fed into an inverting amplifier circuit utilising the AD8001 operational amplifier [167]. The values of R_O, R_F, R_G, and R_T determine the gain of the circuit; these were selected to give a gain of 3. The output of the operational amplifier circuit was connected to a coaxial connector, which was then connected to the DAQ electronics via a coaxial cable.

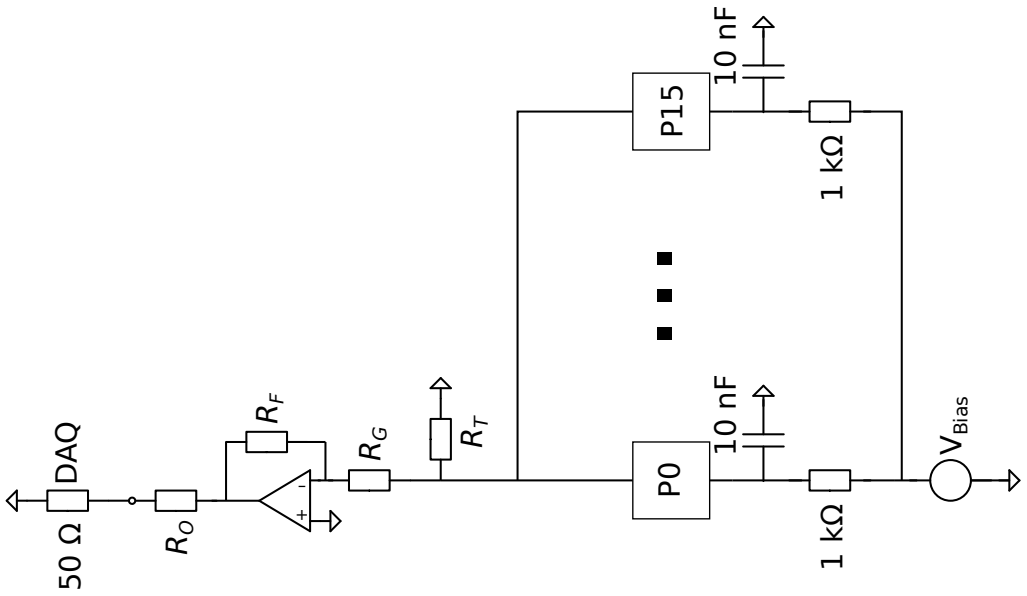

Fig. 7.5 Circuit diagram for the readout board for the SiPM. P_i refers to the individual pixels of the SiPM.

Signal processing was performed using a CAEN V2745B digitiser [157]. The unit operated on DPP-QDC firmware utilising a digital CFD for timing, with data acquisition managed through the CAEN CoMPASS software [104]. The resulting datasets included the integrated charge (ADC channel), CFD-derived timestamps, and trigger channel IDs, which were recorded in the ROOT file format [140] for subsequent analysis.

7.2.2 Crystal Energy Resolution

The energy resolution was characterised using ^{137}Cs, ^{60}Co, and ^{88}Y calibration sources. The raw ADC values from the digitiser were used to construct a histogram, where the full-energy peaks were fitted with a Gaussian function plus a linear background; the Gaussian mean parameter was used as the peak position. The peak positions were calibrated to the gamma-ray energies using a quadratic function to account for non-linearities.

The calibrated spectra were fitted using the same function. The Gaussian σ parameter was used to determine the energy resolution according to

$$\text{Res.} = \frac{2.355\sigma}{E_\gamma} \tag{7.2}$$

where E_γ is the energy of the gamma-ray.

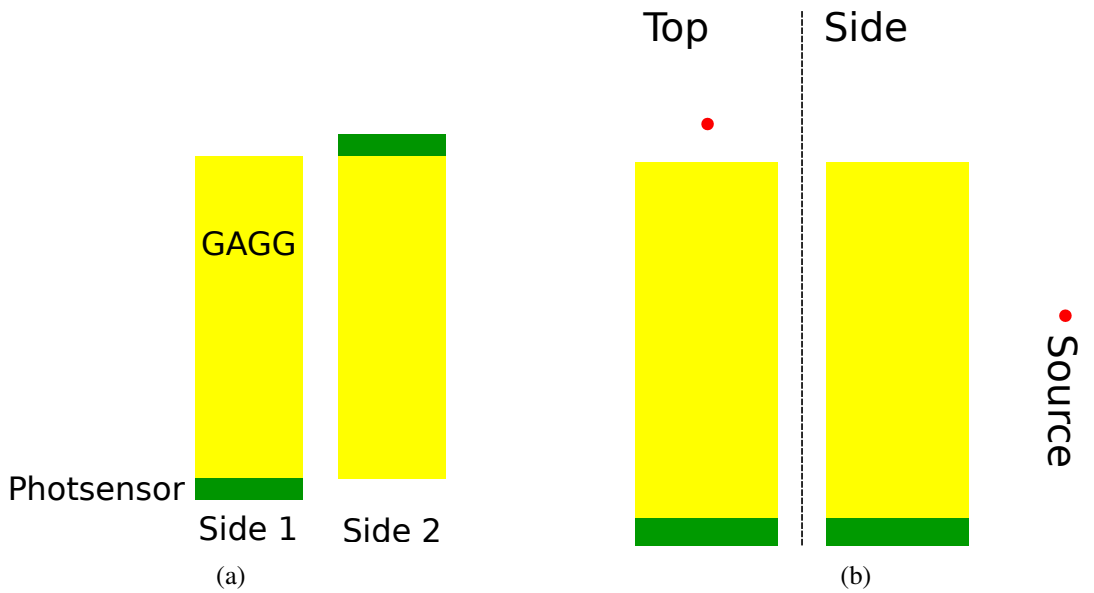

Fig. 7.6 Definitions of different configurations used for testing the energy resolutions of the crystals. (a) shows the definition of different sides 1 and 2 for a detector. The choice of the labelling is arbitrary. (b) shows the definition of top and side illumination. The red dot shows the source location.

The energy resolution was measured in multiple configurations. The SiPMs were placed on both of the small sides of the crystal to check for differences in performance; these configurations can be seen in Figure 7.6a. Secondly, the crystals were illuminated from the top or the side, Figure 7.6b. Illuminating from the side gives an overview of the whole crystal, allowing for the observation of the uniformity. The top illumination provides a performance of a small part of the crystal, allowing for the optimum performance.

The systematic uncertainty in the measurement is primarily due to the peak fitting. To estimate this uncertainty, the peak fitting method was varied in different ways, including: fitting only the peak region with no background, fitting a much larger range of the background and changing the background to a quadratic function. This is shown in Figure 7.7. The energy resolution was determined for each of these cases, and the largest percentage deviation was taken as the relative systematic error. This was repeated for three cases: Kinheng 1, CETC 1, and Epic 1, and the largest systematic uncertainties for the peaks were taken. The systematic uncertainties were determined to be 4 %, 8 %, 10 %, 8 % and 5 % for the 622, 898, 1173, 1333 and 1836 keV peaks, respectively.

Figure 7.8 shows the energy resolutions obtained from these studies. One of the most notable observations is that the energy resolution of the crystals is very dependent on the side to which the photosensor is mounted. This is likely due to a reduced transparency at one end of the crystals due to

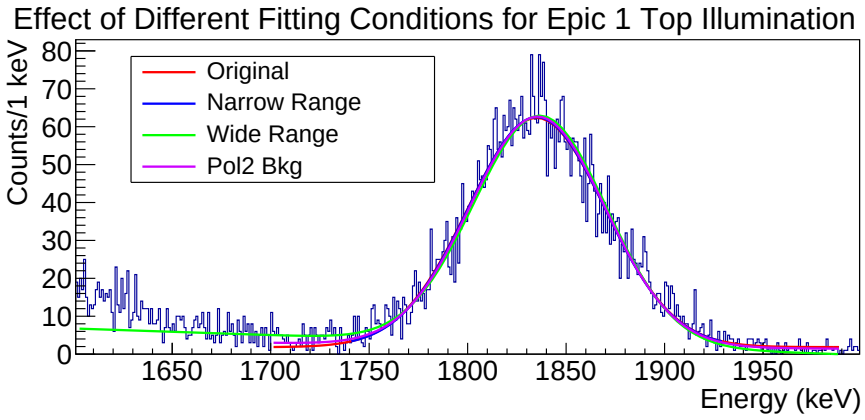

Fig. 7.7 Energy histogram from Epic 1 measurement with top illumination for the 1836 keV ^{88}Y peak. The different fits used in determining the energy resolution and estimating the systematic uncertainty are shown. Original shows the fit used for obtaining the resolution, Narrow Range shows just fitting the region around the peak, Wide Range shows the effect of fitting too large a region, and Pol2 Bkg shows the fit using a quadratic function as the background, as opposed to the linear background used in the remaining cases.

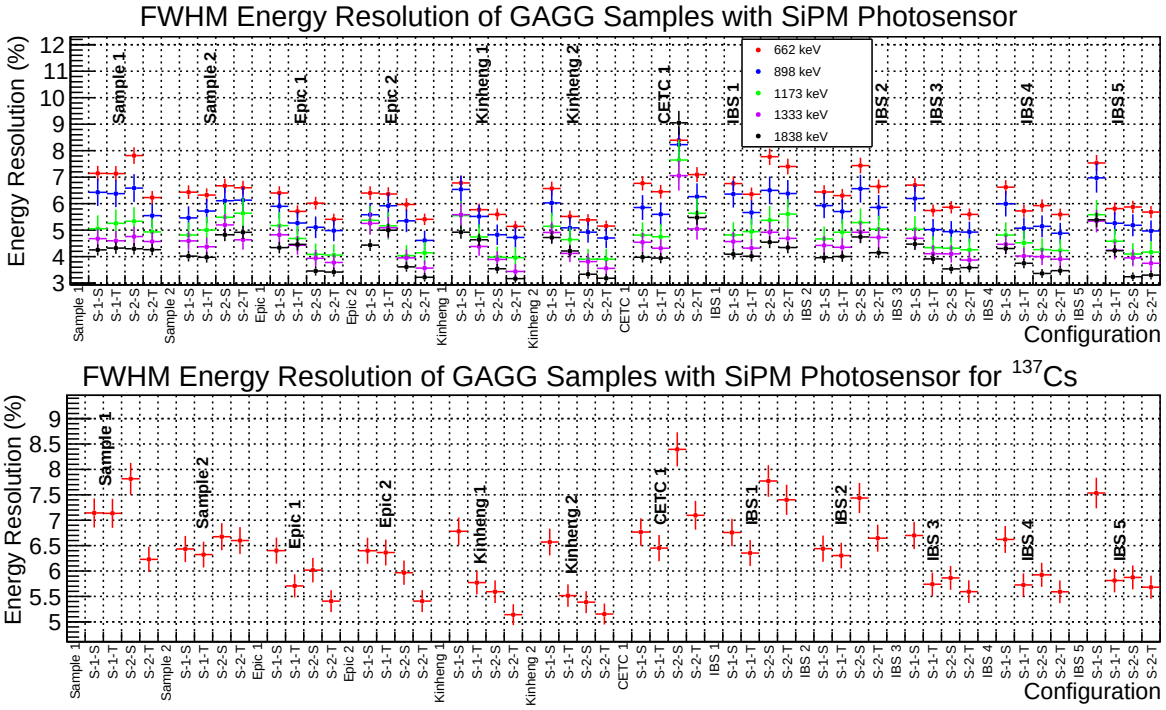

Fig. 7.8 Determined energy resolutions FWHM for different configurations. The top graph shows the energy resolutions for all the tested gamma rays, whilst the lower graph isolates only the resolutions at 662 keV. The labels S-i-S/T refer to Side-i-Side/Top, where side i is the side to which the SiPM is attached and Side/Top refers to whether the illumination is from the side or the top.

a higher concentration of impurities [168]. Additionally, it is observed that illuminating the top of the crystal gives an improved energy resolution compared to illuminating from the side. This indicates non-uniformities across the crystal, leading to peak broadening when illuminating the whole length of the crystal. When mounted in the array, the crystals will be illuminated mainly from the front side in real experiments, so this energy resolution can be taken as the HYPATIA energy resolution for comparison with the benchmark. However, for high-energy gamma rays and add back events, the non-uniformity will be important, and will need to be considered in the simulations used to analyse the data.

Given the limit of < 6 % energy resolution, it can be seen that the two Japanese samples, samples 1 and 2, fail to achieve this benchmark. Both Kinheng and Epic performed exceptionally well, achieving energy resolutions well below the benchmark number. CETC 1 failed to reach the benchmark. CETC 2 is not included here and will be discussed separately. The full-size samples, IBS 1-5, have some variability, but it can be seen that IBS 3, 4, and 5 all achieved the benchmark resolution, whilst IBS 1 and 2 do not. IBS 3, 4, and 5 have worse energy resolution values than the smaller Epic samples (Epic 1 and 2).

CETC 2

Initial tests with CETC 2 found the energy resolution of the crystal was insufficient to resolve the ^{60}Co lines. It was sent back to the company, where the crystal was tested and returned with a specular reflector attached. The crystal was tested using the same method as the other crystals, except with the specular reflector and only testing one side, as the reflector was already attached.

Figure 7.9 shows the spectra obtained from illuminating from the top and the side of the crystal. As can be seen, top illumination produces well-separated peaks with a noticeable asymmetry towards the high-energy side. Whilst illuminating the side of the crystal, the peaks are very broad and non-Gaussian, with the Co peaks unresolved.

To understand this, a crystal scan was done using a 5 mm diameter tungsten collimator. A ^{60}Co source was placed on one side of the collimator and directed to a specific point in the crystal on the other side of the collimator. A DALI2 detector was placed on the ^{60}Co source side of the collimator; the CETC 2 spectrum was produced using events that were in coincidence with the DALI2 detector to reduce the background. A diagram of this setup can be seen in Figure 7.10.

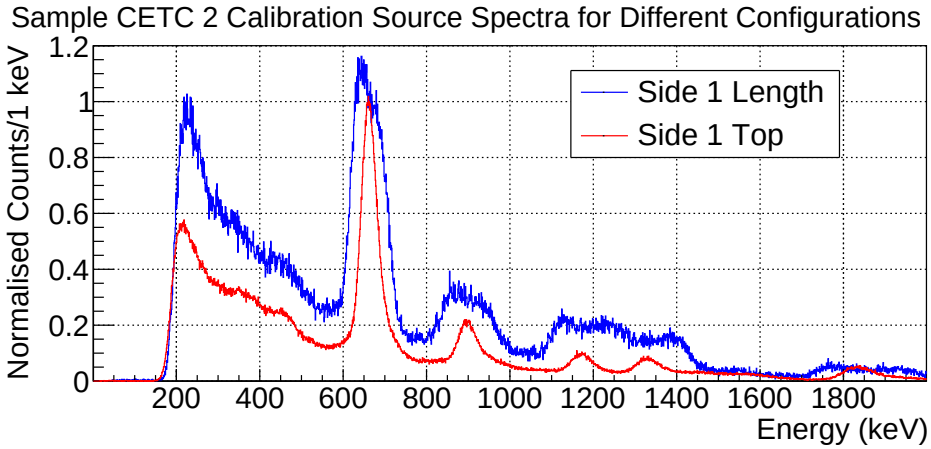

Fig. 7.9 Spectra from CETC 2 obtained with ^{137}Cs, ^{60}Co, ^{88}Y sources, with sources placed at the length of the crystal and at the top of the crystal. The spectra were normalised based on the counts at 662 keV.

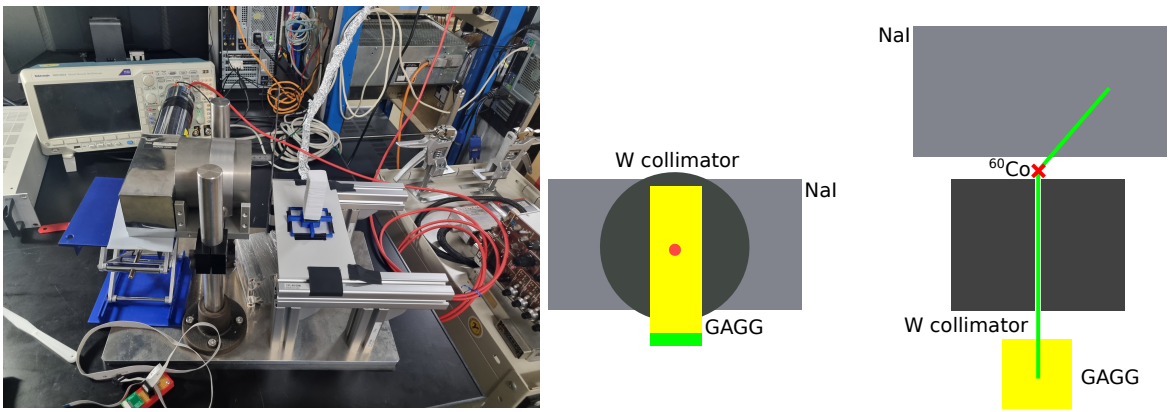

Fig. 7.10 Setup for collimator scan of the crystals. Left shows a picture of the setup, and right shows a schematic of the setup from the side and from the top. The green line shows the cascade gamma rays being measured in coincidence.

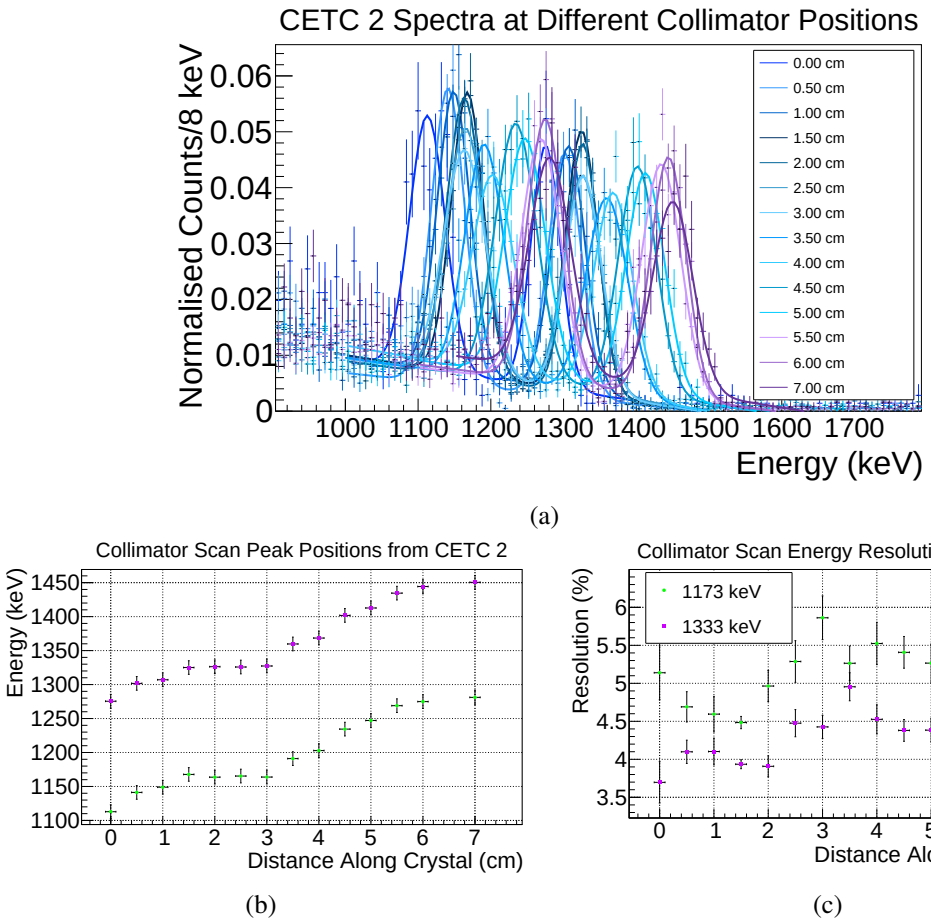

Fig. 7.11 Plots obtained from the collimator scans. 0.0 cm is the top of the crystal, and 7.5 cm is the side with the SiPM. (a) shows the spectra obtained at different collimator positions. Each spectrum has been fitted with a double Gaussian plus a quadratic background. (b) shows the determined peak positions of the ^{60}Co peaks varying with the collimator position. (c) shows the resolution FWHM of the ^{60}Co peaks varying with the collimator position.

In order to reduce effects due to drift over time, the detectors were calibrated before each measurement. For the calibration, the GAGG was illuminated along its length with ^{137}Cs, ^{60}Co, and ^{88}Y sources. Due to the non-Gaussian peak shape, the peak position was estimated by eye, and this value was used for determining the calibration function. Due to this, a 10 keV systematic uncertainty on the peak position is assumed.

Figure 7.11 shows the results from the collimator scan of CETC 2. As can be seen in Figure 7.11a, a large drift in the peak position is seen across the crystal. From Figure 7.11b, it can be seen that a drift equivalent to ≈200 keV is observed across the crystal, explaining the poor performance of the crystal when illuminated along the whole length of the crystal. The collimated energy resolution is

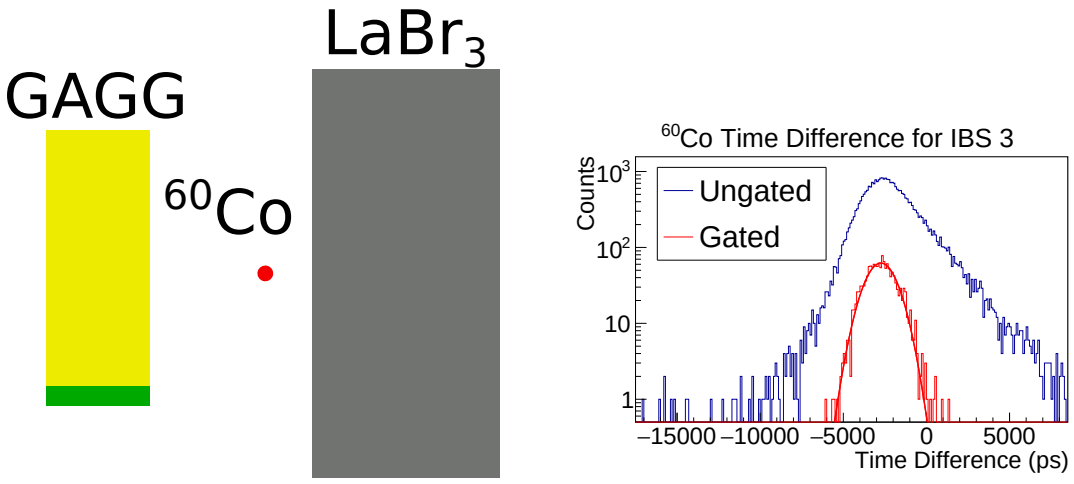

(a) (b)

Fig. 7.12 Diagram of time resolution measurement, and example time difference spectrum obtained from the measurement. (a) shows a schematic diagram of the setup used for measuring the time resolution of the GAGG detectors. (b) is the time difference between IBS 3 and the $LaBr_3$ reference detector. Ungated is for all events, and gated shows the histogram after the energy gates are applied.

comparable to the uncollimated energy resolutions of the other samples, further supporting that the variable response along the crystal length is responsible for the asymmetric peak shape. This would suggest that CETC may be capable of producing crystals that meet the specifications of the array if the uniformity can be improved.

7.2.3 Time Resolution

The time resolution is a critical parameter for reducing the background in experiments. Therefore, the timing performance was tested using the S13361-6050AE-04 [97] SiPM, and R11265U-20 [93] PMT. A time reference is required to test the time resolution. For this, the cascade decay of a ^{60}Co source was used, allowing for a prompt-coincidence measurement between the 1173 and 1333 keV gamma rays in two separate detectors.

For these tests, a large volume $LaBr_3$ detector with a PMT readout was used to provide a reference time. The GAGG and $LaBr_3$ were placed in line with the ^{60}Co source in the centre, illuminating the long sides of both detectors, as shown in Figure 7.12a. Data was collected for $\approx$3 hours to ensure sufficient statistics. The events were then correlated using the measured timestamps to build coincidence events. To reduce time-walk effects, the data were gated on the 1333 keV in the $LaBr_3$ and 1173 keV gamma-ray in the GAGG. A histogram of the time difference between the two detectors

gated on the energies was filled, and the histogram was then fitted with a Gaussian to obtain the coincidence time resolution (CTR) FWHM. An example time difference distribution and fit is shown in Figure 7.12b. The CTR reflects the convoluted timing response of both detectors.

Sample	SiPM/ps	PMT/ps
1	3620(50)	3470(70)
2	3020(150)	2450(30)
Epic 1	1600(30)	1271(14)
Epic 2	1672(24)	1496(8)
Kinheng 1	1631(17)	1328(37)
Kinheng 2	1689(28)	1556(47)
CETC 1	1831(43)	1490(50)
CETC 2	2300(50)	1648(70)
IBS 1	1840(30)	-
IBS 2	1800(14)	-
IBS 3	2220(30)	-
IBS 4	2240(20)	-
IBS 5	2140(10)	-

Table 7.2 Coincidence time resolution (FWHM) of different samples measured in coincidence with a large volume $LaBr_3$ detector.

The CTR FWHM for the crystals can be seen in Table 7.2. From the table, it can be seen that the Japanese samples (samples 1 and 2) have a very poor CTR, suggesting they would not meet the specifications for the array. The Epic 1 and 2 performed nicely, with a similar performance to the Kinheng samples. The CETC samples produced a slightly worse CTR in comparison to the other smaller Japanese samples. Whilst IBS 1-5 had a worse time resolution than the shorter Epic samples (Epic 1 and 2).

Further improvements in the CTR may be possible by using a faster reference detector and optimising the CFD parameters and detector bias. In addition, using a faster digitiser, illuminating the smaller face, and an improved readout circuit may produce an improved time resolution. This will be explored later in this chapter.

7.2.4 Crystal Summary and Conclusions

For the $25\times25\times75$ mm^3 samples, Epic and Kinheng provide an energy resolution equivalent to or better than the required energy resolution, alongside having the best measured CTR, suggesting Epic or Kinheng would be the best manufacturers for use in HYPATIA. However, for the $25\times25\times100$ mm^3

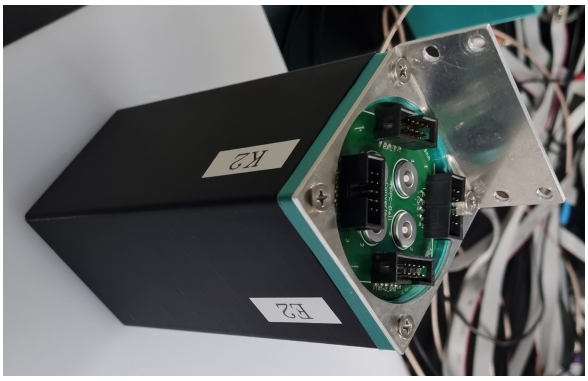

Fig. 7.13 GAGG encapsulated in the plastic housing with the feed-through PCB shown.

Epic crystals (IBS), there is some variance in performance and a small degradation in comparison to the smaller samples, but they still provide energy resolutions that meet the array's specifications. The Japanese samples (1 and 2) provide reasonable energy resolutions, but the time resolution is almost double that of the other samples, suggesting they are incompatible with the desired array performance. Finally, CETC 1 fails to reach the <6 % limit, and CETC 2 has a large inhomogeneity across the length of the crystal, suggesting that CETC-produced GAGG would need improved uniformity in order to be suitable for the array.

7.3 First Generation GAGG Clusters

To test the crystals in in-beam experiments, two quad clusters were constructed. A 3D printed polylactic acid housing was constructed to the same dimensions as a DALI2 detector [24]. The first cluster was made using the two C&A crystals and CETC crystals, all mounted with the S13361-6050AE-04 SiPMs [97], and the inverting operational amplifier readout board (Figure 7.5) with the gain set to 3. The second cluster was made using the Epic and Kinheng crystals using S13361-6050AE-04 [97] for all the crystals except Kinheng 2, which used the S13361-3050AE-08 [97]. The power was supplied using a 16-channel power supply designed and built in-house by P. Schury [169].

The clusters were constructed to have the same cross-section as a DALI2+ detector, 6.6×6.6 cm, so the module could be easily mounted into the DALI2+ frame. The internal cross-section was 5.4×5.4 cm, leaving 0.4 cm for the PTFE wrapping. The housing has a length of 16.6 cm with a front face thickness of 4.5 mm. A circular PCB was used as a feed-through to pass the bias voltages and signal into and out of the housing. A picture of one of the completed modules is shown in Figure 7.13.

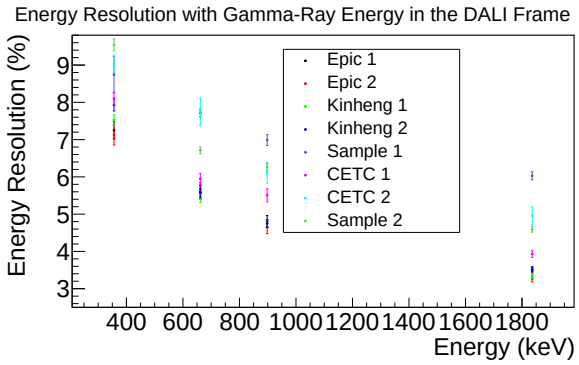

Fig. 7.14 Energy resolution of GAGG crystals mounted in the DALI2 frame using the DALI2 DAQ with calibration sources.

7.3.1 ^{100}Sn Experiment

The first test of these clusters was in the ^{100}Sn experiment, looking to measure the first 2^+ state of ^{100}Sn. The two clusters were mounted in the DALI2+ [24, 84] frame in layer 8, to test the performance of the GAGG clusters in realistic experimental conditions. The signals were processed using the same DAQ electronics as the DALI2+ detectors, see Section 7.1.1.

Several problems were identified from this experiment. The power supply was found to be unstable and caused unpredictable drifts in the peak position. Additionally, it was found that the power supply software would crash unpredictably.

From Figure 7.14, it can be seen that many crystals had an energy resolution worse than previously observed. This poor performance is likely a combination of many factors. The main factor is the shaping amplifier used for DALI2, the CAEN N568B module. This shaping amplifier is designed for use with preamplifier signals with a decay time of ≈ 50 μs, whereas the GAGG signals have a decay time of $O(1\ \mu\text{s})$. This leads to a large undershoot of the shaped output, likely leading to degraded performance.

Despite the many difficulties, many lessons were learnt from this experiment. Improvements were made to the power supply to improve stability. Additionally, it was decided that a digitiser DAQ system would be necessary for the HYPATIA array in order to have the optimal energy and timing properties.

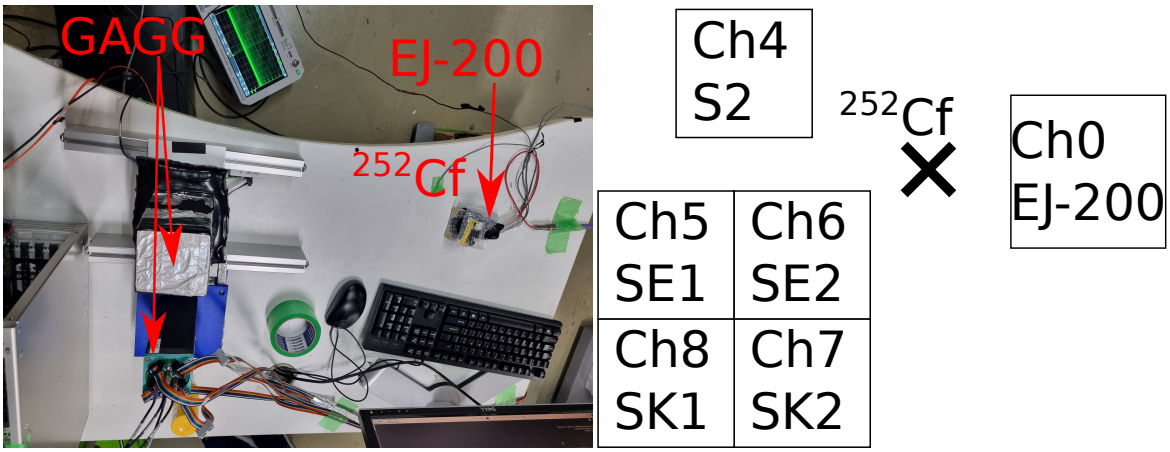

Fig. 7.15 Setup for neutron measurement experiment. One cluster from the in-beam experiment makes up the 2×2 cluster, and a single C&A [33] sample was tested. A EJ-200 [81] scintillator was used as the start time. Right shows the schematic with the detector location and the digitiser channel of the detector; the distances are not to scale. S2 refers to sample 2, SE*i* refers to sample Epic *i*, and SK*i* refers to sample Kinheng *i*. Left shows a picture of the setup. Sample 2 is located in its own housing, whilst the remaining GAGGs are in the 3D printed cluster.

7.3.2 Neutron Discrimination

Due to GAGG containing Gd, it has a large reaction cross-section for thermal neutron capture, such that it is used successfully as a thermal neutron detector [170]. At the RIBF, typical neutron energies range from 100-300 MeV, well above the thermal energy region. It is desirable to be able to detect the RIBF energy neutrons for HYPATIA for reducing the background produced by the neutrons, and possibly measuring the neutrons for particle spectroscopy. The response of HR-GAGG from C&A [33] to high-energy neutrons has been reported once before at UC-Davis Crocker Nuclear Laboratory [171]. Neutrons of energies between 1.9 MeV and 60.5 MeV were produced using the $^{7}\mathrm{Be}(\mathrm{p},\mathrm{n})^{7}\mathrm{Li}$ reaction. HR-GAGG was shown to be sensitive to neutrons at 60.5 MeV via pulse shape discrimination (PSD) techniques, but no PSD sensitivity was seen at 1.9 MeV [171].

It was necessary to test the different crystals for neutron discrimination properties. To do this, a ^{252}Cf source was used. ^{252}Cf undergoes spontaneous fission, emitting neutrons of mean kinetic energy of 2.105(14) MeV [172].

Figure 7.15 shows a picture of the setup used and a schematic diagram of the setup. The GAGG detectors were powered by P. Schury's power supply [169]. The Epic and Kinheng cluster from the ^{100}Sn experiment was used, and Sample 2 on its own. The signals were sent to a CAEN N6730 digitiser [173], and processed with the charge integration firmware, saving the waveform data of

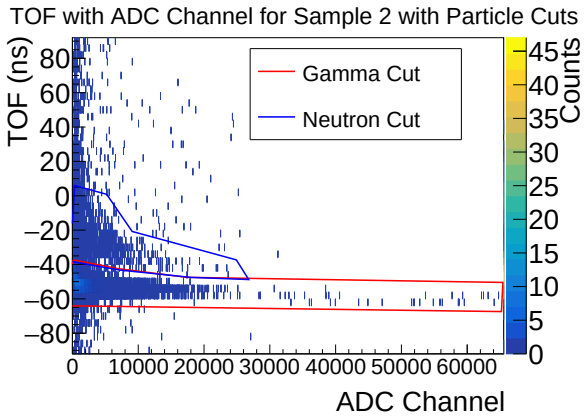

Fig. 7.16 Time difference between Sample 2 and the EJ-200 [81] start detector with the energy deposited in Sample 2. Two bands can be seen corresponding to the fast gamma rays and the slow neutrons. The gates used for gating on gamma-ray and neutron events are shown.

the detectors [104]. A start time was generated from a prompt gamma ray emitted after the fission, interacting in the EJ-200, and the TOF was measured by the GAGG detectors.

Since the neutrons travel slower than gamma rays, by taking the time difference between the EJ-200 and one of the GAGGs, the neutron events can be separated from the gamma-ray events. Figure 7.16 shows the correlation between the TOF and the energy measured with sample 2, where two gates are plotted for gamma rays and neutrons. As can be seen, neutrons at these energies were detected by the GAGG detectors and could be identified via TOF separation.

Additionally, the crystals were tested for PSD ability, using the pulses saved by the digitiser. The TOF gates were used to select data from gamma rays and neutrons. To analyse the pulse shape, firstly, the pulses were aligned by fitting the start of the pulse with

$$f(t) = \begin{cases} a_0 & t < t_0 \\ b_0 + b_1 t & t \geq t_0 \end{cases} \tag{7.3}$$

where $f(t)$ is the fit function of the start of the waveform, and a_0 and b_i are the fit parameters, and t_0 is the start time of the signal, which is set as

$$t_0 = \frac{a_0 - b_0}{b_1} \tag{7.4}$$

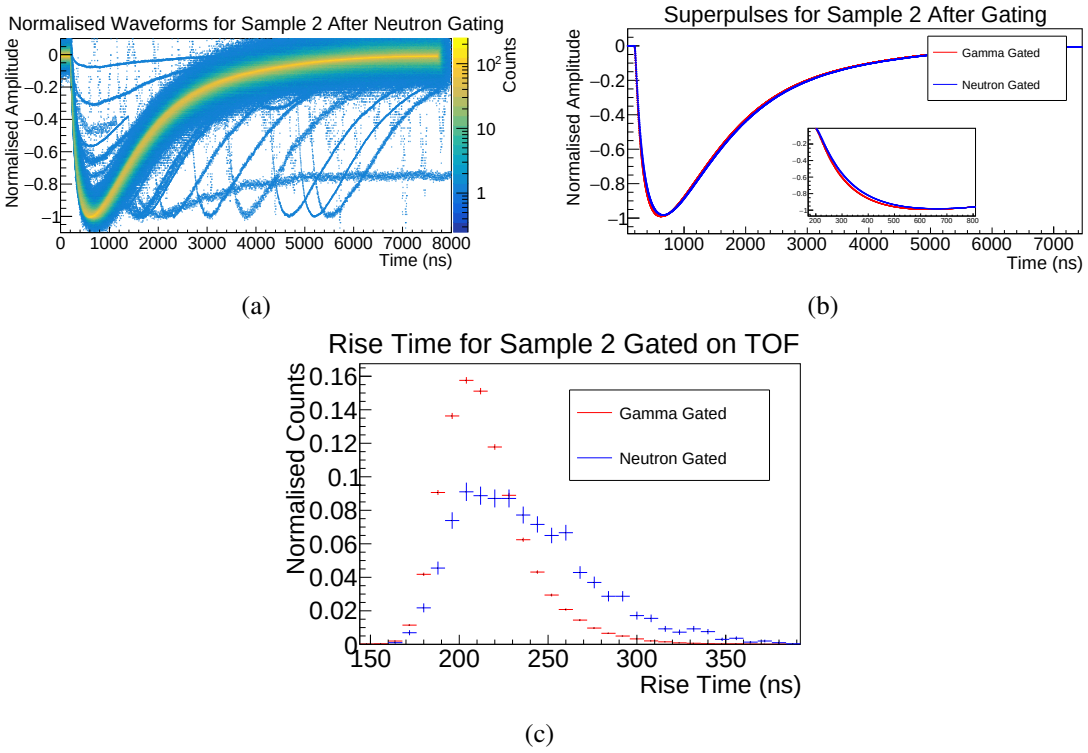

Fig. 7.17 Plots showing the waveform analysis for Sample 2 for neutron and gamma ray gates. (a) shows a histogram of normalised waveforms for sample 2 after gating on neutron events from the TOF. The histogram is filled with each sample from each waveform after normalisation and time alignment. (b) shows a graph of the average of the normalised waveforms gated on the TOF. The inset shows a zoomed-in view showing the point of difference in the two curves. (c) shows the normalised histograms of the 10 % to 90 % rise time for the neutron and gamma TOF gates.

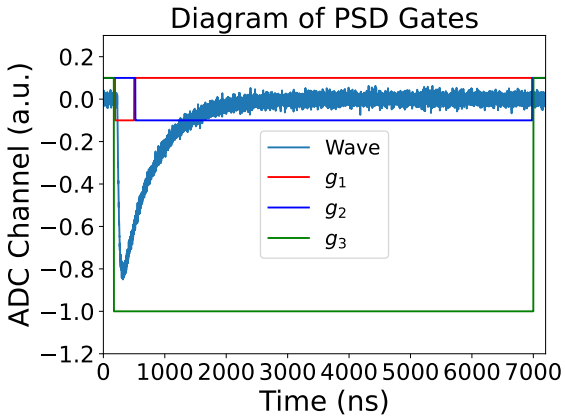

Fig. 7.18 Schematic diagram showing the PSD gates used for discriminating gamma rays and neutrons. g_1 integrates the start of the signal, g_2 integrates the tail of the signal, and g_3 integrates the full signal.

to keep the fit continuous. The signals are baseline corrected, normalised, and aligned so they all start at 200 ns using

$$g_{\text{norm}}(t - t_0 + 200\text{ ns}) = \frac{g(t) - a_0}{|g_{\text{min}} - a_0|} \tag{7.5}$$

where $g(t)$ is the waveform, $g_{\text{norm}}(t')$ is the normalised waveform, and g_{min} is the minimum ADC value of the waveform. To account for noise, a moving average window was used to smooth the waveform and g_{min} was taken as the minimum value of the smoothed waveform. The normalised waveforms were then filled into a 2D histogram; such a histogram can be seen in Figure 7.17a. The TProfile class from ROOT [140] was used to create an averaged waveform graph from the 2D histograms. The averaged waveforms for the gamma and neutron gates can be seen in Figure 7.17b. It appears that the neutron-gated waveform has a longer rise time than the gamma-gated waveform. This is supported by the 10 % to 90 % rise times shown in Figure 7.17c, where the neutrons have a tail into the longer rise time region.

To test the sensitivity, a simple PSD method was used. Three gates were integrated on the signal

$$g_1 = \sum_{t=190\ ns}^{t'} g(t) \tag{7.6}$$

$$g_2 = \sum_{t=t'}^{7000\ ns} g(t) \tag{7.7}$$

$$g_3 = \sum_{t=190\ ns}^{7000\ ns} g(t) \tag{7.8}$$

where t' is a selected gate length, and g_i are the integrated values from the gates. A schematic diagram of this is shown in Figure 7.18. t' values from 300-1200 ns were tested. The g_i values for neutrons and gamma events were filled into two separate histograms, and then the histograms were normalised using their integrals.

The typical test value for neutron discrimination from the PSD is the figure of merit, FOM, defined as

$$\text{FOM} = \frac{\mu_\gamma - \mu_\text{n}}{\text{FWHM}_\gamma + \text{FWHM}_\text{n}} \tag{7.9}$$

where μ_x is the peak of particle x; and FWHM_x is the FWHM of the peak of particle x [174]. To have a good separation between neutrons and gammas, an FOM ≥ 1.27 is required [175]. Due to the asymmetry of the peaks, they were fitted using the function

$$f(x) = \begin{cases} p_0 \exp\left(-\frac{(x-\mu)^2}{2\sigma_1^2}\right) & x < \mu \\ p_0 \exp\left(-\frac{(x-\mu)^2}{2\sigma_2^2}\right) & x \geq \mu \end{cases} \tag{7.10}$$

where p_0 is the amplitude of the function, μ is the peak position, and $\sigma_{1,2}$ are the σ values on the low PSD and high PSD sides, respectively. The FWHM was calculated according to $\text{FWHM} = 2.355(\sigma_1 + \sigma_2)/2$.

Figure 7.19a shows the $\text{PSD} = g_1/g_3$ distributions for neutron and gamma events for different gate lengths. Some difference is observed for the shorter gates; for the longer gates, the difference gets smaller. The neutron peak appears at a lower PSD than the gamma PSD peak, suggesting the rise time of the gamma events is faster than the neutron events, consistent with Figure 7.17b. Figure 7.19b shows the FOMs obtained from the fits to the distributions; a small FOM is observed for Sample 2, but it is well below the required value of 1.27. The FOMs obtained for the other samples are consistent with zero. Figure 7.19c shows the FOM obtained by using $\text{PSD} = g_2/g_3$. None of the detectors had any noticeable pulse shape difference in the tail of the signal.

From this, it can be concluded that for neutron energies of ^{252}Cf, neutrons can be detected by GAGG. PSD methods show a small difference between the neutron and gamma response in sample 2, but the FOM is too small for the two peaks to be resolved from each other. No sensitivity is observed in the other samples, suggesting differences in the Ga:Al ratio [38, 85] may be responsible for the pulse shape sensitivity to neutrons. Sensitivity is not observed when gating on the tail of the signal. Not being able to resolve neutrons from gamma rays in this energy region is consistent with previous

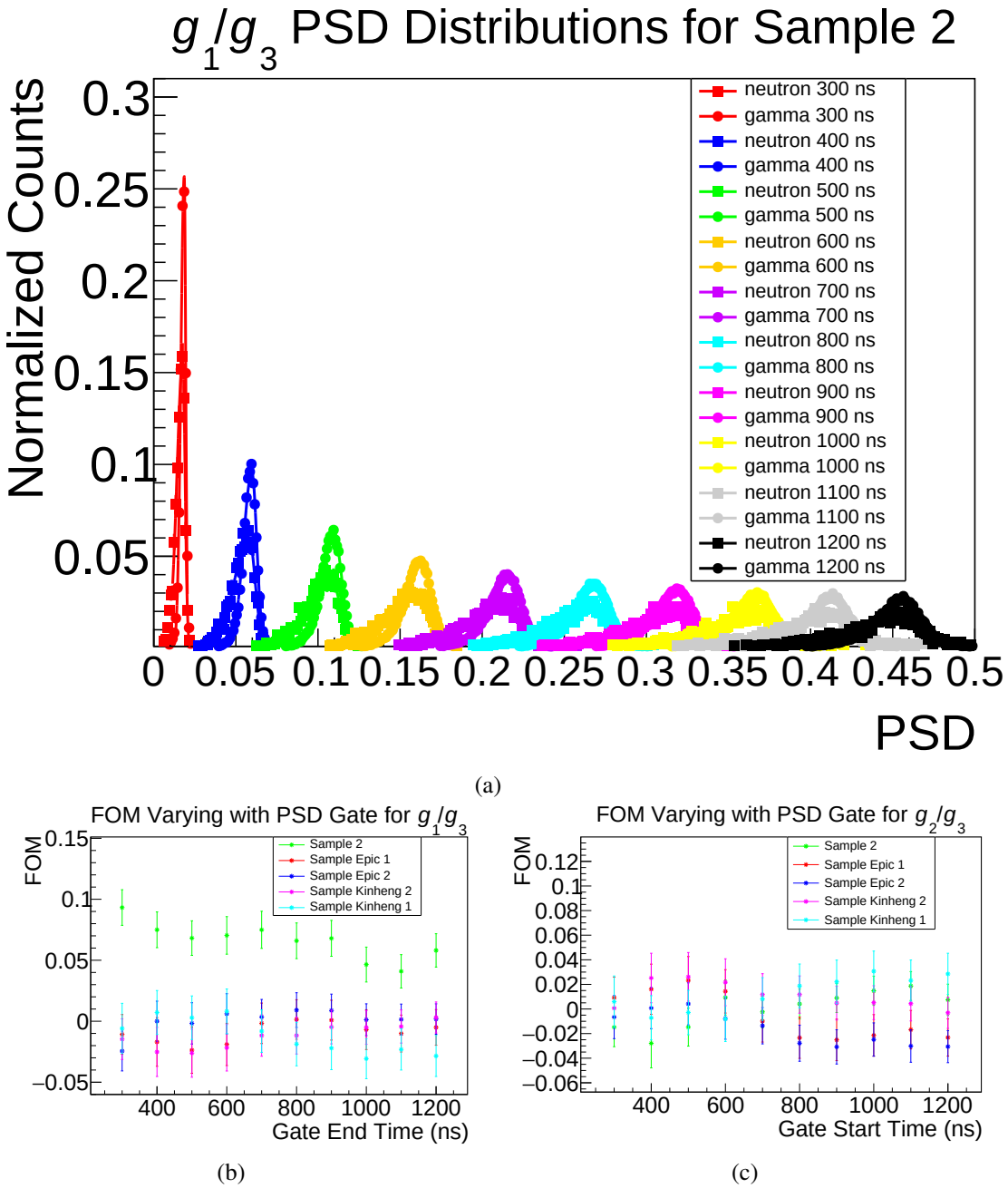

Fig. 7.19 PSD discrimination plots and the corresponding FOM values. (a) shows the PSD peaks for neutron and gamma events for different short gate end points. Using PSD $= g_1/g_3$. The fits used to obtain the FOM values are also shown. (b) shows the FOM values obtained for the PSD $= g_1/g_3$ for different gate lengths. (c) shows the FOM values obtained for the PSD $= g_2/g_3$ for different gate lengths.

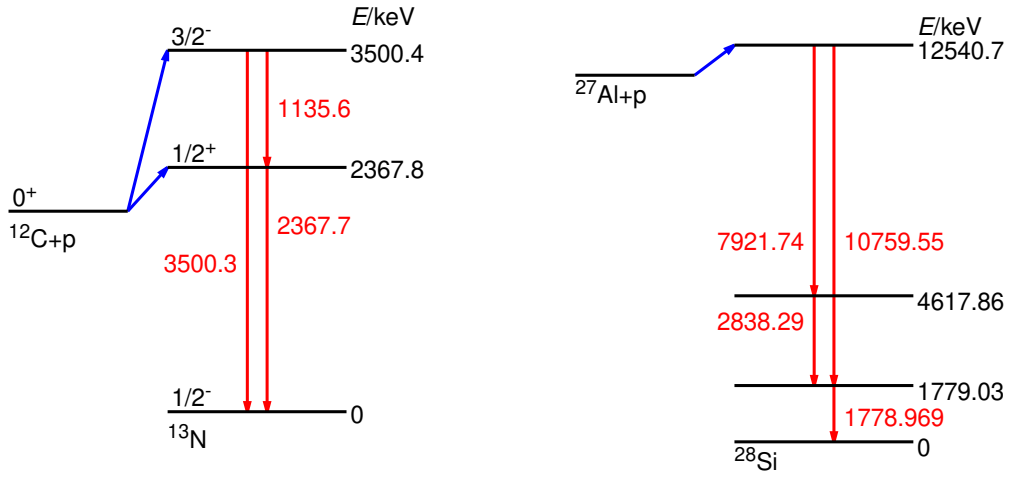

Fig. 7.20 (a) shows the level scheme for the 0.6, and 1.7 MeV resonances in the $^{12}C(p,\gamma)^{13}N$ reaction. Data taken from [60]. (b) shows the level scheme for the 0.992 MeV resonance in the $^{27}Al(p,\gamma)^{28}Si$ reaction. The level scheme has been simplified to only show the decay paths relevant to this analysis. The energies are shown in units of keV. Data taken from [178].

measurements [171]. Neutron PSD sensitivity was observed in GAGG at higher neutron energies [171]. This needs to be tested in the future, possibly using spallation sources [176]. The ability to discriminate the neutrons via TOF will be useful in experiments to reduce the background. Further experiments will be necessary to understand the effect of the chemical structure and neutron energy on the pulse shape response of GAGG to neutrons.

7.3.3 10 MeV Gamma-ray Response

Due to SiPMs' non-linear response, it is necessary to test their performance in detecting high-energy gamma rays. In order to measure 5 MeV rest frame energy gamma rays, it is necessary to have a dynamic range at least up to 10 MeV. Typical lab sources do not reach high enough energies to test in this region, and more exotic sources, such as AmBe, only reach 4.5 MeV [177].

To evaluate the detectors' performance at high energies, (p,γ) reactions were employed. Two resonances in $^{12}C+p$ were populated: one at ≈ 1.7 MeV and the second at ≈ 0.6 MeV [179], producing 2.37, and 3.5 MeV gamma rays; the level scheme is shown in Figure 7.20a. Secondly, the 992 keV resonance in $^{27}Al(p,\gamma)^{28}Si$ was used to produce a 10.8 MeV gamma ray [178]. Figure 7.20b shows the level scheme for this reaction.

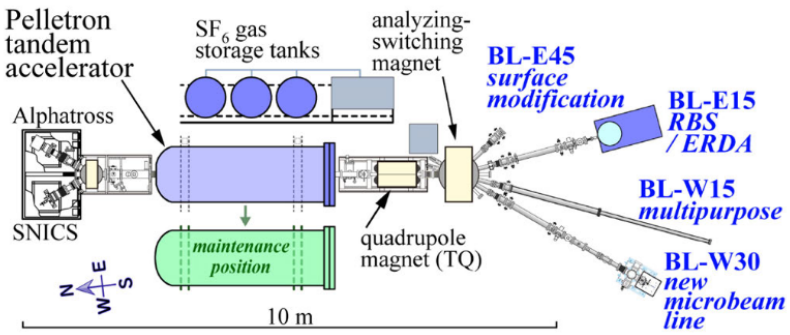

Fig. 7.21 Schematic diagram of the RIKEN Pelletron accelerator facility. The H^- ions are produced in the SNICS (Source of Negative Ions by Caesium Sputtering) [180] ion-source, which are then accelerated by the tandem accelerator, leaving the ions as H^+, which are then directed to the desired beam line using the switching magnet. Reproduced from [181].

A proton beam was provided by the RIKEN Pelletron facility, the schematic of which is presented in Figure 7.21. The process begins with a Caesium sputtering ion-source [180] generating H^- ions. The H^- ions are subsequently accelerated using a tandem accelerator [182], then a charge stripper removes electrons, producing H^+, which are then accelerated further. The charge state conversion allows for the ion to be accelerated twice by the same terminal. The H^+ ions are then bent using a dipole switching magnet onto the desired beam line [181]. For this experiment, the BL-W15 beam line was used. The beam position was determined using a fluorescent screen before the target chamber, and the current supplied to the switching magnet was adjusted to centre the beam on the target.

Experimental Setup

The two clusters used in the first in-beam experiment were placed on either side of the beam line. A picture of the setup can be seen in Figure 7.22a. The GAGG clusters were centred on the target position and surrounded with DALI2 NaI(Tl) detectors for Compton suppression. A mapping of the detectors can be seen in Figure 7.22b.

The GAGG detectors were biased using P. Schury's power supply. Whilst the NaI detectors were biased using a CAEN power supply [136]. Several different SiPM voltage sets were tested, summarised in Table 7.3. The signals were processed using a CAEN V2745B digitiser [157] using the PSD firmware using an LED [104].

Table 7.4 shows the runs of the experiment. The proton beam was 1.7 MeV. A thick carbon target was used to fully stop the beam. Due to energy loss inside the target runs, both 1.7 MeV and 0.6 MeV

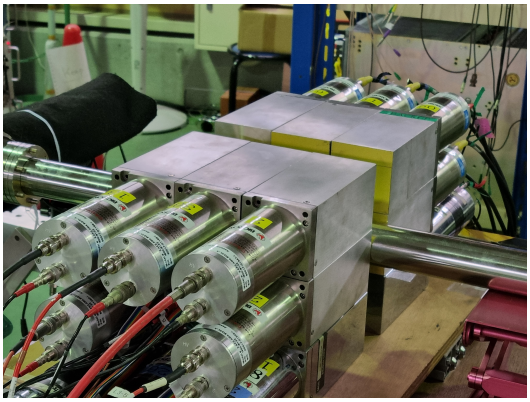

(a)

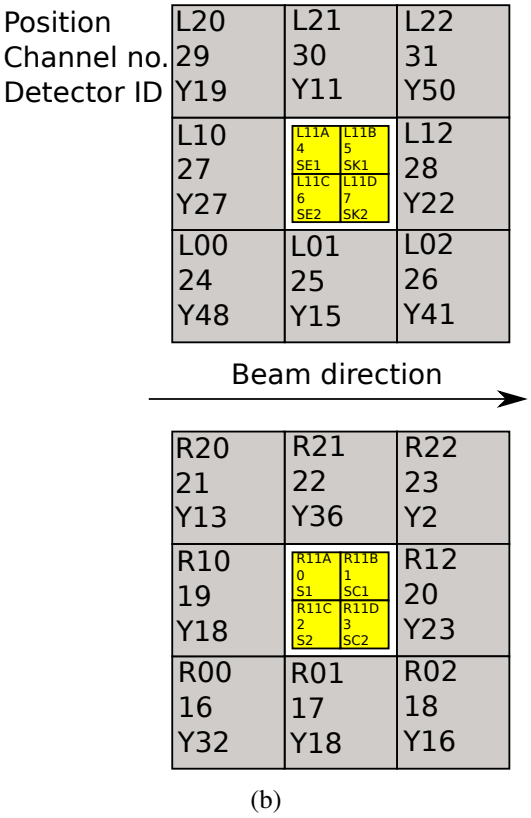

(b)

Fig. 7.22 Setup for the experiment. (a) shows a picture of the detectors surrounding the beam pipe. Beam direction is left to right. (b) shows the setup diagram. The grey detectors are the DALI2 detectors, and the GAGG detectors are shown in yellow. Left and right are defined with respect to the beam direction.

Sample Name	DAQ Channel	Bias Channel	Bias Voltage/V					
			V_0	V_1	V_2	V_3	V_4	V_5
Sample 1	0	0	56.5	57	56.5	57.5	58.5	55.5
CETC 1	1	1	55.3	57	55.3	56.3	57.3	54.3
Sample 2	2	2	56.5	57	56.5	57.5	58.5	55.5
CETC 2	3	3	56.3	57	56.3	57.3	58.3	55.3
Epic 1	4	4	56.5	57	56.5	57.5	58.5	55.5
Kinheng 1	5	5	56.5	57	56.5	57.5	58.5	55.5
Epic 2	6	6	56.3	57	56.3	57.3	58.3	55.3
Kinheng 2	7	7	55	57	57	58	59	56

Table 7.3 Different bias voltages used to power the SiPMs for the different GAGG samples. V_i are the labels for the different voltage conditions used in the experiment.

Run Name	V/kV	E_p/keV	T	Description
run_Cs_210824_1	-	-	-	Cs Calibration V_2
run_Y_210824_1	-	-	-	Y Calibration V_2
run_Co_210824_1	-	-	-	Co Calibration V_2
run_bkg_210824_1	-	-	-	background run V_2
run_Y_220824_1	-	-	-	Y calibration V_2
run_Cs_220824_1	-	-	-	Cs calibration V_2
run_C_beam_220824_1-4	864	1690	C	Carbon run V_2
run_C_beam_220824_5-6	864	1690	C	Carbon run V_3
run_C_beam_220824_7	864	1690	C	Carbon run V_4
run_C_beam_220824_8	864	1690	C	Carbon run V_5
run_Al_2_beam_220824_1-9	544	1050	Al	Al run V_2
run_Y_220824_2	-	-	-	Y calibration V_2
run_Cs_220824_3	-	-	-	Cs calibration V_2
run_Co_220824_2	-	-	-	Co calibration V_2
run_bkg_220824_1	-	-	-	Background run V_2

Table 7.4 List of experimental runs and a description of the conditions used. V shows the voltage of the tandem terminal, E_p shows the estimated proton energy, and T shows the target used. See Table 7.3 for the bias voltage information.

resonances were populated. For the carbon target, the SiPM bias voltage was varied to observe the effect of bias voltage on the non-linearity. Finally, a thick Al target was used to produce the 10.8 MeV gamma ray via the 992 keV resonance. Only one SiPM bias voltage (V_2) was used, as increasing the bias would have saturated the digitiser's dynamic range.

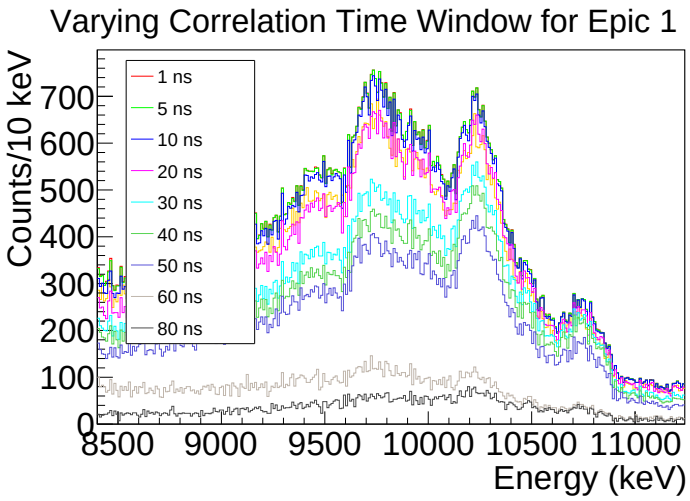

Fig. 7.23 Varying the time window to find the optimal gate length. Al spectrum for Epic 1, varying the event building time window, with Compton suppression. The 10.8 MeV peak and its two escape peaks are visible.

Analysis

The DAQ saved the data as single-channel events. The first step was to correlate the data into multi-channel events. This was done by timestamp merging. The analysis started with the channel with the lowest timestamp t_0; if any of the channels fell into the window $t_0 + \Delta t$, then the channels were correlated, where Δt is the time window. To determine the optimal time window length, the time window in the Al runs was varied to see which gave the optimal Compton suppression properties. The Compton suppression was performed by rejecting events if any other detector was triggered within the time window.

Figure 7.23 shows the spectrum for Epic 1 varying with the time window. As can be seen, time windows ≤ 20 ns produce little reduction in the background, the time windows 30 ns and 40 ns produce a reduction in the background without reducing the peak height. Time windows greater than ≥ 50 ns reduce the background, but also reduce the peak height. It was decided that a time window of 30 ns would be used.

For the Al data, the GAGG detectors were calibrated with the equation

$$\mathrm{ADC}(E) = p_0 + p_1 \exp(p_2 E) \tag{7.11}$$

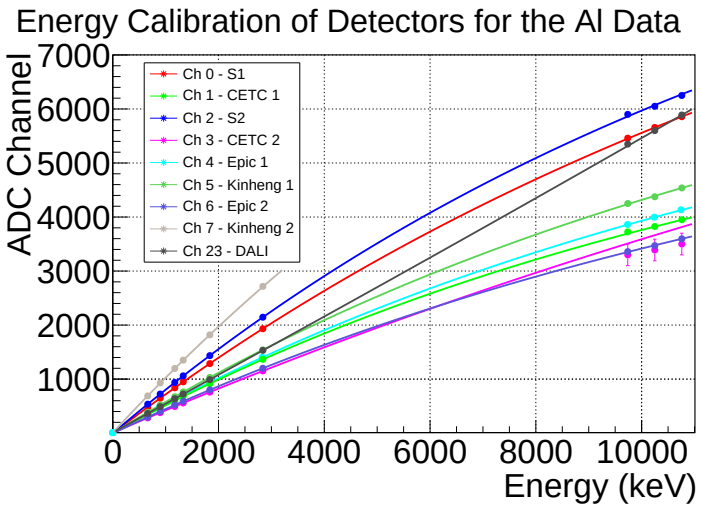

Fig. 7.24 Calibration of Al target runs using ^{88}Y, ^{137}Cs, ^{60}Co, and ^{28}Si lines. Including single and double escape peaks for the 10.8 MeV gamma ray.

where ADC(E) is the ADC channel value of the full-energy peak, E is the gamma-ray energy, and p_i are the calibration parameters obtained from the fit. This equation was chosen to reflect the expected saturation curve of the SiPM [98]. The ADC channel values were determined using a Gaussian plus quadratic fit, and taking the μ parameter of the Gaussian. For the calibration the ^{137}Cs, ^{60}Co, ^{88}Y sources were used alongside the 2.8 MeV and 10.8 MeV plus its escape peaks from the Al data. The same procedure was followed for the NaI detectors using a quadratic calibration function. The carbon target was treated differently and will be discussed later.

Figure 7.24 shows the calibration of the detectors. For channel 7, the detector saturated before 10 MeV; as such, it was only calibrated up to 2.8 MeV. The calibrated spectra were then fitted using a Gaussian plus quadratic background to obtain the energy resolution of the full-energy peaks.

For the carbon measurements, the DALI detectors were calibrated using the ^{137}Cs, ^{88}Y, and ^{60}Co runs before the experiment and the 2.4 and 3.5 MeV gamma rays from the carbon target. The peaks were fitted using the same method as used for the Al data. A quadratic calibration function was used to calibrate the NaI detectors, as shown in Figure 7.25a.

Due to the voltage changes during the carbon runs, the GAGG detectors were calibrated using the in-beam data only. Figure 7.25b shows the calibrated spectrum from the carbon target run with a DALI detector. In the spectrum, the peaks from ^{13}N, 2.4, and 3.5 MeV are observed. Additionally, two gamma rays are seen at 437(1) keV, and 1629(3) keV, likely from proton reactions on surrounding material. Using the gamma rays from the carbon data, the GAGG detectors could be calibrated at

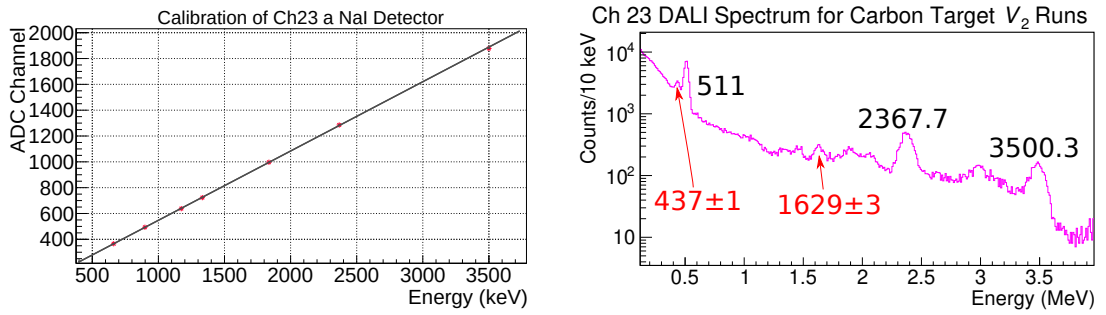

(a) (b)

Fig. 7.25 Plots showing the calibration of DALI detectors. (a) shows the carbon calibration for Ch23, a NaI detector, using the calibration sources and in-beam data. (b) shows the calibrated spectrum from Ch23, a DALI2 detector, for the carbon runs. Can see a 511 keV from pair production, and the 2.4, and 3.5 MeV gamma rays from ^{13}N [60]. In addition, two unknown gamma rays are seen at 437 keV and 1629 keV.

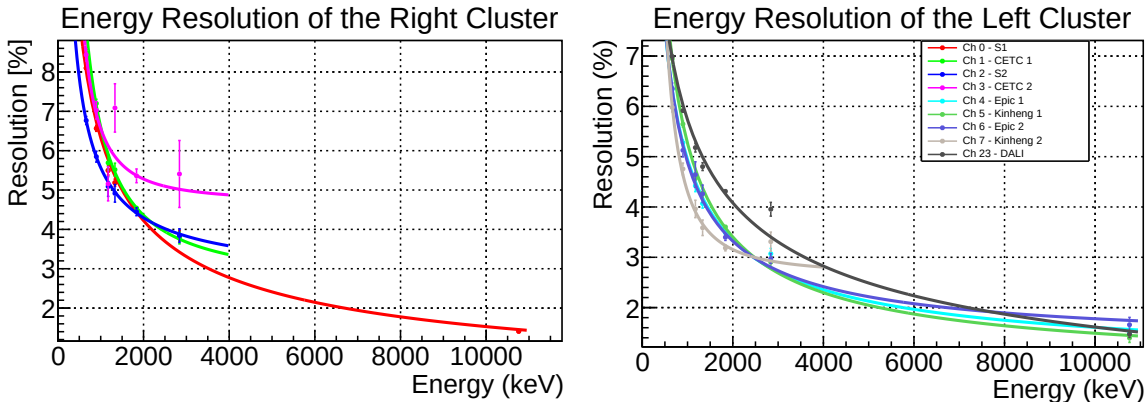

Fig. 7.26 Determined energy resolutions for the different samples using the bias voltage V_2. With the data from the Aluminium target runs and calibration runs after the beam time. The trends are fitted with the $p_0 + p_1 E^{p_2}$ function.

different voltages using a quadratic function. This allows for the extraction of the estimated saturation voltage using the maximum value of the quadratic calibrations according to $\frac{-p_1}{2p_2}$.

Results

Figure 7.26 shows the energy resolutions determined for the full-energy peaks in the Al target run and the calibration runs during the beam time. First, the detectors achieved worse energy resolutions for this experiment than in the lab tests. This can be seen in Kinheng 1, which goes from 5.14(4) % at 57 V with Baba-san's power supply to 6.95(5) % at 56.5 V with P. Schury's power supply [169]. This degradation is likely due to the identified issues with P. Schury's power supply, the lower bias

Sample	Energy Resolution/%
Sample 1	1.4(1)
Epic 1	1.5(1)
Kinheng 1	1.4(1)
Epic 2	1.7(2)
NaI ch23	1.5(1)

Table 7.5 Energy resolution of the 10.8 MeV full-energy peak for the Al runs. Only detectors that resolved the 10.8 MeV peak are included.

voltage, and noise from the accelerator electronics. Some points are missing for different detectors. For CETC 1, 2, and Sample 2, the 10.8 MeV peak was not resolved from the escape peak. Whereas for Kinheng 2, this was due to the detector saturating the DAQ before the 10.8 MeV peak. CETC 2 exhibits strange behaviour due to the inhomogeneity along the length of the crystal, as discussed previously. The DALI detector connected to channel 23 was selected as a reference due to its superior energy resolution. It should be noted that this detector has an exceptionally good energy resolution and is not representative of the average DALI detector performance.

Table 7.5 shows the energy resolution of the 10.8 MeV peak. As can be seen, the GAGG achieves a similar resolution at 10.8 MeV to the DALI detector. This is likely due to several issues, namely the non-linearity of the SiPM, and the worse energy resolution due to the power supply and the noisy environment. However, this is consistent with the value used in the simulations of 1.4 %. Despite this, it has been confirmed that measuring 10 MeV gamma rays is possible with GAGG scintillators coupled with SiPM readout, and that the full-energy peak can be separated from its escape peaks. Additionally, several possibilities exist for improving upon the measured energy resolution.

Figure 7.27 shows the quadratic saturation coefficient varying with the voltage over breakdown. The main sources of uncertainty of the over-voltage come from the variation in breakdown voltage between the different pixels of the different SiPMs. 3 V over-voltage is recommended by Hamamatsu [96, 97]; however, this voltage leads to a poor energy resolution, so higher over-voltages were used. From Figure 7.27, a clear dependence on the non-linearity of the detector is observed with increasing bias. It can be seen that the calibration saturates at less than 10 MeV above 6 V overvoltage.

The experiment successfully confirmed that GAGG scintillators coupled to SiPM photosensors can measure 10 MeV gamma rays corresponding to the desired range of 5 MeV for a 5 MeV gamma ray emitted from a nucleus with $\beta = 0.6$. In addition, the intrinsic resolution is good enough such that the Doppler-corrected energy resolution at 5 MeV will be dominated by the velocity and angular

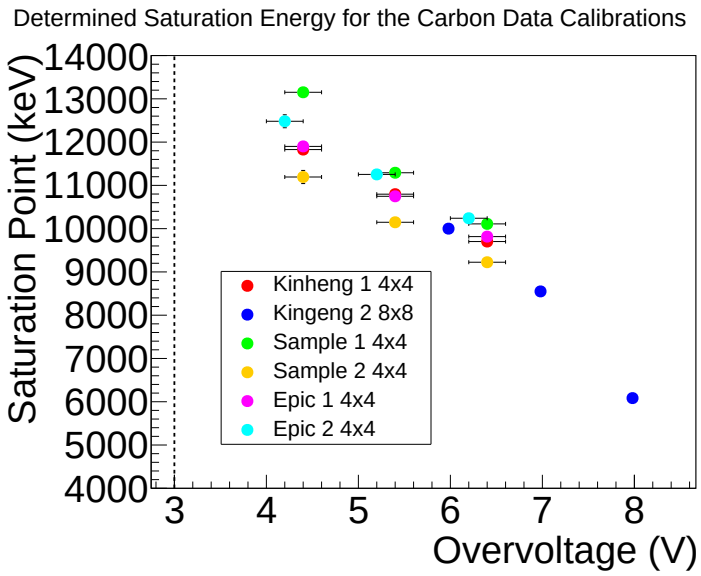

Fig. 7.27 Saturation energy of the quadratic calibration varying with overvoltage from the carbon target data. CETC 1 and 2 are not included due to poor performance. The samples are labelled with the type of SiPM used 4×4 indicates the S13361-6050AE-04 [97], and 8×8 indicates the S13361-3050AE-08 [96]. A dashed line indicates the +3 V recommended by Hamamatsu [96, 97].

uncertainties. Finally, the non-linearity strongly depends on the voltage over breakdown, suggesting that up to a 6 V overvoltage will be appropriate for in-beam conditions at $\beta \approx 0.6$.

7.4 Second Generation GAGG Clusters

All previous measurements were done with S13 generation Hamamatsu SiPMs [96, 97]. However, Hamamatsu has a newer generation of S14 SiPMs [92]. Figure 7.28 shows the quantum efficiency of the S14 SiPM compared to the S13 SiPM overlaid with the GAGG emission spectrum. An improvement in quantum efficiency is present between the two models. An improvement in energy resolution was expected from the S14 compared to the S13. Therefore, it was decided to develop new PCBs to test the suitability of the 4×4 S14161-6050HS-04 SiPM for use in the HYPATIA array [92].

The S14161-6050HS-04 has no connector mounted, so a PCB was designed to connect the copper pads for the cathodes and anodes of SiPM pixels and take them to a usable connector. Additionally, a TMP36 temperature sensor [183] was placed on the board alongside a 10 nF buffer capacitor. A rendering of the design can be seen in Figure 7.29. The boards were printed by an outside company and assembled internally using reflow soldering. The soldered board can be seen in Figure 7.29b.

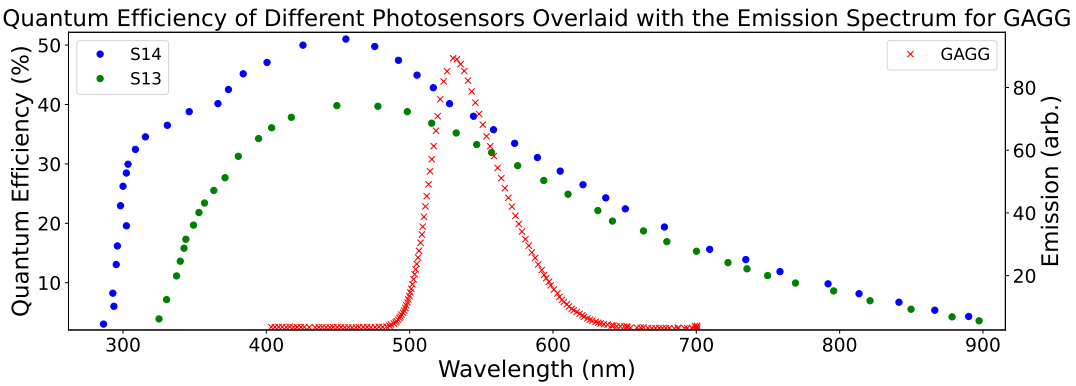

Fig. 7.28 Comparison of S133161-6050, and S144161-6050 SiPM quantum efficiencies data taken from [97, 92]. The GAGG emission spectrum, taken from [38], is overlaid on top. As can be seen, a small improvement in quantum efficiency is observed.

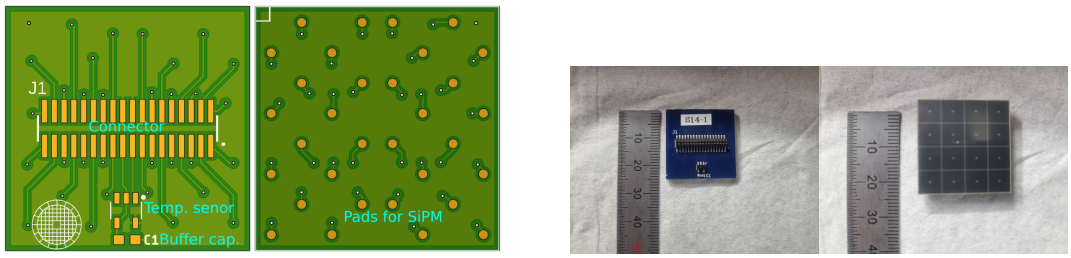

(a) (b)

Fig. 7.29 S14161-6050HS-04 SiPM PCB. (a) shows a rendering of the SiPM PCB for S14161-6050HS-04 with labels of the elements of the PCB. (b) shows the SiPM soldered on the board alongside the other components.

Fig. 7.30 Circuit diagram of simple readout board alongside pictures of the assembled PCB for the circuit shown in Figure 7.5.

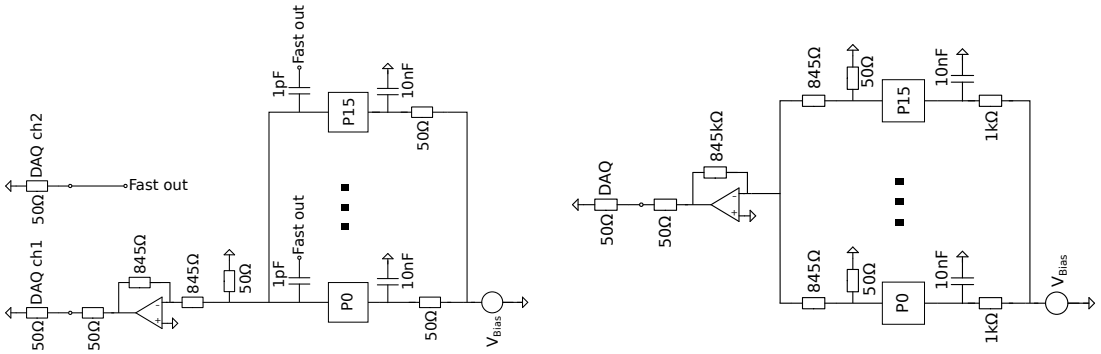

(a) (b)

Fig. 7.31 Circuit diagrams used to test different possible circuit diagrams, looking to reduce the effect of the larger capacitance of the S14 SiPMs. (a) shows the circuit with the capacitively coupled fast output, and (b) shows the sum-amplifier circuit.

To read out the board, two different readout boards were made. The first design mirrored the readout board used for the S13 SiPMs. The circuit diagram is the same as Figure 7.5, and the assembled PCB can be seen in Figure 7.30. A lower gain was necessary to avoid the previous issues with saturating the DAQ; therefore, the resistors were tuned to produce a gain of 1 [167].

One downside of the S14161-6050HS-04 is the higher capacitance in comparison to the S13361-6050AE-04, with the S14 having a capacitance of 2 nF whilst the S13 has a capacitance of 1.3 nF [97, 92]. This extra capacitance increases the decay and rise times of the signals, leading to worse time resolutions.

To identify potential areas for optimisation, various readout configurations were modelled using LTspice [184]. The SiPM pixel simulation was based on the equivalent circuit described in [185]. The values used in the simulation were rough approximations. Therefore, the simulations only provide qualitative comparisons between the different readout schemes. The response was evaluated by simulating a single microcell breakdown using a pulsed current source.

Three different circuits were simulated; the first was the simple readout shown in Figure 7.5 as a reference case, which was simulated with both 16 pixels and one pixel. The second is shown in Figure 7.31a, which uses a second capacitively coupled output to provide a fast signal for timing purposes, and the standard slow signal for energy determination. The third is shown in Figure 7.31b, which uses a sum-amplifier configuration allowing for each pixel to be grounded independently, reducing the effective capacitance.

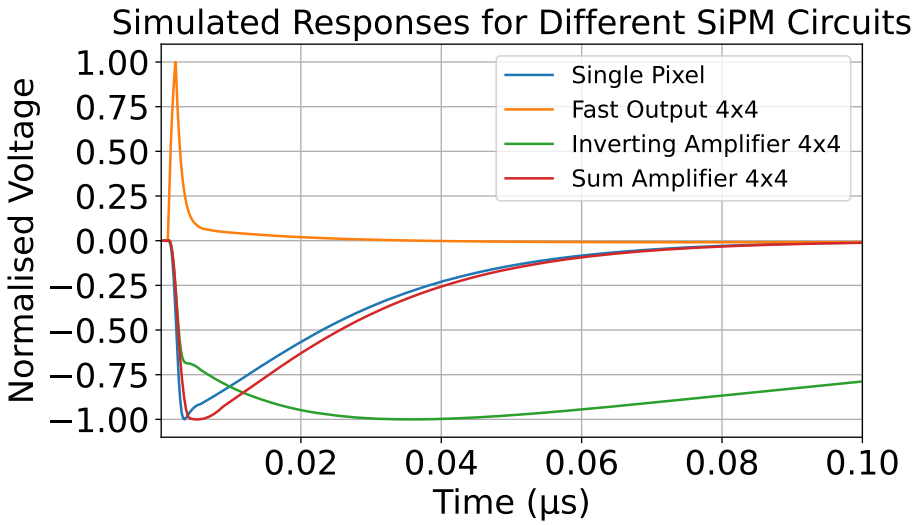

Fig. 7.32 Simulated response of the different readout circuits. Single pixel shows the response of a single pixel passed through an inverting operational amplifier. Fast output 4×4 shows the response of the circuit shown in Figure 7.31a. Inverting amplifier shows the response of 16 pixels connected in parallel with an inverting operational amplifier. Sum amplifier 4×4 shows the response of the circuit shown in Figure 7.31b. The responses have been baseline corrected and normalised to make the comparison easier.

Figure 7.32 shows a comparison of the simulated response for different readout circuits. The single pixel shows the response with one pixel, and the inverting amplifier 4×4 shows the response with 16 pixels connected in parallel to an inverting amplifier, as can be seen, the additional capacitance leads to significantly longer signals. Using the fast output configuration, a fast signal can be recovered for timing. The sum-amplifier configuration with 16 pixels almost recovers the response of a single pixel, due to the grounding resistors for the individual pixels.

It was decided that the sum-amplifier configuration would be pursued. The main reason is that using the fast-output configuration would require two DAQ channels per SiPM, which would increase the cost of the HYPATIA DAQ. In addition, having two signals per channel would introduce additional complexity, requiring a specialised algorithm to combine the fast and slow outputs into an energy and time measurement.

Figures 7.33a, and 7.33b show the constructed PCB for the sum-amplifier configuration. In order to fit the extra resistors into the 25×25 mm^2 board, smaller surface-mount connectors were used. In addition, a potentiometer between the positive input of the operational amplifier and ground was added to perform baseline offset corrections. The initial design used the component values shown in

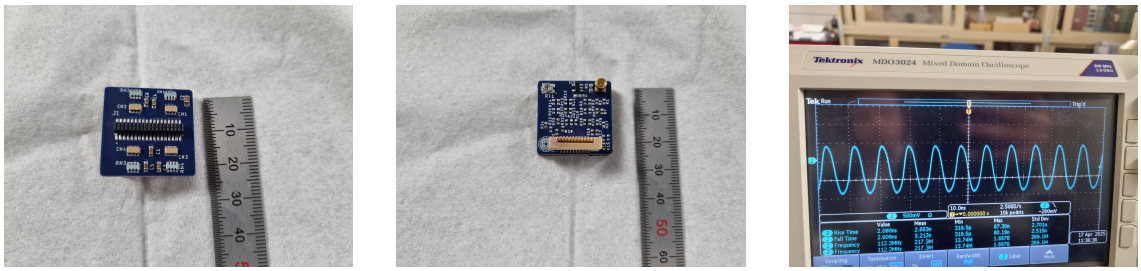

(a) (b) (c)

Fig. 7.33 Constructed readout board PCB with the sum-amplifier configuration. (a) shows the bottom of the PCB, and (b) shows the top of the PCB. (c) shows the oscilloscope output of the initial values, showing the oscillations.

Figure 7.31b, this led to oscillations on the output shown in Figure 7.33c. To remedy this, several different resistor values were tested, finally deciding on the feedback resistor being 1 kΩ, and the drop-down resistor being 20 Ω. These values were chosen as they produced a fast signal and would allow for the measurement of 10 MeV gamma rays, estimated from the amplitude of the ^{60}Co lines.

7.4.1 Board Comparison

In order to determine if the board was suitable for the HYPATIA array, its performance needed to be tested in comparison to other methods. For this, CETC 1 was used, mounting the photosensors to side 1, illuminating the crystals from the top. Two different readout boards, the simple sum of the pixels and the sum-amplifier configuration, were coupled to S14 SiPMs. The S14 SiPMs were biased to 42 V, and 6.0 μs and 1.0 μs integration gates were used for the simple readout and the sum-amplifier readout, respectively. In addition, the CTR was measured using the same method as in Section 7.2. Except that the small face was illuminated instead of the full length of the crystal.

Figure 7.34 shows the results of the energy resolution analysis. As can be seen, the S14 appears to provide an improvement in the energy resolution in comparison to the S13, which is attributed to the higher quantum efficiency. The simple readout board achieves the same or similar energy resolution compared to the sum-amplifier readout board. No significant improvement in energy resolution is achieved from the faster signal.

Table 7.6 shows the time resolutions obtained using the method from Section 7.2. As can be seen, the time resolution is improved by using the sum-amplifier readout board in comparison to the simple readout board. However, the measurement is limited by the large time resolution of the reference detector.

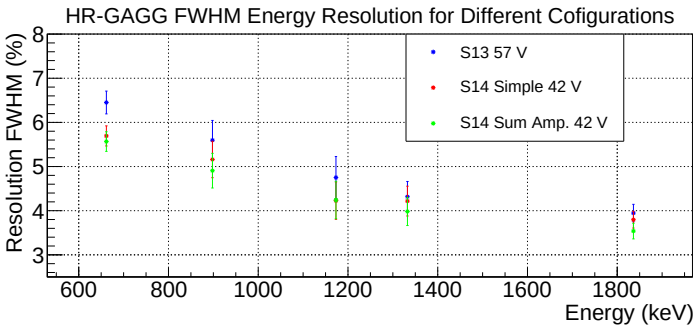

Fig. 7.34 CETC 1 for top illumination energy resolution for different photosensor readouts. The S13 data is repeated from Section 7.2, in comparison to the S14 with simple readout and sum-amplifier readout. The errors are determined using the method from Section 7.2.

Configuration	CTR/ps
S14 Simple Readout	1640(20)
S14 Sum Amp.	1480(10)

Table 7.6 Coincidence time resolutions for CETC 1 taken with ^{60}Co source in coincidence with a large volume $LaBr_3$.

7.4.2 Time Resolution Measurement

Due to the limitations in the previous time resolution measurements, it was decided to benchmark the board performance using a fast reference detector. A cylindrical $LaBr_3$ of dimensions $25\times25\times25$ mm^3 was mounted with an S14 SiPM [92] with the sum-amplifier board attached. The $LaBr_3$ was biased with a CAEN power supply [186]. CETC 1, CETC 2, Sample 1 and Sample 2 with the S14 plus the sum-amplifier board were biased using P. Schury's power supply [169]. The signals were processed with a DT5730 digitiser [187] with a 500 MHz sampling rate, faster than the V2745B with 125 MHz [157]. Two sources were used ^{22}Na and ^{60}Co.

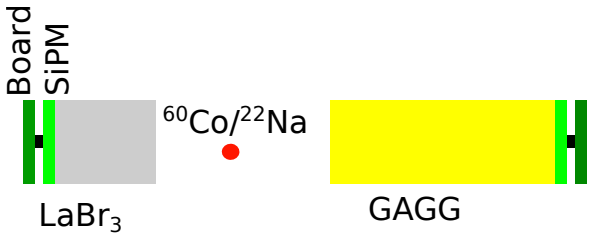

Fig. 7.35 Schematic diagram for the time resolution measurement. The left shows the $LaBr_3$ detector, and the right shows the GAGG detector. The source is shown in red, two sources were used: ^{60}Co and ^{22}Na.

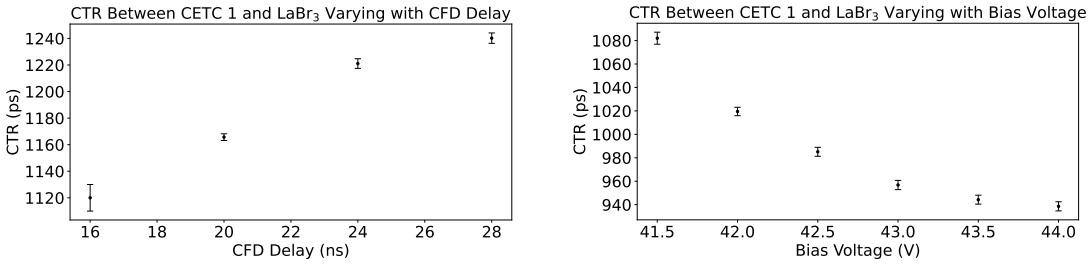

(a) (b)

Fig. 7.36 CTR optimisation with a ^{22}Na source for CETC 1. (a) shows the optimisation of the CFD delay with a bias voltage of 41 V. It appears that the CTR decreases with decreasing CFD delay, but going below 16 ns caused issues with the trigger. A delay of 16 ns was used. (b) shows the optimisation of the bias voltage for CETC 1; it was decided that a bias of 43.5 V was used.

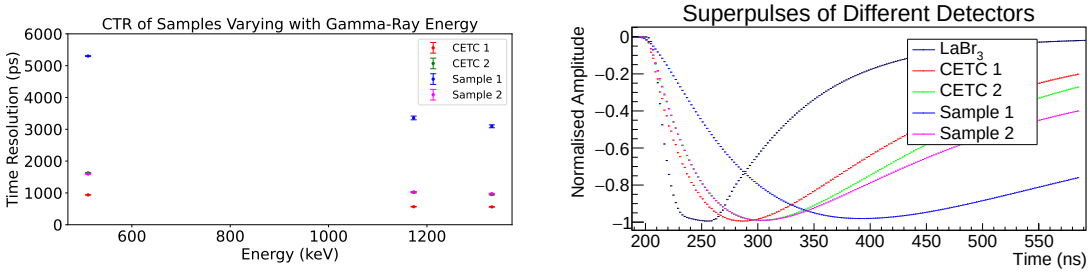

(a) (b)

Fig. 7.37 (a) shows the CTR values obtained for the different samples varying with the gamma ray energy deposited in the GAGG detector. There is a large variation in the performance. (b) shows the average waveforms for 662 keV gamma rays obtained using the same process used in the neutron analysis.

The two detectors were measured in coincidence with gating on the energies. For ^{22}Na, the 511 keV was gated in both detectors, whilst for ^{60}Co, the 1173 keV was gated in one detector and the 1333 keV in the other. The time difference between the energy-gated events was fitted with a Gaussian to obtain the CTR FWHM.

The CFD parameters and bias voltages were optimised using a ^{22}Na source by measuring the CTR. Figure 7.36a shows the CFD delay optimisation for CETC 1; a delay of 16 ns was used. The CFD delay optimisation was repeated independently for all crystals. Figure 7.36b shows the optimisation of the bias voltage for CETC 1; a value of 43.5 V was used for the samples.

Figure 7.37a shows the CTR of the different samples, varying with gamma-ray energy in the GAGG detector. CETC 1 achieves a CTR of 560(8) ps for the 1.3 MeV gamma ray. However, the other samples display a large variance in the CTR. This was explored using the super pulse method

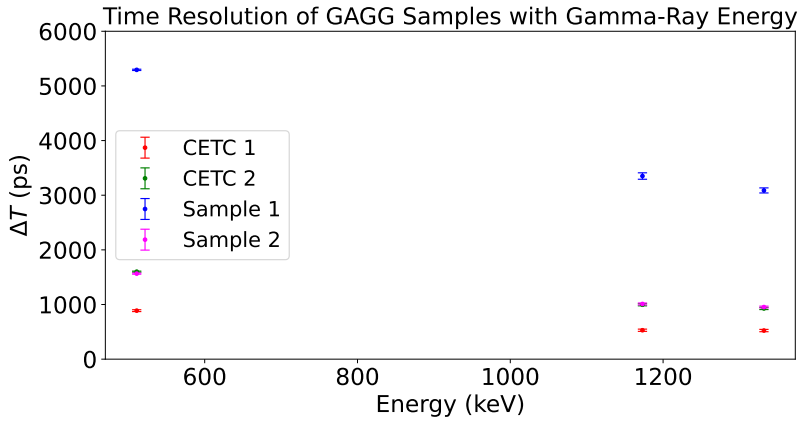

Fig. 7.38 Time resolution after subtraction for the GAGG samples. Due to the fast reference detector, the difference between the CTR and individual resolutions is small.

used in the neutron analysis. Figure 7.37b shows the averaged waveforms of the different samples. It is clear that the detectors with larger time resolutions have longer rise times.

The determination of the GAGG resolution was done by assuming the CTR time resolution was given by

$$\Delta T_{\mathrm{CTR}} = \sqrt{\Delta T^2_{\mathrm{LaBr_3}} + \Delta T^2_{\mathrm{GAGG}}} \tag{7.12}$$

where $\Delta T_{\mathrm{LaBr_3}}$ is the time resolution of the $LaBr_3$, and ΔT_{GAGG} is the time resolution of the GAGG. The $\Delta T_{\mathrm{LaBr_3}}$ was assumed to take values of 300(50) ps at 511 keV, and 200(50) ps for the ^{60}Co energies based on previous measurements with this detector [188]. Figure 7.38 shows the time resolutions after the subtraction of the $LaBr_3$ component. CETC 1 achieves a time resolution of 520(20) ps at 1.3 MeV.

The measured time resolution here is a large improvement on the previously measured values. This is ascribed to the faster reference detector and the faster digitiser used in the measurement. The achieved time resolution of 520(20) ps is well within the time resolution required for the HYPATIA array. There is a large variance between the different crystals, indicating that strict acceptance criteria will be necessary for the array.

7.4.3 Cluster Design and In-Beam Performance

Four prototype clusters were constructed using the S14 SiPMs with the sum-amplifier readout board. These used the same housing design as in Section 7.3, except the 100 mm crystal clusters used a 25 mm longer housing than the 75 mm crystal clusters. Table 7.7 summarises the crystals used in each cluster. Three new crystals were used that had not been discussed previously: Johannes, Zoltan, and

Cluster	Feed-through	Sample
RIKEN 1	1	Kinheng 1
	2	Kinheng 2
	3	Epic 1
	4	Epic 2
RIKEN 2	1	CETC 1
	2	CETC 2
	3	Sample 1
	4	Sample 2
Korean	1	IBS 1
	2	IBS 2
	3	IBS 3
	4	IBS 4
Hungarian	1	Johannes
	2	Zoltan
	3	Gabol
	4	IBS 5

Table 7.7 GAGG prototype clusters used for the experiment. Feed-through refers to the connectors used to pass the HV and signal in and out of the housing.

Gabol. These were three $25\times25\times100$ mm^3 GAGG crystals from C&A. These clusters were mounted into layer 8 of DALI2+ for an in-beam gamma-ray experiment looking at neutron-rich Ca isotopes. These were connected to the standard DALI2 DAQ and biased to 42 V.

The PID analysis was done using the same method as in Chapter 4.3. The detectors were calibrated by fitting the calibration source data with a quadratic calibration function for the GAGG detectors, whilst the DALI detectors used a linear calibration function. The calibration was performed up to 4.4 MeV using an AmBe source. The calibration for Kinheng 1 is shown in Figure 7.39. The

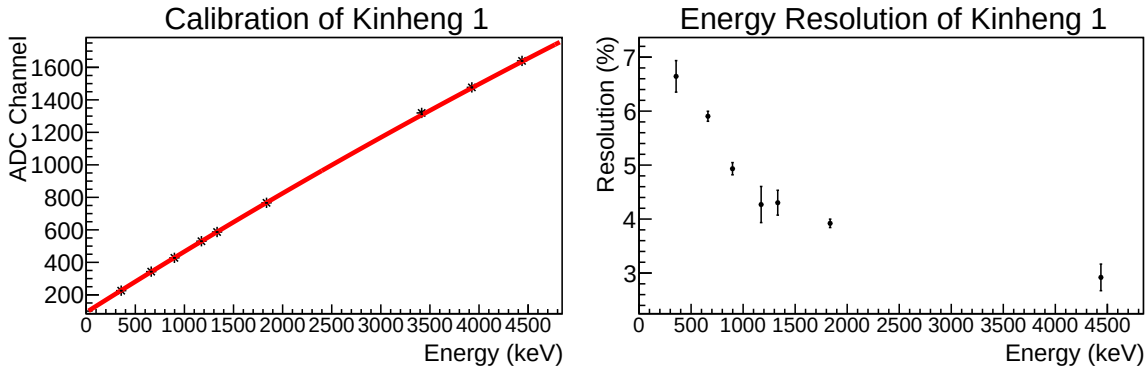

Fig. 7.39 The left graph shows the calibration of Kinheng 1 for the in-beam gamma-ray experiment. Whilst the right graph shows the determined energy resolution after calibration for Kinheng 1.

calibration source peaks were then fitted after calibration to obtain the energy resolution, and this can be seen in Figure 7.39. As can be seen, the energy resolution is worse than that with a digitiser. This is ascribed to the DALI DAQ being poorly matched for the GAGG detectors.

Next, the in-beam data was Doppler corrected using the standard equation where the θ was determined from the detector's position. The velocity was calculated using the $B\rho$ measurement from F5-F7 and F8-F9 on an event-by-event basis. The $B\rho$ values calculated two velocities β_{F57}, and β_{F89}. The Doppler correction velocity is then calculated according to

$$\beta = \frac{\beta_{F57} + \beta_{F89}}{2} + \beta_{off} \tag{7.13}$$

where β is the velocity for the Doppler correction whilst β_{off} is an offset calculated using LISE++. For the Doppler correction, $\beta_{off} = -0.002$ was used in the analysis.

The main purpose of the experiment was to perform Coulomb excitation measurements on neutron-rich Ca isotopes. For this, several targets and beam settings were used. For the analysis of the detector performance, only one case was analysed, where the spectrometers were centred on ^{50,51}Ca and a 5 mm C target was located at the DALI2 centre at the F8 focal plane. The ^{51}Ca(C,X)^{50}Ca channel was examined due to its high statistics for the $2_1^+ \rightarrow 0_1^+$ transition. The analysis was gated on ^{51}Ca in BigRIPS and ^{50}Ca in ZeroDegree, and the Doppler-corrected spectra were produced, separated by detector group.

Figure 7.40 shows the spectra with add back of GAGG clusters 1 and 3 and one DALI detector in layer 8, gated on the ^{51}Ca(C,X)^{50}Ca channel. One peak is observed for the $2_1^+ \rightarrow 0_1^+$ transition, which has previously been observed to have a lifetime of $\tau = 96(3)$ ps [189]. Due to the long lifetime and online Doppler correction, comparing the resolutions for this peak is not representative of the detector performance. The peaks in the different detectors were fitted with a Gaussian plus a linear background in order to obtain the peak height and energy resolution. The obtained values are: 57(6) and 8.1(7) % for DALI-119, 88(8) and 6.3(5) % for cluster 1, and 92(7) and 7.4(5) % for cluster 3. The peak height and energy resolution are clearly improved for the GAGG detectors compared to the NaI detectors with a similar opening angle.

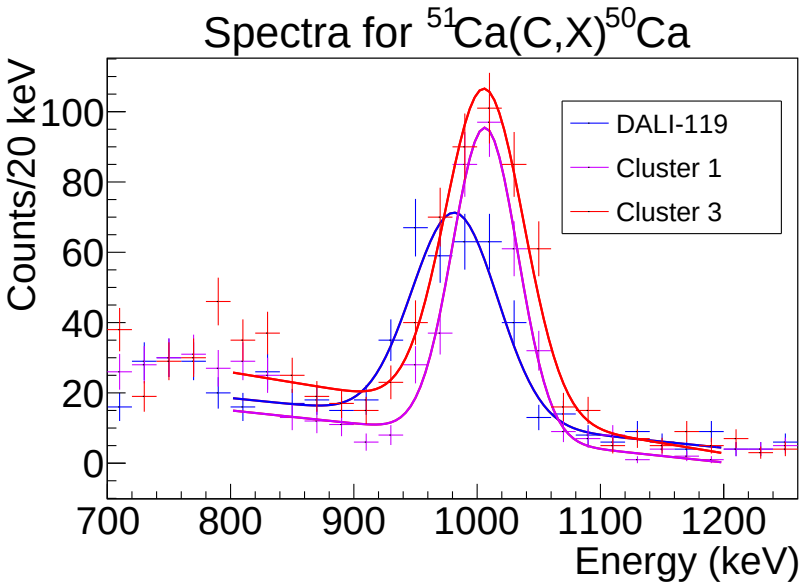

Fig. 7.40 Doppler corrected spectra for events gated on the ^{51}Ca(C, X)^{50}Ca reaction channels for HYPATIA and DALI2+ detectors. The $2_1^+ \rightarrow 0_1^+$ transition is fitted using a Gaussian plus a linear background.

7.5 Conclusion

In order to access unobserved physics, detector developments are required. This is being pursued in the HYPATIA project. To evaluate the expected performance of the array, Geant4 [74] simulations were performed. The results of the simulations show an improvement in energy resolution and full-energy peak efficiency in comparison to the current array, DALI2+ [24, 84]. In addition, preliminary simulations suggest the array is capable of performing the first spectroscopy of ^{79}Ni, providing a full understanding of the $N = 50$ shell closure in the region of ^{78}Ni.

Secondly, several HR-GAGG samples were tested for energy resolution using the S13 SiPMs from Hamamatsu [97]. From these tests, energy resolutions of 5-6 % were achieved for the ^{137}Cs peak for several samples. The best energy resolution was achieved by Kinheng 1, achieving 5.1(2) % at 662 keV. However, degradation of the energy resolution is observed when illuminating the length of the crystal as opposed to the smaller face, indicating some non-uniformity across the crystal. In addition, a dependence on the face to which the SiPM is attached is observed, indicating some non-uniformity in the crystals. This non-uniformity is most apparent in CETC 2, which shows a shift of the full-energy peak position across the length of the crystal equivalent to $\approx$ 200 keV. From these results, it can be concluded that HR-GAGG is appropriate for use in the HYPATIA array, but careful

tests of the crystals are required to verify the performance of the crystal and to optimise the readout of the crystal.

The detectors were clustered into prototype modules, which were used in an in-beam experiment at the RIBF. Several issues were identified, and steps have been taken to mitigate them. The same modules were tested for their response to high-energy gamma rays produced via (p,γ) reactions. The detectors successfully observed a 10.8 MeV gamma ray, indicating they are capable of achieving the desired dynamic range for HYPATIA. The modules were also tested for their response to neutrons from a ^{252}Cf source. From TOF analysis, a clear neutron band is observed in the GAGG detectors, indicating their sensitivity to neutrons. Standard PSD methods were attempted for the detectors, but no clear distinction was seen in the PSD between neutrons and gammas. Previous measurements have shown an improvement in the PSD sensitivity for higher-energy neutrons [171]; future tests with the detectors will allow for a better understanding of the GAGG neutron sensitivity.

The newer S14 generation Hamamatsu SiPMs were tested to see if the improvement in quantum efficiency would provide an improvement over the S13 SiPMs [97, 92]. Due to the higher terminal capacitance of the S14 SiPMs [97, 92], it was found that the timing performance was degraded compared to the S13 when using the same readout method as the S13s. Therefore, a novel readout board was designed, simulated and produced to reduce the impact of the S14's higher capacitance. The tests show an improvement in the energy resolution for the S14 compared to the S13 SiPM. In addition, an improvement in the time resolution is seen when using a sum-amplifier readout compared to a simple readout. Using the sum-amplifier board for the S13 SiPM may provide an even greater improvement in time resolution, which will need to be tested. The time resolution of the board was measured using a fast reference detector and a fast digitiser, measuring a value of 520(20) ps at 1.3 MeV, proving that GAGG is suitable for use in the HYPATIA array.

Finally, the S14 sum-amplifier board was used to construct four GAGG quad clusters, which were placed into the DALI2 array. The clusters were used in a Coulomb excitation experiment of neutron-rich Ca isotopes. The ^{51}Ca$(C,X)^{50}$Ca reaction was analysed, and the GAGG clusters were compared to a DALI2 crystal in the same layer of the array. From the analysis, GAGG detectors provide a better energy resolution and efficiency in comparison to NaI, which indicates HR-GAGG detectors are appropriate and ready for use in the HYPATIA array.

Chapter 8

Conclusion

8.1 Neutron Rich Zn Isotopes

Knockout reactions have been used at the RIBF to study the excited states in ^{78,80}Zn. In-beam gamma-ray spectroscopy with HPGe was performed, and energies and half-lives of excited states in ^{78,80}Zn have been measured.

In ^{78}Zn, the 2_1^+ energy and half-life was measured to be $731(1)(1)$ keV, and $13(1)^{+2}_{-1}$ ps. The energy is in agreement to within 1σ with the literature value of 730.2(4) keV [64], and the half-life is in agreement with the literature value of 18(4) ps [64] to within 2σ. These results correspond to a $B(E2, 2_1^+ \rightarrow 0_1^+) = 206^{+18}_{-29}\, e^2\text{fm}^4$. Several transitions above 1 MeV have been measured, and upper limits for the half-lives have been measured where possible, but these transitions could not be placed in the level scheme. Future experiments with high-efficiency arrays may be able to determine the origin of these transitions.

In ^{80}Zn, the 2_1^+ energy and an upper-limit for the half-life were measured to be $1495(2)\{2\}$ keV, and < 3 ps. The energy is in agreement with literature to within 2σ, and the half-life upper limit is consistent with previous measurements [17, 18, 20]. The 4_1^+ state energy and half-life have been measured to be $1980(2)\{3\}$ keV, and $138(13)^{+10}_{-16}$ ps, both within 1σ of the previous measurement [19, 20], but with the half-life uncertainty significantly reduced. Additionally, the energies of two feeding states were remeasured in agreement with literature [19], and their half-lives have been measured for the first time. Finally, a state feeding directly into the ground state at $2562(5)\{9\}$ keV has been measured, with an upper limit on the half-life of < 2 ps. The energy is within 2σ of the previous value [19] while the half-life was previously unmeasured. These results correspond to a

$B(E2, 4_1^+ \rightarrow 2_1^+) = 153^{+23}_{-16}\, e^2\text{fm}^4$. Leading to an $R_{BE2} = 1.05^{+0.20}_{-0.17}$ inconsistent with the expectations of a pure collective state [58].

The ^{80}Zn measurements were compared to shell model calculations to better understand the observations. Several simple models were applied as part of this thesis work: SDI, SDI+QQ, jun45 [46], and jj44pna [147] interactions, but none reproduced the observations well. State-of-the-art DNO-SM calculations for ^{80}Zn have been performed [21, 22], the prediction of the 2_1^+, and 4_1^+ energies matches the results well. However, the R_{BE2} is underpredicted compared to the measured value, suggesting the necessity for collective effects, indicating that the $N = 50$ shell closure is weaker than expected. In addition, the prediction of a deformed 2_2^+ state is consistent with the observations of a $2562(5)\{9\}$ keV state, suggesting the presence of shape coexistence in this nucleus. The shape coexistence is predicted to emerge from intruder configurations across the $N = 50$ shell gap, further indicating the weakening of the shell gap. From these observations and comparison with state-of-the-art theoretical calculations, it is clear that more information is necessary to fully understand the shell evolution around $N = 50$. This is being pursued in the HYPATIA project.

8.2 HYPATIA Array

The HYPATIA array will allow for the study of nuclei that are currently not accessible [39]. This work has focused on the development of the GAGG detectors for this array. Several samples were tested to find the best manufacturer for the array. The best energy resolution was achieved with Sample Kinheng 1 with 5.1(2) % (FWHM at 662 keV), with similar resolutions being achieved with Kinheng 2 and the Epic samples. The detector time resolutions were measured, and it is clear that the C&A samples have a worse time resolution than the other samples. Based on the present analysis employing a limited number of crystals, it appears that Kinheng or Epic crystals would perform better for the requirements of the HYPATIA array. Several full-length GAGG samples (25x25x100 mm^3) from EPIC were tested, the best energy resolution being achieved with IBS 3, which delivered an energy resolution of 5.6(2) % (FWHM at 662 keV), still within the acceptable range.

The first generation of GAGG prototypes used the S13 SiPMs in a 3D printed housing. These clusters were used successfully in an in-beam experiment, but several issues were identified, and improvements were implemented for future campaigns. In addition, the clusters were used to test the high-energy performance of the detectors using (p, γ) reactions. A 10.8 MeV gamma ray was

successfully observed, and resolved from its escape peaks, achieving an energy resolution of 1.4(1) % following the non-linearity correction. The neutron response was tested with a ^{252}Cf source; the gamma rays and neutrons could clearly be separated with TOF measurements. PSD was attempted, but no clear separation was observed. In the future, the response will be tested with high-energy neutrons to check for PSD separation at RIBF energies.

S14 SiPMs [92] have a higher quantum efficiency for the GAGG emission spectrum than the S13 SiPMs [97]; this is produced at the expense of higher capacitance. It was necessary to test whether this extra quantum efficiency improves the energy resolution and whether the extra capacitance causes issues with the signal length. For this, two boards were developed: one using the pixels connected in parallel to an inverting amplifier, and the second using a sum-amplifier configuration. The boards were tested with the CETC 1 crystal. An improved energy resolution was obtained with the S14 compared to the S13 SiPMs. The CTR was measured and indicated some improvement in the time resolution, as well. An optimised time resolution measurement was performed, achieving a time resolution of 520(20) ps at 1.3 MeV, indicating that GAGG coupled to S14 SiPMs and these dedicated readout boards will provide an excellent timing performance for the array. Finally, using the sum-amplifier board, four quad clusters were constructed. The improved clusters were successfully used in an in-beam experiment. The expected improvements of the HYPATIA array were demonstrated in the improved energy resolution and detection efficiency under realistic conditions at the BigRIPS-ZeroDegree setup integrated into the DALI2+ array.

8.2.1 Outlook

In 2030 (expected), the completed HYPATIA array will expand the region of observability, allowing for the exploration of unexplored areas of the nuclear chart. In the region of ^{78}Ni, several prime candidates for investigation exist in the first spectroscopy of ^{79}Ni, and the Coulomb excitation of ^{78}Ni. The array will not only provide improvements in energy resolution and detection efficiency, but also the improved time resolution will allow for improvements in the peak-to-background ratio, and open up the possibility for direct lifetime measurements of excited states. These measurements will allow for a better understanding of the $N = 50$ shell closure in the region of ^{78}Ni.

Bibliography

[1] Maria G. Mayer. "On Closed Shells in Nuclei". In: *Phys. Rev.* 74 (3 Aug. 1948), pp. 235–239.

[2] Jouni Suhonen. *From nucleons to nucleus : concepts of microscopic nuclear theory / Jouni Suhonen.* eng. Theoretical and mathematical physics. Berlin: Springer, 2007. ISBN: 978-3-540-48859-0.

[3] Sven Gösta Nilsson. *Binding states of individual nucleons in strongly deformed nuclei*. Tech. rep. 16. This document exists only as a journal publication: it is not in the CERN Official Collection bound volume. 1955. URL: https://cds.cern.ch/record/212345.

[4] Kris Heyde and John L. Wood. "Shape coexistence in atomic nuclei". In: *Rev. Mod. Phys.* 83 (4 Nov. 2011), pp. 1467–1521.

[5] Takaharu Otsuka et al. "Evolution of Nuclear Shells due to the Tensor Force". In: *Phys. Rev. Lett.* 95 (23 Nov. 2005), p. 232502.

[6] E. K. Warburton, J. A. Becker, and B. A. Brown. "Mass systematics for A=29–44 nuclei: The deformed A$\sim$32 region". In: *Phys. Rev. C* 41 (3 Mar. 1990), pp. 1147–1166.

[7] E. Caurier et al. "The shell model as a unified view of nuclear structure". In: *Rev. Mod. Phys.* 77 (2 June 2005), pp. 427–488.

[8] T Otsuka and Y Tsunoda. "The role of shell evolution in shape coexistence". In: *Journal of Physics G: Nuclear and Particle Physics* 43.2 (Jan. 2016), p. 024009.

[9] R. Taniuchi et al. "78Ni revealed as a doubly magic stronghold against nuclear deformation". In: *Nature* 569.7754 (May 2019), pp. 53–58. ISSN: 1476-4687.

[10] X. F. Yang et al. "Isomer Shift and Magnetic Moment of the Long-Lived $1/2^+$ Isomer in $^{79}_{30}Zn_{49}$: Signature of Shape Coexistence near ^{78}Ni". In: *Phys. Rev. Lett.* 116 (18 May 2016), p. 182502.

[11] K. Wimmer et al. "HiCARI: High-resolution Cluster Array at RIBF". In: *RIKEN Accel. Prog. Rep.* 54 (2021).

[12] J.M. Daugas et al. "The 8+ isomer in 78Zn and the doubly magic character of 78Ni". In: *Physics Letters B* 476.3 (2000), pp. 213–218. ISSN: 0370-2693.

[13] L. G. Pedersen et al. "First spectroscopic study of odd-odd ^{78}Cu". In: *Phys. Rev. C* 107 (4 Apr. 2023), p. 044301.

[14] D. Kameda et al. "Observation of new microsecond isomers among fission products from in-flight fission of 345 MeV/nucleon ^{238}U". In: *Phys. Rev. C* 86 (5 Nov. 2012), p. 054319.

[15] A. Korgul et al. "β-γ and β-delayed neutron-γ decay of neutron-rich copper isotopes". In: *Phys. Rev. C* 86 (2 Aug. 2012), p. 024307.

[16] J. Van Roosbroeck et al. "Evolution of the nuclear structure approaching ^{78}Ni : β decay of $^{74-78}$Cu". In: *Phys. Rev. C* 71 (5 May 2005), p. 054307.

[17] J. Van de Walle et al. "Coulomb Excitation of Neutron-Rich Zn Isotopes: First Observation of the 2_1^+ State in ^{80}Zn". In: *Phys. Rev. Lett.* 99 (14 Oct. 2007), p. 142501.

[18] J. Van de Walle et al. “Low-energy Coulomb excitation of neutron-rich zinc isotopes”. In: *Phys. Rev. C* 79 (1 Jan. 2009), p. 014309.

[19] Y. Shiga et al. “Investigating nuclear shell structure in the vicinity of ^{78}Ni: Low-lying excited states in the neutron-rich isotopes ^{80,82}Zn”. In: *Phys. Rev. C* 93 (2 Feb. 2016), p. 024320.

[20] M. L. Cortés et al. “Inelastic scattering of neutron-rich Ni and Zn isotopes off a proton target”. In: *Phys. Rev. C* 97 (4 Apr. 2018), p. 044315.

[21] D. D. Dao and F. Nowacki. “Nuclear structure within a discrete nonorthogonal shell model approach: New frontiers”. In: *Phys. Rev. C* 105 (5 May 2022), p. 054314.

[22] L. Nies et al. “Further Evidence for Shape Coexistence in ^{79}Zn^{m} near Doubly Magic ^{78}Ni”. In: *Phys. Rev. Lett.* 131 (22 Nov. 2023), p. 222503.

[23] N. Warr et al. “The Miniball spectrometer”. In: *The European Physical Journal A* 49.3 (Mar. 2013), p. 40. ISSN: 1434-601X.

[24] S. Takeuchi et al. “DALI2: A NaI(Tl) detector array for measurements of gamma rays from fast nuclei”. In: *Nuclear Instruments and Methods in Physics Research Section A: Accelerators, Spectrometers, Detectors and Associated Equipment* 763 (2014), pp. 596–603. ISSN: 0168-9002.

[25] L.P. Gaffney et al. “Studies of pear-shaped nuclei using accelerated radioactive beams”. In: *Nature* 497.7448 (2013). Cited by: 328, pp. 199–204.

[26] D. Steppenbeck et al. “Evidence for a new nuclear ‘magic number’ from the level structure of 54Ca”. In: *Nature* 502.7470 (Oct. 2013), pp. 207–210. ISSN: 1476-4687.

[27] J. Eberth et al. “Agata detector technology: recent progress and future developments”. In: *The European Physical Journal A* 59.8 (Aug. 2023), p. 179. ISSN: 1434-601X.

[28] D. Weisshaar et al. “The performance of the gamma-ray tracking array GRETINA for gamma-ray spectroscopy with fast beams of rare isotopes”. In: *Nuclear Instruments and Methods in Physics Research Section A: Accelerators, Spectrometers, Detectors and Associated Equipment* 847 (2017), pp. 187–198. ISSN: 0168-9002.

[29] S. Paschalis et al. “The performance of the Gamma-Ray Energy Tracking In-beam Nuclear Array GRETINA”. In: *Nuclear Instruments and Methods in Physics Research Section A: Accelerators, Spectrometers, Detectors and Associated Equipment* 709 (2013), pp. 44–55. ISSN: 0168-9002.

[30] Pieter Doornenbal. “In-beam gamma-ray spectroscopy at the RIBF”. In: *Progress of Theoretical and Experimental Physics* 2012.1 (Dec. 2012), p. 03C004. ISSN: 2050-3911.

[31] F. C. L. Crespi et al. “AGATA: performance of gamma-ray tracking and associated algorithms”. In: *The European Physical Journal A* 59.5 (May 2023), p. 111. ISSN: 1434-601X.

[32] Berkley Nucleonics Corp. *Scintillation Detectors*. https://www.berkeleynucleonics.com/products/custom-scintillation-detectors/. Accessed: 26-11-2025.

[33] *HR-GAGG (High Energy Resolution Gd3(Al,Ga)5O12(Ce))*. 103210514. C&A Corporation.

[34] F.G.A. Quarati et al. “Study of 138La radioactive decays using LaBr3 scintillators”. In: *Nuclear Instruments and Methods in Physics Research Section A: Accelerators, Spectrometers, Detectors and Associated Equipment* 683 (2012), pp. 46–52. ISSN: 0168-9002.

[35] Paul Lecoq. “Development of new scintillators for medical applications”. In: *Nuclear Instruments and Methods in Physics Research Section A: Accelerators, Spectrometers, Detectors and Associated Equipment* 809 (2016). Advances in detectors and applications for medicine, pp. 130–139. ISSN: 0168-9002.

[36] B. Moon et al. “Commissioning and performance of IDATEN: A large fast-timing gamma-ray detector array at the RIBF”. In: *Nuclear Instruments and Methods in Physics Research Section A: Accelerators, Spectrometers, Detectors and Associated Equipment* 1084 (2026), p. 171239. ISSN: 0168-9002.

[37] W.M. Higgins et al. “Crystal growth of large diameter LaBr3:Ce and CeBr3”. In: *Journal of Crystal Growth* 310.7 (2008). the Proceedings of the 15th International Conference on Crystal Growth (ICCG-15) in conjunction with the International Conference on Vapor Growth and Epitaxy and the US Biennial Workshop on Organometallic Vapor Phase Epitaxy, pp. 2085–2089. ISSN: 0022-0248.

[38] Pawel Sibczynski et al. “Characterization of GAGG:Ce scintillators with various Al-to-Ga ratio”. In: *Nuclear Instruments and Methods in Physics Research Section A: Accelerators, Spectrometers, Detectors and Associated Equipment* 772 (2015), pp. 112–117. ISSN: 0168-9002.

[39] P. Doornenbal et al. *The HYPATIA Project*. Internal Document. 2023.

[40] Sunflower. *HYbrid Photon detector Array To Investigate Atomic nuclei*. https://www.nishina.riken.jp/collaboration/SUNFLOWER/devices/hypatia/index.php. Accessed: 2025-08-22.

[41] J. L. Friar, B. F. Gibson, and G. L. Payne. “One-pion-exchange potential deuteron”. In: *Phys. Rev. C* 30 (3 Sept. 1984), pp. 1084–1086.

[42] A. Volya. *Nucracker*. https://nucracker.volya.net/. Accessed: 24-10-2025.

[43] Aage Bohr and Ben R. Mottelson. *Nuclear structure / Aage Bohr, Ben R. Mottelson.* eng. Singapore ; World Scientific, <c1998- >. ISBN: 981-02-3197-0.

[44] Kenneth S Krane. *Introductory nuclear physics*. Hoboken NJ: Wiley, 1987. ISBN: 978-0-471-80553-3.

[45] L. Zamick et al. “Spin and orbital g factors with a surface δ interaction”. In: *Phys. Rev. C* 90 (2 Aug. 2014), p. 027305.

[46] M. Honma et al. “New effective interaction for f_5pg_9-shell nuclei”. In: *Phys. Rev. C* 80 (6 Dec. 2009), p. 064323.

[47] Marco Siciliano. “Shape coexistence in the neutron-deficient nucleus 194Po: Gamma-ray and electron spectroscopic study employing the SAGE spectrometer”. PhD thesis. Oct. 2013. DOI: 10.13140/RG.2.1.1885.1365.

[48] Kris L G Heyde. *Basic ideas and concepts in nuclear physics*. Fundamental and applied nuclear physics. Bristol: IOP, 2004. URL: https://cds.cern.ch/record/808336.

[49] Peter Ring and Peter Schuck. *The nuclear many-body problem.* eng. Texts and monographs in physics. New York, etc., Springer, 1980. ISBN: 3-540-09820-8.

[50] *wimmer-k/Nilsson*. https://github.com/wimmer-k/Nilsson. Accessed: 2025-10-06.

[51] I. Ragnarsson et al. “Application of the cranked Nilsson model in some light nuclei: The super backbend in 11B and 11C?” In: *Nuclear Physics A* 361.1 (1981), pp. 1–22. ISSN: 0375-9474. DOI: https://doi.org/10.1016/0375-9474(81)90468-1. URL: https://www.sciencedirect.com/science/article/pii/0375947481904681.

[52] Frédéric Nowacki, Alexandre Obertelli, and Alfredo Poves. “The neutron-rich edge of the nuclear landscape: Experiment and theory.” In: *Progress in Particle and Nuclear Physics* 120 (2021), p. 103866. ISSN: 0146-6410.

[53] Takaharu Otsuka et al. “Evolution of shell structure in exotic nuclei”. In: *Rev. Mod. Phys.* 92 (1 Mar. 2020), p. 015002.

[54] K. Wimmer et al. “Discovery of the Shape Coexisting 0^+ State in ^{32}Mg by a Two Neutron Transfer Reaction”. In: *Phys. Rev. Lett.* 105 (25 Dec. 2010), p. 252501.

[55] Dao, Duy Duc and Nowacki, Frédéric. "Discrete non-orthogonal shell model for nuclear structure: Towards heavy elements". In: *EPJ Web Conf.* 342 (2025), p. 01009.

[56] Alexandra Gade et al. "In-beam spectroscopy reveals competing nuclear shapes in the rare isotope 62Cr". In: *Nature Physics* 21.1 (Jan. 2025), pp. 37–42. ISSN: 1745-2481.

[57] Marie-Martine Bé and Valery P. Chechev. "Recommended standards for gamma ray intensities". In: *Nuclear Instruments and Methods in Physics Research Section A: Accelerators, Spectrometers, Detectors and Associated Equipment* 728 (2013), pp. 157–172. ISSN: 0168-9002.

[58] J. J. Ressler et al. "Transition from the seniority regime to collective motion". In: *Phys. Rev. C* 69 (3 Mar. 2004), p. 034317.

[59] R. B. Cakirli et al. "Highly anomalous yrast $B(E2)$ values and vibrational collectivity". In: *Phys. Rev. C* 70 (4 Oct. 2004), p. 047302.

[60] NNDC. *Evaluated Nuclear Structure Data File (ENSDF)*. Feb. 2022. DOI: 10.18139/nndc.ensdf/1845010. URL: https://www.osti.gov/biblio/1845010.

[61] Louis Olivier. "Nuclear structure in the vicinity of 78Ni : in-beam gamma-ray spectroscopy of 79Cu through proton knockout". Theses. Université Paris-Saclay, Sept. 2017. URL: https://theses.hal.science/tel-01637435.

[62] A. Obertelli et al. "MINOS: A vertex tracker coupled to a thick liquid-hydrogen target for in-beam spectroscopy of exotic nuclei". In: *The European Physical Journal A* 50.1 (Jan. 2014), p. 8. ISSN: 1434-601X.

[63] Toshiyuki Kubo et al. "BigRIPS separator and ZeroDegree spectrometer at RIKEN RI Beam Factory". In: *Progress of Theoretical and Experimental Physics* 2012.1 (Dec. 2012), p. 03C003. ISSN: 2050-3911.

[64] Ameenah R. Farhan and Balraj Singh. "Nuclear Data Sheets for A = 78". In: *Nuclear Data Sheets* 110.9 (2009), pp. 1917–2080. ISSN: 0090-3752.

[65] A. Illana et al. "Coulomb excitation of ^{74,76}Zn". In: *Phys. Rev. C* 108 (4 Oct. 2023), p. 044305.

[66] F. Nowacki et al. "Shape Coexistence in ^{78}Ni as the Portal to the Fifth Island of Inversion". In: *Phys. Rev. Lett.* 117 (27 Dec. 2016), p. 272501.

[67] A. Tichai et al. "Spectroscopy of N = 50 isotones with the valence-space density matrix renormalization group". In: *Physics Letters B* 855 (2024), p. 138841. ISSN: 0370-2693.

[68] Noritaka Shimizu et al. "Monte Carlo shell model studies with massively parallel supercomputers". In: *Physica Scripta* 92.6 (Apr. 2017), p. 063001.

[69] Anil Kumar et al. *Probing the shape evolution and shell structures in neutron-rich N=50 nuclei*. 2025. arXiv: 2510.16775 [nucl-th]. URL: https://arxiv.org/abs/2510.16775.

[70] Glenn F Knoll. *Radiation detection and measurement*. 4th edition. Hoboken, N.J.: Wiley, 2010. ISBN: 978-0-470-13148-0.

[71] Yuji YAZAKI. "How the Klein–Nishina formula was derived: Based on the Sangokan Nishina Source Materials". In: *Proceedings of the Japan Academy, Series B* 93.6 (2017), pp. 399–421.

[72] Kei Kamada et al. "Composition Engineering in Cerium-Doped (Lu,Gd)3(Ga,Al)5O12 Single-Crystal Scintillators". In: *Crystal Growth & Design* 11.10 (2011), pp. 4484–4490.

[73] M. B. Berger et al. *NIST Standard Reference Database 8 (XGAM)*. NIST, PML, Radiation Physics Division, 2010.

[74] S. Agostinelli et al. "Geant4—a simulation toolkit". In: *Nuclear Instruments and Methods in Physics Research Section A: Accelerators, Spectrometers, Detectors and Associated Equipment* 506.3 (2003), pp. 250–303. ISSN: 0168-9002.

[75] Nilgün Demir and Zehra Nur Kuluöztürk. "Determination of energy resolution for a NaI(Tl) detector modeled with FLUKA code". In: *Nuclear Engineering and Technology* 53.11 (2021), pp. 3759–3763. ISSN: 1738-5733.

[76] Helmuth Spieler. *Semiconductor detector systems*. Series on semiconductor science and technology. Oxford: Oxford Univ. Press, 2005. DOI: 10.1093/acprof:oso/9780198527848.001.0001. URL: https://cds.cern.ch/record/1010490.

[77] C. Canali et al. "Electron and hole drift velocity measurements in silicon and their empirical relation to electric field and temperature". In: *IEEE Transactions on Electron Devices* 22.11 (1975), pp. 1045–1047. DOI: 10.1109/T-ED.1975.18267.

[78] Arzoo Sharma et al. "Performance test of a position sensitive planar germanium detector for phase-III DESPEC experiments". In: *Nuclear Instruments and Methods in Physics Research Section A: Accelerators, Spectrometers, Detectors and Associated Equipment* 1051 (2023), p. 168233. ISSN: 0168-9002.

[79] David Jenkins. *Radiation Detection for Nuclear Physics*. 2053-2563. IOP Publishing, 2020. ISBN: 978-0-7503-1428-2.

[80] J. B. Birks. *The theory and practice of scintillation counting / by J.B. Birks.* eng. International series of monographs on electronics and instrumentation ; v. 27. Oxford: Pergamon Press, 1964.

[81] *GENERAL PURPOSE PLASTIC SCINTILLATOR EJ-200, EJ-204, EJ-208, EJ-212*. Eljen Technology. 2021.

[82] *BC-400,BC-404,BC-408,BC-412,BC-416 Premium Plastic Scintillators*. LUXIUM. 2023.

[83] A. Taheri, M.A. Lehdarboni, and R. Gholipour. "Determination of Gaussian energy broadening parameters for organic scintillators". In: *Journal of Instrumentation* 11.05 (May 2016), P05020.

[84] I. Murray et al. "DALI2+ at the RIKEN Nishina Center RIBF". In: *RIKEN Accel. Prog. Rep.* 54 (2021).

[85] Yang Tang et al. "Ga/Al ratio induced afterglow behavior of Ce3+:GAGG scintillation ceramics". In: *Ceramics International* 50.19, Part B (2024), pp. 36286–36294. ISSN: 0272-8842.

[86] *GAGG(Ce) Crystal*. Epic-Crystal.

[87] Ashok K Batra. *Advanced Nuclear Radiation Detectors*. 2053-2563. IOP Publishing, 2021. ISBN: 978-0-7503-2508-0.

[88] Kinheng Crystal. *GAGG:Ce Scintillator, GAGG Crystal, GAGG Scintillation Crystal*. https://www.kinheng-crystal.com/gaggce-scintillator-gagg-crystal-gagg-scintillation-crystal-product/. Accessed: 07-02-2025.

[89] WAN Qianyin et al. "Study on Packaging Technology of GAGG:Ce Scintillation Detector". In: *Atomic Energy Science and Technology* 59.1 (2025), pp. 183–188.

[90] P Buzhan et al. "Silicon photomultiplier and its possible applications". In: *Nuclear Instruments and Methods in Physics Research Section A: Accelerators, Spectrometers, Detectors and Associated Equipment* 504.1-3 (2003), pp. 48–52.

[91] S. España et al. "Performance evaluation of SiPM photodetectors for PET imaging in the presence of magnetic fields". In: *Nuclear Instruments and Methods in Physics Research Section A: Accelerators, Spectrometers, Detectors and Associated Equipment* 613.2 (2010), pp. 308–316. ISSN: 0168-9002.

[92] *MPPC (Multi-Pixel Photon Counter) S14160/S14161 series*. Hamamatsu Photonics. 2024.

[93] *Photomultiplier Tubes and Photomultiplier Tube Assemblies R11265U Series / H11934 Series*. Hamamatsu Photonics. 2024.

[94] P. Buzhan et al. "The Advanced Study of Silicon Photomultiplier". In: *Advanced Technology and Particle Physics*, pp. 717–728. eprint: https://www.worldscientific.com/doi/pdf/10.1142/9789812776464_0101.

[95] Rachel Georgel et al. "Silicon Photomultiplier—A High Dynamic Range, High Sensitivity Sensor for Bio-Photonics Applications". In: *Biosensors* 12.10 (2022). ISSN: 2079-6374.

[96] *MPPC (Multi-Pixel Photon Counter) arrays, S13361-3050 series*. Hamamatsu Photonics. 2024.

[97] *MPPC (Multi-Pixel Photon Counter) arrays, S13361-6050 series*. Hamamatsu Photonics. 2024.

[98] L. Gruber et al. "Over saturation behavior of SiPMs at high photon exposure". In: *Nuclear Instruments and Methods in Physics Research Section A: Accelerators, Spectrometers, Detectors and Associated Equipment* 737 (2014), pp. 11–18. ISSN: 0168-9002.

[99] Sergei Dolinsky, Geng Fu, and Adrian Ivan. "Timing resolution performance comparison for fast and standard outputs of SensL SiPM". In: *2013 IEEE Nuclear Science Symposium and Medical Imaging Conference (2013 NSS/MIC)*. 2013, pp. 1–6.

[100] C. Mihai et al. "Development of large area Silicon Photomultipliers arrays for gamma-ray spectroscopy applications". In: *Nuclear Instruments and Methods in Physics Research Section A: Accelerators, Spectrometers, Detectors and Associated Equipment* 953 (2020), p. 163263. ISSN: 0168-9002.

[101] C. M. Lavelle et al. "Approaches for single channel large area silicon photomultiplier array readout". In: *AIP Advances* 9.3 (Mar. 2019), p. 035123. ISSN: 2158-3226.

[102] *Models 142A, 142B, and 142C Preamplifiers Operating and Service Manual*. Ortec. 2002.

[103] *Model 572A Spectroscopy Amplifier Operating and Service Manual*. Ortec. 2004.

[104] *CoMPASS Multiparametric DAQ Software for Physics Applications*. CAEN SpA. 2025.

[105] F.C.L. Crespi et al. "Alpha–gamma discrimination by pulse shape in LaBr3:Ce and LaCl3:Ce". In: *Nuclear Instruments and Methods in Physics Research Section A: Accelerators, Spectrometers, Detectors and Associated Equipment* 602.2 (2009), pp. 520–524. ISSN: 0168-9002.

[106] Valentin T. Jordanov and Glenn F. Knoll. "Digital synthesis of pulse shapes in real time for high resolution radiation spectroscopy". In: *Nuclear Instruments and Methods in Physics Research Section A: Accelerators, Spectrometers, Detectors and Associated Equipment* 345.2 (1994), pp. 337–345. ISSN: 0168-9002.

[107] U. Köster. "Intense radioactive-ion beams produced with the ISOL method". In: *The European Physical Journal A* 15.1 (Sept. 2002), pp. 255–263. ISSN: 1434-601X.

[108] T. Nakamura, H. Sakurai, and H. Watanabe. "Exotic nuclei explored at in-flight separators". In: *Progress in Particle and Nuclear Physics* 97 (2017), pp. 53–122. ISSN: 0146-6410.

[109] G.D. Alton, Y. Zhang, and Y. Kawai. "Prescriptions for optimizing intensities of short-lived RIBs at ISOL based research facilities". In: *Applied Radiation and Isotopes* 64.12 (2006), pp. 1574–1603. ISSN: 0969-8043.

[110] N. Fukuda et al. "Identification and separation of radioactive isotope beams by the BigRIPS separator at the RIKEN RI Beam Factory". In: *Nuclear Instruments and Methods in Physics Research Section B: Beam Interactions with Materials and Atoms* 317 (2013). XVIth International Conference on ElectroMagnetic Isotope Separators and Techniques Related to their Applications, December 2–7, 2012 at Matsue, Japan, pp. 323–332. ISSN: 0168-583X.

[111] Toshiyuki Kubo et al. "BigRIPS separator and ZeroDegree spectrometer at RIKEN RI Beam Factory". In: *Progress of Theoretical and Experimental Physics* 2012.1 (Dec. 2012), p. 03C003. ISSN: 2050-3911.

[112] S. Hiel. "Electromagnetic Properties of 21O and the Self-Calibration of Compton Tracking Arrays". PhD thesis. Technische Universtat Darmstadt, 2019.

[113] J. Acosta et al. "Excited-state lifetimes in ^{131}In, ^{131}Sn, and ^{136}Te measured with the HiCARI γ-ray spectrometer at RIBF at RIKEN". In: *Phys.Rev. C* 111 (2025), p. 064316.

[114] B.Moon et al. "Triaxial deformation of neutron-rich Zr nuclei explored by high-resolution in-beam γ-ray spectroscopy". In: *Phys.Lett. B* 858 (2024), p. 139047.

[115] H. Okuno et al. "Charge strippers for Radioisotope Beam Factory at RIKEN". In: *Journal of Radioanalytical and Nuclear Chemistry* 299.2 (Feb. 2014), pp. 945–949. ISSN: 1588-2780.

[116] H. Okuno, N. Fukunishi, and O. Kamigaito. "Progress of RIBF accelerators". In: *Progress of Theoretical and Experimental Physics* 2012.1 (Dec. 2012), p. 03C002. ISSN: 2050-3911.

[117] T. Nakagawa et al. "28GHZ SC-ECRIS AT RIBF". In: *Proceedings of CYCLOTRONS 2010, Lanzhou, China* (2010), p. 321.

[118] T. Nakagawa et al. "First results from the new RIKEN superconducting electron cyclotron resonance ion source (invited)a)". In: *Review of Scientific Instruments* 81.2 (Feb. 2010), 02A320. ISSN: 0034-6748.

[119] K. Suda et al. "Design and construction of drift tube linac cavities for RIKEN RI Beam Factory". In: *Nuclear Instruments and Methods in Physics Research Section A: Accelerators, Spectrometers, Detectors and Associated Equipment* 722 (2013), pp. 55–64. ISSN: 0168-9002.

[120] H. Okuno, N. Fukunishi, and O. Kamigaito. "Progress of RIBF accelerators". In: *Progress of Theoretical and Experimental Physics* 2012.1 (Dec. 2012), p. 03C002. ISSN: 2050-3911.

[121] A. Yoshida et al. "Status and overview of production target for BigRIPS separator at RIKEN". In: *Nuclear Instruments and Methods in Physics Research Section A: Accelerators, Spectrometers, Detectors and Associated Equipment* 590.1 (2008). Toward the Realization of Target and Stripper Foil Technologies for High-Power Proton and Radioactive Ion Accelerators, pp. 204–212. ISSN: 0168-9002.

[122] N. Miyauchi. Private Communication.

[123] K. Kusaka et al. "Prototype of superferric quadrupole magnets for the BigRIPS separator at RIKEN". In: *IEEE Transactions on Applied Superconductivity* 14.2 (2004), pp. 310–315.

[124] BigRIPS Team. *Technical Information of BigRIPS, ZeroDegree, SAMURAI Beam Line, and OEDO Beamline*. 2024. (Visited on 06/06/2025).

[125] O.B. Tarasov and D. Bazin. "LISE++: Radioactive beam production with in-flight separators". In: *Nuclear Instruments and Methods in Physics Research Section B: Beam Interactions with Materials and Atoms* 266.19 (2008). Proceedings of the XVth International Conference on Electromagnetic Isotope Separators and Techniques Related to their Applications, pp. 4657–4664. ISSN: 0168-583X.

[126] K. Kimura et al. "High-rate particle identification of high-energy heavy ions using a tilted electrode gas ionization chamber". In: *Nuclear Instruments and Methods in Physics Research Section A: Accelerators, Spectrometers, Detectors and Associated Equipment* 538.1 (2005), pp. 608–614. ISSN: 0168-9002.

[127] H. Kumagai et al. "Development of Parallel Plate Avalanche Counter (PPAC) for BigRIPS fragment separator". In: *Nuclear Instruments and Methods in Physics Research Section B: Beam Interactions with Materials and Atoms* 317 (2013). XVIth International Conference on ElectroMagnetic Isotope Separators and Techniques Related to their Applications, December 2–7, 2012 at Matsue, Japan, pp. 717–727. ISSN: 0168-583X.

[128] H. Kumagai et al. "Delay-line PPAC for high-energy light ions". In: *Nuclear Instruments and Methods in Physics Research Section A: Accelerators, Spectrometers, Detectors and Associated Equipment* 470.3 (2001), pp. 562–570. ISSN: 0168-9002.

[129] Ryo Taniuchi. "In-beam gamma-ray spectroscopy of 78Ni". PhD thesis. The University of Tokyo, 2018.

[130] J. Eberth et al. "MINIBALL A Ge detector array for radioactive ion beam facilities". In: *Progress in Particle and Nuclear Physics* 46.1 (2001), pp. 389–398. ISSN: 0146-6410.

[131] G. Duchêne et al. "The Clover: a new generation of composite Ge detectors". In: *Nuclear Instruments and Methods in Physics Research Section A: Accelerators, Spectrometers, Detectors and Associated Equipment* 432.1 (1999), pp. 90–110. ISSN: 0168-9002.

[132] *Germanium 4 Fold Segmented SuperClover Detector No 2 Operating Manual*. Eurisys Mesures. 2001.

[133] P. Rahkila et al. "Characteristics of Segmented Super Clover Detector in Close Geometry Decay Measurements". In: *Acta Phys. Pol. B* 32 (2001).

[134] A. Korichi and T. Lauritsen. "Tracking gamma rays in highly segmented HPGe detectors: A review of AGATA and GRETINA". In: *The European Physical Journal A* 55.7 (July 2019), p. 121. ISSN: 1434-601X.

[135] T. Ross. "Neutron damage tests of a highly segmented Germanium detector". PhD thesis. University of Surrey, 2008.

[136] *CAENTools for Discoveryn Electronic Instrumentation User Manual UM2462 SY4527 - SY4527LC Power Supply Systems*. CAEN SpA. 2025.

[137] John T. Anderson et al. "Data acquisition and trigger system of the Gamma Ray Energy Tracking In-Beam Nuclear Array (GRETINA)". In: *2007 IEEE Nuclear Science Symposium Conference Record*. Vol. 3. 2007, pp. 1751–1756.

[138] Massyl Kaci. "Spectroscopie γ du noyau exotique 79Cu". Theses. Université Paris-Saclay, Sept. 2024. URL: https://theses.hal.science/tel-04845596.

[139] K. Wimmer. *Simulations for HiCARI the high resolution cluster array at the RIBF*. 2019.

[140] I. Antcheva et al. "ROOT — A C++ framework for petabyte data storage, statistical analysis and visualization". In: *Computer Physics Communications* 180.12 (2009). 40 YEARS OF CPC: A celebratory issue focused on quality software for high performance, grid and novel computing architectures, pp. 2499–2512. ISSN: 0010-4655.

[141] Aoi Nori. Private Communication. 2023.

[142] J. Van de Walle et al. "Low-energy Coulomb excitation of neutron-rich zinc isotopes". In: *Phys. Rev. C* 79 (1 Jan. 2009), p. 014309.

[143] R.J. Barlow. "Practical statistics for particle physics". en. In: *CERN Yellow Reports: School Proceedings* Vol. 5 (2020 2020), 12–25 September 2018.

[144] Zeljko Ilic et al. "Prompt gamma rays induced by inelastic scattering of fission neutrons on iron". In: *Journal of Radioanalytical and Nuclear Chemistry* 325.2 (Aug. 2020), pp. 641–655. ISSN: 1588-2780.

[145] M. Baginova, P. Vojtyla, and P.P. Povinec. "The neutron component of background of an HPGe detector operating in a surface laboratory". In: *Applied Radiation and Isotopes* 166 (2020), p. 109422. ISSN: 0969-8043.

[146] Igal Talmi. *Simple models of complex nuclei : the shell model and interacting boson model / Igal Talmi.* eng. Contemporary concepts in physics ; v. 7. Chur, Switzerland ; Harwood Academic Publishers, 1993. ISBN: 3-7186-0551-1.

[147] A. F. Lisetskiy et al. In: *Phys. Rev. C* 70 (4 Oct. 2004), p. 044314.

[148] Noritaka Shimizu et al. "Thick-restart block Lanczos method for large-scale shell-model calculations". In: *Computer Physics Communications* 244 (2019), pp. 372–384. ISSN: 0010-4655.

[149] P. Van Duppen et al. *Status report of the IS557 experiment: Coulomb excitation of ^{80}Zn ($N = 50$): probing the validity of shell-model descriptions around ^{78}Ni*. INTC Status Report INTC-SR-084. ISOLDE and Neutron Time-of-Flight Committee. Geneva, Switzerland: European Organization for Nuclear Research (CERN), Sept. 2019.

[150] Xiaofei Yu and Larry Zamick. "Surface delta interaction in the g7/2-d5/2 model space". In: *Nuclear Physics A* 949 (2016), pp. 1–7. ISSN: 0375-9474.

[151] J.-M. Régis et al. "The generalized centroid difference method for picosecond sensitive determination of lifetimes of nuclear excited states using large fast-timing arrays". In: *Nuclear Instruments and Methods in Physics Research Section A: Accelerators, Spectrometers, Detectors and Associated Equipment* 726 (2013), pp. 191–202. ISSN: 0168-9002.

[152] Masayasu Ishihara. "RIKEN radioactive beam experiments". In: *Nuclear Physics A* 538 (1992), pp. 309–319. ISSN: 0375-9474.

[153] T. Motobayashi et al. "Large deformation of the very neutron-rich nucleus 32Mg from intermediate-energy Coulomb excitation". In: *Physics Letters B* 346.1 (1995), pp. 9–14. ISSN: 0370-2693.

[154] RIKEN Nishina Center for Accelerator-Based Science (RNC). *RIBF Facility Upgrade Project*. July 2023. URL: https://www.nishina.riken.jp/researcher/RIBFupgrade/RIBF_Upgrade_NCAC.pdf.

[155] X. Liu et al. "In-beam gamma-ray spectroscopy of 100Sn". In: *RIKEN Accel. Prog. Rep.* 58 (2024).

[156] V. Golovin and V. Saveliev. "Novel type of avalanche photodetector with Geiger mode operation". In: *Nuclear Instruments and Methods in Physics Research Section A: Accelerators, Spectrometers, Detectors and Associated Equipment* 518.1 (2004). Frontier Detectors for Frontier Physics: Proceedin, pp. 560–564. ISSN: 0168-9002.

[157] *2740/2745 64 Channel 16 bit 125 MS/s Digitizer*. CAEN SpA. 2025.

[158] P. Doornenbal. *Manual of a GEANT4 Simulation Code for Gamma-Ray Detectors used in the RIKEN-RIBF Facility*. 2011.

[159] G. Hagen, G. R. Jansen, and T. Papenbrock. "Structure of ^{78}Ni from First-Principles Computations". In: *Phys. Rev. Lett.* 117 (17 Oct. 2016), p. 172501.

[160] Kei Kamada et al. "Cz grown 2-in. size Ce:Gd3(Al,Ga)5O12 single crystal; relationship between Al, Ga site occupancy and scintillation properties". In: *Optical Materials* 36.12 (2014), pp. 1942–1945.

[161] *SILICONE GREASE EJ-550, EJ-552*. Eljen Technology. 2023.

[162] Victor R. Weidner and Jack J. Hsia. "Reflection properties of pressed polytetrafluoroethylene powder". In: *J. Opt. Soc. Am.* 71.7 (July 1981), pp. 856–861.

[163] Yao Zhu et al. "Scintillation properties of GAGG:Ce ceramic and single crystal". In: *Optical Materials* 105 (2020), p. 109964. ISSN: 0925-3467.

[164] *NHQ High Voltage Power Supplies*. Iseg. 2025.

[165] *LM94021/LM94021Q Multi-Gain Analog Temperature Sensor*. Texas Instruments. 2013.

[166] Hidetada Baba. Private Communication. 2023.

[167] *800 MHz, 50 mW Current Feedback Amplifier AD8001*. Analog Devices.

[168] Guohao Ren et al. “Non-uniformity of light output in large-sized CsI(Tl) crystals grown by non-vacuum Bridgman method”. In: *Nuclear Instruments and Methods in Physics Research Section A: Accelerators, Spectrometers, Detectors and Associated Equipment* 564.1 (2006), pp. 364–369. ISSN: 0168-9002.

[169] P. Schury et al. “A low-cost power supply for silicon photomultupliers”. In: *RIKEN Accelerator Progress Report* 58 (2025).

[170] M.P. Taggart, M. Nakhostin, and P.J. Sellin. “Investigation into the potential of GAGG:Ce as a neutron detector”. In: *Nuclear Instruments and Methods in Physics Research Section A: Accelerators, Spectrometers, Detectors and Associated Equipment* 931 (2019), pp. 121–126. ISSN: 0168-9002.

[171] Richard S. Woolf et al. “High-Energy Neutron Response of the HR-GAGG Scintillation Crystal”. In: *2020 IEEE Nuclear Science Symposium and Medical Imaging Conference (NSS/MIC)*. 2020, pp. 1–3.

[172] L. Green, J. A. Mitchell, and N. M. Steen. “The Californium-252 Fission Neutron Spectrum from 0.5 to 13 MeV”. In: *Nuclear Science and Engineering* 50.3 (1973), pp. 257–272.

[173] *N6730/N6725 8-Channel 14-bit 500/250 MS/s Waveform Digitizer*. CAEN SpA. 2023.

[174] Natalia Zaitseva et al. “Pulse Shape Discrimination in Impure and Mixed Single-Crystal Organic Scintillators”. In: *IEEE Transactions on Nuclear Science* 58.6 (2011), pp. 3411–3420.

[175] Natalia Zaitseva et al. “Plastic scintillators with efficient neutron/gamma pulse shape discrimination”. In: *Nuclear Instruments and Methods in Physics Research Section A: Accelerators, Spectrometers, Detectors and Associated Equipment* 668 (2012), pp. 88–93. ISSN: 0168-9002.

[176] Suzanne F. Nowicki, Stephen A. Wender, and Michael Mocko. “The Los Alamos Neutron Science Center Spallation Neutron Sources”. In: *Physics Procedia* 90 (2017). Conference on the Application of Accelerators in Research and Industry, CAARI 2016, 30 October – 4 November 2016, Ft. Worth, TX, USA, pp. 374–380. ISSN: 1875-3892.

[177] Hiroshi Ito et al. “Analyzing the neutron and gamma-ray emission properties of an americium–beryllium tagged neutron source”. In: *Nuclear Instruments and Methods in Physics Research Section A: Accelerators, Spectrometers, Detectors and Associated Equipment* 1057 (2023), p. 168701. ISSN: 0168-9002.

[178] Rurie Mizuno et al. “Response of germanium detectors for high-energy gamma-rays by 27Al(p, gamma)28Si at Ep = 992 keV”. In: *Progress of Theoretical and Experimental Physics* 2023.5 (Apr. 2023), 053H01. ISSN: 2050-3911.

[179] H. H. Woodbury, A. V. Tollestrup, and R. B. Day. “Low-Energy Gamma Radiation from the Bombardment of Carbon by Protons”. In: *Phys. Rev.* 93 (6 Mar. 1954), pp. 1311–1314.

[180] R. Middleton. “A survey of negative ions from a cesium sputter source”. In: *Nuclear Instruments and Methods* 144.3 (1977), pp. 373–399. ISSN: 0029-554X.

[181] Y Ikeda, M Hamagaki, and H Sato. “Operation of the Pelletron tandem accelerator”. In: *RIKEN Accelerator Progress Report* 51 (2018).

[182] R.J. Van De Graaff. “Tandem Electrostatic Accelerators”. In: *Nuclear Instruments and Methods* 8.2 (1960), pp. 195–202. ISSN: 0029-554X.

[183] *TMP35/TMP36/TMP37*. Analog Devices.

[184] Analog Devices. *LTspice*. https://www.analog.com/en/resources/design-tools-and-calculators/ltspice-simulator.html. Accessed: 2025-08-15.

[185] Peng Peng et al. “Characterization of silicon photomultipliers and validation of the electrical model”. In: *Nuclear Instruments and Methods in Physics Research Section A: Accelerators, Spectrometers, Detectors and Associated Equipment* 887 (2018), pp. 144–149. ISSN: 0168-9002.

[186] *A7585D / DT5485P-PB Digital Controlled SiPM Power Supplies*. CAEN SpA. 2021.

[187] *DT5730/DT5725 8-Channel 14-bit 500/250 MS/s Digitizer*. CAEN SpA. 2025.

[188] Joshua Sharpe. Private Communication. 2026.

[189] J. J. Valiente-Dobón et al. “Lifetime Measurements of the Neutron-Rich $N = 30$ Isotones ^{50}Ca and ^{51}Sc: Orbital Dependence of Effective Charges in the fp Shell”. In: *Phys. Rev. Lett.* 102 (24 June 2009), p. 242502.